It's about time: novel drug discovery concepts for the molecular pharmacological characterization fo the cannabinoid CB2 receptor

Bouma, J.

It's about time

Novel drug discovery concepts for the molecular pharmacological characterization of the cannabinoid CB_2 receptor

Jara Bouma

Cover design and thesis layout by Jara Bouma

This thesis was printed by Ridderprint, the Netherlands | www.ridderprint.nl

It's about time

Novel drug discovery concepts for the molecular pharmacological characterization of the cannabinoid CB_2 receptor

Proefschrift

ter verkrijging van
de graad van doctor aan de Universiteit Leiden,
op gezag van rector magnificus prof.dr.ir. H. Bijl,
volgens besluit van het college voor promoties
te verdedigen op woensdag 11 september 2024
klokke 13:00 uur

door

Jara Bouma
geboren te Woerden, Nederland
in 1996

Promotores:
Prof.dr. L.H. Heitman
Prof.dr. M. van der Stelt

Promotiecommissie:
Prof.dr. H. Irth
Prof.dr. E.C.M. de Lange
Prof.dr. M. Schmidt (Rijksuniversiteit Groningen)
Prof.dr. M. Glass (University of Otago)
Dr. J.R. Lane (University of Nottingham)
Dr. E. Neubert

The research in this thesis was performed at the Division of Medicinal Chemistry of the Leiden Academic Centre for Drug Research (LACDR), Leiden University, the Netherlands. This project has received funding from the Dutch Research Council (NWO, Vidi #16573).

Table of contents

Chapter 1

General introduction

1.1 G protein-coupled receptors

G protein-coupled receptors (GPCRs) comprise the largest family of membrane-bound proteins in the human body and consist of at least 800 family members. These receptors play a crucial role in the regulation of a plethora of physiological processes due to their activation by hormones, neurotransmitters, ions, lipids, and other stimuli[1,2]. Initially, GPCRs were named according to the A-F system (class A-F and O), which covers on top of human GPCRs also the receptors in vertebrates and invertebrates[3]. An alternative classification system was employed for human GPCRs only, which subdivided them into five families following the GRAFS classification: *glutamate* (corresponding to class C), *rhodopsin* (class A), *adhesion*, *frizzled/taste2* and *secretin* (class B)[4]. Of these, the rhodopsin/class A family is the largest, consisting of over 700 receptors, and most diverse[5]. Although different in their sequences, structure and binding partners, GPCRs share a similar overall structure that is characterized by an extracellular N-terminus (N-term), seven transmembrane (TM) helices that are connected by extra- and intracellular loops (ECLs and ICLs, respectively) and an intracellular C-terminus (C-term) (**Figure 1.1**)[2]. On top of this, unique patterns of conserved amino acids or motifs have been described for this family[6]. Specifically, these include the DRY, CWxP and NPxxY motifs, where the letters refer to the amino acid codes and x indicates variable amino acids[2,6]. These conserved motifs are pivotal for stabilization and activation of GPCRs[2]. Furthermore, conserved amino acids in each of the TM helices are used to assign the Ballesteros-Weinstein numbering[7]. To this end, the helix number, 1-7, is combined with residue numbers based on the most conserved residue being defined as number 50 and the other residues counted directly within the protein sequence[7,8]. This strategy provides the opportunity to consistently describe class A GPCRs and compare structural features across receptor subtypes, species or receptor subfamilies, as well as mutation effects and ligand interactions.

GPCRs may undergo various conformational changes upon binding of endogenous or exogenous agonists, and consequently activate downstream signaling pathways[5,9]. The transduction of extracellular stimuli to intracellular effects is primarily mediated by coupling or recruitment of proteins to the receptor[9–11]. Three classes of signal transducers, i.e., G proteins, G protein-coupled receptor kinases (GRKs) and ß-arrestins, specifically engage with activated GPCRs and induce different cellular effects (**Figure 1.1**)[10].

G protein signaling is considered the canonical pathway after GPCR activation, which follows a general initial mechanism (**Figure 1.1**). The heterotrimeric G proteins, which are composed of α, β and γ subunits, are bound by a guanosine diphosphate (GDP) at the Gα subunit in their inactive state. Upon binding of an extracellular stimulus to the GPCR, GDP is exchanged for guanosine triphosphate (GTP), which promotes conformational changes in the subunits and as a consequence, the Gα and Gβγ subunits dissociate to modulate effector proteins[12,13]. There are various α, β, and γ subunit types, which provides a large assortment of heterotrimeric G protein compositions[13]. The Gα proteins can be divided into four major subfamilies ($G\alpha_s$, $G\alpha_i$, $G\alpha_{q/11}$ and $G\alpha_{12/13}$), which each have distinct activation profiles via different effector proteins[14]. Conversion of adenosine triphosphate (ATP) into cyclic adenosine monophosphate (cAMP) by the adenylate cyclase (AC) can be stimulated via the $G\alpha_s$ subfamily and inhibited via $G\alpha_i$ proteins. On the other hand,

the $G\alpha_{q/11}$ subfamily activates phospholipase C to increase calcium levels, while $G\alpha_{12/13}$ family members activate Rho GTPases[13,15]. Gβγ heterodimeric subunits, which can further be subdivided into five Gβ and thirteen Gγ subunits, may induce the modulation of ion channels, while also acting as scaffolds for other effector proteins[14,16]. Ultimately, effector proteins can regulate downstream signaling processes including, but not limited to, kinase activation, gene transcription, motility and contractility[14,17]. Noteworthy, not all class A GPCRs show detectable coupling with G proteins, evident for the atypical chemokine receptors, which signal solely via recruitment of ß-arrestins[18].

Recruitment of arrestins to an activated GPCR is the consequence of phosphorylation of its ICLs and C-terminus by GRKs (**Figure 1.1**)[19]. There are seven GRK subtypes and four arrestins of which GRK3, 5 and 6 and arrestin isoforms 2 and 3 (ß-arrestin-1 and ß-arrestin-2, respectively) are widely expressed in the human body, while other subtypes are restricted to specific cellular or tissue compartments[19]. The recruitment of ß-arrestins to activated and phosphorylated GPCRs serves various multifaceted functions. First, binding of ß-arrestins to an activated GPCR prevents further coupling of a G protein by steric hindrance and as such leads to the termination of G protein signaling, often referred to as desensitization[20]. Secondly, and probably best known, is the internalization of the active receptor from the membrane to clathrin-coated pits. Subsequently, GPCRs are trafficked to endosomes from where they could be either recycled back to the plasma membrane or degraded (**Figure 1.1**)[21]. Thirdly, ß-arrestins act as scaffolds and regulators for over 100 intracellular proteins, which lead to the activation of various other pathways, including mitogen-activated protein kinase (MAPK) and extracellular signal-related kinase 1 and 2 (ERK1/2) signaling[22–24]. In the past, ß-arrestin signaling has often been called the G protein-independent pathway, however over the years this concept has been challenged. Various studies now report that ß-arrestin recruitment and signaling requires initial G protein coupling[25,26]. Altogether, this underlines the extraordinarily complex nature of GPCR activation and downstream signaling events.

Nevertheless, GPCRs provide great opportunities for pharmacological targeting due to their involvement in the regulation of many physiological processes by binding of a plethora of extracellular ligands. In 2019, at least 36% of the marketed pharmaceutical drugs already targeted GPCRs[27,28]. However, there is a high attrition rate of ligands in clinical development due to efficacy and safety issues, making this an expensive and tedious process[29]. To this end, it has been hypothesized that novel perspectives and drug discovery concepts may aid in selecting better drug candidates for clinical development[30,31]. In this chapter, specifically drug-target binding kinetics, allosteric modulation and biased signaling will be further described.

→ Figure 1.1 Simplified overview of GPCR structure, activation and downstream signaling.
General GPCR structure with N-terminus (N-term), seven transmembrane (TM) helices connected by extracellular and intracellular loops (ECL, ICL) and an intracellular C-terminus (C-term). Upon activation of a GPCR by an agonist, G proteins exchange GDP for GTP, which causes dissociation of the Gα and Gβγ subunits. $G\alpha_i$ and $G\alpha_s$ inhibit and stimulate the adenylate cyclase (AC), respectively, and subsequently the conversion of ATP into cAMP. In turn, this can regulate downstream signaling processes (not shown in figure), ultimately leading to regulation of gene transcription. Binding of an agonist may also induce phosphorylation by G protein-coupled receptor kinases (GRKs) of the C-terminus and recruitment of ß-arrestin. This could initiate internalization to endosomes and either recycling to the cell membrane or degradation of the receptor. Additionally, activation of downstream signaling processes may occur via ß-arrestin (not shown). For simplification, $G\alpha_{q/11}$, $G\alpha_{12/13}$ and Gβγ signaling are not included into the figure. This figure incorporates drawings from Servier Medical Art (smart.servier.com).

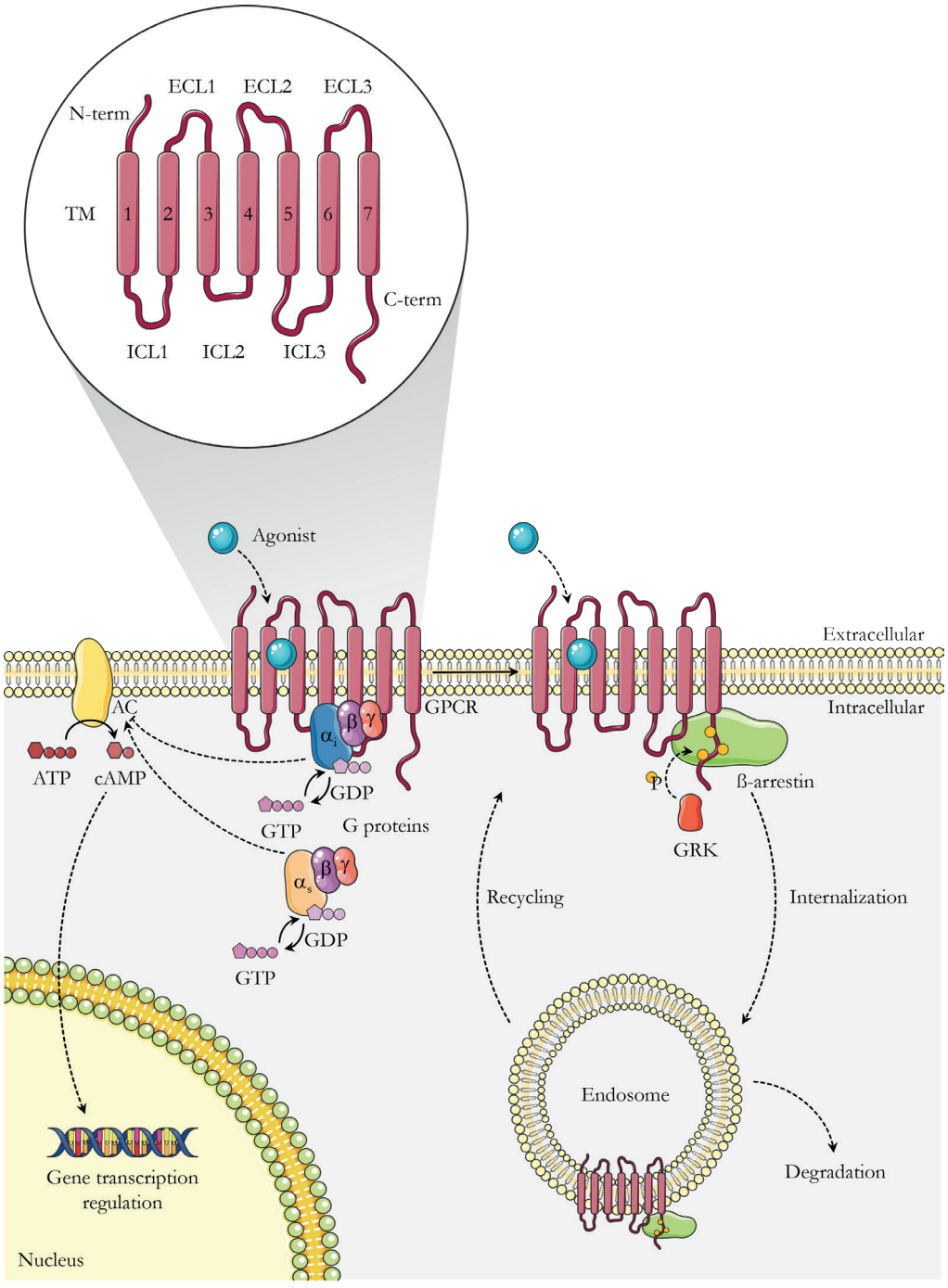
ECL1
ECL2
ECL3
N-term
TM
1
2
3
4
5
6
7
C-term
ICL1
ICL2
ICL3
Agonist
Extracellular
Intracellular
AC
GPCR
ATP
cAMP
GDP
GTP
G proteins
ß-arrestin
P
GRK
Recycling
Internalization
Endosome
Degradation
Gene transcription
regulation
Nucleus

1.2 Drug-target binding kinetics

In 2006, Copeland and colleagues presented the drug-target binding kinetics model, which they suggested would present a better prediction of drug efficacy and safety *in vivo* by focusing on the dynamic interactions between a drug and target[32]. Up until that time, drug discovery focused on the measurement of so-called equilibrium or end-point values, such as target affinity in terms of half-maximal inhibitory concentration (IC_{50}) and inhibition constant (K_i), or functional potency (pEC_{50}) and efficacy (E_{max}). These parameters are often determined in *in vitro* assays under equilibrium conditions, where drug and target concentrations remain constant over time[33]. However, these conditions do not capture the complexity of an open system, such as the human body, in which ligand concentrations vary over time due to pharmacokinetic processes such as absorption, distribution, metabolism and excretion (ADME)[33]. Therefore, it was proposed that the period of time for which a drug is bound to the target and can exert its pharmacological action is more predictive for drug efficacy *in vivo*[32]. The formation of the drug-target, or ligand-receptor, complex is described by two processes; the association of the ligand to the target, defined by the association rate constant (k_{on}), and thereafter the dissociation from the target, defined the by dissociation rate constant (k_{off}) (**Figure 1.2**). Subsequently, the ratio between the k_{off} and the k_{on} values can be defined as the kinetic affinity (K_D)[33]. These rate constants can be adequately determined in *in vitro* assays and the residence time (RT), as a description of the time a ligand is bound to the receptor, can be defined as the reciprocal of the dissociation rate constant[33].

The primary focus since the introduction of the concept has been on the investigation and optimization of RT since a drug is only effective when bound to its target. An increased RT is generally hypothesized to explain the longer duration of *in vivo* efficacy. However, it is dependent on the disease whether a short or long RT ligand is preferred[34,35]. A prolonged duration of action, as a consequence of a long-acting agonist, may be sustained long after

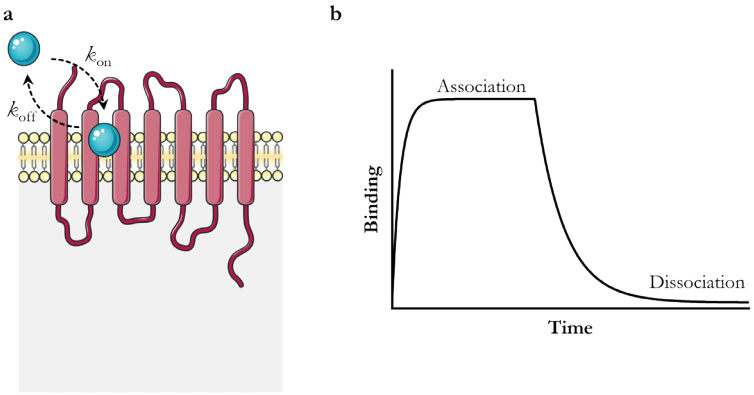

Figure 1.2 Graphical representation of target binding kinetics.
(a) The dynamic process of ligand binding and unbinding to and from a GPCR is characterized by the association rate constant (k_{on}) and the dissociation rate constant (k_{off}) of the ligand. (b) Binding of a (radio)ligand can be measured over time until equilibrium (plateau) is reached. In the absence of free ligand, the ligand can dissociate from the target over time. This figure incorporates drawings from Servier Medical Art (smart.servier.com).

the drug is cleared from the bloodstream, i.e., a long RT could challenge the pharmacokinetic parameters of a ligand[36]. On the other hand, slowly dissociating antagonists, known as insurmountable antagonists, inhibit or attenuate endogenous receptor signaling by sustained receptor blockade for a certain amount of time and as such regulate the native response[35]. The duration of receptor blockade can be increased with the use of irreversible, covalent, binders[37]. Moreover, kinetic selectivity of ligands, characterized by an increased RT for the target of interest, while having a shorter RT for off-target proteins, could contribute to a high target selectivity *in vivo* even in the absence of selectivity in equilibrium assays[38]. Nevertheless, the lifetime of the protein target may limit the utility of long RT ligands, as long RT ligands will be degraded along with the protein in the case of a rapid turnover of the target *in vivo*[36].

Initially, the association rate constant was thought to be diffusion controlled and as such would remain equal to the diffusion rate limit (~10^8 - 10^9 $M^{-1}s^{-1}$)[39]. Nevertheless, various studies have reported different association rate constants, which rejects this hypothesis and emphasizes that the k_{on} value is a ligand-specific parameter[40]. Consequently, the determination of k_{on} values is becoming increasingly more important. However, opposed to the k_{off} value, the k_{on} value is physicochemically and pharmacologically constrained and highly depends on the ligand concentration[32]. This suggests that increasing the ligand concentration, i.e., the dose, can compensate for a low k_{on} value. On the other hand, a high k_{on} value can increase the local concentration of ligand, which in turn will increase the chances of rebinding. Ultimately, this provides the possibility of extending the intracellular RT and as such increase the duration of the pharmacological effect[36,41,42]. In the case of a RT shorter than the pharmacokinetic parameters, increasing the association rate constant may provide an alternative strategy to enhance the target occupation[43]. Furthermore, a high k_{on} value may allow for more rapid therapeutic action, which could be favorable dependent on the disease type[34].

Importantly, investigation of the drug-target binding kinetics of ligands has been shown, albeit retrospectively, to contribute to the success of several marketed drugs on GPCRs[44]. In the case of the muscarinic M_3 receptor antagonist tiotropium, the sustained bronchodilation in chronic obstructive pulmonary disease (COPD) patients is attributed to the slow dissociation rate (RT 27 h) while fast dissociating antagonists with similar affinities and potencies provided less bronchoprotection[45]. Furthermore, tiotropium has a kinetic subtype selectivity for the muscarinic M_3 receptor over the muscarinic M_2 receptor, despite similar affinities for both receptors[45]. This highlights the importance of investigation of drug-target binding kinetics in early drug discovery programs for a more rational selection of hit candidates.

1.3 Allosteric modulation

Another approach of targeting GPCRs is by allosteric modulation of the receptor opposed to more traditional orthosteric binding. Orthosteric ligands bind to the same site as the endogenous ligand(s), i.e., the orthosteric binding site, whereas allosteric ligands target a topographically distinct binding site[46]. While orthosteric binding sites are under strong

evolutionary selection and as such highly conserved among receptor families, allosteric binding sites share a lower sequence homology and are thus generally less conserved between receptor subtypes which might be driven by a need for specificity[47,48]. Consequently, allosteric ligands can provide a greater subtype selectivity[46,49]. While orthosteric binding sites of membrane receptors are usually found at the extracellular site, the locations of allosteric binding sites are diverse and span the entire receptor surface[50]. Allosteric modulators are usually devoid of intrinsic agonistic properties, but upon simultaneous binding with an endogenous or orthosteric agonist they can alter the affinity and efficacy of the orthosteric ligand (**Figure 1.3**)[49,51]. Allosteric modulators that negatively affect affinity and/or efficacy of an orthosteric ligand are called negative allosteric modulators (NAMs), while positive allosteric modulators (PAMs) enhance these parameters (**Figure 1.3a**,**b**). Finally, neutral allosteric ligands (NALs) occupy the allosteric binding pocket without affecting the affinity and/or efficacy of the orthosteric ligand but they prevent further binding of PAMs or NAMs (**Figure 1.3c**)[46,52]. On top of the increased selectivity, allosteric modulators provide more beneficial properties. In the presence of high concentrations of endogenous ligand, allosteric modulators can still decrease the affinity and/or efficacy of the endogenous ligand. Particularly, in disease conditions with increased concentrations of endogenous ligands

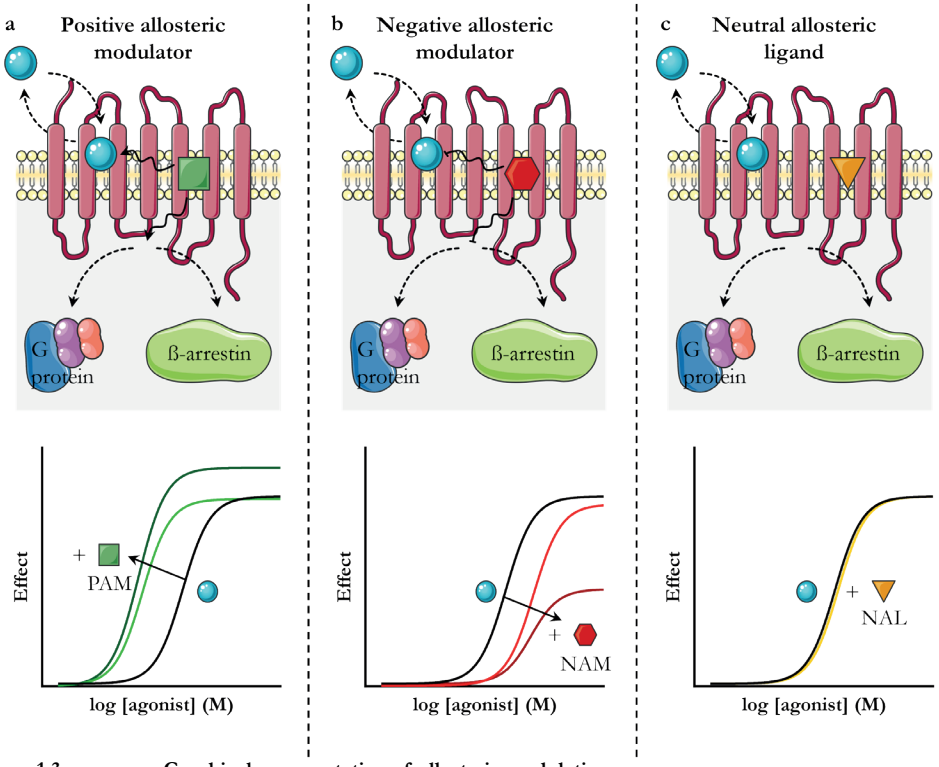

Figure 1.3 **Graphical representation of allosteric modulation.**
Allosteric modulators bind to a binding site topographically distinct from the orthosteric binding site and can affect the binding and functional effect of orthosteric ligands. (a) Positive allosteric modulators (PAMs) enhance the affinity and efficacy of the orthosteric ligand, while (b) negative allosteric modulators (NAMs) inhibit the affinity and efficacy of the orthosteric ligand. (c) Neutral allosteric ligands (NALs) occupy the allosteric binding pocket without affecting the affinity or efficacy of the orthosteric ligand but prevent further binding of PAMs or NAMs. This figure incorporates drawings from Servier Medical Art (smart.servier.com).

this insurmountability of allosteric modulators may play an important role[53]. Moreover, allosteric modulators have a 'ceiling effect', i.e., there is a limit to the pharmacological effect that can be mediated via allosteric binding due to saturation of the effect once the allosteric site is fully occupied[51,53].

Despite these advantages of allosteric over orthosteric targeting, very few allosteric modulators of GPCRs have made it to the market[54]. The first GPCR allosteric modulator that was approved by the United States Food and Drug Administration (FDA) for clinical use was cinacalcet[55,56]. Cinacalcet is a PAM for the calcium-sensing receptor (CaR), a class C GPCR, and is used for treating parathyroid cancer and secondary hyperparathyroidism. Moreover, advanced clinical trials are ongoing with several allosteric modulators for class A GPCRs, such as PAM Mevidalen (LY3154207), which enhances the affinity of dopamine for the dopamine D_1 receptor and is currently investigated for the symptomatic treatment of patients with Parkinson disease[57,58].

1.4 Biased signaling

Biased signaling, also known as ligand bias, biased agonism or functional selectivity, reflects the ability of a ligand to preferentially activate one pathway over another (**Figure 1.4**)[51,59,60]. This concept may become important if a specific signaling pathway is associated with efficacy and the other one with inducing side effects[59]. The rationale behind biased signaling is that different agonists can stabilize different active conformations of the receptor and consequently affect the coupling efficiency to transducers.

Biased signaling has already been described for GPCR families with multiple endogenous agonists, such as the chemokine and opioid receptors[61,62]. Moreover, exogenous biased agonists have been designed and studied, and even biased allosteric modulators (BAMs) are emerging[63]. For GPCR agonists, bias is most often studied between G protein coupling and ß-arrestin recruitment. However, bias may also occur within the G protein or ß-arrestin families[64,65]. Nevertheless, studying ligand bias is very complex and many factors may confound conclusions drawn about bias[31,59]. This can relate to the cellular background, referred to as system bias, by different concentrations and stoichiometry of receptor, transducers and effectors[59]. Alternatively, the experimental setup could introduce observational bias, which may be due to an artificially high level of signal amplification or the choice of specific time points[59,66].

Clinical relevance of biased agonists has only very recently been acknowledged, evident by the FDA approval of the first biased agonist oliceridine in 2020 to adults experiencing moderate to severe acute pain[67]. Oliceridine, a μ-opioid receptor agonist, was at the time described to be biased towards G protein activation over ß-arrestin recruitment. However, its therapeutic efficacy due to a biased profile is currently disputed and may relate to its partial agonism in one pathway[68]. Retrospectively more biased ligands are already on the market but were previously not described as such. An example is carvedilol, a commonly used ß-blocker, which is a functional antagonist for G protein-mediated signaling but an agonist for ß-arrestin-mediated signaling[69].

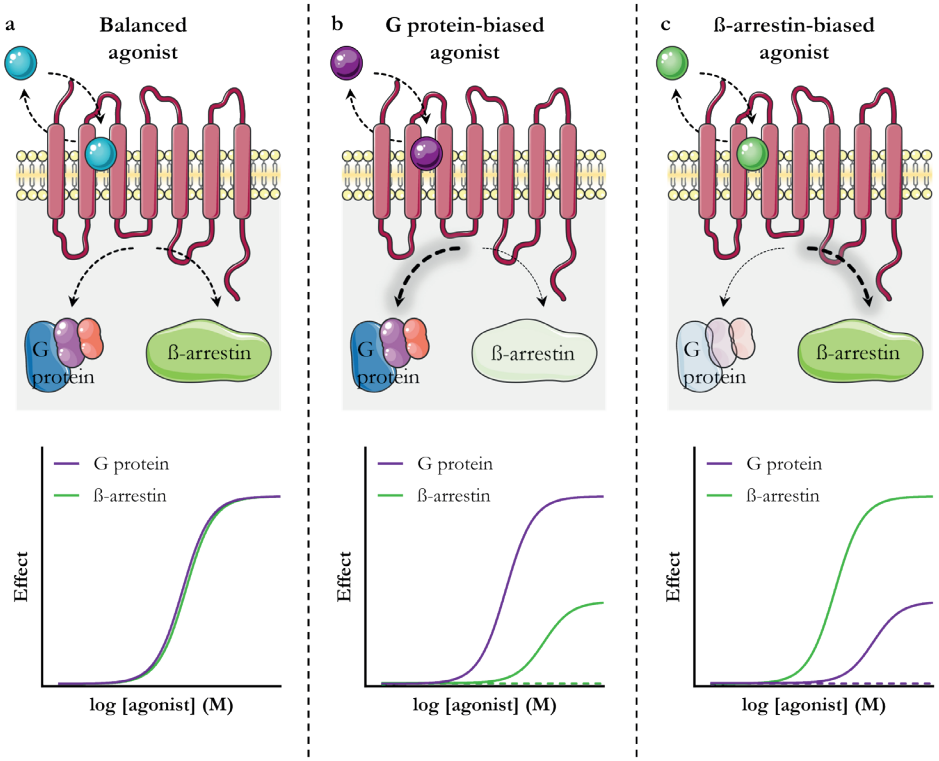

Figure 1.4 **Graphical representation of biased signaling.**
(a) A balanced agonist equally activates two pathways, such as G protein and ß-arrestin signaling. (b) A G protein-biased agonist preferentially activates G protein signaling, while ß-arrestin signaling is reduced or absent. (c) A ß-arrestin-biased agonist preferentially activates ß-arrestin signaling, while G protein activation is reduced or absent. This figure incorporates drawings from Servier Medical Art (smart.servier.com).

1.5 Endocannabinoid system

A family of class A GPCRs are the cannabinoid receptors (CBRs). The CBRs are part of the endocannabinoid system (ECS) in the human body along with their endogenous ligands, *N*-arachidonoylethanolamide (anandamide or AEA) and 2-arachidonoylglycerol (2-AG), and their respective metabolizing enzymes[70–72]. Specifically, *N*-acylphosphatidylethanolamine-specific phospholipase D (NAPE-PLD) and diacylglycerol lipase (DAGL) are involved in the biosynthesis of AEA and 2-AG, respectively, but formation may also occur via parallel routes and proteins. The degradation of AEA and 2-AG is primarily mediated by fatty-acid amide hydrolases (FAAH) and monoacylglycerol lipase (MAGL), respectively[70]. The endocannabinoids (eCBs) AEA and 2-AG activate two types of CBRs, the cannabinoid CB_1 and CB_2 receptors (CB_1R and CB_2R)[72]. The receptors derive their name from the discovery that active components from *Cannabis sativa*, such as the main psychoactive constituent Δ^9-tetrahydrocannabinol (Δ^9-THC), bound and activated these GPCRs. CB_1R and CB_2R share an overall homology of 44% and an even larger homology of 68% in their seven transmembrane domains which includes their ligand binding domains[73]. However, the receptors display a distinct tissue expression. CB_1R is highly expressed in the central

nervous system and is responsible for the psychotropic effects of Δ^9-THC. It is involved in the regulation of various physiological functions, including memory, learning and appetite. Although CB_2R expression in brain regions is heavily debated, it is evident that this receptor is predominantly expressed on immune cells and lymphatic organs. Consequently, activation of CB_2Rs plays a significant role in the regulation of several inflammatory processes[74,75]. After activation both CB_1R and CB_2R couple to $G\alpha_{i/o}$ proteins, which in turn inhibits cAMP production in cells. Furthermore, activation can lead to activation of pERK and G protein-coupled Inward Rectifying K^+-channels (GIRKs) as well as recruitment of ß-arrestin-1 and 2[65,76,77]. CB_1R can additionally bind $G\alpha_{12/13}$ proteins and activate their corresponding transduction pathways[65], which has not been shown for CB_2R.

Currently, several drugs are on the market that rely on components from *Cannabis sativa* or synthetic analogs thereof[75]. Dronabinol, synthetic Δ^9-THC, is prescribed to patients suffering from anorexia, cachexia and chemotherapy-induced emesis[78]. Similarly, a synthetic Δ^9-THC analog, Nabilone, is also approved for its antiemetic effects and specifically used for the treatment of chemotherapy-induced nausea and vomiting (CINV)[75]. Cannabidiol (CBD), marketed as Epidiolex, is prescribed to patients over 1 year old with severe forms of epilepsy such as the Lennox-Gastaut and Dravet syndrome[79]. Furthermore, CBD-containing oils and infused beverages are sold over the counter to the general public[80]. Finally, mixtures of Δ^9-THC and CBD, e.g., Sativex® (1:1 ratio) are approved for the treatment of multiple sclerosis-associated spasticity[81]. Nevertheless, Dronabinol and Nabilone bind and activate both CB_1R and CB_2R, whereas CBD exerts its effects via various additional proteins[75,82]. As activation of CB_1R is associated with the psychoactive effects of cannabinoid ligands, selective activation of CB_2R may provide a therapeutically interesting treatment strategy without inducing psychotropic effects[83].

1.6 Therapeutic potential for CB_2R

The protective effect of CB_2R activation has been indicated for neuroinflammatory and neurodegenerative disorders, including severe diseases as Alzheimer's disease (AD), Parkinsons's disease (PD), multiple sclerosis (MS) and amyotrophic lateral sclerosis (ALS), via dampening the inflammatory responses[84,85]. Furthermore, a reduction in the inflammatory response, by inhibition of leukocyte proliferation and reduced secretion of pro-inflammatory cytokines, may be beneficial in autoimmune diseases such as arthritis, scleroderma and inflammatory bowel disease (IBS)[86]. CB_2R agonists could also provide antinociceptive effects in various pain conditions, both in acute and persistent pain as well as for neuropathic pain[87]. Moreover, increased CB_2R levels have been reported in various cancer types, and agonists are described to have antitumor effects on top of the current palliative use of cannabinoid-based treatments[88–91].

To date, a large diversity of selective CB_2R agonists has been developed for preclinical investigation, which increases our understanding of targeting CB_2R[83]. Multiple CB_2R agonists have progressed to clinical development since 2010, but the majority has been discontinued due to a variety of reasons including a narrow safety margin, lack of pharmacological effect, or development has been halted due to practical reasons such as the closure of the

company[75]. Challenges in the poor preclinical to clinical translation of CB_2R agonists have been hypothesized to include, but are not limited to, a lack of translational animal models for proper biological evaluation or the potential of differential signaling bias at the receptor level although disease relevant pathways have not yet been demonstrated[75,83,92].

1.7 Aim and outline of this thesis

The potential for incorporating novel concepts in early phases of drug discovery to provide a more accurate translational perspective has been receiving increasing attention. However, limited number of studies are available for CB_2R agonist binding kinetics[93,94], allosteric modulation[95] or biased signaling[76,77,96–101] and they are generally considered as individual concepts. Therefore, *it's about time* that we further investigate and connect these novel concepts on CB_2R to improve our molecular pharmacological understanding of targeting the receptor. In this thesis, the target-binding kinetics and biased signaling of CB_2R agonists are explored, as well as allosteric modulation of the receptor by small molecules. To this end, state-of-the-art assays are used in conjunction with the design of novel methodologies. Central to the investigation of CB_2R pharmacology is providing an overall kinetic view on drug discovery.

Chapter 2 provides a step-by-step protocol for the quick and straightforward investigation of ß-arrestin-2 recruitment to stimulated CB_2R and CB_1R by agonists and inverse agonists, which is further applied in **Chapter 5**. **Chapter 3** reports a novel assay to simultaneously and kinetically detect cAMP signaling and ß-arrestin-2 recruitment after CB_2R stimulation in one cellular system. This multiplex assay is applied to a set of clinically relevant CB_2R agonists and the time-dependency of biased signaling is explored. Functional and binding kinetics are combined to obtain a holistic overview of the kinetic context of agonist-mediated CB_2R. **Chapter 4** describes the extensive profiling of a novel hydrophilic CB_2R-selective ligand, LEI-102, by the use of structural, *in vitro* and *in vivo* experimentation. Combining mutagenesis data and target binding kinetics suggests a distinct entry pathway for lipophilic agonists. In **Chapter 5**, allosteric modulation of CB_2R by small molecules is explored. CBD-DMH emerged from a newly adapted radioligand dissociation assay and is further screened on allosteric and orthosteric behavior in *in vitro* assays, including the methodology described in **Chapter 2**. In **Chapter 6,** a translation to the patient is made by investigation of the effect of cancer-associated mutations in CB_2R on receptor activation and ligand binding. Finally, **Chapter 7** provides an overall conclusion of the novel findings described in this thesis and new perspectives and opportunities for drug discovery on CB_2R and other GPCRs.

References

1. Rosenbaum, D. M., Rasmussen, S. G. F. & Kobilka, B. K. The structure and function of G-protein-coupled receptors. *Nature* **459**, 356–363 (2009).
2. Schiöth, H. B. & Lagerström, M. C. Structural diversity of G protein-coupled receptors and significance for drug discovery. *Nat Rev Drug Discov* **7**, 339–357 (2008).
3. Attwood, T. K. & Findlay, J. B. C. Fingerprinting G-protein-coupled receptors. *Protein Eng* **7**, 195–203 (1994).
4. Fredriksson, R., Lagerström, M. C., Lundin, L.-G. & Schiöth, H. B. The G-Protein-Coupled Receptors in the Human Genome Form Five Main Families. Phylogenetic Analysis, Paralogon Groups, and Fingerprints. *Mol Pharmacol* **63**, 1256–1272 (2003).
5. Yang, D. *et al.* G protein-coupled receptors: structure- and function-based drug discovery. *Signal Transduct Target Ther* **6**, (2021).
6. Rovati, G. E., Capra, V. & Neubig, R. R. The highly conserved DRY motif of class A G protein-coupled receptors: Beyond the ground state. *Mol Pharmacol* **71**, 959–964 (2007).
7. Ballesteros, J. A. & Weinstein, H. [19] Integrated Methods for the Construction of Three-Dimensional Models and Computational Probing of Structure-Function Relations in G Protein-Coupled Receptors. in *Methods in neurosciences* 336–428 (Academic Press, 1995).
8. Isberg, V. *et al.* Generic GPCR residue numbers - Aligning topology maps while minding the gaps. *Trends Pharmacol Sci* **36**, 22–31 (2015).
9. Gurevich, V. V. & Gurevich, E. V. Molecular mechanisms of GPCR signaling: A structural perspective. *Int J Mol Sci* **18**, (2017).
10. Eichel, K. & von Zastrow, M. Subcellular Organization of GPCR Signaling. *Trends Pharmacol Sci* **39**, 200–208 (2018).
11. Pavlos, N. J. & Friedman, P. A. GPCR Signaling and Trafficking: The Long and Short of It. *Trends in Endocrinology and Metabolism* **28**, 213–226 (2017).
12. Mahoney, J. P. & Sunahara, R. K. Mechanistic insights into GPCR–G protein interactions. *Curr Opin Struct Biol* **41**, 247–254 (2016).
13. Syrovatkina, V., Alegre, K. O., Dey, R. & Huang, X. Y. Regulation, Signaling, and Physiological Functions of G-Proteins. *J Mol Biol* **428**, 3850–3868 (2016).
14. Wootten, D., Christopoulos, A., Marti-Solano, M., Babu, M. M. & Sexton, P. M. Mechanisms of signalling and biased agonism in G protein-coupled receptors. *Nat Rev Mol Cell Biol* **19**, 638–653 (2018).
15. Rasheed, S. A. K. *et al.* The emerging roles of Gα12/13 proteins on the hallmarks of cancer in solid tumors. *Oncogene* **41**, 147–158 (2022).
16. Ford, C. E. *et al.* Molecular Basis for Interactions of G Protein Subunits with Effectors. *Science (1979)* **280**, 1271–1273 (1998).
17. Neves, S. R., Ram, P. T. & Iyengar, R. G Protein Pathways. *Science (1979)* **296**, 1636–1639 (2002).
18. Dekkers, S. *et al.* Small Molecule Fluorescent Ligands for the Atypical Chemokine Receptor 3 (ACKR3). *ACS Med Chem Lett* **15**, 143–148 (2024).
19. Luttrell, L. M. & Gesty-Palmer, D. Beyond Desensitization: Physiological Relevance of Arrestin-Dependent Signaling. *Pharmacol Rev* **62**, 305–330 (2010).
20. Shenoy, S. K. & Lefkowitz, R. J. β-arrestin-mediated receptor trafficking and signal transduction. *Trends Pharmacol Sci* **32**, 521–533 (2011).
21. DeWire, S. M., Ahn, S., Lefkowitz, R. J. & Shenoy, S. K. β-Arrestins and Cell Signaling. *Annu Rev Physiol* **69**, 483–510 (2007).
22. Kawakami, K. *et al.* Heterotrimeric Gq proteins act as a switch for GRK5/6 selectivity underlying β-arrestin transducer bias. *Nat Commun* **13**, (2022).
23. Crépieux, P. *et al.* A comprehensive view of the ß-arrestinome. *Front Endocrinol (Lausanne)* **8**, (2017).
24. Kahsai, A. W. *et al.* Signal transduction at GPCRs: Allosteric activation of the ERK MAPK by β-arrestin. *Proc Natl Acad Sci U S A* **120**, (2023).
25. Grundmann, M. *et al.* Lack of beta-arrestin signaling in the absence of active G proteins. *Nat Commun* **9**, (2018).
26. Gurevich, V. V. & Gurevich, E. V. Arrestins and G proteins in cellular signaling: The coin has two sides. *Sci Signal* **11**, (2018).
27. Hauser, A. S., Attwood, M. M., Rask-Andersen, M., Schiöth, H. B. & Gloriam, D. E. Trends in GPCR drug discovery: New agents, targets and indications. *Nat Rev Drug Discov* **16**, 829–842 (2017).
28. Chan, H. C. S., Li, Y., Dahoun, T., Vogel, H. & Yuan, S. New Binding Sites, New Opportunities for GPCR Drug Discovery. *Trends Biochem Sci* **44**, 312–330 (2019).

29. Waring, M. J. *et al.* An analysis of the attrition of drug candidates from four major pharmaceutical companies. *Nat Rev Drug Discov* **14**, 475–486 (2015).
30. Janero, D. R. Current strategic trends in drug discovery: the present as prologue. *Expert Opin Drug Discov* **19**, 147–159 (2023).
31. Nagi, K. How can we improve the measurement of receptor signaling bias? *Expert Opin Drug Discov* **18**, 575–578 (2023).
32. Copeland, R. A., Pompliano, D. L. & Meek, T. D. Drug–target residence time and its implications for lead optimization. *Nat Rev Drug Discov* **5**, 730–739 (2006).
33. Copeland, R. A. The drug–target residence time model: a 10-year retrospective. *Nat Rev Drug Discov* **15**, 87–95 (2016).
34. van der Velden, W. J. C., Heitman, L. H. & Rosenkilde, M. M. Perspective: Implications of Ligand−Receptor Binding Kinetics for Therapeutic Targeting of G Protein-Coupled Receptors. *ACS Pharmacol. Transl. Sci* **2020**, 179–189 (2020).
35. Guo, D., Hillger, J. M., IJzerman, A. P. & Heitman, L. H. Drug-Target Residence Time-A Case for G Protein-Coupled Receptors. *Med Res Rev* **34**, 856–892 (2014).
36. Knockenhauer, K. E. & Copeland, R. A. The importance of binding kinetics and drug–target residence time in pharmacology. *Br J Pharmacol* (2023).
37. Vauquelin, G., Van Liefde, I., Birzbier, B. B. & Vanderheyden, P. M. L. New insights in insurmountable antagonism. *Fundam Clin Pharmacol* **16**, 263–272 (2002).
38. Tonge, P. J. Drug-Target Kinetics in Drug Discovery. *ACS Chem Neurosci* **9**, 29–39 (2018).
39. Smith, G. F. Medicinal chemistry by the numbers: the physicochemistry, thermodynamics and kinetics of modern drug design. *Prog Med Chem* **48**, 1–29 (2009).
40. IJzerman, A. P. & Guo, D. Drug–Target Association Kinetics in Drug Discovery. *Trends Biochem Sci* **44**, 861–871 (2019).
41. Vauquelin, G. Effects of target binding kinetics on in vivo drug efficacy: k_{off}, k_{on} and rebinding. *Br J Pharmacol* **173**, 2319–2334 (2016).
42. Vauquelin, G. & Charlton, S. J. Long-lasting target binding and rebinding as mechanisms to prolong in vivo drug action. *Br J Pharmacol* **161**, 488–508 (2010).
43. de Witte, W. E. A., Vauquelin, G., van der Graaf, P. H. & de Lange, E. C. M. The influence of drug distribution and drug-target binding on target occupancy: The rate-limiting step approximation. *European Journal of Pharmaceutical Sciences* **109**, S83–S89 (2017).
44. Liu, H., Zhang, H., IJzerman, A. P. & Guo, D. The translational value of ligand-receptor binding kinetics in drug discovery. *Br J Pharmacol* (2023).
45. Casarosa, P. *et al.* Preclinical evaluation of long-acting muscarinic antagonists: Comparison of tiotropium and investigational drugs. *Journal of Pharmacology and Experimental Therapeutics* **330**, 660–668 (2009).
46. Christopoulos, A. *et al.* International union of basic and clinical pharmacology. XC. Multisite pharmacology: Recommendations for the nomenclature of receptor allosterism and allosteric ligands. *Pharmacol Rev* **66**, 918–947 (2014).
47. Wagner, J. R. *et al.* Emerging Computational Methods for the Rational Discovery of Allosteric Drugs. *Chem Rev* **116**, 6370–6390 (2016).
48. Hedderich, J. B. *et al.* The pocketome of G-protein-coupled receptors reveals previously untargeted allosteric sites. *Nature Communications 2022 13:1* **13**, 1–12 (2022).
49. Christopoulos, A. & Kenakin, T. G protein-coupled receptor allosterism and complexing. *Pharmacol Rev* **54**, 323–374 (2002).
50. Thal, D. M., Glukhova, A., Sexton, P. M. & Christopoulos, A. Structural insights into G-protein-coupled receptor allostery. *Nature* **559**, 45–53 (2018).
51. Kenakin, T. P. Biased signalling and allosteric machines: new vistas and challenges for drug discovery. *Br J Pharmacol* **165**, 1669 (2012).
52. Lane, J. R., May, L. T., Parton, R. G., Sexton, P. M. & Christopoulos, A. A kinetic view of GPCR allostery and biased agonism. *Nat Chem Biol* **13**, 929–937 (2017).
53. Ortiz Zacarías, N. V., Lenselink, E. B., IJzerman, A. P., Handel, T. M. & Heitman, L. H. Intracellular Receptor Modulation: Novel Approach to Target GPCRs. *Trends Pharmacol Sci* **39**, 547–559 (2018).
54. Wenthur, C. J., Gentry, P. R., Mathews, T. P. & Lindsley, C. W. Drugs for allosteric sites on receptors. *Annu Rev Pharmacol Toxicol* **54**, 165–184 (2014).
55. Nemeth, E. F. Allosteric modulators of the extracellular calcium receptor. *Drug Discov Today Technol* **10**, (2013).

56. Jensen, A. A. & Bräuner-Osborne, H. Allosteric Modulation of the Calcium-Sensing Receptor. *Curr Neuropharmacol* **5**, 180–186 (2007).

57. Wilbraham, D. *et al.* Safety, Tolerability, and Pharmacokinetics of Mevidalen (LY3154207), a Centrally Acting Dopamine D1 Receptor–Positive Allosteric Modulator, in Patients With Parkinson Disease. *Clin Pharmacol Drug Dev* **11**, 324–332 (2022).

58. Hao, J. *et al.* Synthesis and Pharmacological Characterization of 2-(2,6-Dichlorophenyl)-1-((1 S,3 R)-5-(3-hydroxy-3-methylbutyl)-3-(hydroxymethyl)-1-methyl-3,4-dihydroisoquinolin-2(1 H)-yl)ethan-1-one (LY3154207), a Potent, Subtype Selective, and Orally Available Positive Allosteric Modulator of the Human Dopamine D1 Receptor. *J Med Chem* **62**, 8711–8732 (2019).

59. Kolb, P. *et al.* Community guidelines for GPCR ligand bias: IUPHAR review 32. *Br J Pharmacol* **179**, 3651–3674 (2022).

60. Kenakin, T. Biased Receptor Signaling in Drug Discovery. *Pharmacol Rev* **71**, 267–315 (2019).

61. Steen, A., Larsen, O., Thiele, S. & Rosenkilde, M. M. Biased and G protein-independent signaling of chemokine receptors. *Front Immunol* **5**, (2014).

62. Gomes, I. *et al.* Biased signaling by endogenous opioid peptides. *Proceedings of the National Academy of Sciences* **117**, 11820–11828 (2020).

63. Slosky, L. M., Caron, M. G. & Barak, L. S. Biased Allosteric Modulators: New Frontiers in GPCR Drug Discovery. *Trends Pharmacol Sci* **42**, 283–299 (2021).

64. French, A. R., Meqbil, Y. J. & van Rijn, R. M. ClickArr: a novel, high-throughput assay for evaluating β-arrestin isoform recruitment. *Front Pharmacol* **14**, (2023).

65. Hauser, A. S. *et al.* Common coupling map advances GPCR-G protein selectivity. *Elife* **11**, (2022).

66. Klein Herenbrink, C. *et al.* The role of kinetic context in apparent biased agonism at GPCRs. *Nat Commun* **7**, 10842 (2016).

67. Markham, A. Oliceridine: First Approval. *Drugs* **80**, 1739–1744 (2020).

68. Mullard, A. FDA approves first GPCR biased agonist. *Nat Rev Drug Discov* **19**, 659 (2020).

69. Kim, J. *et al.* The β-arrestin-biased β-adrenergic receptor blocker carvedilol enhances skeletal muscle contractility. *Proceedings of the National Academy of Sciences* **117**, 12435–12443 (2020).

70. Maccarrone, M. *et al.* Goods and Bads of the Endocannabinoid System as a Therapeutic Target: Lessons Learned after 30 Years. *Pharmacol Rev* **75**, 885–958 (2023).

71. Howlett, A. C. *et al.* International Union of Pharmacology. XXVII. Classification of cannabinoid receptors. *Pharmacol Rev* **54**, 161–202 (2002).

72. Pertwee, R. G. *et al.* International Union of Basic and Clinical Pharmacology. LXXIX. Cannabinoid Receptors and Their Ligands: Beyond CB_1 and CB_2. *Pharmacol Rev* **62**, 588–631 (2010).

73. Munro, S., Thomas, K. L. & Abu-Shaar, M. Molecular characterization of a peripheral receptor for cannabinoids. *Nature* **365**, 61–65 (1993).

74. Simard, M., Rakotoarivelo, V., Di Marzo, V. & Flamand, N. Expression and Functions of the CB_2 Receptor in Human Leukocytes. *Front Pharmacol* **13**, (2022).

75. Brennecke, B. *et al.* Cannabinoid receptor type 2 ligands: An analysis of granted patents since 2010. *Pharm Pat Anal* **10**, 111–163 (2021).

76. Soethoudt, M. *et al.* Cannabinoid CB_2 receptor ligand profiling reveals biased signalling and off-target activity. *Nat Commun* **8**, 1–14 (2017).

77. Ibsen, M. S., Connor, M. & Glass, M. Cannabinoid CB_1 and CB_2 Receptor Signaling and Bias. *Cannabis Cannabinoid Res* **2**, 48–60 (2017).

78. Badowski, M. E. & Yanful, P. K. Dronabinol oral solution in the management of anorexia and weight loss in AIDS and cancer. *Ther Clin Risk Manag* **14**, 643–651 (2018).

79. Zhou, Q. *et al.* Adverse events of epidiolex: A real-world drug safety surveillance study based on the FDA adverse event reporting system (FAERS) database. *Asian J Psychiatr* **90**, 103828 (2023).

80. Miller, O. S., Elder, E. J., Jones, K. J. & Gidal, B. E. Analysis of cannabidiol (CBD) and THC in nonprescription consumer products: Implications for patients and practitioners. *Epilepsy & Behavior* **127**, 108514 (2022).

81. Jones, É. & Vlachou, S. A Critical Review of the Role of the Cannabinoid Compounds Δ^9-Tetrahydrocannabinol (Δ^9-THC) and Cannabidiol (CBD) and their Combination in Multiple Sclerosis Treatment. *Molecules* **25**, 4930 (2020).

82. Castillo-Arellano, J., Canseco-Alba, A., Cutler, S. J. & León, F. The Polypharmacological Effects of Cannabidiol. *Molecules* **28**, (2023).

83. Whiting, Z. M., Yin, J., de la Harpe, S. M., Vernall, A. J. & Grimsey, N. L. Developing the Cannabinoid Receptor 2 (CB2) pharmacopoeia: past, present, and future. *Trends Pharmacol Sci* **43**, 754–771 (2022).

84. Cassano, T. *et al.* Cannabinoid receptor 2 signaling in neurodegenerative disorders: From pathogenesis to a promising therapeutic target. *Front Neurosci* **11**, 30 (2017).

85. Cabral, G. A. & Griffin-Thomas, L. T. Emerging role of the cannabinoid receptor CB_2 in immune regulation: Therapeutic prospects for neuroinflammation. *Expert Rev Mol Med* **11**, (2009).

86. Katchan, V., David, P. & Shoenfeld, Y. Cannabinoids and autoimmune diseases: A systematic review. *Autoimmun Rev* **15**, 513–528 (2016).

87. Guindon, J. & Hohmann, A. G. Cannabinoid CB_2 receptors: a therapeutic target for the treatment of inflammatory and neuropathic pain. *Br J Pharmacol* **153**, 319–334 (2008).

88. Hinz, B. & Ramer, R. Anti-tumour actions of cannabinoids. *Br J Pharmacol* **176**, 1384–1394 (2019).

89. Mangal, N. *et al.* Cannabinoids in the landscape of cancer. *J Cancer Res Clin Oncol* **147**, 2507–2534 (2021).

90. Ladin, D. A., Soliman, E., Griffin, L. T. & Van Dross, R. Preclinical and clinical assessment of cannabinoids as anti-cancer agents. *Front Pharmacol* **7**, 361 (2016).

91. Gambacorta, N. *et al.* Exploring the 1,3-benzoxazine chemotype for cannabinoid receptor 2 as a promising anti-cancer therapeutic. *Eur J Med Chem* **259**, 115647 (2023).

92. Carruthers, E. R. & Grimsey, N. L. Cannabinoid CB_2 receptor orthologues; in vitro function and perspectives for preclinical to clinical translation. *Br J Pharmacol* (2023).

93. Soethoudt, M. *et al.* Structure-kinetic relationship studies of cannabinoid CB_2 receptor agonists reveal substituent-specific lipophilic effects on residence time. *Biochem Pharmacol* **152**, 129–142 (2018).

94. Martella, A. *et al.* A Novel Selective Inverse Agonist of the CB_2 Receptor as a Radiolabeled Tool Compound for Kinetic Binding Studies. *Mol Pharmacol* **92**, 389–400 (2017).

95. Gado, F. *et al.* Allosteric modulators targeting cannabinoid cb1 and cb2 receptors: implications for drug discovery. *Future Med Chem* **11**, 2019–2037 (2019).

96. Dhopeshwarkar, A. & Mackie, K. Functional selectivity of CB_2 cannabinoid receptor ligands at a canonical and noncanonical pathways. *Journal of Pharmacology and Experimental Therapeutics* **358**, 342–351 (2016).

97. Zagzoog, A. *et al.* Assessment of select synthetic cannabinoid receptor agonist bias and selectivity between the type 1 and type 2 cannabinoid receptor. *Sci Rep* **11**, 10611 (2021).

98. Oyagawa, C. R. M. *et al.* Cannabinoid Receptor 2 Signalling Bias Elicited by 2,4,6-Trisubstituted 1,3,5-Triazines. *Front Pharmacol* **9**, 1202 (2018).

99. Atwood, B. K., Wager-Miller, J., Haskins, C., Straiker, A. & Mackie, K. Functional Selectivity in CB_2 Cannabinoid Receptor Signaling and Regulation: Implications for the Therapeutic Potential of CB_2 Ligands. *Mol Pharmacol* **81**, 250–263 (2012).

100. Sharma, R. *et al.* Novel Cannabinoid Receptor 2 (CB2) Low Lipophilicity Agonists Produce Distinct cAMP and Arrestin Signalling Kinetics without Bias. *Int J Mol Sci* **24**, 6406 (2023).

101. Patel, M., Grimsey, N. L., Banister, S. D., Finlay, D. B. & Glass, M. Evaluating signaling bias for synthetic cannabinoid receptor agonists at the cannabinoid CB_2 receptor. *Pharmacol Res Perspect* **11**, (2023).

Chapter 2

Cellular assay to study β-arrestin recruitment by the cannabinoid CB_1 and CB_2 receptor

Jara Bouma, Marjolein Soethoudt, Noortje van Gils, Lizi Xia,
Mario van der Stelt, Laura H. Heitman

Adapted from: *Endocannabinoid Signaling. Methods in Molecular Biology*
(2022) **2576**, 189-199

Abstract

Cannabinoid CB_1 and CB_2 receptors (CB_1R and CB_2R) are G protein-coupled receptors (GPCRs) that activate a variety of pathways upon activation by (partial) agonists, including the G protein pathway and the recruitment of β-arrestins. Differences in activation level of these pathways leads to biased signaling. In this chapter, we describe a detailed protocol to characterize the potency and efficacy of ligands to induce or inhibit β-arrestin-2 recruitment to the human CB_1R and CB_2R using the PathHunter® assay. This is a cellular assay that uses a β-galactosidase complementation system which has a chemiluminescent read-out and can be performed in 384-well plates. We have successfully used this assay to characterize a set of reference ligands (both agonists, antagonists, and an inverse agonist) on human CB_1R and CB_2R, of which some examples will be presented here.

2.1 Introduction

Cannabinoid CB_1 and CB_2 receptors (CB_1R, CB_2R) are members of the G protein-coupled receptor (GPCR) superfamily[1]. Due to their localization, they regulate distinct physiological processes such as the control of cognition, memory and motor function for CB_1R, while CB_2R modulates (neuro)inflammatory processes[2]. Both receptors couple mostly to $G\alpha_{i/o}$ proteins to inhibit the activity of adenylate cyclase, activate the mitogen-activated protein kinase (MAPK) pathway and influence several ion channels[3,4]. Additionally, upon agonist stimulation CB_1R and CB_2R both recruit β-arrestin-2 to inactivate the receptors due to desensitization and internalization, but they only have a weak interaction with β-arrestin-1[5–7].

Following GPCR activation, some ligands preferentially modulate specific pathways over others. This concept of biased signaling, biased agonism or functional selectivity may increase drug effectiveness by selectively targeting the signaling pathways involved in the therapeutic effects and to move away from on-target side effects through other pathways[8–10]. This concept has also been thoroughly investigated and reviewed for both CB_1R and CB_2R, indicating biased signaling between G proteins and β-arrestin-2[11–18].

To characterize the potency and efficacy of cannabinoid receptor ligands to recruit β-arrestin-2, we have employed the previously reported β-arrestin PathHunter® assay[19,20]. This assay is an easy-to-use endpoint assay that has shown to deliver reproducible results and was successfully applied to measure β-arrestin-2 recruitment for a variety of cannabinoid receptor ligands[21–25]. In this assay, β-arrestin-2 activity is measured in live cells by using a

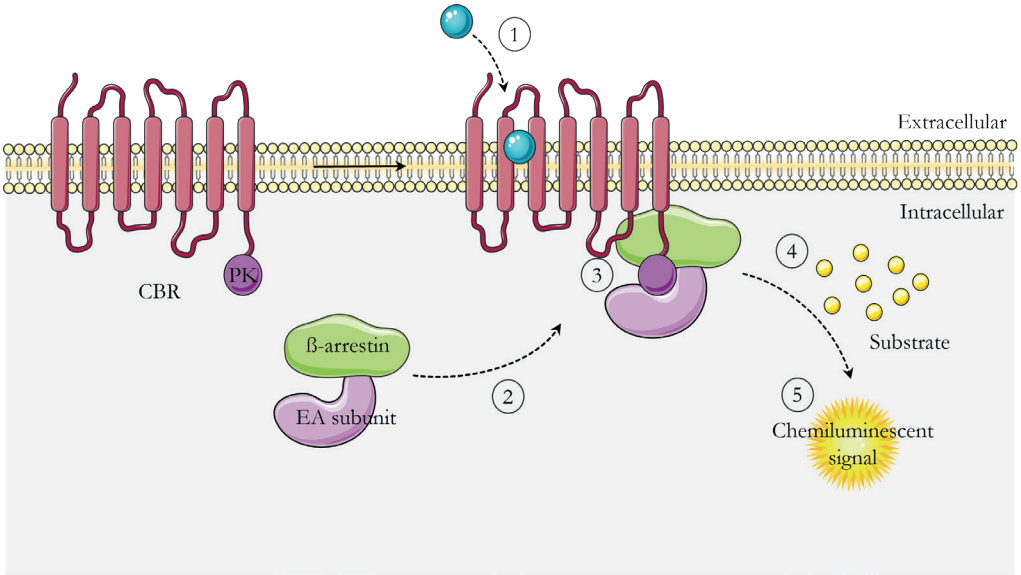

Figure 2.1 Schematic representation of the β-arrestin recruitment assay.
Upon activation of the receptor by a ligand (1), the inactive β-arrestin-EA complex is recruited to the receptor (2). This induces the complementation with the ProLink™ enzyme fragment (PK) to form an active β-galactosidase enzyme (3). The enzyme then reacts with the substrate in the PathHunter® detection reagent mixture (4), which results in a chemiluminescent signal that is directly related to the amount of β-arrestin-2 recruited to the activated receptor (5). The complemented enzyme remains receptor bound, but this is not shown in the figure for clarity reasons. This figure incorporates drawings from Servier Medical Art (smart.servier.com).

β-galactosidase fragment complementation technology and a chemiluminescent read-out (**Figure 2.1**)[26,27]. The DiscoverX PathHunter® cell lines overexpress a GPCR of interest, in this case either the human CB_1R or CB_2R, which are tagged at the C-terminus by a small donor fragment of β-galactosidase called ProLink™ (PK). Additionally, these cells stably co-express β-arrestin-2, which is fused with the catalytically inactive N-terminal deletion mutant fragment of the β-galactosidase, i.e. the enzyme acceptor (EA)[20,26]. Activation of CB_1R or CB_2R will cause recruitment of the β-arrestin-EA complex to the PK-tagged receptor, which induces the complementation of the two enzyme fragments. Subsequently, this results in the formation of an active β-galactosidase. The active enzyme is able to convert an added substrate into a chemiluminescent product[19,20,26]. The light emission by this product is directly related to the activity of the β-galactosidase, and thus the level of β-arrestin-2 recruitment to the receptor after ligand binding[23,26,28]. In addition, its 384-well format enables high-throughput screening, a useful feature in early drug discovery research.

Of note, recent observations have shown that kinetics of cell signaling processes are important for the interpretation of agonist behavior and biased signaling[29–32]. As a consequence, novel β-arrestin assays have been developed which focus on a kinetic readout such as the bioluminescence resonance energy transfer (BRET) assays[5,33] and the luminescent NanoBiT assay[34]. In these assays, the receptor of interest is transfected into a chosen cell system. This provides an added advantage, since the effect of "system bias", i.e., bias caused by differential expression or amplification of second messengers depending on tissue or cell background, can be eliminated by the use of one cell system[8,35]. We envision that the field of cannabinoid receptor research will also move into the direction of kinetic signaling assays to further explore the concept of biased signaling.

2.2 Materials

All buffers and solutions are prepared using Millipore water (deionized using a MilliQ A10 Biocel™, with a 0.22 μm filter) and analytical grade reagents and solvents. Buffers are prepared at room temperature (rt) and stored at 4 °C, unless stated otherwise. Cannabinoid receptor reference ligand CP55,940 was obtained from Sigma Aldrich (St. Louis, MO), JWH133 was from Tocris BioScience (Bristol, United Kingdom), SR144528 and SR141716A were from Cayman Chemical Company (Ann Arbor, MI) and WIN55,212-2 was received from Hoffman-La Roche (Basel, Switzerland).

2.2.1 Cell Culture

1. Cells: PathHunter® CHO-K1 β-Arrestin Cell Line CNR1 or CNR2 (DiscoverX), overexpressing the CB_1R or CB_2R respectively. In this thesis, these cells are named $CHOK1hCB_1$_bgal or $CHOK1hCB_2$_bgal.
2. Phosphate buffered saline (PBS): 1.9 mM KH_2PO_4, 136.9 mM NaCl, 8.0 mM Na_2HPO_4, 3.4 mM KCl.
3. Trypsin solution: 0.25% trypsin in PBS, containing 0.44 mM EDTA.

4. Cell culture medium: Ham's F12 Nutrient Mixture supplemented with 10% (v/v) fetal calf serum (FCS), 2 mM Glutamax, 50 µg/mL Penicillin/Streptomycin, 800 µg/mL G418 and 300 µg/mL Hygromycin. The antibiotic stock solutions can be pre-made and stored at -20 °C. Once the medium is made, store at 4 °C, but warm to 37 °C before use.
5. 10 cm ø culture dishes.
6. To count cells prior to seeding into plates, an automatic cell counter can be used, such as a TC10™ automated cell counter.

2.2.2 Assay

1. Ligands are prepared as DMSO stock solutions prior to testing, for example as 10 mM stocks. However, the endocannabinoids (anandamide and 2-arachidonoylglycerol) are unstable in DMSO, and therefore stock solutions (e.g., 10 mM) are prepared in acetonitrile. Stock solutions of most ligands are stable at -20 °C, but one should always be cautious with using stock solutions for longer periods of time. Product stability and purity should be checked regularly.
2. Cells are seeded into white walled, solid bottom 384-well assay plates with low fluorescence background (*see* **Note 1** and **2**).

2.2.3 Detection and data processing

1. Detection is done with the PathHunter detection kit® (DiscoverX). The detection mixture is prepared as follows (*see* **Note 3**): Cell assay buffer = 19 parts, Substrate Reagent 1 = 5 parts, Substrate Reagent 2 = 1 part, according to the manufacturer's protocol[36].
2. Measurement of the plates can be done by any multimode, or luminescence plate reader, for example a Wallac EnVision™ 2104 Multilabel reader.
3. Analysis of raw experimental data can be performed using the nonlinear regression curve fitting program GraphPad Prism 9.0.

2.3 Methods

All procedures should be carried out at rt, unless specified otherwise.

2.3.1 Cell culture

1. The CHOK1hCB$_1$_bgal and CHOK1hCB$_2$_bgal cells are subcultured twice a week when reaching ~85-90% confluency on 10 cm ø plates in cell culture medium in a humidified atmosphere at 37 °C and 5% CO_2.

2. Remove medium from the plate and wash the cells with 5 mL PBS.
3. Add 1 mL trypsin solution and incubate at 37 °C for maximally 5 minutes.
4. Gently detach the cells and resuspend in 4 mL cell culture medium.
5. Subculture the cells according to their confluence in fresh cell culture medium, for example in a ratio between 1:12-1:20. Each subculture step is one passage.
6. For the assay, cells should be passaged at least 3× and no more than 24× (max. 3 months in culture). Additionally, do not let the cells grow >90% confluency prior to harvesting for the assay.

2.3.2 Ligands under investigation

1. High throughput screening can be performed using a single high concentration of each ligand (Z' factor > 0.7[37]). Often a final concentration of 10 μM is used. Full dose-response curves of ligands are necessary for determination of their potency and efficacy.
2. Stock solutions of ligands under investigation are made in DMSO or acetonitrile. These stock solutions should be diluted to the desired concentration in cell culture medium. Make sure there is an equal amount of organic solvent (e.g., DMSO or acetonitrile) present in every dilution (*see* **Note 4**). For (inverse) agonistic assays, compound dilutions should be 5× the desired final concentration, while for antagonistic assays (and the EC_{80} of a reference agonist) the pre-made concentrations should be 10x the desired final concentration.
3. In all assays the E_{max} of a reference full agonist should be taken along (e.g., CP55,940 at 1 μM final concentration).
4. When investigating activation by the endocannabinoids, cells should be preincubated for 30 minutes with 50 μM phenylmethylsulphonyl fluoride (PMSF, final concentration) prior to endocannabinoid treatment (*see* **Note 5**).

2.3.3 Cell seeding

1. Remove the medium and wash the cells with 5 mL PBS.
2. Harvest the cells with 1 mL trypsin solution and incubate for maximally 5 min. at 37 °C and 5% CO_2.
3. Inactivate the trypsin solution by addition of 4 mL cell culture medium.
4. Transfer the cells to a Falcon tube and spin down (5 min. at 1000 rpm/200 × g).
5. Resuspend the pellet well in 1 mL cell culture medium and count living cells in an automated cell counter by addition of 10 μL cell suspension to 10 μL Trypan Blue.
6. Dilute the cells further with cell culture medium to get a density of 250,000 cells/mL (= 5,000 cells/well).
7. Add 20 μL of cell suspension per well of the 384-well plate. Make sure that you fill enough wells for control measurements: only medium (negative control),

unstimulated cells with organic solvent equal to assay (basal activity), cells stimulated by a full agonist, e.g., CP55,940 (positive control), cells stimulated by EC_{80} of reference agonist (positive control in case of an antagonistic assay).

8. Incubate cells overnight (between 16-18 hours) at 37 °C and 5% CO_2.

2.3.4 Cell stimulation and incubation

2.3.4.1 Antagonistic assay

1. Dilute antagonists of interest into cell culture medium to 10× the desired final concentration (*see* **Note 4**).
2. Add 2.5 µL antagonist solution per well.
3. Incubate 30 min. at 37 °C and 5% CO_2.
4. Add 2.5 µL of a 10× EC_{80} solution of CP55,940 to all wells (EC_{80} of CP55,940 needs to be determined prior to this assay), including wells for background measurements.
5. Incubate 90 min. at 37 °C and 5% CO_2.

2.3.4.2 Agonistic assay

1. Dilute agonists of interest into cell culture medium to 5× the desired final concentration (*see* **Note 4**).
2. Add 5 µL agonist solution per well.
3. Incubate 90 min. at 37 °C and 5% CO_2.

2.3.4.3 Inverse agonistic assay

1. Dilute inverse agonists of interest into cell culture medium to 5× the desired final concentration (*see* **Note 4**).
2. Add 5 µL inverse agonist solution per well.
3. Incubate 6 hours at 37 °C and 5% CO_2.

2.3.5 Detection and measurements

1. Add 12.5 µL/well of detection mixture to all wells.
2. Incubate 60 min. **in the dark** at rt.
3. Measure the chemiluminescent response by a multimode or luminescence plate reader (*see* **Note 6**).

2.3.6 Data analysis

Raw experimental data is analyzed using the nonlinear regression curve fitting program GraphPad Prism. All data points are corrected for all background conditions (negative control and basal activity). The response of (inverse) agonists is normalized to the maximum effect of a reference agonist (e.g., 1 µM CP55,940) and the response of antagonists is normalized to the EC_{80} of a reference full agonist (e.g., CP55,940). Basal activity of the cells is set at 0%. Potency, inhibitory potency, or efficacy values (EC_{50}, IC_{50} or E_{max}, respectively) of ligands can be obtained by choosing the nonlinear regression option "log (agonist or inhibitor) vs response".

2.3.7 Results

We applied the protocol described here to characterize the well-known cannabinoid receptor reference ligands CP55,940, WIN55,212-2, JWH133, SR141716A (Rimonabant) and SR144528 (see **Figure 2.2** and **Table 2.1**). We found that our findings correlate well with literature[18,38,39].

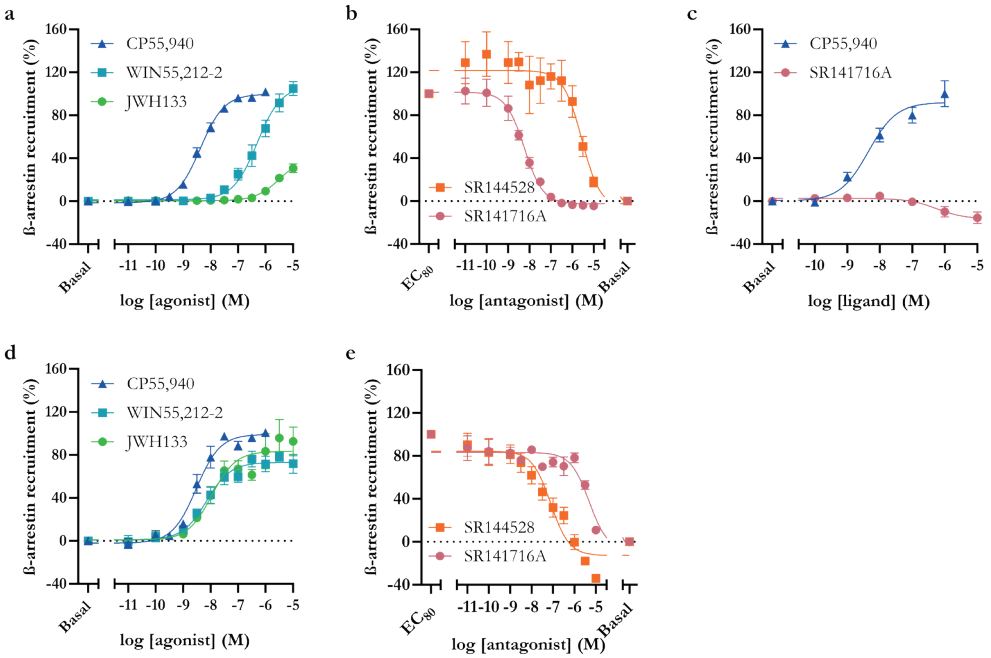

Figure 2.2 Dose-response curves of cannabinoid ligands on β-arrestin recruitment in PathHunter® CHOK1hCB$_1$_bgal or CHOK1hCB$_2$_bgal cells.

β-arrestin recruitment after activation for 90 min with increasing concentrations of (a, d) agonists, (b, e) pre-incubation with the EC_{80} concentration of CP55,940 followed by antagonist treatment or (c) stimulation with (inverse) agonist for 6 hours on human CB_1R or CB_2R. Basal activity of the cells was set at 0% and the efficacy was calculated as (a, c, d) a percentage of the maximum effect induced by 1 µM CP55,940 or (b, e) EC_{80} concentration of CP55,940 (25 or 46 nM for CB_1R and CB_2R, respectively). Data represent the mean ± SEM from at least three independent experiments performed in duplicate. Figure adapted from Soethoudt *et al.* (2016) and Xia *et al.* (2018)[40,41].

Table 2.1 **Potency and efficacy data of cannabinoid receptor ligands obtained with the PathHunter® β-arrestin recruitment assay.**

	hCB_1R		hCB_2R	
Agonists	**pEC_{50} ± SEM**	**E_{max} (%) ± SEM[a]**	**pEC_{50} ± SEM**	**E_{max} (%) ± SEM**
CP55,940	8.37 ± 0.08	102 ± 1	8.33 ± 0.18	101 ± 1
WIN55,212-2	6.30 ± 0.17	105 ± 7	8.04 ± 0.31	72 ± 9
JWH133	5.50 ± 0.01	31 ± 4	7.97 ± 0.15	93 ± 13
Antagonists	**pIC_{50} ± SEM[b]**		**pIC_{50} ± SEM**	
SR141716A	8.24 ± 0.06		5.31 ± 0.05	
SR144528	5.56 ± 0.11		7.12 ± 0.19	
Inverse agonist	**pIC_{50} ± SEM[c]**	**E_{min} (%) ± SEM[d]**	**pIC_{50} ± SEM**	**E_{min} (%) ± SEM**
SR14716A	6.25 ± 0.18	-15 ± 5	N.D.	N.D.

[a] Maximum effect (E_{max}) is determined as percentage of the maximum effect induced by 1 μM CP55,940. [b] Inhibitory potency (pIC_{50}) determined in the antagonistic assay by pre-incubation with EC_{80} of CP55,940 followed by antagonist treatment. [c] Inhibitory potency (pIC_{50}) as obtained from the inverse agonistic assay in the absence of any agonist. [d] Maximum inhibition (E_{min}) is determined in an inverse agonistic assay and normalized to the maximum effect induced by 1 μM CP55,940. Data represent the mean ± SEM from at least three independent experiments performed in duplicate. N.D. = not determined.

2.4 Notes

1. Perkin Elmer's white walled, solid bottom CulturPlate 384-well assay plates are delivered in a sterile environment. They should be kept that way by opening them only in an appropriate flow cabinet. Do not touch the plates at the bottom since greasy fingerprints can give extra background and/or decrease reading efficiency of the plate reader. Also make sure there is no dust in the wells which will give extra background and will increase well-to-well variation.
2. When working with 384-well plates, edge (or well-position) effects might occur due to differing evaporation rates of the outer wells compared to the central wells. This problem could be overcome by for example pre-incubation of the seeded cells at rt for at least 30 minutes before transferring the plate to the incubator. Alternatively, the less insulated outer wells could be filled with a fluid (sterile water/PBS/culture medium) and discarded from the experiment or a Breathe-Easy® sealing membrane (Sigma-Aldrich) could be used.
3. All PathHunter® detection reagents should be aliquoted in Eppendorf tubes and stored at -20 °C upon receipt. Reagents can only be thawed and refrozen twice. When the reagents are used for the detection mixture, they are thawed to **rt in the dark** and then mixed in the previously mentioned ratio. Once the detection mixture is made, it is stable for 24 hours at **rt in the dark**.
4. Stock solutions of ligands under investigation are made in DMSO or acetonitrile. Always make sure that there is an equal amount of organic solvent present in every dilution (≤1%) to avoid effects of the solvent. To obtain an equal concentration of organic solvent in every dilution, a dilution series in 100% DMSO or

acetonitrile should be made that is no less than 100× (agonist and inverse agonist) or 200× (antagonist or EC_{80} reference agonist) the desired final concentration. Dilute this series accordingly in cell culture medium to 5× or 10× the desired final concentration, depending on whether an agonistic or antagonistic assay is performed. Make sure there is also an equal amount of DMSO or acetonitrile in the wells for background measurements.

5. The endocannabinoids can be degraded by a variety of enzymes like fatty acid amide hydrolase (FAAH) and monoacylglycerol lipase (MAGL). To prevent this degradation in the assay, the cells should be preincubated with a serine protease inhibitor, for example PMSF, before addition of the endocannabinoids.
6. The exposure time to read samples can depend on the instrument used. For example, the settings for a Wallac EnVision™ 2104 Multilabel reader should be:
    a. Instrument settings: EnVision Single emission with single emission mirror block.
    b. Filters:
        i. Emission filter: Luminescence 700
        ii. Mirror module: Luminescence
        iii. Install the emission filter in the Emission Filter Slide correctly. The filters must occupy adjacent slots in the Emission Filter Slide.
    c. The mirror needs to be manually changed to the top position within the machine and selected in the software before use.
    d. Allow the lamp to warm up for at least 10 min.
    e. Use protocol LUM Single (1.0 s read).

References

1. Howlett, A. C. *et al.* International Union of Pharmacology. XXVII. Classification of cannabinoid receptors. *Pharmacol Rev* **54**, 161–202 (2002).
2. Pertwee, R. G. *et al.* International Union of Basic and Clinical Pharmacology. LXXIX. Cannabinoid Receptors and Their Ligands: Beyond CB_1 and CB_2. *Pharmacol Rev* **62**, 588–631 (2010).
3. Di Marzo, V., Bifulco, M. & De Petrocellis, L. The endocannabinoid system and its therapeutic exploitation. *Nat Rev Drug Discov* **3**, 771–784 (2004).
4. Ibsen, M. S., Connor, M. & Glass, M. Cannabinoid CB 1 and CB 2 Receptor Signaling and Bias. *Cannabis Cannabinoid Res* **2**, 48–60 (2017).
5. Ibsen, M. S. *et al.* Cannabinoid CB1 and CB2 Receptor-Mediated Arrestin Translocation: Species, Subtype, and Agonist-Dependence. *Front Pharmacol* **10**, (2019).
6. Luttrell, L. M. & Gesty-Palmer, D. Beyond Desensitization: Physiological Relevance of Arrestin-Dependent Signaling. *Pharmacol Rev* **62**, 305–330 (2010).
7. Gyombolai, P., Boros, E., Hunyady, L. & Turu, G. Differential β-arrestin2 requirements for constitutive and agonist-induced internalization of the CB1 cannabinoid receptor. *Mol Cell Endocrinol* **372**, 116–127 (2013).
8. Smith, J. S., Lefkowitz, R. J. & Rajagopal, S. Biased signalling: from simple switches to allosteric microprocessors. *Nat Rev Drug Discov* **17**, 243–260 (2018).
9. Kenakin, T. & Christopoulos, A. Signalling bias in new drug discovery: detection, quantification and therapeutic impact. *Nat Rev Drug Discov* **12**, 205–216 (2012).
10. Priestley, R., Glass, M. & Kendall, D. Functional Selectivity at Cannabinoid Receptors. *Adv Pharmacol* **80**, 207–221 (2017).
11. Wouters, E. *et al.* Assessment of Biased Agonism among Distinct Synthetic Cannabinoid Receptor Agonist Scaffolds. *ACS Pharmacol Transl Sci* **3**, 285 (2020).
12. Soethoudt, M. *et al.* Cannabinoid CB_2 receptor ligand profiling reveals biased signalling and off-target activity. *Nat Commun* **8**, 1–14 (2017).
13. Al-Zoubi, R., Morales, P. & Reggio, P. H. Structural insights into CB1 receptor biased signaling. *Int J Mol Sci* **20**, 1837 (2019).
14. Morales, P., Goya, P. & Jagerovic, N. Emerging strategies targeting CB_2 cannabinoid receptor: Biased agonism and allosterism. *Biochem Pharmacol* **157**, 8–17 (2018).
15. Manning, J. J., Green, H. M., Glass, M. & Finlay, D. B. Pharmacological selection of cannabinoid receptor effectors: Signalling, allosteric modulation and bias. *Neuropharmacology* **193**, 108611 (2021).
16. Wouters, E., Walraed, J., Banister, S. D. & Stove, C. P. Insights into biased signaling at cannabinoid receptors: synthetic cannabinoid receptor agonists. *Biochem Pharmacol* **169**, 113623 (2019).
17. Leo, L. M. & Abood, M. E. CB1 Cannabinoid Receptor Signaling and Biased Signaling. *Molecules* **26**, 5413 (2021).
18. Atwood, B. K., Wager-Miller, J., Haskins, C., Straiker, A. & Mackie, K. Functional Selectivity in CB_2 Cannabinoid Receptor Signaling and Regulation: Implications for the Therapeutic Potential of CB_2 Ligands. *Mol Pharmacol* **81**, 250–263 (2012).
19. Patel, A. *et al.* A combination of ultrahigh throughput PathHunter and cytokine secretion assays to identify glucocorticoid receptor agonists. *Anal Biochem* **385**, 286–292 (2009).
20. Zhao, X. *et al.* A Homogeneous Enzyme Fragment Complementation-Based β-Arrestin Translocation Assay for High-Throughput Screening of G-Protein-Coupled Receptors. *J Biomol Screen* **13**, 737–747 (2008).
21. Soethoudt, M. *et al.* Cannabinoid CB_2 receptor ligand profiling reveals biased signalling and off-target activity. *Nat Commun* **8**, 1–14 (2017).
22. Xia, L. *et al.* Kinetics of human cannabinoid 1 (CB1) receptor antagonists: Structure-kinetics relationships (SKR) and implications for insurmountable antagonism. *Biochem Pharmacol* **151**, 166–179 (2018).
23. van der Lee, M. M. C. *et al.* Pharmacological characterization of receptor redistribution and beta-arrestin recruitment assays for the cannabinoid receptor 1. *J Biomol Screen* **14**, 811–823 (2009).
24. Zagzoog, A. *et al.* Assessment of select synthetic cannabinoid receptor agonist bias and selectivity between the type 1 and type 2 cannabinoid receptor. *Sci Rep* **11**, 10611 (2021).
25. Soethoudt, M. *et al.* Selective Photoaffinity Probe That Enables Assessment of Cannabinoid CB_2 Receptor Expression and Ligand Engagement in Human Cells. *J Am Chem Soc* **140**, 6067–6075 (2018).

26. DiscoverX. PathHunter® β-Arrestin Assays. https://www.discoverx.com/technologies-platforms/enzyme-fragment-complementation-technology/cell-based-efc-assays/protein-protein-interactions/gpcrs-b-arrestin.
27. Olson, K. R. & Eglen, R. M. Galactosidase Complementation: A Cell-Based Luminescent Assay Platform for Drug Discovery Analysis of Cell Signaling and Enzyme Fragment Complementation. *Assay Drug Dev Technol* **5**, (2007).
28. van der Lee, M. M. C., Bras, M., van Koppen, C. J. & Zaman, G. J. R. β-Arrestin recruitment assay for the identification of agonists of the sphingosine 1-phosphate receptor EDG1. *J Biomol Screen* **13**, 986–998 (2008).
29. Klein Herenbrink, C. *et al.* The role of kinetic context in apparent biased agonism at GPCRs. *Nat Commun* **7**, 10842 (2016).
30. Lane, J. R., May, L. T., Parton, R. G., Sexton, P. M. & Christopoulos, A. A kinetic view of GPCR allostery and biased agonism. *Nat Chem Biol* **13**, 929–937 (2017).
31. Hoare, S. R. J., Tewson, P. H., Quinn, A. M. & Hughes, T. E. A kinetic method for measuring agonist efficacy and ligand bias using high resolution biosensors and a kinetic data analysis framework. *Scientific Reports 2020 10:1* **10**, 1766 (2020).
32. Zhu, X., Finlay, D. B., Glass, M. & Duffull, S. B. Evaluation of the profiles of CB1 cannabinoid receptor signalling bias using joint kinetic modelling. *Br J Pharmacol* **177**, 3449–3463 (2020).
33. Turu, G. *et al.* Biased Coupling to β-Arrestin of Two Common Variants of the CB_2 Cannabinoid Receptor. *Front Endocrinol (Lausanne)* **12**, 903 (2021).
34. Cannaert, A., Storme, J., Franz, F., Auwärter, V. & Stove, C. P. Detection and Activity Profiling of Synthetic Cannabinoids and Their Metabolites with a Newly Developed Bioassay. *Anal Chem* **88**, 11476–11485 (2016).
35. Gundry, J., Glenn, R., Alagesan, P. & Rajagopal, S. A practical guide to approaching biased agonism at G protein coupled receptors. *Front Neurosci* **11**, 1–6 (2017).
36. DiscoverX. User Manual PathHunter® Detection Kit. https://www.discoverx.com/DiscoveRx/media/ContentFiles/DataSheets/93-0001L.pdf.
37. DiscoverX. Enzyme Fragment Complementation Technology. https://www.discoverx.com/technologies-platforms/enzyme-fragment-complementation-technology.
38. van der Lee, M. M. C. *et al.* Pharmacological characterization of receptor redistribution and beta-arrestin recruitment assays for the cannabinoid receptor 1. *J Biomol Screen* **14**, 811–823 (2009).
39. Yin, H. *et al.* Lipid G protein-coupled receptor ligand identification using beta-arrestin PathHunter assay. *J Biol Chem* **284**, 12328–12338 (2009).

Chapter 3

Kinetic multiplex assay to assess biased signaling of clinical agonists at the cannabinoid CB_2 receptor

Jara Bouma, Sanjay Sunil Kumar, Barry J.W. van den Berg, Cas van der Horst, Samuel R.J. Hoare, Matthias Wittwer, Wolfgang Guba, Uwe Grether, Mario van der Stelt, Laura H. Heitman

Manuscript in preparation.

Abstract

Studying biased signaling of G protein-coupled receptors (GPCRs) holds promise for the identification of ligands with a better therapeutic window. However, proper examination of biased signaling remains challenging by risking introduction of system or observation bias. Therefore, we developed a novel multiplex assay that simultaneously and kinetically detects cAMP production and ß-arrestin-2 recruitment in the same well. To investigate the applicability of the kinetic multiplex assay, we investigated seventeen clinically tested agonists for the cannabinoid CB_2 receptor (CB_2R), a promising GPCR for treating tissue injury and inflammation. Additionally, we included four widely used preclinical agonists and the endocannabinoids. Kinetic binding parameters were determined to extensively profile each agonist. Time-dependent activation was investigated by applying endpoint, semi-kinetic and kinetic analyses. Agonist-mediated CB_2R activation and signaling was time sensitive for several agonists, including Nabilone and LY-2828360, whereas this did not apply to the endocannabinoids. Similar potency and efficacy parameters were obtained from semi-kinetic and kinetic methods of analysis, while the latter provided additional signaling rate constants k_1 and k_2. Fast CB_2R engagement (k_{on}) of agonists resulted in increased affinity and potency, while slowly dissociating agonists extended the interaction between CB_2R and ß-arrestin-2. Moreover, superagonists Tedalinab, Olorinab, PRS-211375 and ART-27.13 were characterized by fast k_1 values. No significant biased signaling was observed in our system. Altogether, this chapter accentuates the potential of multiplexing functional responses and performing kinetic analyses to provide an extensive preclinical profile for agonists that may better predict their *in vivo* pharmacological effects. Ultimately, providing a full kinetic context for binding and activation of GPCR ligands could advance drug discovery efforts.

3.1 Introduction

Biased signaling, also known as ligand bias, biased agonism or functional selectivity, describes the ability of a ligand to preferentially activate one pathway over another by stabilizing distinct conformations of the receptor[1–4]. Bias on G protein-coupled receptors (GPCRs) is most frequently observed between G proteins and ß-arrestins but may also occur amongst the G protein or ß-arrestin family subtypes[5,6]. Consequently, activation of distinct pathways by an agonist may lead to different biological effects. Therefore, studying biased signaling may provide the potential to increase the therapeutic window if a specific signaling pathway is associated with efficacy, while another with side effects[1–4,7]. Recently, this was exemplified by the FDA approval of the first GPCR biased agonist, oliceridine, for the μ-opioid receptor to treat moderate to severe acute pain in adults[8]. G protein signaling after μ-opioid receptor activation improved antinociception, while ß-arrestin recruitment was related to adverse effects such as respiratory repression[9].

The *in vitro* study of biased signaling, however, is challenging and influenced by many factors[1,10,11]. Different receptor, transducer or effector levels, or stoichiometry between these components in various cellular backgrounds may introduce system bias[1,12]. Furthermore, interpretation of bias is dependent on the choice of reference ligand, such as a tool compound to report 'ligand benchmark-bias' or the endogenous ligand for quantification of 'ligand physiology-bias'. A tool compound with a balanced profile across studied pathways allows for the identification of 'ligand pathway-bias'[1]. Moreover, most commonly used functional assays are employed as endpoint assays, i.e., measured at one specific time point. However, agonist-mediated receptor activation may change over time and could be influenced by the dynamics and kinetics of the ligand-receptor interaction[1,10]. The importance of kinetic context for biased signaling was first highlighted in a study on the dopamine D_2 receptor, which demonstrated that the direction of ligand bias changed over time and conclusions on bias were therefore highly dependent on the selected time point[13]. In addition, biased agonists displayed a longer residence time (RT) at the receptor compared to the endogenous agonist [13]. Functional parameters have previously been correlated to the target-binding kinetics of agonists at several GPCRs[14–16]. Important developments in the field such as the TRUPATH platform, which allows for screening of biased G protein signaling in separate assays, are made to include the kinetic context of signaling[17,18]. Nevertheless, the majority of studies that report on biased signaling are performed with separate cellular assays for the different signaling pathways, use endpoint assays and/or do not quantify the kinetic signaling traces with fit-for-purpose mathematical analyses. Thus, a novel design of *in vitro* assays and methods of data analysis to report functional parameters in conjunction with kinetic parameters, such as binding kinetics and signaling constants, is warranted to study the *in vitro* pharmacology profile of candidate drugs[19,20].

Targeting of cannabinoid CB_2 receptor (CB_2R) has demonstrated great potential in preclinical studies for the treatment of autoimmune conditions, pain and diseases with an inflammatory component. This receptor is predominantly expressed on immune cells and plays a key role in the regulation of several inflammatory processes via activation by the endocannabinoids (eCBs) anandamide (AEA) and 2-arachidonoylglycerol (2-AG)[21–25]. To date, the focus has been on activation of CB_2R to enhance immunosuppressive effects[25,26]. A recent review by

Brennecke *et al.* analyzed all granted patents for CB_2R ligands since 2010 and described at least twenty CB_2R agonists that have progressed to clinical development[25]. Of these, only three are currently on the market that are described to non-selectively activate CB_2R, i.e., Dronabinol; a synthetic Δ^9-tetrahydrocannabinol (Δ^9-THC), Nabilone; a synthetic Δ^9-THC analogue and cannabidiol (CBD) (**Figure 3.1**, **Table 3.1**)[21,25]. Additionally, combinations of THC and CBD have been approved for the treatment of multiple sclerosis-associated spasticity[27]. Of note, we recently demonstrated that CBD does not bind or activate CB_2R, and the therapeutic effect might be due to polypharmacology at other proteins[28,29]. Five CB_2R agonists are currently still in clinical trials, whereas the development of the remaining agonists has been discontinued due to a variety of reasons[25]. Several issues have been hypothesized to explain the poor preclinical to clinical translation, including, but not limited to, a lack of translational animal models or differential signaling bias at the receptor level[25,30].

In various studies, biased signaling of diverse agonists and inverse agonists at CB_2R has been investigated[31–38]. A large consensus study combined the results from several independent academic and industry laboratories for a well-defined set of commonly used CBR ligands[35]. All ligands were screened on activation in five separate *in vitro* endpoint assays, i.e., GTPγS binding, cAMP production, ß-arrestin-2 recruitment, pERK stimulation and GIRK

Table 3.1 **Clinical CB_2R agonists, developmental status and indications.**

Agonist	Highest phase of development	Status	Indication(s)
Dronabinol	Launched	Active	Appetite loss, anorexia, chemotherapy-induced nausea and vomiting
Nabilone	Launched	Active	Chemotherapy-induced nausea and vomiting
Cannabidiol	Launched	Active	Dravet syndrome, Lennox-Gastaut syndrome
Lenabasum	Phase 3	Active	Dermatomyositis, cystic fibrosis, diffuse cutaneous systemic sclerosis, systemic lupus erythematosus
Olorinab	Phase 2	Active	Inflammatory bowel disease-related pain
CMX-020	Phase 2	Active	Osteoarthritis, knee osteoarthritis, pain, chronic pain
Cannabinol	Phase 2	Active	Chronic insomnia disorder, epidermolysis bullosa
KN 387271	Phase 2	Discontinued	Traumatic brain injury, stroke
GW-842166X	Phase 2	Discontinued	Dental and musculoskeletal pain
S-777469	Phase 2	Discontinued	Atopic dermatitis, pruritis
LY-2828360	Phase 2	Discontinued	Osteoarthritic knee pain
PRS-211375	Phase 2	Discontinued	Dental pain, coronary artery bypass graft
ART-27.13	Phase 1	Active	Anorexia, pain, cachexia, chemotherapy-induced nausea and vomiting
NTRX-07	Phase 1	Active	Alzheimer's disease, neuropathic pain
EHP-101	Phase 1	Discontinued	Multiple sclerosis, scleroderma, cutaneous systemic sclerosis
Tedalinab	Phase 1	Discontinued	Neuropathic pain, osteoarthritis, inflammatory pain disorders
TAK-937	Phase 1	Discontinued	Stroke

Information obtained from Brennecke *et al.* (2021)[25] and clinicaltrails.gov (accessed in January 2024).

activation. The most prominent bias at CB_2R was found between inhibition of cAMP production and ß-arrestin-2 recruitment, although bias factors remained low compared to other GPCRs. Furthermore, agonists HU308, HU910 and JWH133 were most balanced between all pathways and were thus recommended by the authors for use in further bias studies. To the best of our knowledge, bias at CB_2R has not been studied with a focus on the kinetic context and in general little is known about the binding kinetics of CB_2R agonists.

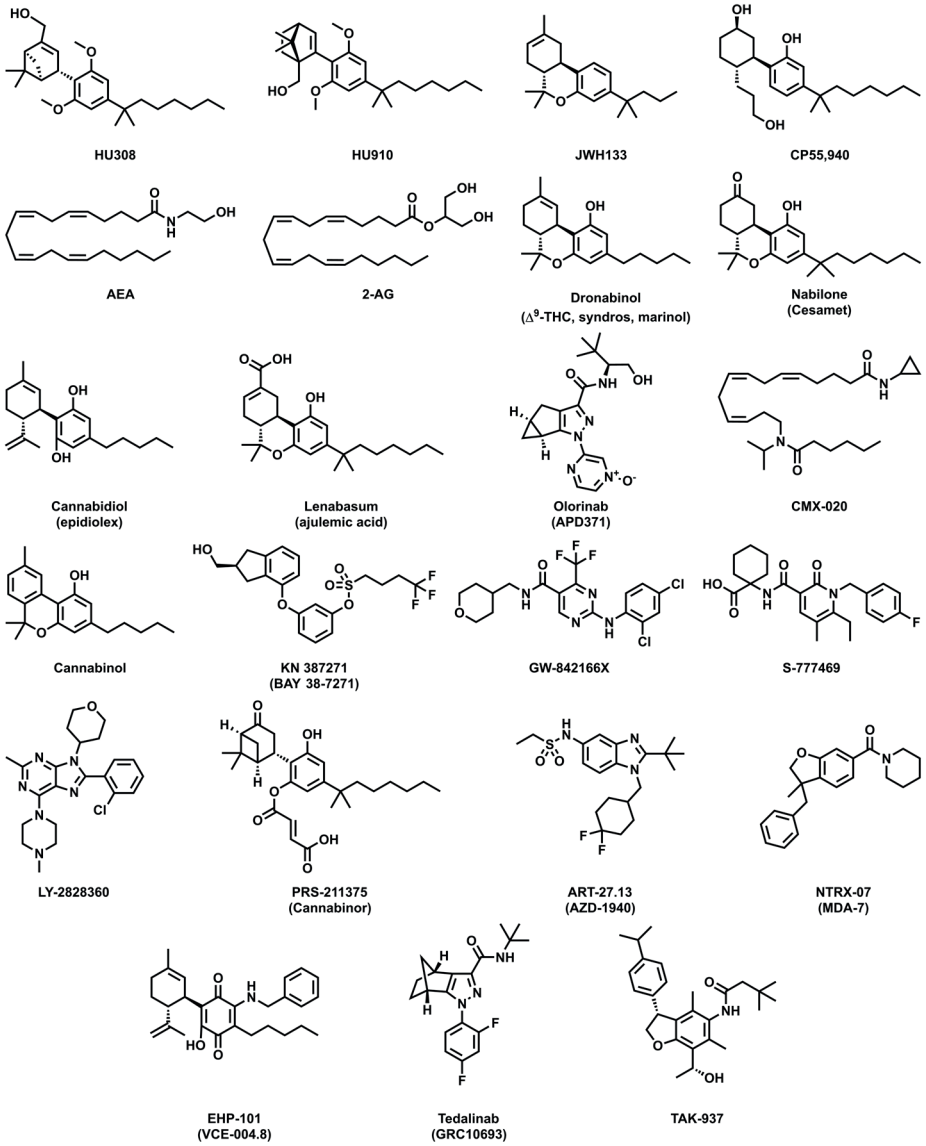

Figure 3.1 Chemical structures of cannabinoid CB_2 receptor agonists used in this study.
Benchmark agonists (HU308, HU910, JWH133 and CP55,940) and endocannabinoids (AEA, 2-AG). Clinical agonists ordered on highest phase of clinical development reached (in January 2024): launched (Dronabinol, Nabilone, Cannabidiol), phase 3 (Lenabasum), phase 2 (Olorinab, CMX-020, Cannabinol, KN 387271, GW-842166X, S-777469, LY-282360, PRS-211375), phase 1 (ART-27.13, NTRX-07, EHP-101, Tedalinab, TAK-937) with alternative names in between brackets.

Here, we aimed to develop a novel multiplex assay that simultaneously detects cAMP production and ß-arrestin-2 recruitment after receptor activation in a time-dependent manner in a single well. Seventeen CB_2R agonists that were examined in clinical trials were screened to investigate the applicability of this novel multiplex assay (**Figure 3.1**, **Table 3.1**). These agonists encompassed various chemotypes, clinical development phases and indications (**Figure 3.1**, **Table 3.1**), which are further specified in a review by Brennecke *et al.*[25]. This highlights the broad spectrum of CB_2R drug discovery and the adaptability of CB_2R to accommodate distinct agonists in the orthosteric binding pocket that can all activate the receptor. Furthermore, we included four widely used preclinical agonists and the endocannabinoids as benchmarks. Affinity and binding kinetics of the agonists were determined to ensure interaction with CB_2R and to obtain a more complete preclinical profile of the agonists. We explored the time-dependency of receptor activation by use of various methods of data analysis for the multiplex assay, i.e., endpoint, semi-kinetic and kinetic. We found that there were different time-dependent effects in inhibition of cAMP production and ß-arrestin-2 recruitment and that time-dependency varied per agonist used. Moreover, results from the semi-kinetic and kinetic analyses were well correlated, while the kinetic analysis additionally provided signaling rate constants k_1 and k_2. Superagonists in ß-arrestin-2 recruitment, i.e., agonists with higher efficacy compared to full agonist CP55,940, were characterized by fast k_1 values, whereas not all agonists with fast k_1 values behaved as superagonists. Moreover, a quick engagement of agonists with the receptor, i.e., fast association rate constant k_{on}, resulted in high affinity and kinetic potency (pIR_{50}). In our novel multiplex system, we did not detect statistically significant bias for any of the agonists relative to HU308. However, small differences were observed in trends for bias signaling, which were in some cases dependent on the method of analysis. Altogether, this study highlights and provides the potential of multiplexing functional readouts and including a kinetic view to CB_2R drug discovery programs, which can be extended to other GPCRs for an improved screening of biased signaling.

3.2 Results

3.2.1 Detection of binding affinity and kinetics of agonists at CB_2R

The investigated agonist set including benchmark agonists, endocannabinoids and clinical agonists displayed a high variety in chemotypes (**Figure 3.1**). Moreover, the agonists were highly diverse in terms of lipophilicity (LogD, K_{ow}LogP), solubility, brain lipid binding, membrane permeation and protein binding (**Table S3.1**), providing a structurally and chemically diverse set of agonists to demonstrate the applicability of the new signaling assay.

Prior to the development of the new signaling assay, all agonists were screened for their binding affinity and binding kinetics at CB_2R in [^{3}H]RO6957022 binding assays to ensure interaction with CB_2R (**Figure 3.2**, **Table 3.2**). From [^{3}H]RO6957022 displacement assays, it was observed that most agonists displayed affinity for CB_2R, which ranged from a moderate pK_i value of 6.30 ± 0.07 for AEA to high affinities below 10 nM for CP55,940, Dronabinol, ART-27.13, Tedalinab and TAK-937 (**Table 3.2**). In contrast, cannabidiol

(CBD), GW-842166X and EHP-101 were not able to displace [^{3}H]RO6957022 even at high concentrations, indicative of no affinity for CB_2R.

All agonists for which affinity could be determined were subjected to competition association assays to determine their binding kinetics at CB_2R (**Figure 3.2**, **Table 3.2**). The association of [^{3}H]RO6957022 to CB_2R was followed for 2 h in the absence (control) or presence of an IC_{50} concentration of competing agonist. Agonists with similar residence times (RT) to the radioligand used, such as CP55,940, displayed an association curve with a similar shape to the control curve (**Figure 3.2a**). Agonists with a longer RT compared to [^{3}H]RO6957022, such as HU308 presented a characteristic overshoot (**Figure 3.2b**). On the other hand, a slowly ascending curve was characteristic for agonists with a shorter RT compared to the radioligand, such as 2-AG and Tedalinab (**Figure 3.2c**,**d**). Using the Motulsky-Mahan equation, the kinetic binding parameters k_{on} and k_{off} were determined and subsequently these parameters were converted into engagement time (ET) for 1 μM of agonist and RT, respectively. ETs differed by 260-fold, with the fastest engagement to CB_2R for CP55,940 of below 1 s, and the slowest ETs for HU308 and AEA of 144 ± 48 s and 152 ± 10 s, respectively (**Table 3.2**). On the other hand, RTs only differed 44-fold. Dronabinol had the shortest interaction with CB_2R as represented by a RT of 2.1 ± 1.0 min, while TAK-937 displayed the longest RT of 93.2 ± 13.9 min (**Table 3.2**). Of note, due to the fast binding kinetics of CMX-020, CBN and KN 387271, their binding kinetics could not be quantified as these fell outside the assay's resolution.

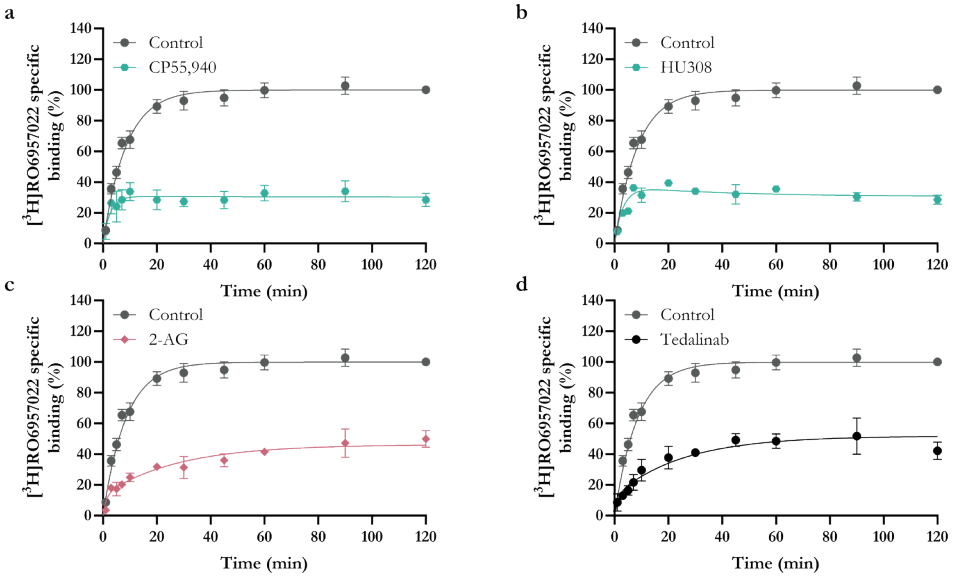

Figure 3.2 Evaluation of CB_2R target binding kinetics of representative benchmark agonists CP55,940 and HU308, endocannabinoid 2-AG, and clinical agonist Tedalinab.
Competition association assay with [^{3}H]RO6957022 on CB_2R in the absence (control) or presence of an IC_{50} concentration of representative competing agonists with (a) similar, (b) longer or (c, d) shorter receptor residence time (RT) compared to control, i.e., the radioligand used. Benchmark agonists are turquoise hexagons (⬢), 2-AG coral diamonds (◆) and clinical agonist Tedalinab black circles (●). Data are shown as mean ± SEM from three independent experiments performed in duplicate.

Table 3.2 Binding affinity and kinetic binding parameters of benchmark agonists, endocannabinoids (eCB) and clinical agonists on CB_2R.

	Agonist	CB_2R pK_i (K_i in nM) or displacement at 10 µM (%)[a]	k_{on} (M^{-1} s^{-1})[b]	ET (s)[c]	k_{off} (s^{-1})[d]	RT (min)[e]	K_D (nM)[f]	CB_1R pK_i (K_i in nM) or displacement at 10 µM (%)[g]	CB_2R selectivity[h]
Benchmark	**HU308**†	7.03 ± 0.10 (92.4)	(7.0 ± 2.3) × 10^3	143.5 ± 47.9	(2.3 ± 0.4) × 10^{-4}	71.0 ± 11.3	33.7	21 ± 9	>100
	HU910	7.18 ± 0.09 (65.7)	(1.4 ± 0.2) × 10^4	72.4 ± 11.9	(4.5 ± 1.0) × 10^{-4}	37.0 ± 7.9	32.6	5.62 ± 0.13 (2384)	36.3
	JWH133	7.40 ± 0.07 (39.7)	(7.6 ± 3.6) × 10^4	13.1 ± 6.2	(2.5 ± 1.1) × 10^{-3}	6.7 ± 3.0	32.6	48 ± 2	>250
	CP55,940†	8.85 ± 0.08 (1.4)	(1.8 ± 0.4) × 10^6	0.6 ± 0.1	(5.2 ± 0.9) × 10^{-4}	32.3 ± 5.5	0.3	8.91 ± 0.16 (1.2)	0.9
eCB	**AEA**†	6.31 ± 0.07 (484.5)	(6.6 ± 0.5) × 10^3	152.3 ± 10.4	(2.4 ± 0.1) × 10^{-3}	6.8 ± 0.4	371.7	6.60 ± 0.07 (254.1)	0.5
	2-AG†	7.01 ± 0.06 (97.3)	(5.3 ± 1.0) × 10^4	18.8 ± 3.6	(2.3 ± 0.3) × 10^{-3}	7.4 ± 1.0	42.7	6.60 ± 0.15 (251.8)	2.6
Clinical	**Dronabinol**	8.07 ± 0.26 (8.6)	(3.5 ± 1.5) × 10^5	2.9 ± 1.2	(7.8 ± 3.7) × 10^{-3}	2.1 ± 1.0	22.5	7.70 ± 0.09 (20.0)	2.3
	Nabilone	7.85 ± 0.07 (14.1)	(1.0 ± 0.2) × 10^5	9.9 ± 1.6	(6.3 ± 0.3) × 10^{-4}	26.6 ± 1.3	6.2	8.17 ± 0.06 (6.8)	0.5
	Cannabidiol	53 ± 2	N.A.	N.A.	N.A.	N.A.	N.A.	10 ± 7	N.A.
	Lenabasum	6.51 ± 0.11 (310.0)	(1.8 ± 0.9) × 10^4	55.8 ± 29.1	(2.6 ± 0.4) × 10^{-3}	6.4 ± 1.0	144.9	6.49 ± 0.08 (321.9)	1.0
	Olorinab†	7.45 ± 0.09 (35.3)	(2.5 ± 0.4) × 10^4	40.1 ± 5.9	(3.7 ± 0.6) × 10^{-4}	44.9 ± 6.6	14.9	-15 ± 8	>280
	CMX-020	6.37 ± 0.15 (428.9)	N.D.	N.D.	N.D.	N.D.	N.D.	7.05 ± 0.01 (88.2)	0.2
	Cannabinol	7.44 ± 0.16 (36.3)	N.D.	N.D.	N.D.	N.D.	N.D.	6.91 ± 0.07 (122.3)	3.4
	KN 387271	7.40 ± 0.08 (39.6)	N.D.	N.D.	N.D.	N.D.	N.D.	7.84 ± 0.05 (14.5)	0.4
	GW-842166X	27 ± 1	N.A.	N.A.	N.A.	N.A.	N.A.	2 ± 1	N.A.
	S-777469	6.37 ± 0.02 (423.3)	(1.0 ± 0.1) × 10^4	96.2 ± 10.5	(2.5 ± 0.7) × 10^{-3}	6.7 ± 2.0	239.1	-11 ± 3	>20
	LY-2828360	7.43 ± 0.14 (36.9)	(5.5 ± 0.7) × 10^4	18.1 ± 2.3	(1.8 ± 0.5) × 10^{-3}	9.2 ± 2.3	32.9	5.69 ± 0.06 (2040)	55.3
	PRS-211375	7.45 ± 0.11 (35.4)	(2.7 ± 0.7) × 10^4	36.8 ± 10.1	(5.3 ± 0.6) × 10^{-4}	31.6 ± 3.8	19.4	6.13 ± 0.06 (743.6)	21.0
	ART-27.13	8.93 ± 0.05 (1.2)	(4.1 ± 0.3) × 10^5	2.4 ± 0.2	(2.9 ± 0.4) × 10^{-4}	57.4 ± 8.4	0.7	7.71 ± 0.01 (19.7)	16.7
	NTRX-07	6.47 ± 0.09 (337.5)	(4.0 ± 1.1) × 10^4	25.3 ± 6.9	(6.5 ± 0.9) × 10^{-3}	2.6 ± 0.4	163.6	31 ± 3	>29
	EHP-101	24 ± 22	N.A.	N.A.	N.A.	N.A.	N.A.	-25 ± 11	N.A.
	Tedalinab	8.23 ± 0.08 (5.9)	(8.3 ± 1.5) × 10^5	1.2 ± 0.2	(2.4 ± 0.4) × 10^{-3}	7.0 ± 1.0	2.9	6.05 ± 0.05 (885.1)	149.9
	TAK-937	8.89 ± 0.05 (1.3)	(6.1 ± 1.6) × 10^5	1.6 ± 0.4	(1.8 ± 0.3) × 10^{-4}	93.2 ± 13.9	0.3	8.12 ± 0.11 (7.6)	5.8

To obtain a better understanding of the relationship between the affinity and kinetic binding parameters several correlation plots were constructed (**Figure S3.1**). The equilibrium pK_i and kinetic pK_D values were significantly correlated, validating the competition association assay (R^2 0.93, p <0.0001) (**Figure S3.1a**). Furthermore, association rate constant k_{on} significantly correlated with affinity (R^2 0.78, p <0.0001), while dissociation rate constant k_{off} did not correlate to affinity (**Figure S3.1b**,**c**). This indicated that fast association is the driving factor for high affinity on CB_2R. The kinetic map, which presents the connection between k_{on} (x-axis), k_{off} (y-axis) and kinetic affinity K_D (diagonals lines), highlighted the diversity of combinations between k_{on} and k_{off} to reach similar affinities. Furthermore, it indicated no clear clustering of groups of agonists based on one of the binding parameters, underlining the chemical diversity of the agonists (**Figure S3.1d**).

To get insight in selectivity over CB_1R, binding affinities of all agonists were determined in [^{3}H]CP55,940 displacement assays at this receptor (**Table 3.2**). Agonists CBD, GW-842166X and EHP-101 were devoid of CB_1R affinity, as was the case for CB_2R. As expected, no pronounced selectivity for either CBR was found for the endocannabinoids or CMX-020, a 2-AG derivative. Similarly, no selectivity was observed for CP55,940, Dronabinol, Nabilone, Lenabasum, Cannabinol, KN 387271 and TAK-937. A maximum 150-fold selectivity for CB_2R was found for Tedalinab and more than 15-fold CB_2R selectivity was detected for HU910, LY-2828360, PRS-211375 and ART-27.13. Furthermore, exclusive CB_2R affinity was observed for HU308, JWH133, Olorinab, S-777469 and NTRX-07.

To draw connections between molecular descriptors of CB_2R agonists and their binding, various correlation plots were constructed (**Figure S3.2**). None of the physicochemical parameters PSA, LogD or LogP of the agonists were correlated with either affinity (pK_i) or association and dissociation rate constants k_{on} and k_{off} (**Figure S3.2**). This suggested that the overall lipophilicity of the molecules, represented by different parameters, is not predictive for equilibrium or kinetic binding parameters at CB_2R. Altogether, structurally and chemically diverse CB_2R agonists varied greatly in affinity for CB_2R and selectivity over CB_1R. Affinity was predominantly driven by association rate constants of the agonists, but a general kinetic profile was not observed for the structurally diverse agonists investigated in this study.

← **Table 3.2** *(continued legend)*

[a, b, d] Binding parameters of agonists on CB_2R were determined in [^{3}H]RO6957022 displacement (affinity pK_i) and competition association (association, k_{on}, and dissociation, k_{off}, rate constants) assays on CHOK1_hCB_2bgal membranes at 10 °C. [c] Engagement time (ET) of the agonist to the receptor was determined for 1 μM agonist by employing equation 2 and is expressed in seconds (s), whereas k_{on} is expressed in M^{-1} s^{-1}. [e] Residence time (RT) was determined following equation 3 and is expressed in min, whereas k_{off} is expressed in s^{-1}. [f] Kinetic K_D values were determined using equation 4. [g] Binding affinity (pK_i) of agonists on CB_1R was determined in [^{3}H]CP55,940 displacement assays on CHOK1_hCB_1bgal membranes at 25 °C and [h] CB_2R selectivity was calculated using equation 1 or in the absence of CB_1R affinity defined as at least fold over highest concentration tested (10 μM). Values represent the mean ± SEM of at least three independent experiments performed in duplicate (*n* indicates the number of biological replicates). N.A is not applicable, N.D. is not detectable. [†] CB_2R data previously published[39].

3.2.2 Development and validation of a kinetic multiplex assay for CB_2R

To investigate biased signaling in one cellular system and in a kinetic context, we developed a novel multiplex assay. The new signaling assay incorporated two luminescent technologies for detection of inhibition of cAMP production, via $G\alpha_i$ activation, and ß-arrestin-2 recruitment after CB_2R activation to improve the detection of potential biased signaling of clinically relevant agonists. The inhibition of cAMP production was measured via the GloSensor technology, which was visualized by addition of GloSensor cAMP reagent. The NanoBiT technology was used to detect ß-arrestin-2 recruitment to CB_2R for which Vivazine was used as substrate (**Table S3.2**). The two technologies were combined in a multiplex assay to simultaneously measure both signaling events under the same assay conditions and in the same cellular background, and as such improve the validity of any observed signaling bias.

The multiplex assay was validated using full agonist CP55,940 as a reference (**Figure 3.3**). The pGloSensor plasmid was transfected into HEK293T cells already stably expressing CB_2R-SmBiT and LgBiT-ß-arrestin-2 (**Table S3.2**). After transfection, the cells were equilibrated with either cAMP reagent, Vivazine or a combination of cAMP reagent and Vivazine (i.e., termed "multiplex reagent") for 2 hours. Subsequently, cells were stimulated with 1 µM FSK to increase cAMP levels prior to inhibition due to CB_2R activation, which did not induce any detectable ß-arrestin-2 recruitment (**Figure S3.3**). After 1 hour, cells were stimulated with increasing concentrations of CP55,940 and the responses for the three different reagents were monitored on the cAMP channel (595 nm filter) and ß-arrestin channel (460 nm filter). Specific luminescent signals were only detected on the cAMP channel, but not the ß-arrestin channel, for cells that were pre-equilibrated with cAMP reagent (**Figure 3.3a**,**b**). *Vice versa*, in the presence of Vivazine, luminescent signals were only evident on the ß-arrestin channel and not the cAMP channel (**Figure 3.3c**,**d**). Pre-equilibration with the multiplex reagent resulted in the detection of CB_2R activation on both channels, and the traces were similar to the individually observed cAMP and ß-arrestin responses (**Figure 3.3a-f**). To quantify the results, the area under the curve (AUC) was determined from all time traces and presented in dose-response curves (**Figure 3.3g**,**h**). This confirmed the lack of agonist-mediated responses measured on the cAMP channel for Vivazine only, whereas the pEC_{50} values of CP55,940 obtained with cAMP reagent or multiplex reagent were similar, 8.86 and 8.55, respectively (**Table S3.3**). Similarly, CP55,940-induced ß-arrestin-2 recruitment was only measured in the presence of Vivazine or multiplex reagent, which resulted in similar pEC_{50} values, i.e., 8.20 and 8.16, respectively.

As this protocol clearly distinguished between the responses obtained for inhibition of cAMP production and ß-arrestin-2 recruitment of full agonist CP55,940, we continued screening the remaining benchmark agonists, endocannabinoids and clinical agonists with the FSK-induced multiplex assay.

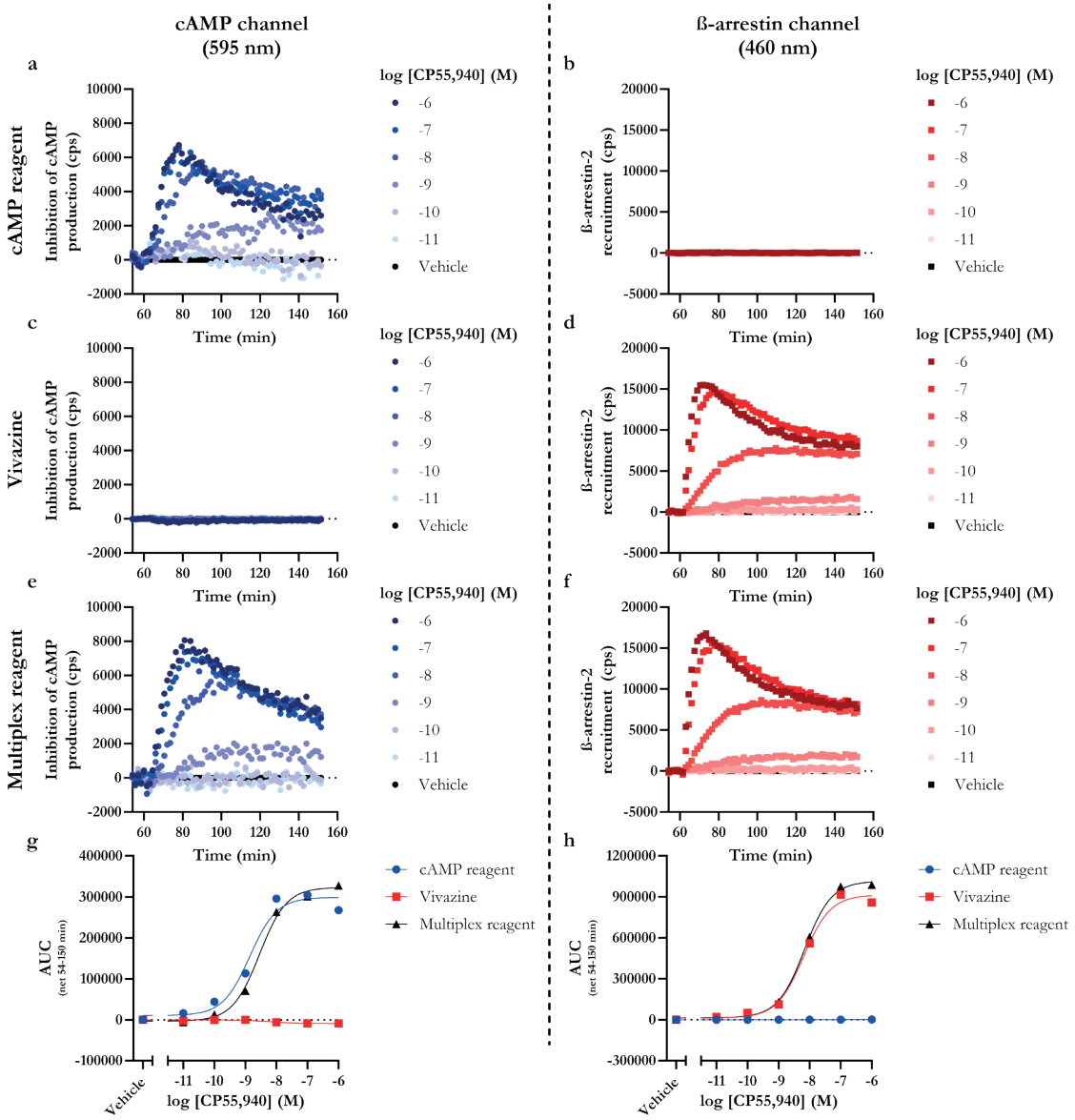

Figure 3.3 Validation and characterization of the multiplexed cAMP production and ß-arrestin-2 recruitment assay on HEK293T CB_2R-SmBiT LgBiT-ß-arrestin-2 cells with full agonist CP55,940.
Representative forskolin- and vehicle-corrected time traces of CP55,940 stimulation on HEK293T CB_2R-SmBiT LgBiT-ß-arrestin-2 cells pre-equilibrated with (a, b) only cAMP reagent, (c, d) only Vivazine, or (e, f) multiplex reagent (cAMP reagent and Vivazine) for 2 h at 25 °C. The signals were simultaneously recorded at the (a, c, e) cAMP channel (595 nm) and (b, d, f) ß-arrestin channel (460 nm). Area Under the Curve (AUC) was determined from the time traces after detection on the (g) cAMP channel or (h) ß-arrestin channel. Data are shown as mean from a (a-f) representative experiment or (g-h) mean of two independent experiments all performed in duplicate.

3.2.3 Characterization of time traces by benchmark agonists, endocannabinoids and clinical agonists in the multiplex assay

All benchmark agonists, endocannabinoids and clinical agonists were screened in the multiplex assay and the signaling time traces at different concentrations of agonist were recorded in the two specific readouts (**Figure 3.4**, **S3.4-S3.7**, **Table 3.3**, **3.4**). Typically, at high concentrations of agonist the inhibition of cAMP production increased for the first 20 minutes after which the signals decreased with a tendency to return to baseline levels, although a complete return was not observed within the selected assay time (**Figure 3.4**, **S3.4**, **S3.5**). At lower concentrations of agonist, the inhibition of cAMP production increased, although at a lower rate than with high agonist concentrations, to reach a steady plateau within our assay time.

Strikingly, for several clinical agonists (AEA, Dronabinol, CBD, Lenabasum, CMX-020, CBN, KN 387271, GW-842166X, NTRX-07 and EHP-101), the cAMP production by 10 μM of agonist did not return to basal levels, whereas by 1 μM agonist it did (**Figure S3.4**, **S3.5**). Of note, CBD and EHP-101 only modified cAMP levels at 10 μM. Intriguingly, 10 μM Olorinab induced a small inhibition of cAMP levels, which quickly returned to forskolin baseline levels and even further increased cAMP levels (**Figure S3.5a**). To this end, the cAMP production of saturating concentrations (>100x K_i value) or 10 μM of all agonists was investigated in parental HEK293T cells devoid of CB_2R expression (**Figure S3.8**). For multiple agonists (Dronabinol, CBD, Lenabasum, Olorinab, CMX-020, CBN, KN 387271, GW-842166X, LY-2828360, ART-27.13, NTRX-07 and TAK-937), we observed CB_2R-independent cAMP responses. Consequently, for these agonists 10 μM was removed from the dose-response curves in the semi-kinetic and kinetic analysis, i.e., the methods of analysis using the full time traces.

In almost all cases, a high concentration of agonist induced a quick increase in ß-arrestin-2 recruitment, which fell back to a steady state above baseline (**Figure 3.4**, **S3.6**, **S3.7**). On the other hand, lower concentrations of agonist caused recruitment of ß-arrestin-2, which increased towards a steady plateau above baseline. No increase in luminescence, as a consequence of ß-arrestin-2 recruitment to CB_2R, was observed for any concentration of CBD or EHP-101, while a small increase in luminescence was observed by 10 and 1 μM GW-842166X (**Figure S3.6i**, **S3.7k**).

An advantage of the multiplex assay is the possibility of observing the difference in initiation of the two signaling events over time, which was visualized for agonists CP55,940, HU308, HU910, 2-AG, PRS-211375 and Tedalinab at a saturating concentration (**Figure 3.4**, **S3.4-S3.7**). In all cases, the peak response of ß-arrestin-2 recruitment was reached earlier than the peak response of the inhibition of cAMP production. The peak response for both ß-arrestin-2 recruitment and inhibition of cAMP production for PRS-211375 was markedly higher than the peak responses of CP55,940-mediated activation (**Figure 3.4a**,**e**). Similarly, the peak response for ß-arrestin-2 recruitment by Tedalinab was higher than by CP55,940, while the cAMP peak responses were similar (**Figure 3.4a**,**f**). Moreover, agonist-induced differences between the steepness of the decline phase after the peak responses are observed. For instance, a steep decline in ß-arrestin-2 recruitment is observed for CP55,940,

2-AG, PRS-211375 and Tedalinab, while the decline is more moderate for HU308 and HU910. Altogether, the shape of the curves is a first indication towards agonist-mediated differences in functional responses. In particular, differences in maximal effect are observed, but the time traces also accentuate variations in the responses over time.

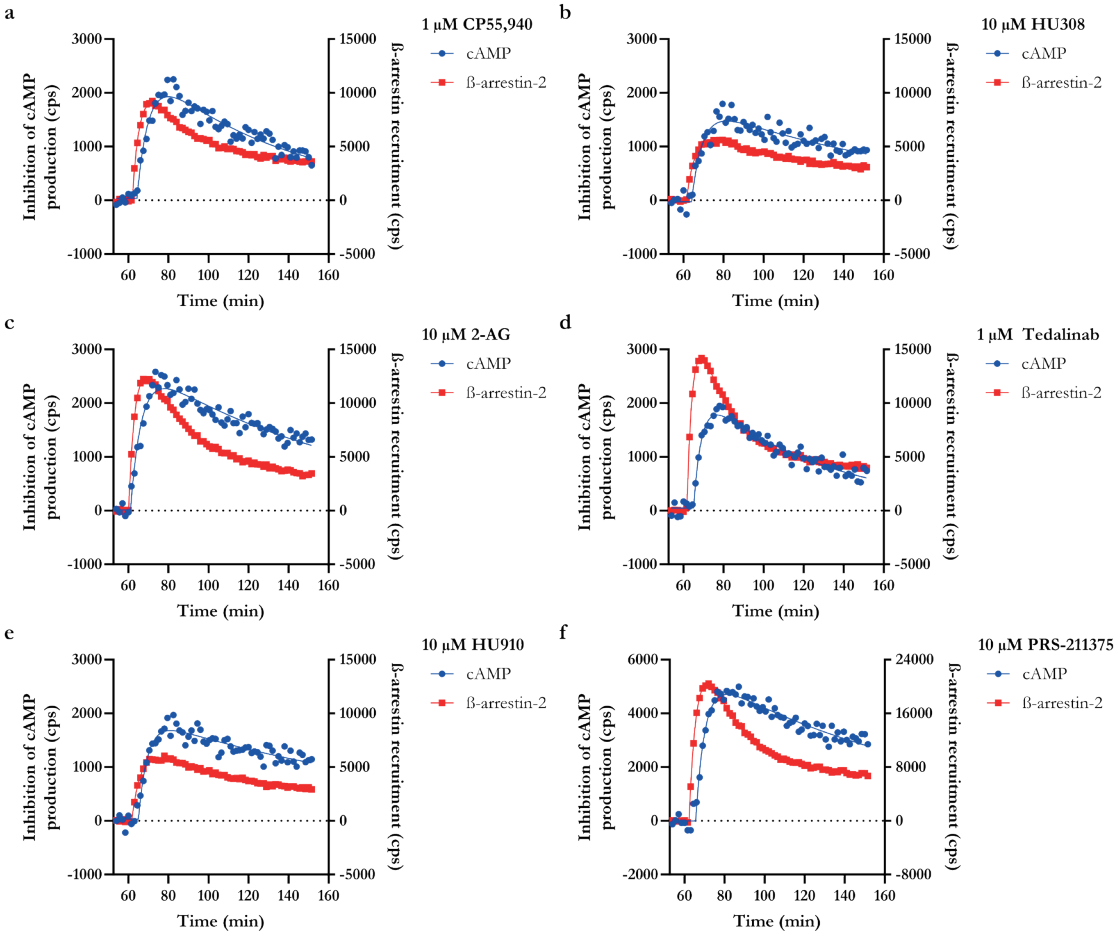

Figure 3.4 Kinetic functional characterization of representative agonists CP55,940, HU308, HU910, 2-AG, PRS-211375 and Tedalinab in the multiplex assay on HEK293T CB_2R-SmBiT LgBiT-ß-arrestin-2 cells. Representative forskolin- and vehicle-corrected time traces for inhibition of cAMP production (left y-axis) and ß-arrestin-2 recruitment (right y-axis) by (a) 1 µM CP55,940, (b) 10 µM HU308, (c) 10 µM HU910, (d) 10 µM 2-AG, (e) 10 µM PRS-211375 or (f) 1 µM Tedalinab in the multiplex assay on CB_2R. Data are shown as mean from a representative experiment all performed in duplicate. Representative dose-dependent time traces of all agonists can be found in Figures 3.S4-3.S7.

3.2.4 Endpoint quantification of CB_2R activation by benchmark agonists, endocannabinoids and clinical agonists in the multiplex assay

To quantify the effects of the benchmark agonists, endocannabinoid and clinical agonists in the multiplex assay, their potency and efficacy values were determined with three different methods of analysis. Initially, all data was analyzed at four different time points to investigate the time-dependency of activation. To this end, dose-response curves of cAMP production and ß-arrestin-2 recruitment were created for 7.5, 15, 30 and 60 min after agonist addition (**Figure S3.9-S3.12**). Note that, no dose-response curves could be generated for 90 min after agonist addition as cAMP production returned to vehicle conditions for all agonist concentrations. No potency values could be determined for the inhibition of cAMP production or ß-arrestin-2 recruitment by CBD, GW-842166X or EHP-101, which is in line with their lack of CB_2R affinity (**Table 3.2**, **S3.4**, **S3.5**). Potency and efficacy values were only quantified for the early (7.5 min) and late (60 min) time point and the differences between those were calculated (**Figure 3.5**, **Table S3.4**, **S3.5**).

Potency and efficacy values of HU910, JWH133, AEA, 2-AG, Dronabinol, Lenabasum, CBN, KN 387271, S-777469 and Tedalinab remained unaffected over time (**Figure 3.5**, **S3.9b**,**c**,**f**,**j**, **S3.10f**,**l**, **Table S3.4**). On the other hand, potency values for CP55,940, Nabilone, Olorinab, PRS-211375, ART-27.13 and TAK-937 were significantly increased over time, whereas there was no time-dependent effect on efficacy (**Figure 3.5**, **S3.9d**,**h**, **S3.10a**,**h**,**i**,**m**, **Table S3.4**). Interestingly, NTRX-07's potency was significantly decreased over time, while a seeming increase in efficacy was not statistically significant (**Table S3.4**). While no pEC_{50} value could be determined for LY-2828360 after 7.5 min (pEC_{50} <10 µM),

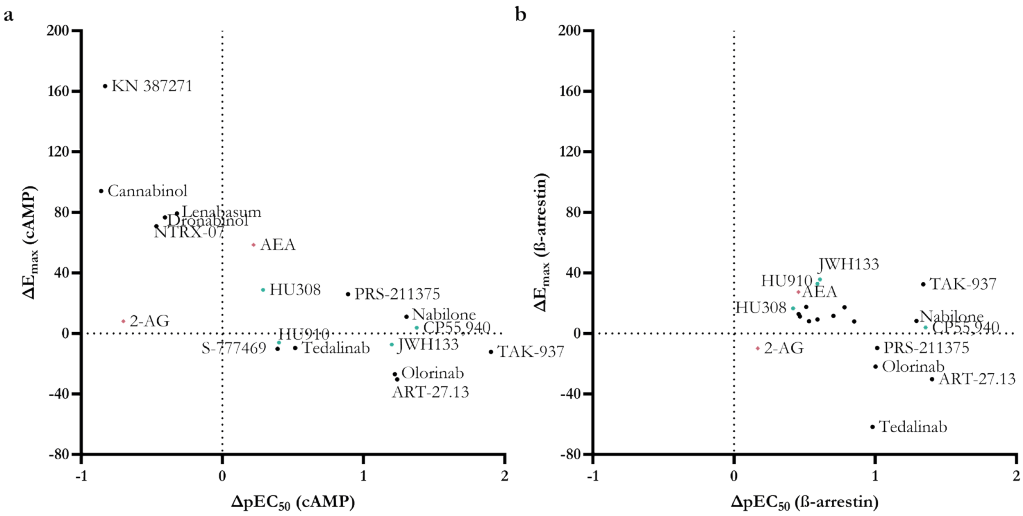

Figure 3.5 Time-dependent effect on potency and efficacy of benchmark agonists, endocannabinoids and clinical agonists in the multiplex assay on HEK293T CB_2R-SmBiT LgBiT-ß-arrestin-2 cells.
Differences in potency (ΔpEC_{50}) and efficacy (ΔE_{max}) from (a) cAMP production and (b) ß-arrestin-2 recruitment assays by benchmark agonists, endocannabinoids and clinical agonists after 60 min of stimulation compared to 7.5 min. Benchmark agonists are turquoise hexagons (⬢), endocannabinoids coral diamonds (◆) and clinical agonists black circles (●). Data are shown as mean from at least three independent experiments performed in duplicate.

its potency increased over time to 7.45 ± 0.38 (**Figure S3.9g**, **Table S3.4**). Alternatively, HU308's potency was not dependent on time, but its efficacy was significantly increased from partial (78 ± 4%) to full agonism (106 ± 7%, **Figure 3.5**, **S3.9a**, **Table S3.4**).

The potency and efficacy of HU308 and 2-AG for ß-arrestin-2 recruitment were not dependent on time (**Figure 3.5**, **S3.11a,f**, **Table S3.5**). Endocannabinoid AEA's potency was unaffected by longer incubation, but AEA's efficacy was significantly increased to 53 ± 3% after 60 min compared to 26 ± 0% at 7.5 min (**Figure 3.5**, **S3.11e**, **Table S3.5**). The potency of the seventeen remaining agonists was significantly increased over time with varying effects on efficacy. Specifically, the efficacy was significantly increased for HU910, JWH133, CP55,940, Dronabinol, CMX-020, KN 387271, LY-2828360 and TAK-937, while the efficacy of Nabilone, Lenabasum, CBN, S-777469, PRS-211375 and NTRX-07 remained unaffected (**Figure 3.5**, **S3.11**, **S3.12**, **Table S3.5**). On the other hand, the efficacy of Tedalinab was significantly decreased over time, and a similar trend was observed for Olorinab and ART-27.13 (**Figure 3.5**, **S3.12a,i,l**, **Table S3.5**).

This method of analysis showed that activation by certain agonists is not time-dependent, whereas for other agonists potency and/or efficacy might be increased or decreased over time, and this may differs depending on functional assay. Furthermore, it suggests that interpretation of results is highly dependent on the selected time point for data analysis, i.e., endpoint analyses (and assays) can influence conclusions on ligand function and bias.

3.2.5 Semi-kinetic quantification of CB_2R activation by benchmark agonists, endocannabinoids and clinical agonists in the multiplex assay

To incorporate the kinetic time traces, a second semi-kinetic method of analysis was pursued, which is commonly used to analyze time traces obtained from functional assays. To this end, the AUC of the full 90 min of activation was plotted against the agonist concentration and potency and efficacy values were determined for cAMP production and ß-arrestin-2 recruitment. For agonists that showed CB_2R-independent cAMP production (Dronabinol, CBD, Lenabasum, Olorinab, CMX-020, CBN, KN 387271, GW-842166X, LY-2828360, ART-27.13, NTRX-07 and TAK-937), the curves were analyzed up to 1 µM in cAMP production (**Figure S3.8-S3.10**). Furthermore, no potency values were determined for CBD, GW-842166X and EHP-101 due to their lack of cAMP production or ß-arrestin-2 recruitment, which is in line with their lack of CB_2R affinity (**Table 3.2- 3.4**).

Potency values determined for inhibition of cAMP production spanned a wide range. Dronabinol and CBN displayed the lowest potencies with pEC_{50} values of 5.66 ± 0.06 and 5.70 ± 0.05, respectively, whereas agonists CP55,940, ART-27.13 and Tedalinab were full agonists and exhibited sub nanomolar potency with pEC_{50} values of 9.15 ± 0.16, 9.5 ± 0.27 and 9.38 ± 0.25, respectively (**Table 3.3**). HU308, HU910, 2-AG, Nabilone, Lenabasum, CMX-020, PRS-211375 and NTRX-07 behaved as full agonists with E_{max} values >90%, but with lower potency values compared to the before mentioned agonists, i.e., pEC_{50} values between 6.15 ± 0.17 and 7.80 ± 0.17.

Table 3.3 **Inhibition of forskolin-induced cAMP production by benchmark agonists, endocannabinoids (eCB) and clinical agonists determined in the multiplex assay on CB_2R.**

	Agonist	pEC_{50}	E_{max} or activation at 1 μM (%)	pIR_{50}	IR_{max} or activation at 10 μM (%)	k_1 (min^{-1})	k_2 (min^{-1})
Benchmark	**HU308**	6.57 ± 0.03	95 ± 3	6.03 ± 0.11	90 ± 4	0.26 ± 0.08	0.012 ± 0.002
	HU910	6.93 ± 0.08	102 ± 5	6.44 ± 0.17	89 ± 9	0.24 ± 0.08	0.012 ± 0.005
	JWH133	6.96 ± 0.07	88 ± 5	6.46 ± 0.12	79 ± 10	0.15 ± 0.01	0.026 ± 0.005
	CP55,940	9.15 ± 0.16	103 ± 5	7.90 ± 0.22	102 ± 1	0.24 ± 0.07[§]	0.015 ± 0.002[§]
eCB	**AEA**	6.41 ± 0.12	73 ± 12	5.73 ± 0.21	65 ± 5	0.15 ± 0.05[§]	N.A.
	2-AG	6.15 ± 0.17	92 ± 16	6.16 ± 0.26	94 ± 7	0.26 ± 0.04	0.011 ± 0.001
Clinical	**Dronabinol**	5.66 ± 0.06	79 ± 19	6.65 ± 0.20	24 ± 1	0.08 ± 0.03	N.A.
	Nabilone	7.80 ± 0.17	99 ± 13	6.85 ± 0.19	81 ± 12	0.23 ± 0.02	0.004 ± 0.001
	Cannabidiol	N.D.	-8 ± 2[§]	N.D.	4 ± 0[#]	N.D.	N.D.
	Lenabasum	6.50 ± 0.07	132 ± 19	6.13 ± 0.15	93 ± 11	0.14 ± 0.01[§]	0.007 ± 0.001[§]
	Olorinab	7.88 ± 0.08	61 ± 14	6.92 ± 0.14	79 ± 10	0.14 ± 0.04[§]	0.042 ± 0.015[§]
	CMX-020	6.47 ± 0.13	109 ± 7	6.70 ± 0.58	53 ± 11	0.14 ± 0.03[§]	N.A.
	Cannabinol	5.70 ± 0.05	81 ± 17	6.53 ± 0.02	10 ± 1	0.04 ± 0.01	N.A.
	KN 387271	7.96 ± 0.20	78 ± 11	7.29 ± 0.08	109 ± 29	0.30 ± 0.11[§]	0.009 ± 0.002[§]
	GW-842166X	N.D.	37 ± 3[§]	N.D.	65 ± 13[#]	0.19 ± 0.01[§]	N.D.
	S-777469	7.04 ± 0.12	86 ± 12	6.71 ± 0.20	88 ± 10	0.22 ± 0.02	0.011 ± 0.002
	LY-2828360	6.89 ± 0.25	26 ± 5	6.33 ± 0.18	43 ± 7	0.24 ± 0.05	0.014 ± 0.003
	PRS-211375	7.18 ± 0.33	94 ± 11	6.41 ± 0.17	105 ± 4	0.24 ± 0.01	0.005 ± 0.002
	ART-27.13	9.15 ± 0.27	96 ± 11	7.93 ± 0.33	113 ± 23	0.24 ± 0.01[§]	0.012 ± 0.000[§]
	NTRX-07	6.70 ± 0.17	110 ± 27	6.59 ± 0.26	79 ± 3	0.20 ± 0.03[§]	0.006 ± 0.002[§]
	EHP-101	N.D.	19 ± 2[§]	N.D.	5 ± 1[#]	N.D.	N.D.
	Tedalinab	9.38 ± 0.25	97 ± 6	8.53 ± 0.14	114 ± 16	0.26 ± 0.03[§]	0.018 ± 0.002[§]
	TAK-937	8.56 ± 0.11	81 ± 3	7.07 ± 0.16	85 ± 3	0.20 ± 0.01[§]	0.008 ± 0.001[§]

Potency (pEC_{50}, pIR_{50}) and efficacy (E_{max}, IR_{max}) values were determined from AUC and initial rate dose-response curves, respectively, derived from the cAMP time traces in the multiplex assay. In the absence of a DRC, maximal activation (%) was determined at 10 (#) or 1 μM (§) of agonist. Signaling rate constants k_1 and k_2 were determined at 10 μM or 1 μM (§) of agonist. Data are mean from at least three independent experiments performed in duplicate. N.A is not applicable, N.D. is not detectable.

Table 3.4 ß-arrestin-2 recruitment by benchmark agonists, endocannabinoids (eCB) and clinical agonists determined in the multiplex assay on CB_2R.

	Agonist	pEC_{50}	E_{max} or activation at 1 µM (%)	pIR_{50}	IR_{max} or activation at 10 µM (%)	k_1 (min^{-1})	k_2 (min^{-1})
Benchmark	**HU308**	6.57 ± 0.03	95 ± 3	6.03 ± 0.11	90 ± 4	0.26 ± 0.08	0.012 ± 0.002
	HU910	6.93 ± 0.08	102 ± 5	6.44 ± 0.17	89 ± 9	0.24 ± 0.08	0.012 ± 0.005
	JWH133	6.96 ± 0.07	88 ± 5	6.46 ± 0.12	79 ± 10	0.15 ± 0.01	0.026 ± 0.005
	CP55,940	9.15 ± 0.16	103 ± 5	7.90 ± 0.22	102 ± 1	0.24 ± 0.07[§]	0.015 ± 0.002[§]
eCB	**AEA**	6.41 ± 0.12	73 ± 12	5.73 ± 0.21	65 ± 5	0.15 ± 0.05[§]	N.A.
	2-AG	6.15 ± 0.17	92 ± 16	6.16 ± 0.26	94 ± 7	0.26 ± 0.04	0.011 ± 0.001
Clinical	**Dronabinol**	5.66 ± 0.06	79 ± 19	6.65 ± 0.20	24 ± 1	0.08 ± 0.03	N.A.
	Nabilone	7.80 ± 0.17	99 ± 13	6.85 ± 0.19	81 ± 12	0.23 ± 0.02	0.004 ± 0.001
	Cannabidiol	N.D.	-8 ± 2[§]	N.D.	4 ± 0[#]	N.D.	N.D.
	Lenabasum	6.50 ± 0.07	132 ± 19	6.13 ± 0.15	93 ± 11	0.14 ± 0.01[§]	0.007 ± 0.001[§]
	Olorinab	7.88 ± 0.08	61 ± 14	6.92 ± 0.14	79 ± 10	0.14 ± 0.04[§]	0.042 ± 0.015[§]
	CMX-020	6.47 ± 0.13	109 ± 7	6.70 ± 0.58	53 ± 11	0.14 ± 0.03[§]	N.A.
	Cannabinol	5.70 ± 0.05	81 ± 17	6.53 ± 0.02	10 ± 1	0.04 ± 0.01	N.A.
	KN 387271	7.96 ± 0.20	78 ± 11	7.29 ± 0.08	109 ± 29	0.30 ± 0.11[§]	0.009 ± 0.002[§]
	GW-842166X	N.D.	37 ± 3[§]	N.D.	65 ± 13[#]	0.19 ± 0.01[§]	N.D.
	S-777469	7.04 ± 0.12	86 ± 12	6.71 ± 0.20	88 ± 10	0.22 ± 0.02	0.011 ± 0.002
	LY-2828360	6.89 ± 0.25	26 ± 5	6.33 ± 0.18	43 ± 7	0.24 ± 0.05	0.014 ± 0.003
	PRS-211375	7.18 ± 0.33	94 ± 11	6.41 ± 0.17	105 ± 4	0.24 ± 0.01	0.005 ± 0.002
	ART-27.13	9.15 ± 0.27	96 ± 11	7.93 ± 0.33	113 ± 23	0.24 ± 0.01[§]	0.012 ± 0.000[§]
	NTRX-07	6.70 ± 0.17	110 ± 27	6.59 ± 0.26	79 ± 3	0.20 ± 0.03[§]	0.006 ± 0.002[§]
	EHP-101	N.D.	19 ± 2[§]	N.D.	5 ± 1[#]	N.D.	N.D.
	Tedalinab	9.38 ± 0.25	97 ± 6	8.53 ± 0.14	114 ± 16	0.26 ± 0.03[§]	0.018 ± 0.002[§]
	TAK-937	8.56 ± 0.11	81 ± 3	7.07 ± 0.16	85 ± 3	0.20 ± 0.01[§]	0.008 ± 0.001[§]

Potency (pEC_{50}, pIR_{50}) and efficacy (E_{max}, IR_{max}) values were determined from AUC and initial rate dose-response curves, respectively, derived from the ß-arrestin-2 recruitment time traces in the multiplex assay. In the absence of a DRC, maximal activation (%) was determined at 10 (#) or 1 µM (§) of agonist. Signaling rate constants k_1 and k_2 were determined at 10 µM or 1 µM (§) of agonist. Data are mean from at least three independent experiments performed in duplicate. N.A is not applicable, N.D. is not detectable.

Secondly, the recruitment of ß-arrestin-2 to CB_2R was determined in the multiplex assay (**Table 3.4**). Potency values, calculated from the AUC-derived dose-response curves, ranged from 5.90 ± 0.14 for 2-AG to 8.54 ± 0.04 for CP55,940. Various degrees of partial agonism were observed in the agonist set. HU910, JWH133 were full agonists with E_{max} values > 90%, while Olorinab, PRS-211375, ART-27.13 and Tedalinab recruited ß-arrestin-2 to CB_2R with a higher efficacy than reference full agonist CP55,940 with E_{max} values of 114 ± 1%, 108 ±2%, 107 ±1% and 137 ± 5%, respectively, and could therefore be described as superagonists in this readout. All remaining fourteen agonists displayed partial agonism in ß-arrestin-2 recruitment with E_{max} values between 10 and 90%.

3.2.6 Kinetic quantification of CB_2R activation by benchmark agonists, endocannabinoids and clinical agonists in the multiplex assay

To use the kinetic data to its fullest potential, kinetic signaling parameters were calculated using the kinetic mathematical model by Hoare *et al.*, i.e., currently the only equations available for such analysis[20]. The initial rate (IR) was determined for each time trace and the kinetic potency (pIR_{50}) and kinetic efficacy (IR_{max}) were obtained from the generated dose-response IR curve. Furthermore, the signaling rate constants k_1 and k_2 were determined at a saturating concentration of agonist, i.e., 10 µM or 1 µM agonist (**Table 3.3**, **3.4**). From the kinetic trace fits, peak responses were obtained and also used to generate dose-response curves for parameter quantification. However, these results were identical to the AUC data and therefore not further analyzed (data not shown). No potency values were determined for CBD, GW-842166X and EHP-101 due to their lack of inhibition of cAMP production or ß-arrestin-2 recruitment to CB_2R, which is in line with their lack of CB_2R affinity (**Table 3.2-3.4**).

Based on the shape of the agonist-induced inhibition of cAMP production time traces, a statistical comparison between two rise-and-fall equations was performed, i.e., the simpler 'rise-and-fall to baseline' which describes a decline of signaling, and more complex 'rise-and-fall to steady state', which describes a decline to levels above baseline. The first fit was statistically preferred for inhibition of cAMP production. The kinetic potencies ranged from pIR_{50} values of 5.73 ± 0.21 for AEA to 8.53 ± 0.14 for Tedalinab (**Table 3.3**). A large variety in kinetic efficacy was observed with full agonists HU308, CP55,940, 2-AG, Lenabasum, KN 387271, PRS-211375, ART-27.13 and Tedalinab displaying IR_{max} values over 90%. All other twelve agonists displayed partial agonism, which ranged from 10 ± 1% for CBN to 89 ± 9 % for HU910. Moreover, two signaling rate constants k_1 and k_2 for the agonist-mediated inhibition of cAMP production were calculated, where the rising phase of the curve is characterized by k_1, and the fall phase by k_2. These constants were determined at saturating concentrations of agonist, i.e., 10 µM for most agonists and 1 µM for potent agonists CP55,940, ART-27.13, Tedalinab and TAK-9337 (**Table 3.3**). Values for k_1 ranged from 0.04 ± 0.01 min^{-1} for slowly activating agonist CBN to 0.30 ± 0.11 min^{-1} for faster agonist KN 387271, a difference of maximally 7.5-fold, while k_2 values differed maximally 10-fold between fastest agonist Olorinab (0.042 ± 0.015 min^{-1}) and slowest detectable agonist Nabilone (0.004 ± 0.001 min^{-1}).

Based on the shape of the ß-arrestin-2 recruitment traces, a statistical comparison between the two available rise-and-fall fits was performed, i.e., 'rise-and-fall to baseline' and 'rise-and-fall to steady state' equations, where in this case the latter was statistically preferred. The kinetic potencies ranged from pIR_{50} values of 5.19 ± 0.02 for AEA to 7.5 ± 0.07 for Tedalinab (**Table 3.4**). Superagonists Olorinab, PRS-211375, ART-27.13 and Tedalinab displayed high IR_{max} values of 157 ± 2%, 133 ± 12%, 148 ± 3% and 234 ±10%, respectively, while 2-AG behaved as a full agonist with a kinetic efficacy of 90 ± 17%. All thirteen remaining agonists displayed partial agonism in ß-arrestin-2 recruitment to CB_2R with IR_{max} values ranging from 4 ± 1% for Dronabinol to 80 ± 10% for HU308. The two signaling rate constants k_1 and k_2 for the agonist-mediated ß-arrestin recruitment were determined at saturating concentrations of agonist, i.e., 10 μM for most agonists and 1 μM for potent agonists (**Table 3.4**). The rising phase of the curve and corresponding parameter k_1 only differed less than 4-fold from slow agonist JWH133 (0.18 ± 0.01 min^{-1}) to faster agonist CMX-020 (0.63 ± 0.11 min^{-1}). The rate constant of the fall phase k_2 showed major differences with a maximal 32-fold difference between fastest agonist Tedalinab (0.063 ± 0.008 min^{-1}) and slowest detectable agonist Dronabinol (0.002 ± 0.001 min^{-1}).

The kinetic mathematical model allowed for a robust quantification of agonist-mediated inhibition of cAMP production and ß-arrestin-2 recruitment. The two potency values from the semi-kinetic and kinetic analyses, i.e., pEC_{50} and pIR_{50}, respectively, correlated for both the inhibition of cAMP production (R^2 0.73, $p < 0.0001$) and ß-arrestin-2 recruitment (R^2 0.90, $p < 0.0001$) (**Figure S3.13a,i**). Furthermore, efficacy E_{max} and kinetic efficacy IR_{max} values were well correlated for both pathways (R^2 0.44, p 0.0006 and R^2 0.80, $p < 0.0001$) (**Figure S3.13b,j**). The signaling rate constants, k_1 and k_2, of the agonists were not predictive for the kinetic potencies for either inhibition of cAMP production or ß-arrestin recruitment (**Figure S3.13c,d,k,l**). However, k_1 values from the inhibition of cAMP production were significantly correlated with ΔE_{max} values from the time-dependent analysis, i.e., agonists with fast k_1 values tended to gain efficacy over time (**Figure S3.13g**). For ß-arrestin-2 recruitment signaling parameters, only a fast k_2 value positively correlated with ΔE_{max} values, whereas no statistically significant correlation was found between k_1 values and ΔE_{max} values (**Figure S3.13o,p**). Interestingly, superagonists relative to CP55,940 in ß-arrestin-2 recruitment were characterized by a decrease in efficacy over time, i.e., negative ΔE_{max} values, and all displayed fast k_1 values (**Figure S3.13o**). Lastly, the interplay between inhibition of cAMP production and ß-arrestin-2 recruitment was investigated in terms of the kinetic parameters. Kinetic potency values for all agonists in inhibition of cAMP production and ß-arrestin-2 recruitment were significantly correlated (R^2 0.93, $p < 0.0001$) and only differed maximally 10-fold, indicating no overall pathway bias in the diverse agonist set (**Figure S3.13q**). Similarly, kinetic efficacy (IR_{max}) values were significantly correlated (R^2 0.53, p 0.0002) (**Figure S3.13r**). On the contrary, signaling rate constants k_1 and k_2 values were not correlated between the two readouts (p 0.7044, p 0.4600) (**Figure S3.13s,t**).

Altogether, investigation of benchmark agonists, endocannabinoids and clinical agonists in the multiplex assay highlighted the diversity of signaling potencies and efficacies at CB_2R within this large set of agonists. Furthermore, it emphasized the possibility and importance of kinetic evaluation, including kinetic mathematical analysis, of receptor signaling. The kinetic mathematical equations allowed quantification of common pharmacological

parameters, although with a kinetic context, i.e., kinetic potency (pIR_{50}) and kinetic efficacy (IR_{max}). Moreover, signaling rate constants k_1 and k_2 could be determined, which were not correlated between inhibition of cAMP production and ß-arrestin-2 recruitment suggesting these parameters may play a role in biased signaling.

3.2.7 Exploration of the kinetic context of CB_2R agonists

To investigate whether kinetic binding parameters of CB_2R agonists could be predictive for signaling parameters various correlation plots were generated (**Figure S3.14**). A fast association with CB_2R was significantly correlated with kinetic potencies pIR_{50} in both inhibition of cAMP production (R^2 0.66, $p < 0.0001$) and ß-arrestin-2 recruitment (R^2 0.73, $p < 0.0001$) (**Figure S3.14a**,**i**). In other words, the faster engaging agonists displayed higher kinetic functional potencies than the slowly engaging agonists. In contrast, no correlation was found between association rate constants and kinetic efficacy IR_{max} or the time-dependent increase in efficacy in either readout (**Figure S3.14b**,**d**,**j**,**l**). Unexpectedly, a quick engagement did not correlate with a quick activation, evident by the lack of statistically significant correlations between association rate constant k_{on} and signaling constant k_1 for either inhibition of cAMP production (R^2 <0.01, p 0.8045) or ß-arrestin-2 recruitment (R^2 0.03, p 0.5064) (**Figure S3.14c**,**k**).

Dissociation rate constants k_{off} were not correlated with pIR_{50} nor IR_{max} in both inhibition of cAMP production (R^2 0.02, p 0.5736; R^2 0.12, p 0.1512) or ß-arrestin-2 recruitment (R^2 0.04, p 0.4569; R^2 0.06, p 0.3127) (**Figure S3.14e**,**f**,**m**,**n**). On the contrary, a statistically significant correlation was observed for k_{off} values and time-dependent differences in efficacy for inhibition cAMP production (R^2 0.34, p 0.0139), but not ß-arrestin-2 recruitment (R^2 <0.01, p 0.9673) (**Figure S3.14h**,**p**). Specifically, fast dissociating agonists displayed an increase in cAMP efficacy over time (**Figure S3.14h**). Furthermore, no statistically significant correlations were found between dissociation rate constants and signaling (deactivation) rate constants k_2 in cAMP production ($R^2 < 0.01$, p 0.8798) or ß-arrestin-2 recruitment (R^2 0.19, p0.0705) (**Figure S3.14g**,**o**). Although, a small trend was displayed for slow dissociating agonists and slow deactivation in ß-arrestin-2 recruitment (**Figure S3.14o**).

Altogether, these correlations highlight that optimization of association rate constants rather than dissociation rate constants may contribute to high kinetic potencies but does not affect kinetic efficacy. Nevertheless, agonists with a fast dissociation rate constant might gain efficacy over time in inhibition of cAMP production and a fast k_{off} may play a role in deactivation of ß-arrestin-2 recruitment. This emphasizes the importance of providing a full kinetic overview of agonist-mediated CB_2R signaling.

3.2.8 Determination of ligand bias at CB_2R

Ultimately, biased signaling at CB_2R was investigated by using the different methods of analysis, i.e., an endpoint, a semi-kinetic and a kinetic analysis. The operational model was used to derive transduction coefficients LogR from the inhibition of cAMP production and

ß-arrestin-2 recruitment dose-response curves. To investigate the time-dependency of bias and the impact of different analysis strategies, the model was applied to the dose-response curves generated after 7.5 and 60 min of agonist activation (endpoint), AUC (semi-kinetic) and IR (kinetic) determination. In all cases, the LogR values were normalized to most balanced agonist HU308 resulting in ΔLogR for each agonist per pathway. Subsequently, these ratios were compared per agonist between the cAMP and ß-arrestin-2 pathways, which presented the relative bias ΔΔLogR (**Figure 3.6**, **Table S3.6**). As mentioned earlier, CBD, GW-842166X and EHP-101 failed to activate (or bind to) CB_2R, and consequently no LogR values were calculated for these agonists.

No clear preference for either pathway was observed for Olorinab, S-777469, ART-27.13, NTRX-07 and Tedalinab relative to HU308 using any of the methods of analysis. HU910 displayed a slight preference for inhibition of cAMP production over ß-arrestin-2 recruitment in the endpoint analysis after 7.5 and 60 min of activation, whereas in the semi-kinetic determination the preference flipped to ß-arrestin-2 recruitment and no clear

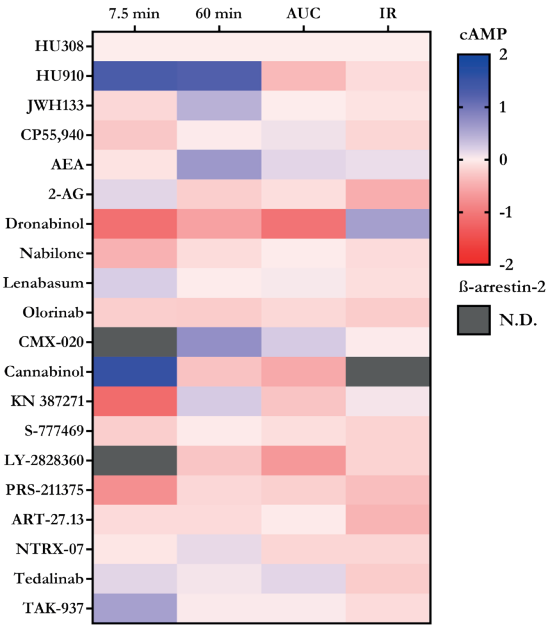

Figure 3.6 Quantification of biased agonism between inhibition of cAMP production and ß-arrestin-2 recruitment by benchmarks agonists, endocannabinoids and clinical agonists determined in the multiplex assay on CB_2R using an endpoint, semi-kinetic or kinetic analysis.
The dose response curves of all agonists based on endpoint (i.e., 7.5 and 60 min after agonist addition), semi-kinetic (AUC) or kinetic (IR) analysis were analyzed using the operational model of agonism to obtain transduction coefficients LogR, which were normalized to the balanced agonist HU308 per pathway (ΔLogR ratios). The bias between the two pathways was reported as ΔΔLogR and is shown in the heatmap. Blue indicates bias towards cAMP production, whereas red indicates bias towards ß-arrestin-2 recruitment. Agonists for which bias could not be determined (N.D.) due to absence of a dose response curve are presented in grey. CBD, GW-842166X and EHP-101 are omitted from the heatmap due to lack of receptor affinity and activation. One-way ANOVA was performed to analyze differences in ΔΔLogR values of agonists compared to HU308 (* $p<0.05$). Data are mean from at least three independent experiments performed in duplicate. Bias factors can be found in Table 3.S6.

bias was observed when analyzing the kinetic dose-response curves. On the other hand, after 7.5 min of activation, Nabilone and PRS-211375 demonstrated a small bias towards ß-arrestin-2 recruitment over inhibition of cAMP production relative to HU308, but the preference for ß-arrestin-2 recruitment was attenuated after 60 min of activation, as well as in the semi-kinetic and kinetic analysis. Time-dependent bias was observed for JWH133, AEA, 2-AG, CBN, KN 387271 evident by switched preferences after either 7.5 or 60 min of activation. A bias towards ß-arrestin-2 recruitment over inhibition of cAMP production was observed for Dronabinol in the endpoint and semi-kinetic analysis, whereas the bias was flipped towards inhibition of cAMP production in the kinetic analysis. No bias factor could be calculated for LY-2828360 after 7.5 min of activation due to the absence of a complete dose-response curve in the inhibition of cAMP production, while potency could be determined in ß-arrestin-2 recruitment. This may suggest that at the early time point LY-2828360 is strongly biased towards ß-arrestin-2 recruitment over inhibition of cAMP production, which is also observed in the semi-kinetic and kinetic analysis although slightly less pronounced. Although trends in biased signaling were observed for all other agonists, no statistically significant bias between inhibition of cAMP production and ß-arrestin-2 recruitment was found relative to HU308 in our system independent of the method of analysis used. However, in general a small trend towards ß-arrestin bias may be observed for several agonists (**Figure 3.6**).

Ultimately, we explored whether CB_2R binding kinetics could be predictive for the degree of bias. To maintain the kinetic context, correlation plots were generated for association and dissociation rate constants and the ΔΔLogR values obtained from kinetic analysis. No statistically significant correlation was found between k_{on} or k_{off} values and ΔΔLogR values of the agonists (R^2 <0.01, p 0.9865; R^2 0.15, p 0.1296) (**Figure S3.14q,r**).

Altogether, no statistically significant bias was observed for any of the agonists between the inhibition of cAMP production and ß-arrestin-2 recruitment determined in our multiplex assay. Small differences were observed in trends for biased signaling, which were in some cases dependent on the method of analysis (**Figure 3.6**, **Table S3.6**).

3.3 Discussion

Ligand bias is an emerging concept that holds great promise to advance drug discovery by selectively targeting therapeutic relevant signaling pathways[1–3]. However, examination of ligand bias *in vitro* is rather challenging, and experiments need to be designed with great caution to reduce system or observation bias[1]. To this end, we developed a novel multiplex assay that simultaneously detects cAMP production and ß-arrestin-2 recruitment in a kinetic manner in the same cells. We demonstrated the applicability of this kinetic multiplex assay on CB_2R by screening a large panel of diverse agonists (**Figure 3.1**, **Table 3.1**).

Multiplex assays have been designed to better capture the complexity of biological measurements as opposed to results obtained from a single screening unit. Most multiplex applications rely on fluorescent labeling, but multiplex luciferase reporters have also emerged for detection of genes as indicator of downstream signaling[39,40]. Nevertheless, these

technologies often rely on sequential analysis of two (or more) luciferases by quenching the light of the first enzyme before addition of the second substrate. On top of this, cells often need to be lysed, which removes the dynamic context of signaling events[40,41]. In the multiplex assay presented in this study, we successfully combined the GloSensor technology for capturing differences in cAMP production and NanoBiT for ß-arrestin-2 recruitment to CB_2R (**Figure 3.3**, **Table S3.3**), which generated similar potency values for reference agonist CP55,940 as previously seen in literature[28,35,42].

To investigate the time-dependency of activation and the impact of data analysis approaches, we analyzed the multiplex data using three methods: 1) as endpoint, i.e., after 7.5 and 60 min, 2) semi-kinetic AUC analysis, both methods provide the traditional potency and efficacy values, and 3) kinetic analysis using mathematical models that provided kinetic potency and kinetic efficacy based on initial rates (pIR_{50}, IR_{max}) and signaling rate constants k_1 and k_2[20]. Since the recent introduction of these novel curve fitting models, they are carefully being incorporated in pharmacological studies to aid more accurate characterization of ligand-receptor interactions for a variety of receptors and pathways[5,43–47]. Importantly, the impact of the chosen method of data analysis became clear in ligand bias analyses (**Figure 3.6**, **Table S3.6**). A trend in increased bias towards cAMP over time was observed for HU910, while the slight cAMP bias of TAK-937 was attenuated and 2-AG switched from cAMP preference at 7.5 min to ß-arrestin-2 preference after 60 min. These results are in line with results on the dopamine D_2 receptor, where it was demonstrated that ligand bias could change over time[13]. Biased signaling at CB_2R has never been investigated in a kinetic context and, to our knowledge, experiments have always been conducted in different functional (endpoint) assays with different cellular backgrounds, which could potentially introduce system bias[31,33–35,37]. Furthermore, incubation times with agonists spanned a wide range from 5 min to 90 min and sometimes even differed between assays within the same study. However, our results clearly demonstrate that time-dependence should be considered when studying biased signaling to reduce the effect of system and observation bias and thus draw proper conclusions on ligand bias.

To this end, the semi-kinetic and kinetic analyses were employed to reduce the influence of time and use the obtained signaling time traces to their fullest extent. In general, the observed potency values for inhibition of cAMP production and ß-arrestin-2 recruitment were slightly lower compared to literature[28,35,48–50]. On the other hand, Lin *et al.* observed no ß-arrestin-2 recruitment to CB_2R after activation by LY-2828360, whereas in our multiplex assay we found a low potency for LY-2828360 although with low efficacy (**Table 3.4**)[50]. Not only were previously reported pharmacological parameters determined at specific time points, but the performed assays also relied on lysis of cells or measurement of cAMP accumulation and/or irreversible ß-arrestin-2 recruitment and thus removing the dynamic context. Noteworthy, we observed strong correlations between the potency and efficacy values from the semi-kinetic (AUC) compared to the kinetic analysis for both inhibition of cAMP production and ß-arrestin-2 recruitment (**Figure S3.13**), which indicates that the novel kinetic analyses are fit to rapport 'classical' pharmacological parameters, such as potency and efficacy. Moreover, the observed statistically significant correlations between the pIR_{50} and IR_{max} values from inhibition of cAMP production and ß-arrestin-2 recruitment suggest a lack of bias in the overall agonist set. However, the signaling rate

constants k_1 and k_2 were not correlated and as such may contribute to the small trends in bias that were observed for Dronabinol and 2-AG. We envision that kinetic analysis, or early time point analysis, in *in vitro* assays generates parameters that better predict the *in vivo* pharmacological effects, i.e., starting GPCR activation and signal transduction without interference of artificial regulation mechanisms[20]. As such, kinetic potency (pIR_{50}) and efficacy (IR_{max}) as well as signaling rate constant k_1 require more attention. Interestingly, a faster engagement (k_{on}) of agonists with CB_2R correlated with both a higher affinity as well as a higher potency in both inhibition of cAMP production and ß-arrestin-2 recruitment (**Figure S3.1b**, **S3.14a**,**i**), and as such is a driving force for CB_2R binding and activation. While a quick engagement with CB_2R did not result in a quick activation (k_1), we found that superagonists Olorinab, PRS-211375, ART-27.13 and Tedalinab in ß-arrestin-2 recruitment were characterized by fast signaling rate constants k_1 in the kinetic analysis. However, not all agonists with fast k_1 values behaved as superagonists. Although no correlation was found for k_{off} and affinity or potency (**Figure S3.1c**, **S3.14e**,**m**), we observed that slowly dissociating agonists exhibited slow deactivation of ß-arrestin-2 recruitment, which may suggest that extended agonist binding results in a longer receptor interaction with ß-arrestin-2. Since the introduction of the target binding kinetics concept, the primary focus has been on optimization of RT, rather than on association rate constants[51]. However, this study clearly indicates that optimization of the association rate constants for CB_2R agonists is equally valuable to improvement of the dissociation rate constants.

The applied kinetic signaling models do not only allow for quantification of signaling parameters, but the shape of the traces may also be indicative of regulation mechanisms. Our inhibition of cAMP production data, after corrections and inversion, was best fit by the 'Baseline then rise-and-fall to baseline' model, which was also previously reported for cAMP production after activation of the adenosine A_1 receptor and $ß_2$-adrenoceptor[44,46]. This shape is generally described for second messenger signaling when there is no additional regulation of signaling by inhibitors, such as phosphodiesterase (PDE) inhibitors[43]. Agonist-dependent differences were observed in the time traces. Some agonists, such as Tedalinab, displayed a steep decrease of the inhibition of cAMP production, which was also reflected by higher signaling rate k_2 values (**Figure 3.4f**, **Table 3.3**). Yet the exact mechanism behind these differences requires more experimental validation, which could benefit from the use of PDE inhibitors to simplify the system[44]. On the other hand, the ß-arrestin-2 recruitment time traces were analyzed using the 'Baseline then rise-and-fall to steady state' model (**Figure 3.4**, **Table 3.4**), which has been previously used for ß-arrestin-2 recruitment time traces to other GPCRs[5,43,46]. As a general model, the 'rise-and-fall to steady state' equation was generated to capture complex regulation mechanisms, which in the case of ß-arrestin-2 recruitment has been hypothesized to refer to receptor desensitization, internalization, recycling to the cell membrane or degradation[43]. Several studies have reported that agonist-stimulated CB_2R also undergoes these processes[52–59]. Grimsey *et al.* described that HU308-induced internalization of CB_2R did not result in degradation of the receptor, but rather recycling of the receptor to the cell membrane. However, a remaining proportion of the receptors was not recycled nor degraded but remained in the cytoplasm[54]. The remaining luminescence above baseline in our assays, as a measure for complementation of CB_2R and ß-arrestin-2, may reflect the proportion of receptors that have been internalized,

but not (yet) recycled or degraded (**Figure 3.4**, **S3.6**, **S3.7**). Furthermore, since signaling rate constants k_1 and k_2 are not assigned to particular regulation mechanisms, the exact mechanisms, i.e., internalization, recycling or degradation, upon CB_2R activation by the different agonists cannot be deciphered. This would require additional investigation to reveal differential agonist-dependency for initiation of ß-arrestin-mediated internalization, recycling, or degradation at CB_2R, alike results found at the $ß_2$-adrenergic receptor[60]. Altogether, this study advocates the use of the kinetic multiplex assay with novel analyses to determine potency and efficacy in a kinetic context with the advantage of additional signaling rate constants k_1 and k_2, which can reveal differences between agonists that are otherwise overlooked.

For proper use of the Black-Leff operational model for bias analysis the maximal response of the system needs to be accurately estimated[61,62]. Several agonists displayed superagonism in ß-arrestin-2 recruitment compared to full agonist CP55,940, which was most prominent for Tedalinab (**Table 3.3**, **3.4**). Therefore, Tedalinab was used as full agonist, which also improved the fits on all other agonists (data not shown). Similar to previous work, benchmark agonists HU308, HU910 and JWH133 remained balanced between the two studied pathways (**Figure 3.6**, **Table S3.6**)[35]. Although some trends towards biased signaling were observed, none of the calculated ΔΔLogR values were significantly different from balanced agonist HU308 (**Figure 3.6**, **Table S3.6**). Previously reported biased signaling of CB_2R agonists (bias factors ranging between 0.0015 and 90) may have been influenced by system and observational bias due to the use of a biased reference agonist, different cellular backgrounds, time points and measurements used to report bias amongst pathways[31,33–35,37]. FDA approved μ-opioid receptor biased agonist oliceridine only displayed a bias factor of 3 for G protein activation over ß-arrestin-2 recruitment, while bias factors up until 85 have been reported on the same receptor[63,64]. Nevertheless, more recent studies have hypothesized that the partial agonism of oliceridine may be responsible for the beneficial therapeutic effect rather than its biased profile[65]. It is important to note that bias factors only provide a ratio compared to a selected reference agonist in a specific system, which aids in prioritizing or selecting agonists for further testing in therapeutically relevant systems or *in vivo* models[11]. In this study, we did not observe significant degrees of bias signaling for the clinically relevant CB_2R agonists, which may be the reason for failure of several of these agonists in clinical trails. However to date, the mechanism of therapeutic effects at CB_2R and the potential importance of biased signaling is largely unknown. To prove whether signaling bias on CB_2R has therapeutic relevance, the mechanism should be further explored. This may be done by *in vitro* in relevant native cell background and/or *in vivo* by knockout studies of ß-arrestin-2 or $G\alpha_i$ proteins to specify which signaling pathway is therapeutically relevant[1,11].

In conclusion, this study describes the development and application of a novel multiplex assay that simultaneously detects cAMP production and ß-arrestin-2 recruitment in a time-dependent manner in the same cells. We demonstrate that agonist-mediated CB_2R activation and biased signaling is time sensitive dependent on the specific agonist used. Similar potency and efficacy parameters can be obtained from semi-kinetic and kinetic methods of analysis, while the latter additionally provides signaling rate constants that may accentuate differences between agonist-dependent signaling and bias. Moreover, this study demonstrates the

importance of fast agonist engagement (k_{on}) with CB_2R for increased affinity and potency, while slowly dissociating agonists extended the interaction between CB_2R and ß-arrestin-2. We envision that kinetic parameters that capture the early response, such as pIR_{50}, IR_{max} and signaling rate constant k_1, could be applied to *in vitro* studies as better predictors of their pharmacological effects *in vivo*. Ultimately, combining these parameters with binding kinetics results in more extensively profiled GPCR agonists to advance future drug discovery efforts.

3.4 Materials and methods

3.4.1 Chemical and reagents

RO6957022 and [^{3}H]RO6957022 (specific activity 82.83 Ci mmol^{-1}) were synthesized in-house as previously published [66]. [^{3}H]CP55,940 (specific activity 108.5 Ci mmol^{-1} #NET1051250UC), [^{35}S]GTPγS (specific activity 1250 Ci mmol^{-1} #NEG030H250UC), and GF/C filter plates (#6055690) were purchased from Revvity (Waltham, MA, USA). Bicinchoninic acid (BCA) and BCA protein assay reagent were obtained from Pierce Chemical Company (Rockford, IL, USA). CP55,940 (#C1112), AM630 (#SML0327), and DL-dithiothreitol (DTT, #646563) were obtained from Sigma-Aldrich (Saint Louis, MO, USA). Tedalinab (#T013730) and forskolin (FSK, #F701800) were from Toronto Research Chemicals. Δ^9-THC (#12068) and LY-2828360 (#26791) from Cayman Chemical (Ann Arbor, MI, USA). Anandamide (AEA, #1339), 2-Arachidonylglycerol (2-AG, #1298), JWH-133 (#1343), cannabidiol (CBD, #1570), cannabinol (CBN, #3130) and phenylmethylsulfonyl fluoride (PMSF, #4486) were purchased from Tocris Bioscience (Bristol, UK). GDP (#J61646) was from Thermo Fisher Scientific (Waltham, MA, USA), EHP-101 (#HY-128872) from MedChemExpress (Monmouth Junction, NJ, USA) and HU308 (#H800010) was obtained from LKT Laboratories (St. Paul, MN, USA). Nabilone, Lenabasum, Olorinab, CMX-020, KN 387271, GW-842166X, S-777469, PRS-211375, ART-27.13, NTRX-07 and TAK-937 were provided by F. Hoffmann-La Roche Ltd (Basel, Switzerland) and HU910 was a kind gift from Pal Pacher (NIH, MD, USA). FuGENE® 6 Transfection Reagent (#E2692), Nano-Glo® Vivazine™ Substrate (#N2581), GloSensor™ cAMP reagent (#E1291) and pGloSensor™-22F cAMP Plasmid (#E2301) were from Promega (Madison, WI, USA) and 96-well solid white flat bottom microplates (#3917) were obtained from Corning (Corning, NY, USA). All buffers and solutions were prepared using Millipore water (deionized using a MilliQ A10 Biocel™ with a 0.22 µm filter) and analytical grade reagents and solvents. Buffers were prepared at room temperature (rt) and stored at 4 °C, unless stated otherwise.

3.4.2 Physicochemical properties and pharmacokinetic properties determination

3.4.2.1 Lipophilicity

For the determination of the octanol/water distribution coefficient (LogD), the Carrier-Mediated Distribution System (CAMDIS)-assay was used as described previously[67].

3.4.2.2 Kinetic aqueous solubility (Lysa)

The compounds' solubility was assessed in a phosphate buffer with a pH of 6.5, originating from a 10 mM stock solution in DMSO that had been evaporated. For each compound, two samples were desiccated and reconstituted in the pH 6.5 phosphate buffer. Post-dissolution, the solutions underwent filtration and were subsequently diluted to three distinct concentrations. RapidFire mass spectrometry analysis was conducted on these dilutions. Quantification of each compound was achieved using a calibration curve comprising six points, which was established using the initial DMSO solution.

3.4.2.3 Lipid membrane binding assay (Limba LogDbrain)

The Lipid Membrane Binding Assay (LIMBA LogDbrain) was conducted consistent with previously published methods, allowing for high to medium throughput analysis[68].

3.4.2.4 Passive membrane permeability assay (PAMPA)

The PAMPA assay was carried out as a high-throughput experiment as previously described[68].

3.4.2.5 Human plasma protein binding (free fraction %)

Human plasma with EDTA as an anticoagulant was sourced from BioreclamationIVT (New York, USA)[69,70]. To determine the free fraction of a agonist, a 96-well equilibrium dialysis device with a Teflon build and a 150 µL half-cell volume was used. This device featured a membrane with a molecular weight cut-off between 12 and 14 kDa, chosen to reduce non-specific binding. Both the test compound and a known reference, diazepam, were assessed in groups ranging from 2 to 5 wells, starting at a concentration of 1000 nM. Each well was filled with equal amounts of a plasma sample containing the test compound or diazepam and a blank dialysis buffer, specifically Soerensen's buffer. The pH of the plasma and buffer was adjusted to 7.4 on the day of the experiment. The dialysis unit was then incubated at 37 °C with 5% CO_2 for 5 hours, which is generally sufficient for equilibrium to be reached for most small molecules under 600 Da. Following incubation, the samples were prepared for LC-MS/MS analysis. Each protein binding assessment was conducted in triplicate to ensure accuracy. The integrity of the dialysis membrane was verified by measuring the unbound fraction of diazepam in each well. At equilibrium, the concentration of the unbound drug in the plasma should equal that in the buffer, allowing for the calculation of the unbound fraction as the buffer concentration post-dialysis divided by the plasma concentration post-dialysis, multiplied by 100. Additionally, the recovery of the device was evaluated by comparing the concentration of the compound in the plasma before and after dialysis, with acceptable recovery rates ranging from 80% to 120% for the data to be considered valid.

3.4.2.6 P-glycoprotein-mediated efflux ratio

The generation of human P-gp efflux ratio values was conducted as previously reported[68].

3.4.3 Cell culture and membrane preparation

For functional assays, human embryonic kidney 293T cells (HEK293T, ATCC #CRL-3216) and HEK293T cells stably expressing full-length hCB_2R-SmBiT and LgBiT-ß-arrestin-2 constructs (HEK293T CB_2R-SmBiT LgBiT-ß-arrestin-2, a kind gift by Christophe Stove, Ghent University, Belgium [71]) were grown in monolayers. Both cell lines were cultured in Dulbecco's Modified Eagle's Medium supplemented with 10% FCS, 2 mM Glutamax, 100 IU/mL penicillin and 100 µ/mL streptomycin in a humidified atmosphere at 37 °C and 5% CO_2. For binding assays, Chinese Hamster Ovary (CHO) cells stably expressing hCB_2R or hCB_1R (CHOK1_hCB_2bgal, #93-0706C2 and CHOK1_hCB_1bgal, #93-0959C2, PathHunter EA Parental cell line, female, DiscoverX) were cultured in Ham's F12 Nutrient Mixture supplemented with 10% (v/v) fetal calf serum (FCS), 2 mM Glutamax, 100 IU/mL penicillin, 100 µg/mL streptomycin, 300 µg/mL hygromycin and 800 µg/mL G418 in a humidified atmosphere at 37 °C and 5% CO_2. All cells were subcultured twice weekly when reaching 80-90% confluence on 10 or 15 cm ø plates by trypsinization and used for further experiments within 20 passages.

3.4.4 Membrane preparation

HEK293T CB_2R-SmBiT LgBiT-ß-arrestin-2, CHOK1_hCB_2bgal and CHOK1_hCB_1bgal cells were harvested when reaching 80-90% confluence in 15 cm ø plates after one week subculture at a 1:15, 1:6 or 1:6 ratio, respectively. The cells were detached by scraping into 5 mL phosphate-buffered saline (PBS) and subsequently centrifuged at 2,000 × g for 5 min. Pellets were resuspended in ice-cold Tris buffer (50 mM Tris-HCl, pH 7.4) and homogenized with an Ultra Turrax homogenizer (IKA-Werke GmbH & Co. KG, Staufen, Germany). Cytosolic and membrane fractions were separated using an Optima LE-80 K ultracentrifuge (Beckman Coulter, Inc., Fullerton, CA) at 100,000 × g for 20 min at 4 °C. The membrane fractions were subjected to another round of homogenization and centrifugation. The final pellets were resuspended and homogenized in ice-cold Tris buffer and subsequently aliquoted and stored in 100 µL aliquots at -80 °C. Membrane protein concentrations were determined using a BCA protein determination assay, as described by the manufacturer (Pierce BCA protein assay kit)[72].

3.4.5 [^{3}H]RO6957022 binding assays

[^{3}H]RO6957022 displacement and competition association assays have previously been described with the main difference that the incubation temperature was changed to 10 °C for improved separation of kinetic differences[66]. In short, CHOK1_hCB_2bgal or HEK293T CB_2R-SmBiT LgBiT-ß-arrestin-2 membranes were thawed and subsequently homogenized using the Ultra Turrax homogenizer. For experiments with endocannabinoids and CMX-020, membranes were preincubated for 30 min with 50 µM PMSF. The reactions were carried out in 100 µL assay buffer (50 mM Tris-HCl (pH 7.4), 0.1% (w/v) bovine serum albumin (BSA)) containing 1 µg (CHOK1_hCB_2bgal) or 10 µg (HEK293T CB_2R-SmBiT LgBiT-ß-

arrestin-2) of membrane protein and 1.5 nM [^{3}H]RO6957022. Incubations were performed at 10 °C. Therefore, assay buffer, (radio)ligands and membranes were precooled to 10 °C prior to the experiment. Nonspecific binding (NSB) was determined using 10 μM AM630 and vehicle (i.e., acetonitrile for endocannabinoids and CMX-020, and DMSO for all other compounds) concentrations were constant and kept < 1% in all samples. Total radioligand binding (TB) did not exceed 10% of the amount added to prevent ligand depletion. For all assays, incubations were terminated by rapid vacuum filtration with ice-cold 50 mM Tris-HCl (pH 7.4), 0.1% (w/v) BSA buffer through Whatman GF/C filters using a Filtermate 96-well harvester (Revvity, Waltham, MA, USA). Filters were dried for at least 30 min at 55 °C and subsequently 25 μL MicroScint scintillation cocktail was added per well. Filter-bound radioactivity was measured by scintillation spectrometry using a Microbeta^2 2450 counter (Revvity, Waltham, MA, USA).

3.4.5.1 Displacement assays

Binding affinity of all clinical agonists for CB_2R was determined in displacement assays using radioligand and six increasing concentrations of competing compound (ranging from 0.01 nM to 10 μM) on CHOK1_hCB_2bgal membranes. Homologous displacement assays were performed on HEK293T CB_2R-SmBiT LgBiT-ß-arrestin-2 membranes with three concentrations of [^{3}H]RO6957022 of ~0.5 nM, ~1.5 nM and ~5.0 nM in the presence of competing RO6957022 (ranging from 0.01 nM to 1 μM) in assay buffer. The reaction mixture was incubated for 2 h at 10 °C, after which incubations were terminated and receptor-bound radioactivity was determined as described in section **3.4.5 [^{3}H]RO6957022 binding assays**.

3.4.5.2 Competition association assays

Binding kinetics were assessed in competition association experiments using radioligand and competing compound at its IC_{50} concentration obtained from displacement assays. Competition was initiated by addition of CHOK1_hCB_2bgal membrane homogenates at different time points for 2 h, after which incubations were terminated and receptor-bound radioactivity was determined as described in section **3.4.5 [^{3}H]RO6957022 binding assays**.

3.4.6 [^{3}H]CP55,940 displacement assays

Binding affinity for CB_1R was determined in [^{3}H]CP55,940 displacement assays. CHOK1_hCB_1bgal membranes were homogenized and diluted to 2.5 μg protein per well in assay buffer (50 mM Tris-HCl (pH 7.4), 5 mM $MgCl_2$, 0.1% (w/v) BSA). Membranes were incubated with six increasing concentrations (ranging from 0.01 nM to 10 μM) of competing compound in the presence of 1.5 nM [^{3}H]CP55,940. Incubations were for 2 h at 25 °C. NSB was determined using 10 μM SR141716A and vehicle (i.e., acetonitrile for endocannabinoids and CMX-020, and DMSO for all other compounds) concentrations were constant and kept < 1% in all samples. TB did not exceed 10% of the amount added to prevent ligand depletion. Incubations were terminated as described in section **3.4.5 [^{3}H]RO6957022 binding assays** except using ice-cold wash buffer containing 50 mM Tris-HCl, 5 mM $MgCl_2$ and 0.1% BSA.

3.4.7 Multiplexed cAMP production and ß-arrestin-2 recruitment assay

Inhibition of cAMP production and ß-arrestin-2 recruitment after CB_2R activation were measured using the GloSensor™ and NanoBiT® technologies, respectively, in a multiplexed manner. To this end, HEK293T CB_2R-SmBiT LgBiT-ß-arrestin-2 cells were seeded as 2×10^6 cells on 10 cm ø plates to reach 60% confluence on the day of transfection. The next day, cells were transfected with 10 µg pGloSensor™-22F cAMP plasmid using FuGENE® 6 transfection in a 3:1 reagent:DNA ratio [73]. In short, a mix of 10 µg GloSensor plasmid and 30 µL FuGENE® 6 was incubated in 850 µL Opti-MEM™ at room temperature (rt) for 15 minutes. The mixture was added to the cells without replacing the medium. Cells were left to grow overnight at 37 °C with 5% CO_2 to reach ~90% confluence. The next day, transfected cells were seeded at a density of 50,000 cells/well in poly-D-lysine treated solid white, flat bottom 96-well plates in culture medium and incubated for another 22-24 h at 37 °C with 5% CO_2. On the assay day, the culture medium was replaced by 30 µL assay medium (CO_2 independent medium + 10% (v/v) FCS) and 50 µL equilibration reagent in assay medium. The equilibration reagent for the GloSensor™ only contained 4% (v/v) GloSensor™ cAMP reagent, NanoBiT® reagent contained 2% (v/v) Vivazine™ substrate and the "multiplex reagent" contained a combination of the two reagents, i.e., 2% (v/v) Vivazine™ substrate and 4% (v/v) GloSensor™ cAMP reagent. The plate was incubated at 25 °C for 2 h in the dark after which baseline cAMP levels and ß-arrestin recruitment were measured for 7.5 min in the plate reader using the protocol as described below.

To induce cAMP production, cells were prestimulated with 1 µM forskolin (FSK) until reaching a stable plateau of cAMP production. Specifically, induction of cAMP production was initiated by addition of 10 µL FSK mixture and luminescence was monitored for 52.5 min in the plate reader. For experiments with endocannabinoids or CMX-020, the FSK prestimulation mixture additionally contained 50 µM phenylmethylsulfonyl fluoride (PMSF). Immediately after, cells were stimulated with 10 µL increasing concentrations of compound of interest (ranging from 0.01 nM to 10 µM). Compounds were added using a MINI 96 portable electronic pipette to ensure no time delay (INTEGRA Biosciences, Tokyo, Japan). The maximal response was determined by 1 µM CP55,940 and vehicle (i.e., acetonitrile for endocannabinoids and CMX-020, and DMSO for all other compounds) concentrations were constant and kept < 1% in all samples. Luminescence was measured for another 90 min in the plate reader resulting in a total read time of 150 min.

The simultaneous luminescent signals were measured in a Wallac EnVision 2104 Multilabel reader (Revvity, Waltham, MA, USA). To this end, the individual signals were detected by two emission filters in a dual luminescent manner. Specifically, the Cy3 595 filter (595/60 nm, barcode 229) was used to detect the cAMP responses and emission filter NanoBRET Blue (460/80 nm, barcode 703) was used to detect ß-arrestin-2 recruitment to CB_2R. Each wavelength was measured for 250 ms/well and the total interval between plate repeats was 90 s.

To investigate cAMP responses independent of CB_2R, the same protocol was applied to parental HEK293T cells, but only using the GloSensor™ equilibration reagent containing 4% (v/v) GloSensor™ cAMP reagent.

3.4.8 Data analysis and statistics

All experimental data were analyzed using GraphPad Prism 9.0 (GraphPad Software Inc., San Diego, CA, USA). All values obtained are means ± standard error of the mean (SEM) of at least three independent experiments performed in duplicate, unless stated otherwise.

3.4.8.1 Displacement assays

[^{3}H]RO6957022 (CB_2R) and [^{3}H]CP55,940 (CB_1R) assays were baseline-corrected with NSB and normalized to this value (0%) and TB (100%). The equilibrium dissociation constant (K_D) of [^{3}H]RO6957022 and receptor expression level (B_{max}) were calculated from homologous displacements by non-linear regression analysis, using the "one-site homologous" model. The half-maximal inhibitory concentrations (pIC_{50}) of the compounds in [^{3}H]RO6957022 and [^{3}H]CP55,940 displacement assays were obtained by non-linear regression analysis of the displacement curves and further converted into inhibitory constant pK_i using the Cheng-Prusoff equation[74] with the experimentally determined K_D values 0.78 nM and 0.84 nM, respectively (data not shown). CB_2R selectivity of the compounds was determined when two pK_i values were obtained using **Equation 3.1**:

$$\text{Selectivity}=10^{(pK_i\ CB_2R-pK_i\ CB_1R)} \qquad \textbf{(Equation 3.1)}$$

3.4.8.2 Competition association assays

From [^{3}H]RO6957022 competition association assays, the k_{on} and k_{off} values of compounds of interest were determined by non-linear regression analysis, using the "kinetics of competitive binding" model as described by Motulsky and Mahan[75]:

$$K_a=k_1[L]\cdot10^{-9}+k_2$$

$$K_b=k_3[I]\cdot10^{-9}+k_4$$

$$S=\sqrt{(K_a-K_b)^2+4\cdot k_1\cdot k_3\cdot[L]\cdot[I]\cdot10^{-18}}$$

$$K_f=0.5(K_a+K_b+S)$$

$$K_s=0.5(K_a+K_b-S)$$

$$Q=\frac{B_{max}\cdot k_1\cdot[L]\cdot10^{-9}}{K_f-K_s}$$

$$[Y]=Q\left(\frac{k_4\cdot(K_f-K_s)}{K_f\cdot K_s}+\frac{k_4-K_f}{K_f}\cdot e^{(-K_f\cdot X)}-\frac{k_4-K_s}{K_s}\cdot e^{(-K_S\cdot X)}\right)$$

Where [L] is the radioligand concentration per experiment (~1.5 nM), I is the IC_{50} concentration of compound (nM), X is the time (s), and Y is the specific binding of the radioligand (dpm). K_a and K_b are the observed association rate constants (k_{obs}) of the radioligand and the compound of interest, respectively. k_1 and k_3 are the association rate constants (k_{on} in $M^{-1}s^{-1}$) of [^{3}H]RO6957022 (determined per experiment) and the compound of interest, respectively. Similarly, k_2 and k_4 are the dissociation rate constants

(k_{off} in s^{-1}) of [^{3}H]RO6957022 (experimentally determined at 4.3×10^{-4} s^{-1}, data not shown) and the compound of interest, respectively. The engagement time (ET in seconds) of the compounds of interest was determined at 1 μM of compound using **Equation 3.2**[76]:

$$ET = \frac{1}{k_{on} \cdot 10^{-6}} \quad \textbf{(Equation 3.2)}$$

The residence time (RT in min) was calculated using **Equation 3.3**[14]:

$$RT = \frac{1}{k_{off} \cdot 60} \quad \textbf{(Equation 3.3)}$$

The association and dissociation rate constants were used to calculate the kinetic K_D using **Equation 3.4**:

$$K_D = \frac{k_{off}}{k_{on}} \quad \textbf{(Equation 3.4)}$$

3.4.8.3 Inhibition of forskolin-induced cAMP production (multiplex signal 1)

Functional forskolin-induced cAMP data from the multiplex assay was analyzed based on an endpoint, semi-kinetic and kinetic approach. Forskolin-induced cAMP responses after 7.5, 15, 30 and 60 min of agonist addition were baseline-corrected with the vehicle response and normalized to 1 μM CP55,940. Dose-response curves were generated and pEC_{50} and E_{max} values were determined using non-linear regression curve fitting 'log(agonist) vs. response' (three parameters).

Forskolin-induced cAMP time traces from the multiplex assay was corrected for well-to-well variation by subtracting the mean of the baseline measurement and subsequently subtracting the mean of the final five FSK measurements. Next, vehicle response was subtracted, and the data was inverted to represent inhibition of cAMP production. The agonist-induced inhibition of cAMP production was quantified by taking the net area under the curve (AUC) from the final five FSK measurements until the end of agonist measurement (54 - 150 min). Dose-response curves were generated and pEC_{50} and E_{max} values were determined using non-linear regression curve fitting 'log(agonist) vs. response' (three parameters) after normalization to 1 μM CP55,940.

The agonist-induced inhibition of cAMP production was further kinetically analyzed by applying the 'Baseline then rise-and-fall to baseline time course' equation according to Hoare *et al.*[20]. This equation (**3.5**) was provided as a plug-in, which was downloaded into GraphPad Prism[77]:

$$Y = IF\left(X<X_0, \text{Baseline}, \text{Baseline} + \left(\frac{IR}{k_1 - k_2}\left(e^{-k_2(X-X_0)} - e^{-k_1(X-X_0)}\right)\right)\right) \quad \textbf{(Equation 3.5)}$$

Where 'IR' is a fitting constant (cps min^{-1}), which is equal to the initial rate of signaling and represented by the initial linear phase of signal generation after receptor activation, X is the time (min), X_0 is the time at which the signal starts, and Y is the luminescent signal (cps). k_1 and k_2 are the observed signaling rate constants (min^{-1}), where k_1 is constrained to be greater than k_2. When time traces did not fall back to baseline in the assay time, as was the case for lower agonist concentrations, the 'baseline then rise to steady state time course' was fitted

according to **Equation 3.6**:

$$Y=IF\left(X<X_0, Baseline, SSR \cdot \left(1-e^{-k(X-X_0)}\right)+Baseline\right) \quad \textbf{(Equation 3.6)}$$

Where SSR is the steady-state response representing the maximal activation as time reaches infinity (cps), X is the time (min), X_0 is the time at which the signal starts, and Y is the luminescent signal (cps). k is the observed signaling rate constant (min^{-1}).

Dose-response curves were generated from the Initial Rate data and pIR_{50} and IR_{max} values were determined using non-linear regression curve fitting 'log(agonist) vs. response' (three parameters) after normalization to 1 μM CP55,940. More detailed information on the use of these models and a step-by-step procedure can be found in **Supplementary methods 3.S1.2.1**.

3.4.8.4 ß-arrestin-2 recruitment (multiplex signal 2)

Functional ß-arrestin-2 recruitment data from the multiplex assay was analyzed based on an endpoint, semi-kinetic and kinetic approach. Recruitment of ß-arrestin-2 after 7.5, 15, 30 and 60 min of agonist addition were baseline-corrected with the vehicle response and normalized to 1 μM CP55,940. Dose-response curves were generated and pEC_{50} and E_{max} values were determined using non-linear regression curve fitting 'log(agonist) vs. response' (three parameters).

Functional ß-arrestin-2 recruitment time traces from the multiplex assay was corrected for well-to-well variation by subtracting the mean of the baseline (final five FSK measurements count as baseline) and subsequently vehicle response was subtracted. The ß-arrestin-2 recruitment to CB_2R was quantified by taking the net area under the curve (AUC) from the baseline measurements until the end of agonist measurement (54 - 150 min). Dose-response curves were generated and pEC_{50} and E_{max} values were determined using non-linear regression curve fitting 'log(agonist) vs. response' (three parameters) after normalization to 1 μM CP55,940.

The ß-arrestin-2 recruitment was further kinetically analyzed by applying the 'Baseline then rise-and-fall to steady state time course' equation according to Hoare *et al.*[20]. This equation (**3.7**) was provided as a plug-in, which was downloaded into GraphPad Prism[77]:

$$Y=IF\left(X<X_0, Baseline, Baseline+SSR\left(1-D \cdot e^{-k_1(X-X_0)}+(D-1)e^{-k_2(X-X_0)}\right)\right) \quad \textbf{(Equation 3.7)}$$

Where SSR is the steady-state response representing the maximal activation as time reaches infinity (cps), D is a unitless fitting constant, X is the time (min), X_0 is the time at which the signal starts, and Y is the luminescent signal (cps). k_1 and k_2 are the observed signaling rate constants (min^{-1}), where k_1 is constrained to be greater than k_2. Initial rate can be calculated using **Equation 3.8**:

$$IR=SSR(D \cdot k_1-(D-1)k_2) \quad \textbf{(Equation 3.8)}$$

When time traces did not fall back to baseline in the assay time, as was the case for lower agonist concentrations, the 'baseline then rise to steady state time course' was fitted as described for **3.4.8.3 Inhibition of forskolin-induced cAMP production.**

Dose-response curves were generated from the Initial Rate data and pIR_{50} and IR_{max} values were determined using non-linear regression curve fitting 'log(agonist) vs. response' (three parameters) after normalization to 1 μM CP55,940. More detailed information on the use of these models and a step-by-step procedure can be found in **Supplementary methods 3.S1.2.2**.

3.4.8.5 Bias calculation

Dose-response curves from the endpoint analysis (early and late time point), semi-kinetic AUC and kinetic initial rate analysis for all compounds and for each functional readout were analyzed using the Black and Leff operational model to calculate the transduction coefficient $Log(\tau/K_A)$ or LogR values as previously described[61,78]. In the model, the slope (n) was set to 1, basal to 0 as the data was baseline corrected and E_{max} was set to the maximal activation in the system (Tedalinab). For each functional readout, the LogR value of the agonists was compared to most balanced agonist HU308 generating transduction ratios ΔLogR using **Equation 3.9**:

$$\Delta LogR_{agonist} = LogR_{agonist} - LogR_{HU308} \quad \textbf{(Equation 3.9)}$$

The relative bias of each agonist between the cAMP and ß-arrestin-2 pathway, represented as ΔΔLogR, was calculated using **Equation 3.10**:

$$\Delta\Delta LogR_{agonist} = \Delta LogR_{agonist,\ cAMP} - \Delta LogR_{agonist,\ \beta\text{-arrestin}} \quad \textbf{(Equation 3.10)}$$

Ultimately, the bias factor was calculated as the inverse logarithm of the ΔΔLogR values using **Equation 3.11**:

$$\text{Bias factor} = 10^{\Delta\Delta LogR_{agonist}} \quad \textbf{(Equation 3.11)}$$

Statistical analysis was performed on ΔΔLogR values to test for significance of ligand bias relative to balanced agonist HU308. To this end, a one-way ANOVA with Dunnett's multiple comparisons test was performed. $p < 0.05$ was considered statistically significant.

3.5 Acknowledgements

We thank Christophe Stove (Ghent University) for sharing the cell line for NanoBiT assays, Isabelle Geron (Revvity) for the technical support on the Envision plate reader and Isabelle Kaufmann, Björn Wagner, Carina Cantrill, Janneke Keemink, Elisa Di Lenarda, Anne Christine Cascais and Marie-Elise Brun (all Roche) for their excellent support in sample handling and compound characterization.

References

1. Kolb, P. *et al.* Community guidelines for GPCR ligand bias: IUPHAR review 32. *Br J Pharmacol* **179**, 3651–3674 (2022).
2. Kenakin, T. & Christopoulos, A. Signalling bias in new drug discovery: detection, quantification and therapeutic impact. *Nat Rev Drug Discov* **12**, 205–216 (2012).
3. Kenakin, T. Biased Receptor Signaling in Drug Discovery. *Pharmacol Rev* **71**, 267–315 (2019).
4. Kenakin, T. P. Biased signalling and allosteric machines: new vistas and challenges for drug discovery. *Br J Pharmacol* **165**, 1669 (2012).
5. French, A. R., Meqbil, Y. J. & van Rijn, R. M. ClickArr: a novel, high-throughput assay for evaluating β-arrestin isoform recruitment. *Front Pharmacol* **14**, (2023).
6. Hauser, A. S. *et al.* Common coupling map advances GPCR-G protein selectivity. *Elife* **11**, (2022).
7. Caroli, J. *et al.* A community Biased Signaling Atlas. *Nat Chem Biol* **19**, 531–535 (2023).
8. Mullard, A. FDA approves first GPCR biased agonist. *Nat Rev Drug Discov* **19**, 659 (2020).
9. Stahl, E. L. & Bohn, L. M. Low Intrinsic Efficacy Alone Cannot Explain the Improved Side Effect Profiles of New Opioid Agonists. *Biochemistry* **61**, 1923–1935 (2022).
10. Nagi, K. How can we improve the measurement of receptor signaling bias? *Expert Opin Drug Discov* **18**, 575–578 (2023).
11. Kenakin, T. Bias translation: The final frontier? *Br J Pharmacol* 1–16 (2024).
12. Pineyro, G. & Nagi, K. Signaling diversity of mu- and delta- opioid receptor ligands: Re-evaluating the benefits of β-arrestin/G protein signaling bias. *Cell Signal* **80**, (2021).
13. Klein Herenbrink, C. *et al.* The role of kinetic context in apparent biased agonism at GPCRs. *Nat Commun* **7**, 10842 (2016).
14. Copeland, R. A., Pompliano, D. L. & Meek, T. D. Drug–target residence time and its implications for lead optimization. *Nat Rev Drug Discov* **5**, 730–739 (2006). Guo, D., Mulder-Krieger, T., IJzerman, A. P. & Heitman, L. H. Functional efficacy of adenosine A_{2A} receptor agonists is positively correlated to their receptor residence time. *Br J Pharmacol* **166**, 1846–1859 (2012).
15. Rosethorne, E. M. *et al.* Long receptor residence time of C26 contributes to super agonist activity at the human β2 adrenoceptor. *Mol Pharmacol* **89**, 467–475 (2016).
16. Olsen, R. H. J. *et al.* TRUPATH, an open-source biosensor platform for interrogating the GPCR transducerome. *Nat Chem Biol* **16**, 841–849 (2020).
17. Von Moo, E. *et al.* Ligand-directed bias of G protein signaling at the dopamine D2 receptor. *Cell Chem Biol* **29**, 226-238.e4 (2022).
18. Kise, R. & Inoue, A. GPCR signaling bias: an emerging framework for opioid drug development. *The Journal of Biochemistry* mvae013 (2024).
19. Hoare, S. R. J., Tewson, P. H., Quinn, A. M., Hughes, T. E. & Bridge, L. J. Analyzing kinetic signaling data for G-protein-coupled receptors. *Sci Rep* **10**, 12263 (2020).
20. Maccarrone, M. *et al.* Goods and Bads of the Endocannabinoid System as a Therapeutic Target: Lessons Learned after 30 Years. *Pharmacol Rev* **75**, 885–958 (2023).
21. Howlett, A. C. *et al.* International Union of Pharmacology. XXVII. Classification of cannabinoid receptors. *Pharmacol Rev* **54**, 161–202 (2002).
22. Pertwee, R. G. *et al.* International Union of Basic and Clinical Pharmacology. LXXIX. Cannabinoid Receptors and Their Ligands: Beyond CB_1 and CB_2. *Pharmacol Rev* **62**, 588–631 (2010).
23. Simard, M., Rakotoarivelo, V., Di Marzo, V. & Flamand, N. Expression and Functions of the CB_2 Receptor in Human Leukocytes. *Front Pharmacol* **13**, (2022).
24. Brennecke, B. *et al.* Cannabinoid receptor type 2 ligands: An analysis of granted patents since 2010. *Pharm Pat Anal* **10**, 111–163 (2021).
25. Whiting, Z. M., Yin, J., de la Harpe, S. M., Vernall, A. J. & Grimsey, N. L. Developing the Cannabinoid Receptor 2 (CB2) pharmacopoeia: past, present, and future. *Trends Pharmacol Sci* **43**, 754–771 (2022).
26. Jones, É. & Vlachou, S. A Critical Review of the Role of the Cannabinoid Compounds Δ^9-Tetrahydrocannabinol (Δ^9-THC) and Cannabidiol (CBD) and their Combination in Multiple Sclerosis Treatment. *Molecules* **25**, 4930 (2020).

27. Bouma, J. *et al.* Dual allosteric and orthosteric pharmacology of synthetic analog cannabidiol-dimethylheptyl, but not cannabidiol, on the cannabinoid CB_2 receptor. *Biochem Pharmacol* **218**, 115924 (2023). **(Chapter 5)**
28. Castillo-Arellano, J., Canseco-Alba, A., Cutler, S. J. & León, F. The Polypharmacological Effects of Cannabidiol. *Molecules* **28**, (2023).
29. Carruthers, E. R. & Grimsey, N. L. Cannabinoid CB_2 receptor orthologues; in vitro function and perspectives for preclinical to clinical translation. *Br J Pharmacol* (2023).
30. Dhopeshwarkar, A. & Mackie, K. Functional selectivity of CB_2 cannabinoid receptor ligands at a canonical and noncanonical pathways. *Journal of Pharmacology and Experimental Therapeutics* **358**, 342–351 (2016).
31. Ibsen, M. S., Connor, M. & Glass, M. Cannabinoid CB_1 and CB_2 Receptor Signaling and Bias. *Cannabis Cannabinoid Res* **2**, 48–60 (2017).
32. Zagzoog, A. *et al.* Assessment of select synthetic cannabinoid receptor agonist bias and selectivity between the type 1 and type 2 cannabinoid receptor. *Sci Rep* **11**, 10611 (2021).
33. Oyagawa, C. R. M. *et al.* Cannabinoid Receptor 2 Signalling Bias Elicited by 2,4,6-Trisubstituted 1,3,5-Triazines. *Front Pharmacol* **9**, 1202 (2018).
34. Soethoudt, M. *et al.* Cannabinoid CB_2 receptor ligand profiling reveals biased signalling and off-target activity. *Nat Commun* **8**, 1–14 (2017).
35. Atwood, B. K., Wager-Miller, J., Haskins, C., Straiker, A. & Mackie, K. Functional Selectivity in CB_2 Cannabinoid Receptor Signaling and Regulation: Implications for the Therapeutic Potential of CB_2 Ligands. *Mol Pharmacol* **81**, 250–263 (2012).
36. Sharma, R. *et al.* Novel Cannabinoid Receptor 2 (CB2) Low Lipophilicity Agonists Produce Distinct cAMP and Arrestin Signalling Kinetics without Bias. *Int J Mol Sci* **24**, 6406 (2023).
37. Patel, M., Grimsey, N. L., Banister, S. D., Finlay, D. B. & Glass, M. Evaluating signaling bias for synthetic cannabinoid receptor agonists at the cannabinoid CB_2 receptor. *Pharmacol Res Perspect* **11**, (2023).
38. Graham, H., Chandler, D. J. & Dunbar, S. A. The genesis and evolution of bead-based multiplexing. *Methods* **158**, 2–11 (2019).
39. Sarrion-Perdigones, A. *et al.* Examining multiple cellular pathways at once using multiplex hextuple luciferase assaying. *Nat Commun* **10**, 1–16 (2019).
40. Thorne, N., Inglese, J. & Auld, D. S. Illuminating Insights into Firefly Luciferase and Other Bioluminescent Reporters Used in Chemical Biology. *Chem Biol* **17**, 646–657 (2010).
41. Felder, C. C. *et al.* Comparison of the Pharmacology and Signal Transduction of the Human Cannabinoid CB_1 and CB_2 Receptors. *Mol Pharmacol* **48**, 443–450 (1995).
42. Hoare, S. R. J. *et al.* Quantifying the Kinetics of Signaling and Arrestin Recruitment by Nervous System G-Protein Coupled Receptors. *Front Cell Neurosci* **15**, 84457 (2022).
43. Cullum, S. A., Veprintsev, D. B. & Hill, S. J. Kinetic analysis of endogenous β_2-adrenoceptor-mediated cAMP GloSensor™ responses in HEK293 cells. *Br J Pharmacol* **180**, 1304–1315 (2022).
44. Manning, J. J., Rawcliffe, G., Finlay, D. B. & Glass, M. Cannabinoid 1 (CB_1) receptor arrestin subtype-selectivity and phosphorylation dependence. *Br J Pharmacol* **180**, 369–382 (2023).
45. Saecker, L., Häberlein, H. & Franken, S. Investigation of adenosine A1 receptor-mediated β-arrestin 2 recruitment using a split-luciferase assay. *Front Pharmacol* **14**, (2023).
46. Grätz, L. *et al.* NanoBiT- and NanoBiT/BRET-based assays allow the analysis of binding kinetics of Wnt-3a to endogenous Frizzled 7 in a colorectal cancer model. *Br J Pharmacol* (2023).
47. Bouma, J. *et al.* Cellular Assay to Study β-Arrestin Recruitment by the Cannabinoid Receptors 1 and 2. in *Endocannabinoid Signaling. Methods in Molecular Biology* (ed. Maccarrone, M.) vol. 2576 189–199 (Humana, New York, NY, 2022). **(Chapter 2)**
48. Han, S. *et al.* Discovery of APD371: Identification of a Highly Potent and Selective CB_2 Agonist for the Treatment of Chronic Pain. *ACS Med Chem Lett* **8**, 1309–1313 (2017).
49. Lin, X., Dhopeshwarkar, A. S., Huibregtse, M., MacKie, K. & Hohmann, A. G. Slowly signaling G protein-biased CB_2 cannabinoid receptor agonist LY2828360 suppresses neuropathic pain with sustained efficacy and attenuates morphine tolerance and dependence. *Mol Pharmacol* **93**, 49–62 (2018).
50. IJzerman, A. P. & Guo, D. Drug–Target Association Kinetics in Drug Discovery. *Trends Biochem Sci* **44**, 861–871 (2019).

51. Chen, X. *et al.* Involvement of ß-arrestin-2 and Clathrin in Agonist-Mediated Internalization of the Human Cannabinoid CB2 Receptor. *Curr Mol Pharmacol* **7**, 67–80 (2014).

52. Derocq, J. M. *et al.* Genomic and functional changes induced by the activation of the peripheral cannabinoid receptor CB2 in the promyelocytic cells HL-60. Possible involvement of the CB2 receptor in cell differentiation. *Journal of Biological Chemistry* **275**, 15621–15628 (2000).

53. Grimsey, N. L., Goodfellow, C. E., Dragunow, M. & Glass, M. Cannabinoid receptor 2 undergoes Rab5-mediated internalization and recycles via a Rab11-dependent pathway. *Biochim Biophys Acta* **1813**, 1554–1560 (2011).

54. Carrier, E. J. *et al.* Cultured Rat Microglial Cells Synthesize the Endocannabinoid 2-Arachidonylglycerol, Which Increases Proliferation via a CB_2 Receptor-Dependent Mechanism. *Mol Pharmacol* **65**, 999–1007 (2004).

55. Bouaboula, M., Dussossoy, D. & Casellas, P. Regulation of peripheral cannabinoid receptor CB_2 phosphorylation by the inverse agonist SR 144528. Implications for receptor biological responses. *Journal of Biological Chemistry* **274**, 20397–20405 (1999).

56. Patel, M. *et al.* Delineating the interactions between the cannabinoid CB_2 receptor and its regulatory effectors; β-arrestins and GPCR kinases. *Br J Pharmacol* **179**, 2223–2239 (2022).

57. Ibsen, M. S. *et al.* Cannabinoid CB1 and CB2 Receptor-Mediated Arrestin Translocation: Species, Subtype, and Agonist-Dependence. *Front Pharmacol* **10**, (2019).

58. Moo, E. Von, van Senten, J. R., Bräuner-Osborne, H. & Møller, T. C. Arrestin-dependent and -independent internalization of G protein–coupled receptors: Methods, mechanisms, and implications on cell signaling. *Mol Pharmacol* **99**, 242–255 (2021).

59. Nobles, K. N. *et al.* Distinct Phosphorylation Sites on the $ß_2$-Adrenergic Receptor Establish a Barcode That Encodes Differential Functions of ß-Arrestin. *Sci Signal* **185**, ra51 (2011).

60. van der Westhuizen, E. T., Breton, B., Christopoulos, A. & Bouvier, M. Quantification of ligand bias for clinically relevant b2-adrenergic receptor ligands: Implications for drug taxonomy s. *Mol Pharmacol* **85**, 492–509 (2014).

61. Kenakin, T., Watson, C., Muniz-Medina, V., Christopoulos, A. & Novick, S. A simple method for quantifying functional selectivity and agonist bias. *ACS Chem Neurosci* **3**, 193–203 (2012).

62. DeWire, S. M. *et al.* A G protein-biased ligand at the μ-opioid receptor is potently analgesic with reduced gastrointestinal and respiratory dysfunction compared with morphines. *Journal of Pharmacology and Experimental Therapeutics* **344**, 708–717 (2013).

63. Schmid, C. L. *et al.* Bias Factor and Therapeutic Window Correlate to Predict Safer Opioid Analgesics. *Cell* **171**, 1165–1175 (2017).

64. Kelly, E., Conibear, A. & Henderson, G. Biased Agonism: Lessons from Studies of Opioid Receptor Agonists. *Annu. Rev. Pharmacol. Toxicol.* **63**, 491–515 (2023).

65. Martella, A. *et al.* A Novel Selective Inverse Agonist of the CB_2 Receptor as a Radiolabeled Tool Compound for Kinetic Binding Studies. *Mol Pharmacol* **92**, 389–400 (2017).

66. Wagner, B., Fischer, H., Kansy, M., Seelig, A. & Assmus, F. Carrier Mediated Distribution System (CAMDIS): A new approach for the measurement of octanol/water distribution coefficients. *European Journal of Pharmaceutical Sciences* **68**, 68–77 (2015).

67. He, Y. *et al.* Discovery, synthesis and evaluation of novel reversible monoacylglycerol lipase radioligands bearing a morpholine-3-one scaffold. *Nucl Med Biol* **108–109**, 24–32 (2022).

68. Banker, M. J., Clark, T. H. & Williams, J. A. Development and Validation of a 96-Well Equilibrium Dialysis Apparatus for Measuring Plasma Protein Binding. *J Pharm Sci* **92**, 967–974 (2003).

69. Zamek-Gliszczynski, M. J. *et al.* Validation of 96-well equilibrium dialysis with non-radiolabeled drug for definitive measurement of protein binding and application to clinical development of highly-bound drugs. *J Pharm Sci* **100**, 2498–2507 (2011).

70. Cannaert, A., Franz, F., Auwärter, V. & Stove, C. P. Activity-Based Detection of Consumption of Synthetic Cannabinoids in Authentic Urine Samples Using a Stable Cannabinoid Reporter System. *Anal Chem* **89**, 9527–9536 (2017).

71. Smith, P. K. *et al.* Measurement of protein using bicinchoninic acid. *Anal Biochem* **150**, 76–85 (1985).

72. Jacobsen, L. B., Calvin, S. A., Colvin, K. E. & Wright, M. J. FuGENE 6 Transfection Reagent: The gentle power. *Methods* **33**, 104–112 (2004).

73. Cheng, Y.-C. & Prusoff, W. H. Relationship between the inhibition constant (K1) and the concentration of inhibitor which causes 50 per cent inhibition (I50) of an enzymatic reaction. *Biochem Pharmacol* **22**, 3099–3108 (1973).

74. Motulsky, H. J. & Mahan, L. C. The kinetics of competitive radioligand binding predicted by the law of mass action. *Mol Pharmacol* **25**, 1–9 (1984).

75. Li, X. *et al.* Structural basis of selective cannabinoid CB_2 receptor activation. *Nat Commun* **14**, 1447 (2023). **(Chapter 4)**

76. Hoare, S. R. J. Pharmechanics time course equations in GraphPad Prism. https://www.pharmechanics.com/time-course-tool-pack (2023).

77. Black, J. W. & Leff, P. Operational models of pharmacological agonism. *Proc. R. Soc. Lond. B* **220**, 141–162 (1983).

3.S1 Supplementary methods

3.S1.1 [^{35}S]GTPγS assays

G protein activation of CB_2R was measured by binding of [^{35}S]GTPγS as previously described[39]. In short, HEK293T CB_2R-SmBiT LgBiT-ß-arrestin-2 membrane homogenates (5 µg) were diluted in assay buffer (50 mM Tris-HCl, 5 mM $MgCl_2$, 150 mM NaCl, 1 mM EDTA, 0.05% BSA (w/v) and 1 mM DTT, freshly prepared each day) and supplemented with 5 µg saponin and 1 µM GDP to a total volume of 100 µL. For endocannabinoid and CMX-020 samples, the membranes were additionally preincubated for 30 min with 50 µM PMSF. To determine pEC_{50} and E_{max} values, increasing concentrations of compound of interest (ranging from 0.01 nM to 10 µM) were incubated with [^{35}S]GTPγS (0.3 nM) for 90 minutes at 25 °C while shaking at 400 rpm. The basal activity was measured in the presence of vehicle and the maximal response was determined by 10 µM CP55,940. Vehicle (i.e., acetonitrile for endocannabinoids and CMX-020, and DMSO for all other compounds) concentrations were constant and kept < 1% in all samples. Incubations were terminated by rapid vacuum filtration with ice-cold 50 mM Tris-HCl (pH 7.4) and 5 mM $MgCl_2$ buffer through Whatman GF/C filters using a Filtermate 96-well harvester (PerkinElmer). Filters were dried for at least 30 min at 55 °C and subsequently 25 µL MicroScint scintillation cocktail was added per well. Filter-bound radioactivity was measured by scintillation spectrometry using a Microbeta^2 2450 counter (Revvity, Waltham, MA, USA).

3.S1.2 Data analysis

3.S1.2.1 Inhibition of forskolin-induced cAMP production (step-by-step)

The inhibition of cAMP production can be kinetically analyzed for each agonist concentration by applying time course equations according to Hoare *et al.*[20]. The equations can be downloaded from https://www.pharmechanics.com/time-course-tool-pack. The following directions are for GraphPad Prism v9.0, which requires some manual calculations. In newer versions more parameters are already calculated by the software.

1. Insert all time trace data per concentration in Prism and add vehicle in column A.
   i. The model requires X values to be greater than 0. Enter the time values as they are in reality, with baseline starting at 0 min. This allows X_0, the signal rise start time, to be a fitted parameter in the analysis resulting in better fits.
   ii. Insert average of the five baseline measurements in the top row for ease of correction, without an X value.
   iii. For the same reason, add the average of the final five FSK measurements in the bottom row, without an X value.
2. Correct for well-to-well variation by first subtracting the average of the baseline measurement and subsequently average of the FSK measurement.
   i. Select 'Repeated measures' in the baseline correction in GraphPad Prism, which will use the values from the specific well when you have duplicates.

3. Correct for vehicle and invert the data by transforming the Y values using Y= 0 -Y.
4. Allow Prism to compare between two non-linear fits based on the time trace using the F-test:
   i. Use simplest model first 'Baseline then rise to steady state' and compare to the more complex model 'Baseline then rise-and-fall to baseline'.
   ii. Constrain the following parameters for better fitting results:
      a. Baseline then rise to steady state:
         1. X_0 must be greater than 0
         2. Baseline no constraint
         3. SteadyState must be greater than 0
         4. k must be greater than 0
      b. Baseline then rise-and-fall to baseline
         1. X_0 must be greater than 0
         2. Baseline no constraint
         3. Initial Rate must be greater than 0
         4. k_1 no constraint
         5. k_2 must be greater than 0
         6. k_1 must be greater than 1 times k_2
      c. Don't constrain X_0 to the time of agonist addition as there might be a delay in the response, which will now be captured by the model.
      d. Don't constrain Baseline to allow some more flexibility of the model.
   iii. For all curves manually change the Initial Value (in the corresponding tab) for X_0 to the time of agonist addition or slightly before.
      a. This helps the model to better guess when your baseline run-in period turns into a response.
   iv. Only analyze the data from the final five FSK measurements (baseline) to the end of the assay.
   v. In the 'Confidence' tab change the Confidence Intervals (CI) of the parameters to the 'Symmetrical (asymptotic) approximate CI' if you do not need the CI.
      a. This mainly allows for a quicker fitting of the curves and does not influence the calculation of the fitted parameter but will only not report the CI.
   vi. From these analyses, the Initial Rate, Peak Response (given as SteadyState), and k_1 and k_2 values are determined.
5. The inactive concentrations, i.e., concentrations at which no inhibition of cAMP production is detected anymore, can also be analyzed to determine the slope. This will be (close to) 0.
   i. Use the 'Straight line time course' equation as described by Hoare *et al.*[20] with default parameters. The reported slope is the same as initial rate.

3.S1.2.2 ß-arrestin-2 recruitment (step-by-step)

The ß-arrestin-2 recruitment data can be kinetically analyzed for each agonist concentration by applying time course equations according to Hoare *et al.*[20]. The equations can be downloaded from https://www.pharmechanics.com/time-course-tool-pack. The following directions are for GraphPad Prism v9.0, which requires some manual calculations. In newer versions more parameters are already calculated by the software.

1. Insert all time trace data per concentration in Prism and add vehicle in column A.
   i. The model requires X values to be greater than 0. Enter the time values as they are in reality, with baseline starting at 0 min. This allows X_0, the signal rise start, to be a fitted parameter in the analysis resulting in better fits.
   ii. Insert the average of the final five FSK measurements (to represent baseline) in the bottom row for ease of correction, without an X value.
2. Correct for well-to-well variation by subtracting the FSK measurement.
   i. Select 'Repeated measures' in the baseline correction in GraphPad Prism, which will use the values from the specific well when you have duplicates.
3. Correct for vehicle.
4. Allow Prism to compare between two non-linear fits based on the time trace using the F-test:
   i. Use simplest model first 'Baseline then rise to steady state' and compare to the more complex model 'Baseline then rise-and-fall to steady state'.
   ii. Constrain the following parameters for better fitting results:
      a. Baseline then rise to steady state:
         1. X_0 must be greater than 0
         2. Baseline no constraint
         3. SteadyState must be greater than 0
         4. k must be greater than 0
      b. Baseline then rise-and-fall to baseline
         1. X_0 must be greater than 0
         2. Baseline no constraint
         3. SteadyState must be greater than 0
         4. D must be greater than 0
         5. k_1 no constraint
         6. k_2 must be greater than 0
         7. k_1 must be greater than 1 times k_2
      c. Don't constrain X_0 to the time of agonist addition as there might be a delay in the response, which will now be captured by the model.
      d. Don't constrain Baseline to allow some more flexibility of the model.
   iii. For all curves manually change the Initial Value (in the corresponding tab) for X_0

to the time of agonist addition or slightly before.

a. This helps the model to better guess when your baseline run-in period turns into a response.

iv. Only analyze the data from the final five FSK measurements (baseline) to the end of the assay.

v. In the 'Confidence' tab change the Confidence Intervals (CI) of the parameters to the 'Symmetrical (asymptotic) approximate CI' if you do not need the CI.

a. This mainly allows for a quicker fitting of the curves and does not influence the calculation of the fitted parameter but will only not report the CI.

vi. From these analyses, the k_1 and k_2 values are determined, but Initial Rate and Peak Response need to be calculated[77]:

$$IR=SSR(D \cdot k_1-(D-1)k_2)$$

$$\text{Peak time}=\frac{1}{k_2-k_1}\ln\left(\frac{(D-1)k_2}{Dk_1}\right)$$

$$\text{Peak response}=SSR(1-De^{-k_1 \cdot \text{Peak time}}+(D-1)e^{-k_2 \cdot \text{Peak time}}$$

5. The inactive concentrations, i.e., concentrations at which no inhibition of ß-arrestin-2 recruitment is detected anymore, can also be analyzed to determine the slope. This will be (close to) 0.

i. Use the 'Straight line time course' equation as described by Hoare *et al.*[20] with default parameters. The reported slope is the same as initial rate.

3.S1.2.3 [^{35}S]GTPγS assays

Functional agonist responses from the [^{35}S]GTPγS binding assays were baseline-corrected with the basal activity and normalized to 10 μM of CP55,940. pEC_{50} and E_{max} values were determined using non-linear regression curve fitting 'log(agonist) vs. response' (three parameters).

3.S2 Supplementary figures

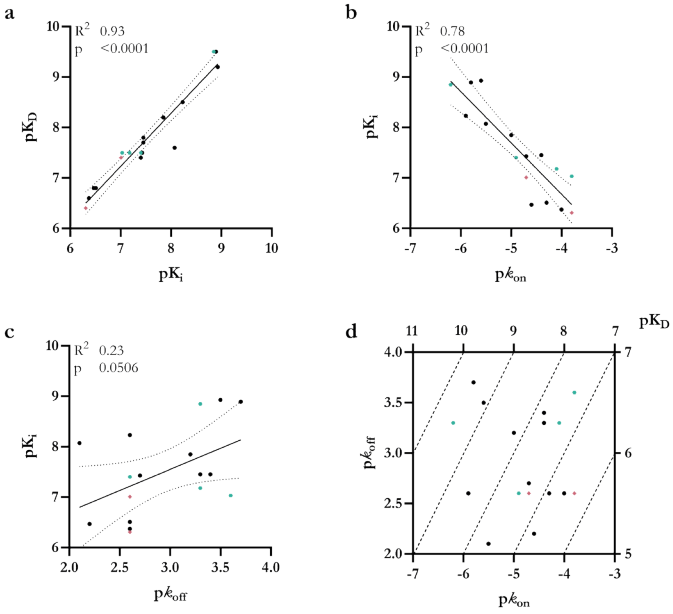

Figure 3.S1 Correlation plots between affinity and binding kinetic parameters of benchmark agonists, endocannabinoids and clinical agonists from [^{3}H]RO6957022 binding assays on CB_2R.
Correlation plots with parameters from [^{3}H]RO6957022 binding assays on CB_2R comparing (a) equilibrium affinity pK_i and kinetic affinity pK_D, (b) pk_{on} and pK_i, and (c) pk_{off} and pK_i. (d) Kinetic map representing the relationship between pk_{on}, pk_{off} and pK_D. Benchmark agonists are turquoise hexagons (⬢), endocannabinoids coral diamonds (◆) and clinical agonists black circles (●). Data are mean from at least three independent experiments performed in duplicate. The solid line represents a linear correlation between the parameters and the dotted lines indicate the 95% confidence interval. R^2 values represent a measure of goodness-of-fit of the simple linear regression and $p < 0.05$ indicate a slope statistically significant different from 0.

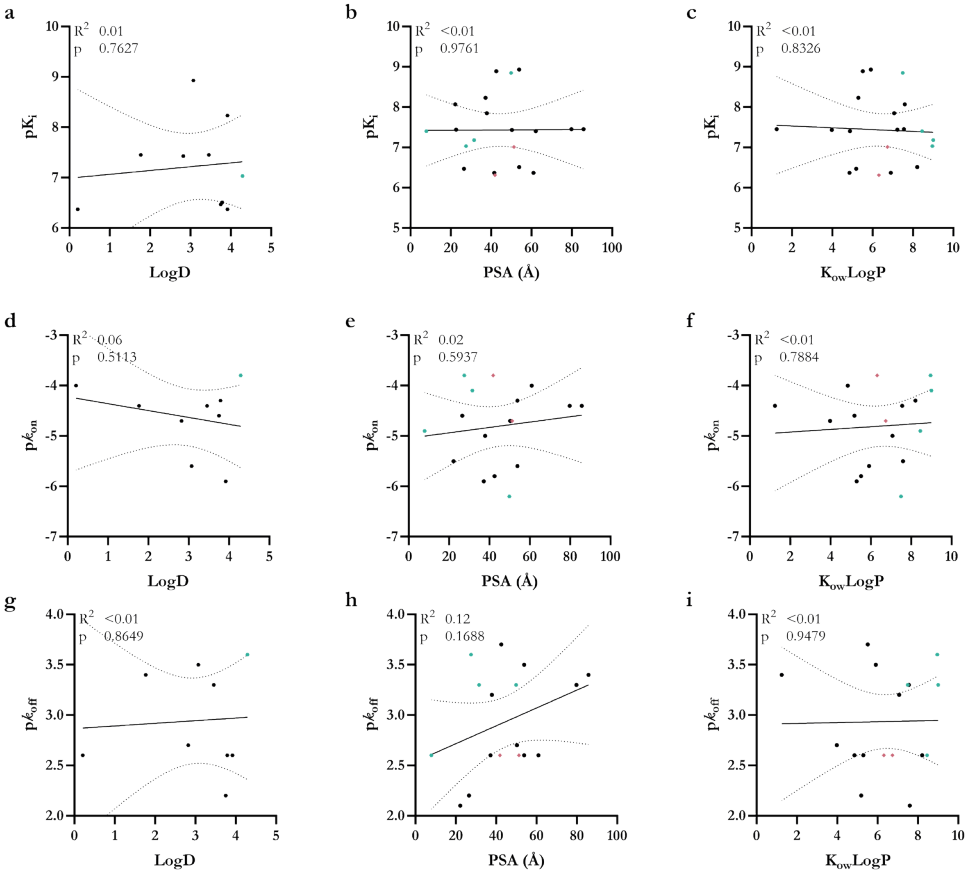

Figure 3.S2 Correlation plots between physicochemical parameters and binding affinity and binding kinetic parameters for benchmark agonists, endocannabinoids and clinical agonists on CB_2R.
Correlation plots comparing (a) distribution coefficient LogD, (b) polar surface area PSA and (c) calculated partition coefficient K_{ow}LogP with equilibrium affinity pK_i. Correlation plots comparing (d) LogD, (e) PSA and (f) K_{ow}LogP with association rate constant pk_{on}. Correlation plots comparing (g) LogD, (h) PSA and (i) K_{ow}LogP with dissociation rate constant pk_{off}. Benchmark agonists are turquoise hexagons (⬢), endocannabinoids coral diamonds (◆) and clinical agonists black circles (●). Data are mean from at least three independent experiments performed in duplicate. The solid line represents a linear correlation between the parameters and the dotted lines indicate the 95% confidence interval. R^2 values represent a measure of goodness-of-fit of the simple linear regression and $p < 0.05$ indicate a slope statistically significant different from 0.

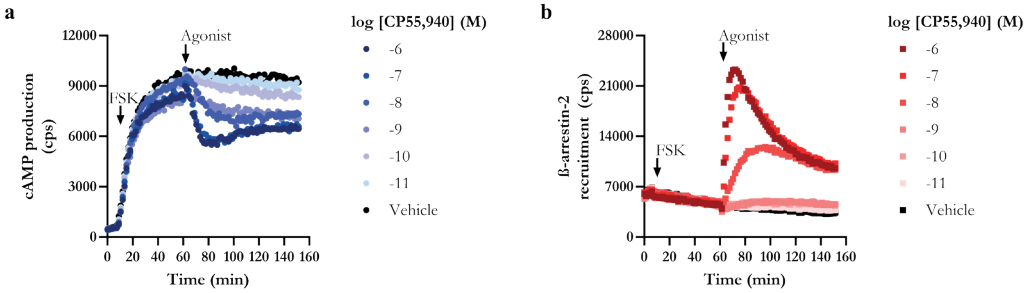

Figure 3.S3 Raw time traces from the multiplexed cAMP production and ß-arrestin-2 recruitment assay on HEK293T CB_2R-SmBiT LgBiT-ß-arrestin-2 cells with full agonist CP55,940.

Representative luminescent time traces indicative of (a) cAMP production and (b) ß-arrestin-2 recruitment simultaneously recorded in the multiplex assay on HEK293T CB_2R-SmBiT LgBiT-ß-arrestin-2 cells. Baseline luminesce was measured for 7.5 min prior to forskolin (FSK) addition to induce cAMP production. After 1 h, cells were stimulated with increasing concentrations of agonist CP55,940 and luminescence was recorded for 90 min. Data are shown as mean from a representative experiment performed in duplicate.

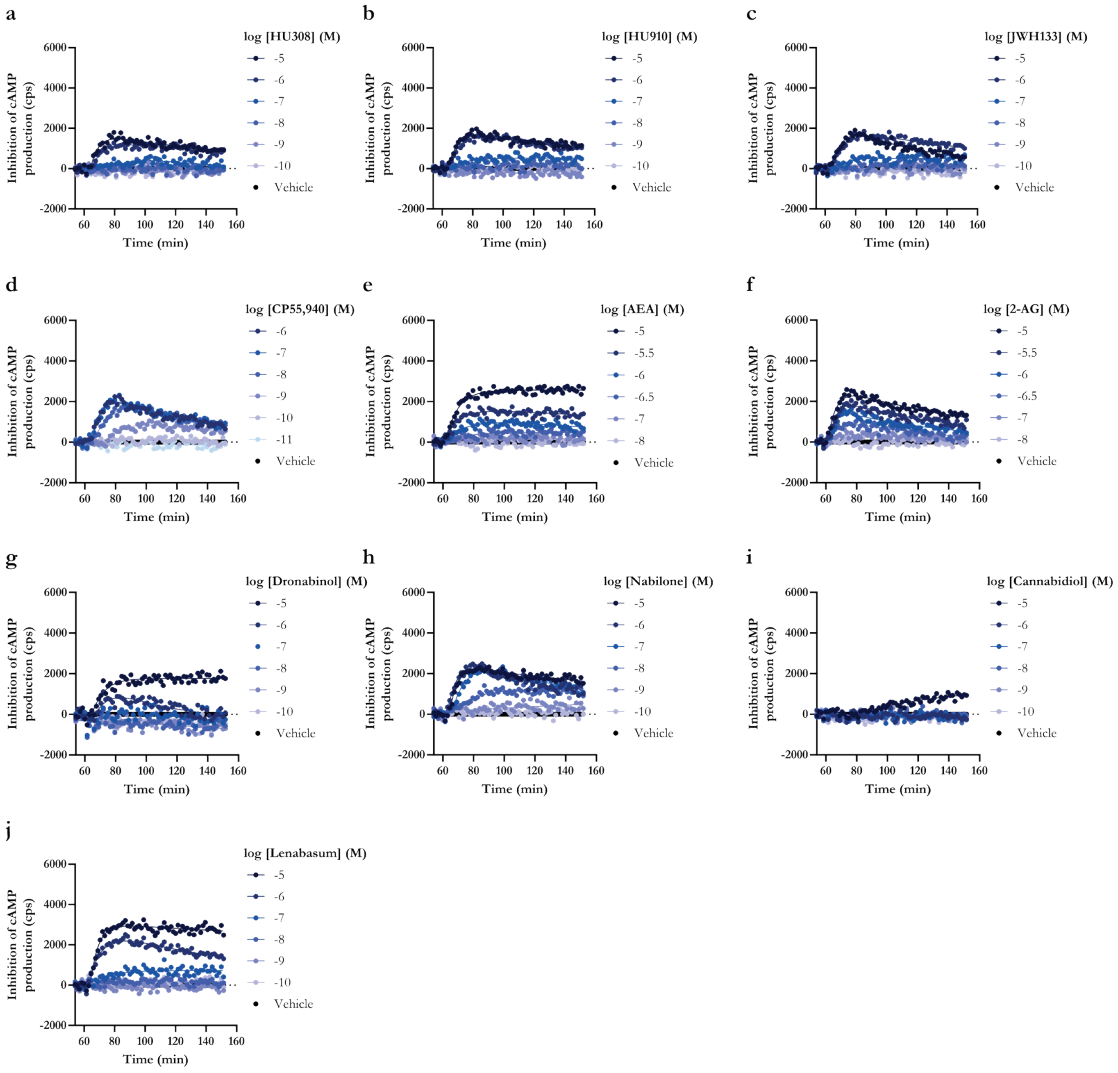

Figure 3.S4 Time traces of inhibition of cAMP production by benchmark agonists, endocannabinoids, launched and clinical agonists from the multiplex assay on HEK293T CB_2R-SmBiT LgBiT-ß-arrestin-2 cells. Representative forskolin- and vehicle-corrected time traces for inhibition of cAMP production by increasing concentrations of (a-d) benchmark agonists, (e, f) endocannabinoids, clinical agonists that (g-i) are on the market or (j) reached phase 3. Data are shown as mean from a representative experiment performed in duplicate.

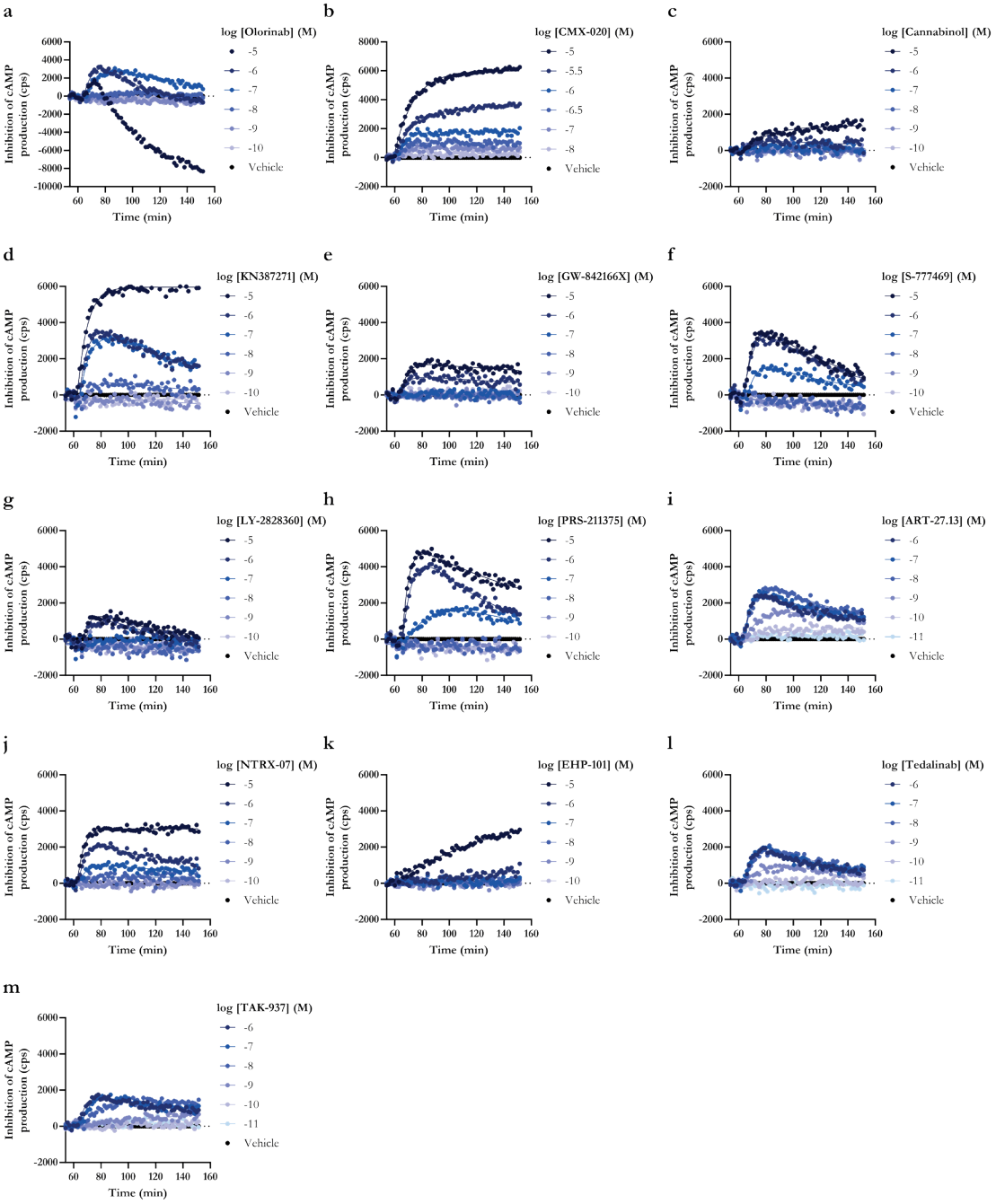

Figure 3.S5 Time traces of inhibition of cAMP production by benchmark agonists, endocannabinoids, launched and clinical agonists from the multiplex assay on HEK293T CB_2R-SmBiT LgBiT-ß-arrestin-2 cells. Representative forskolin- and vehicle-corrected time traces for inhibition of cAMP production by increasing concentrations of clinical agonists that (a-h) reached phase 2 or (i-m) phase 1. Data are shown as mean from a representative experiment performed in duplicate.

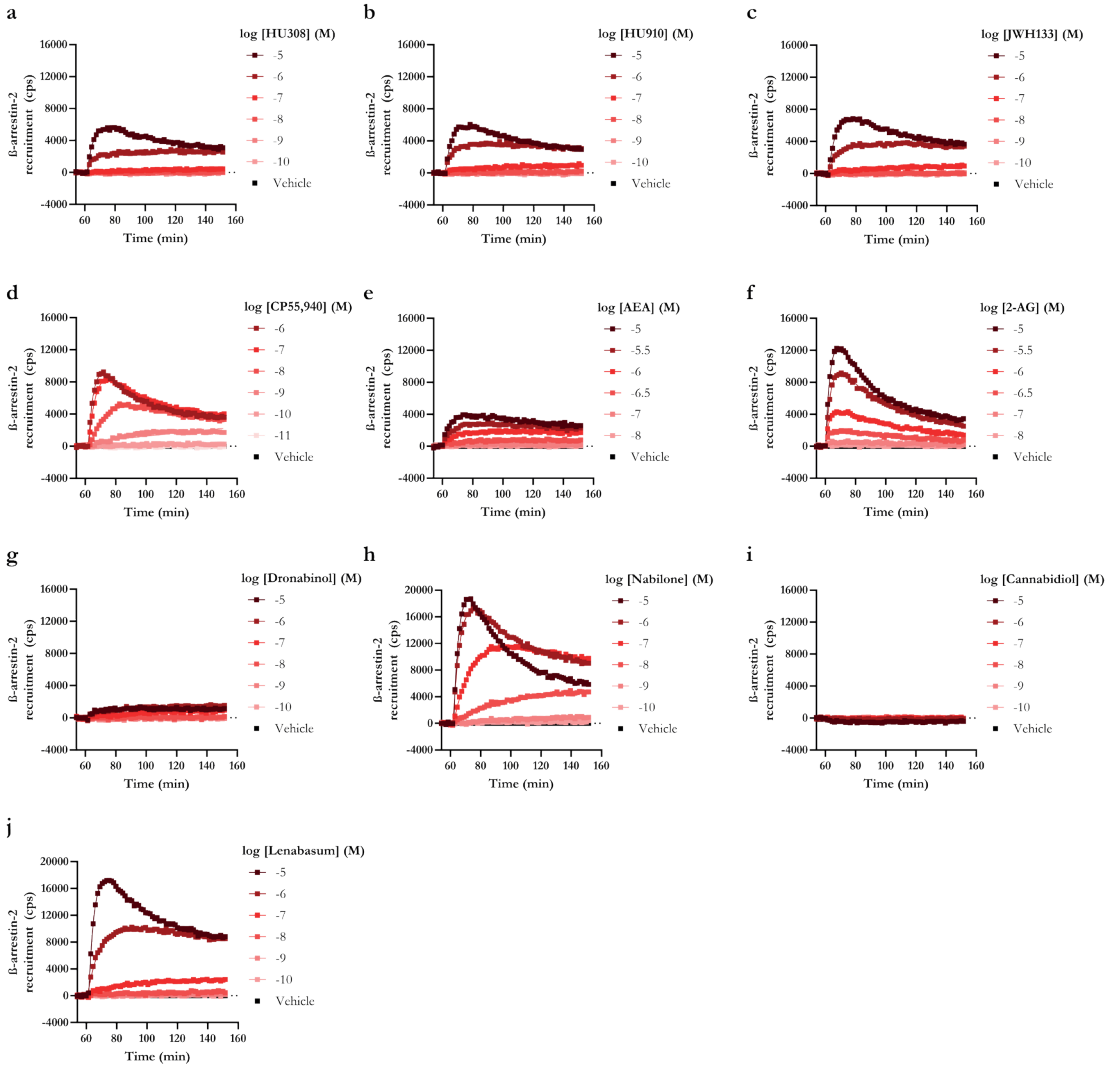

Figure 3.S6 Time traces of ß-arrestin-2 recruitment by benchmark agonists, endocannabinoids, launched and clinical agonists from the multiplex assay on HEK293T CB_2R-SmBiT LgBiT-ß-arrestin-2 cells. Representative vehicle-corrected time traces for ß-arrestin-2 recruitment to CB_2R by increasing concentrations of (a-d) benchmark agonists, (e, f) endocannabinoids, clinical agonists that (g-i) are on the market or (j) reached phase 3. Data are shown as mean from a representative experiment performed in duplicate.

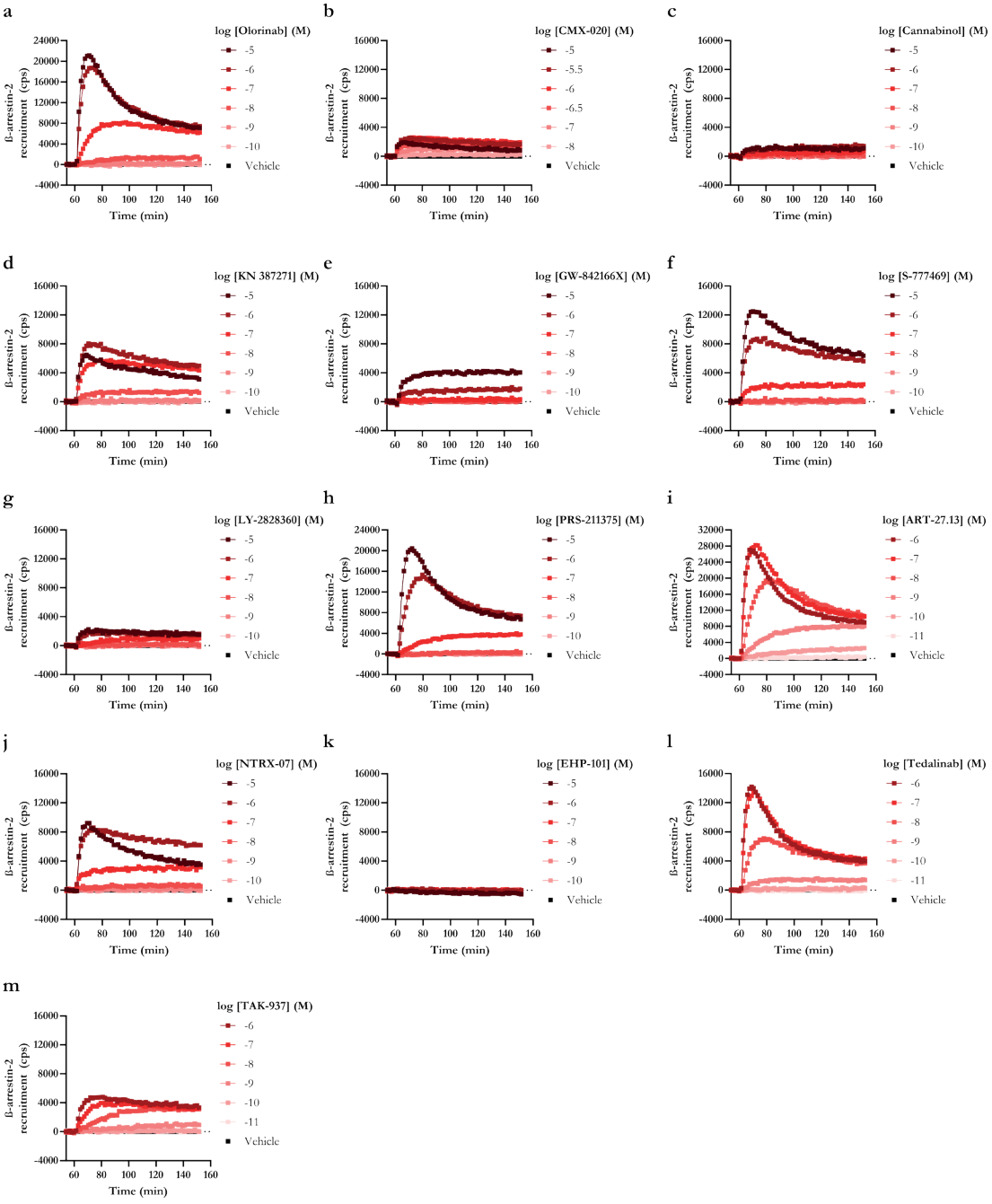

Figure 3.S7 Time traces of ß-arrestin-2 recruitment by clinical agonists from the multiplex assay on HEK293T CB_2R-SmBiT LgBiT-ß-arrestin-2 cells.

Representative vehicle-corrected time traces for ß-arrestin-2 recruitment to CB_2R by increasing concentrations of clinical agonists that (a-h) reached phase 2 or (i-m) phase 1. Data are shown as mean from a representative experiment performed in duplicate.

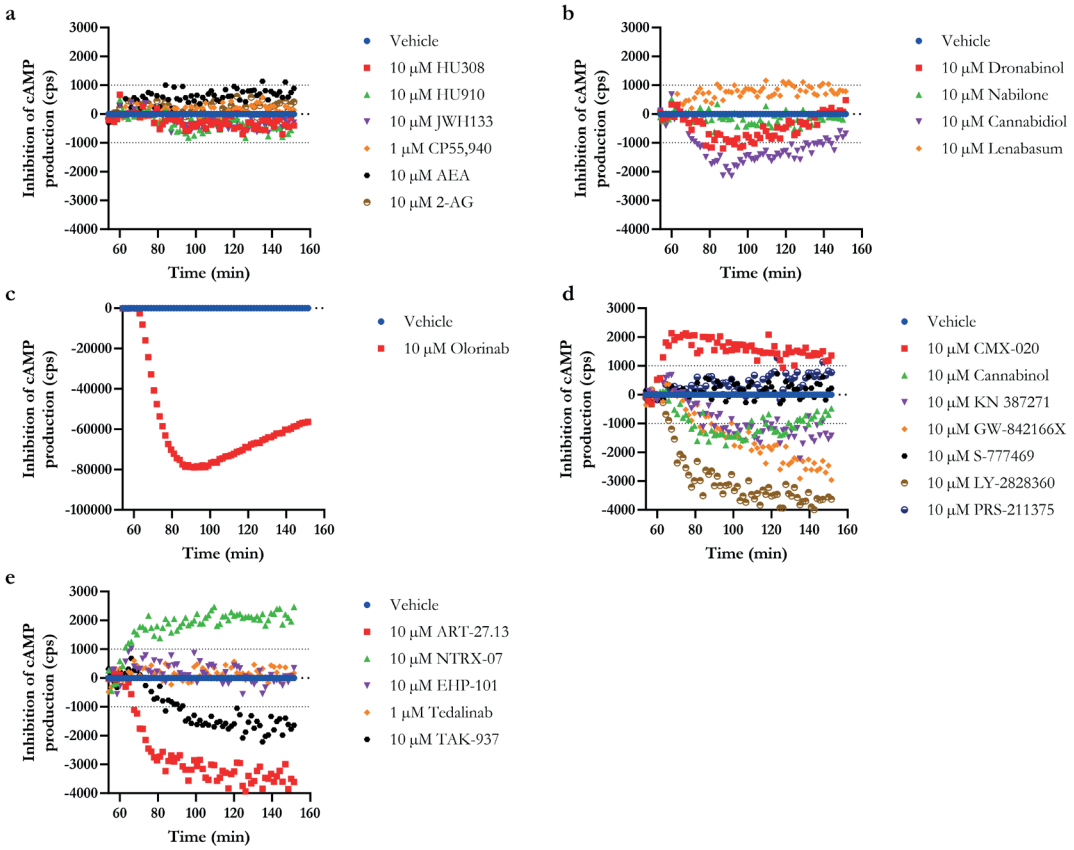

Figure 3.S8 CB_2R-independent modulation of cAMP production by benchmark agonists, endocannabinoids and clinical agonists in a forskolin-induced cAMP assay on HEK293T cells.
Representative time traces of 10 or 1 µM (a) benchmark agonists and endocannabinoids, agonists that are (b) launched or clinically investigated in phase 3, (c, d) phase 2, (e) phase 1. Data are shown as mean from a representative experiment performed in duplicate.

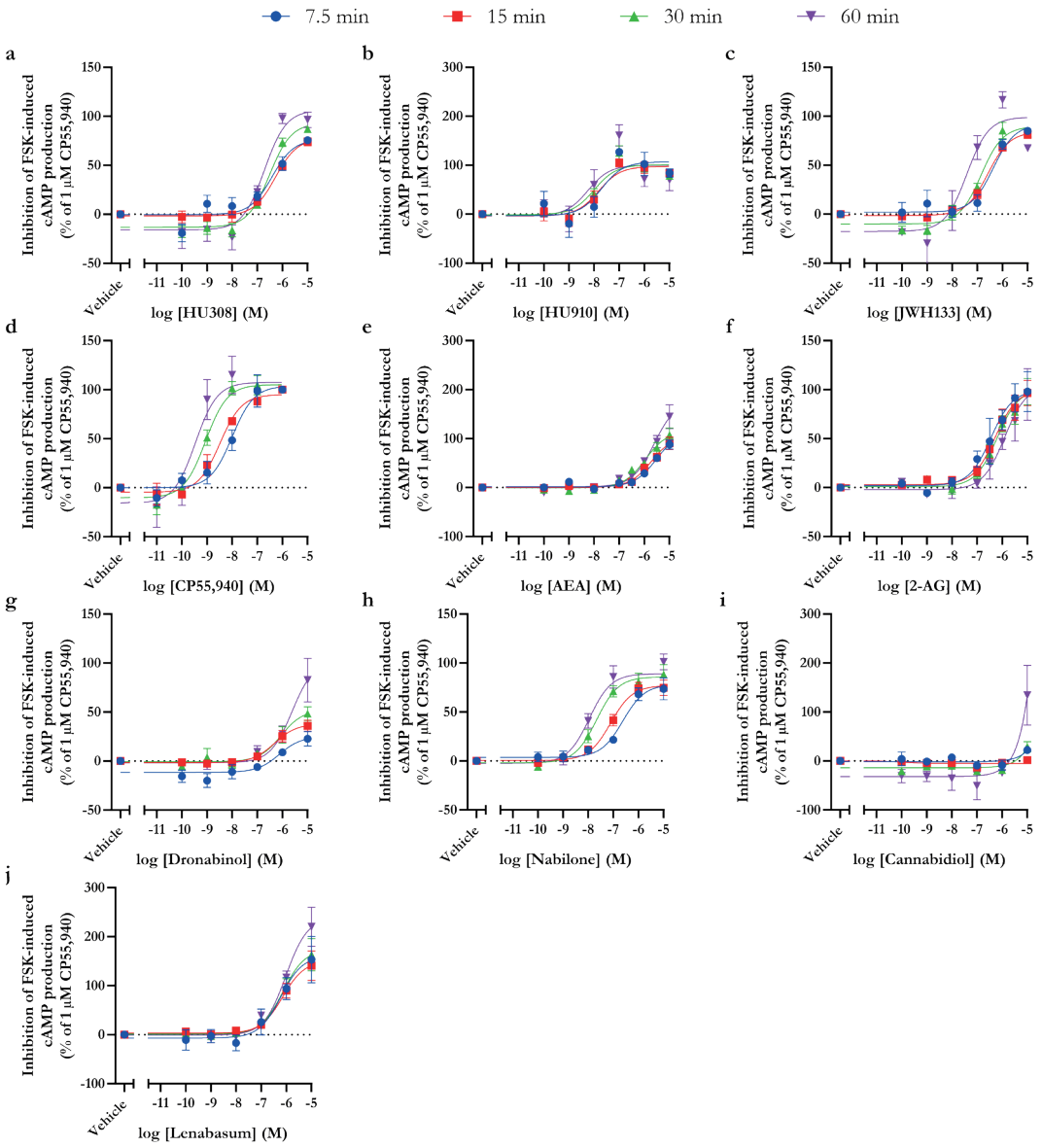

Figure 3.S9 Time-dependent inhibition of cAMP production by benchmark agonists, endocannabinoids, launched and clinical agonists from the multiplex assay on HEK293T CB_2R-SmBiT LgBiT-ß-arrestin-2 cells.

Inhibition of cAMP production at 7.5, 15, 30 or 60 min after addition of increasing concentrations of (a-d) benchmark agonists, (e, f) endocannabinoids, clinical agonists that (g-i) are on the market or (j) reached phase 3. Efficacy was calculated as percentage of the maximum effect induced by 1 µM CP55,940 at the specific time point. Data are shown as mean ± SEM from at least three independent experiments performed in duplicate.

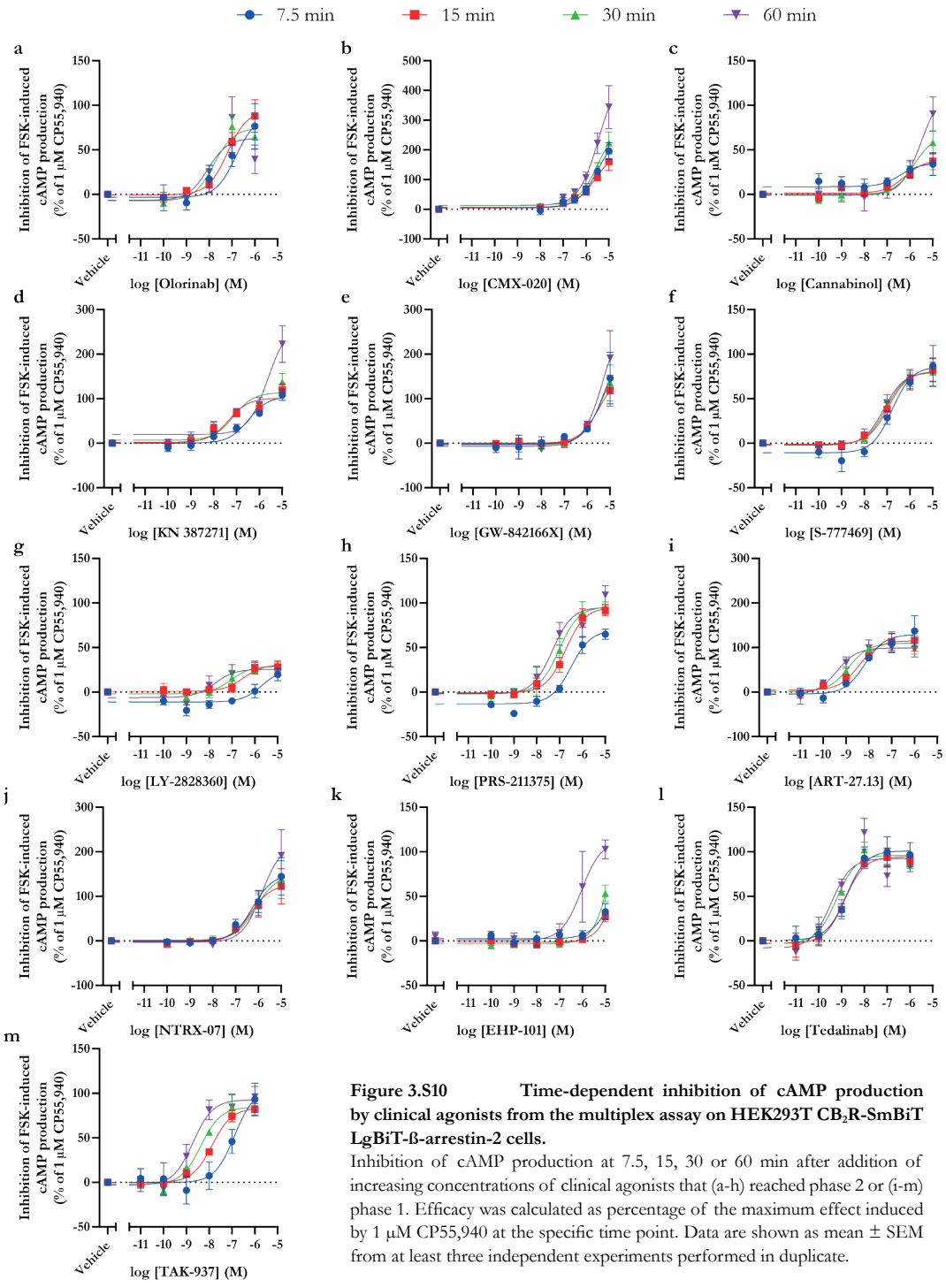

Figure 3.S10 Time-dependent inhibition of cAMP production by clinical agonists from the multiplex assay on HEK293T CB_2R-SmBiT LgBiT-ß-arrestin-2 cells.

Inhibition of cAMP production at 7.5, 15, 30 or 60 min after addition of increasing concentrations of clinical agonists that (a-h) reached phase 2 or (i-m) phase 1. Efficacy was calculated as percentage of the maximum effect induced by 1 µM CP55,940 at the specific time point. Data are shown as mean ± SEM from at least three independent experiments performed in duplicate.

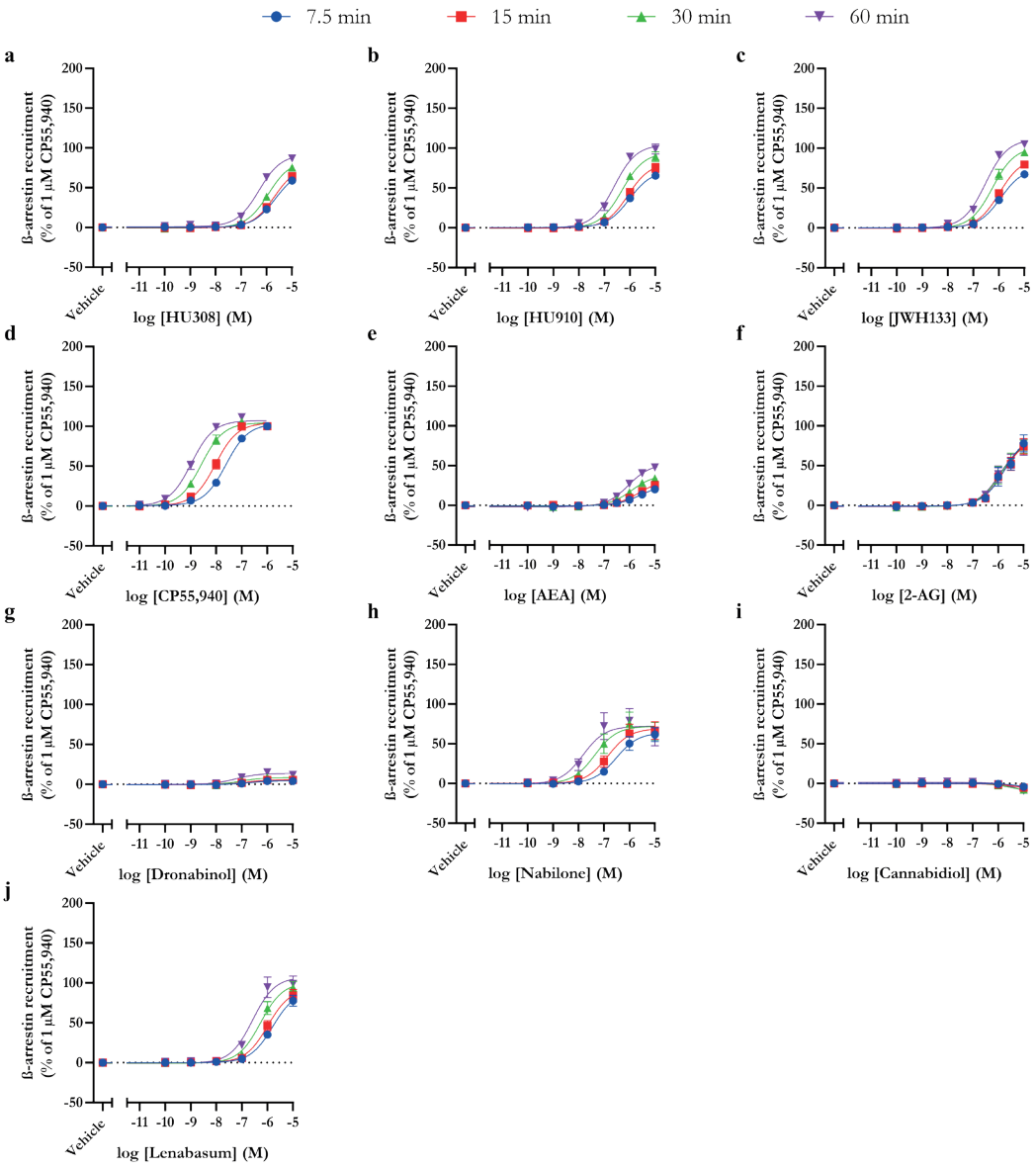

Figure 3.S11 Time-dependent ß-arrestin-2 recruitment to CB_2R by benchmark agonists, endocannabinoids, launched and clinical agonists from the multiplex assay on HEK293T CB_2R-SmBiT LgBiT-ß-arrestin-2 cells.

Recruitment of ß-arrestin-2 at 7.5, 15, 30 or 60 min after addition of increasing concentrations of (a-d) benchmark agonists, (e, f) endocannabinoids, clinical agonists that (g-i) are on the market or (j) reached phase 3. Efficacy was calculated as percentage of the maximum effect induced by 1 µM CP55,940 at the specific time point. Data are shown as mean ± SEM from at least three independent experiments performed in duplicate.

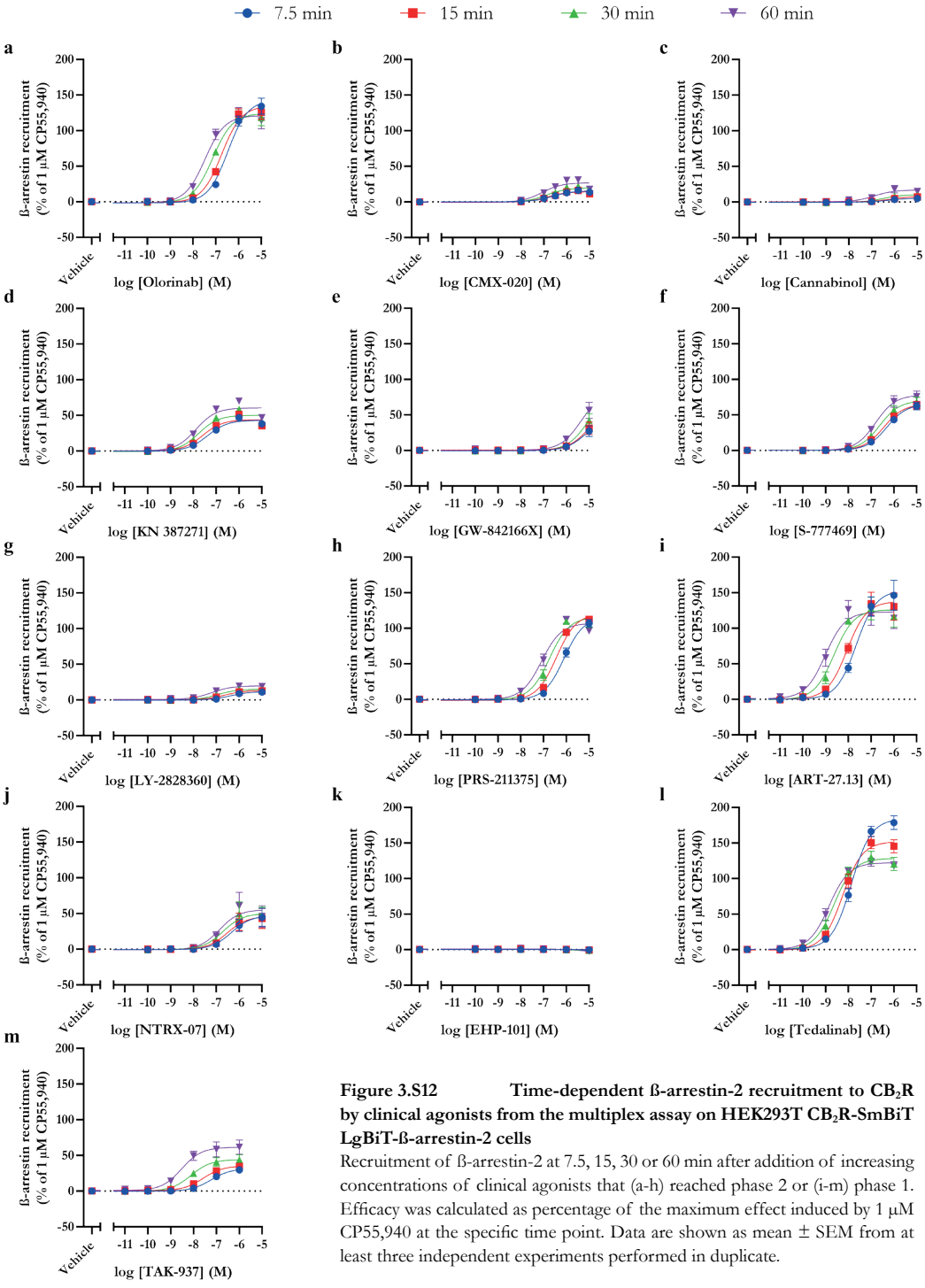

Figure 3.S12 Time-dependent ß-arrestin-2 recruitment to CB_2R by clinical agonists from the multiplex assay on HEK293T CB_2R-SmBiT LgBiT-ß-arrestin-2 cells

Recruitment of ß-arrestin-2 at 7.5, 15, 30 or 60 min after addition of increasing concentrations of clinical agonists that (a-h) reached phase 2 or (i-m) phase 1. Efficacy was calculated as percentage of the maximum effect induced by 1 µM CP55,940 at the specific time point. Data are shown as mean ± SEM from at least three independent experiments performed in duplicate.

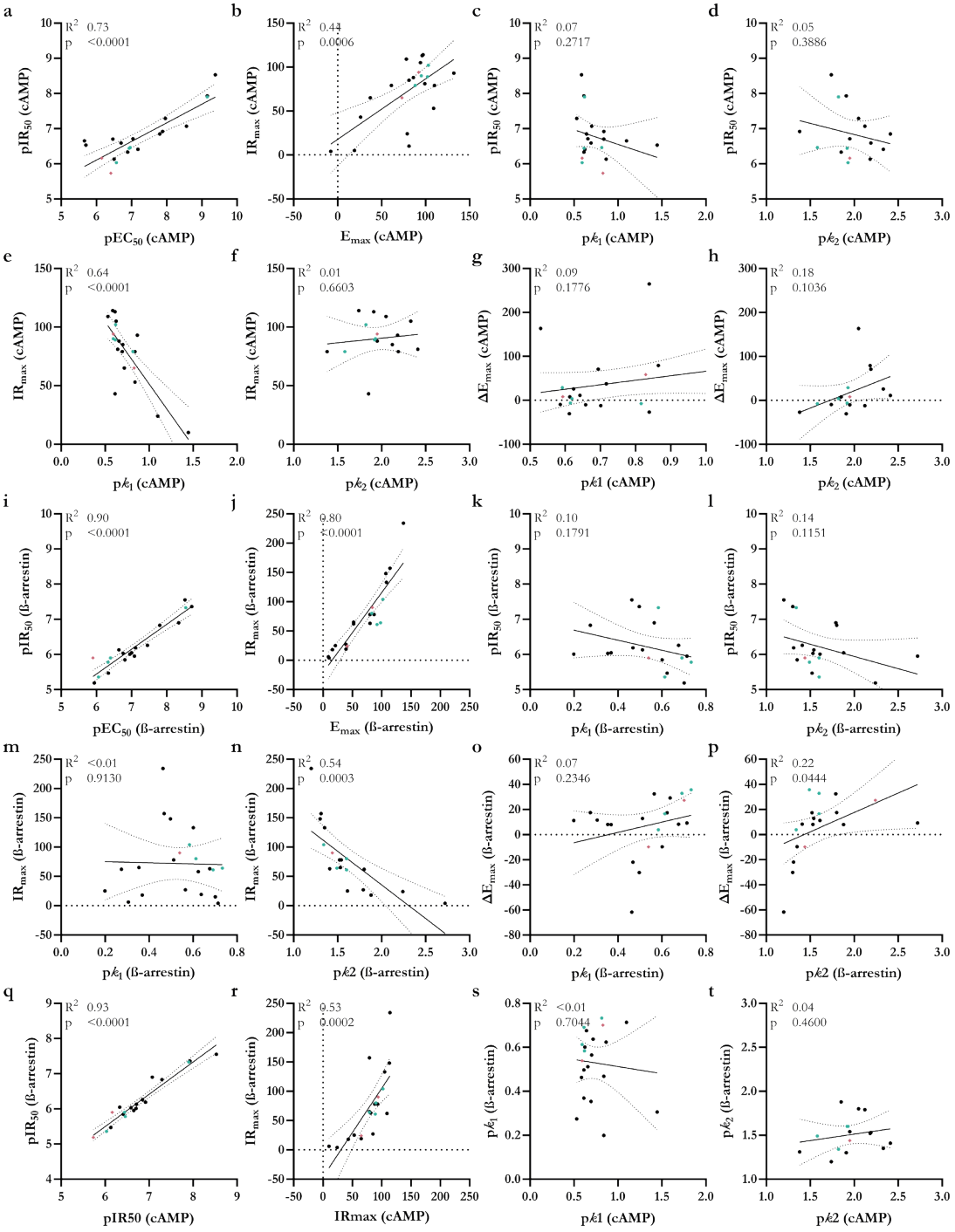
a
R² 0.73
p <0.0001
pIR50 (cAMP)
pEC50 (cAMP)
b
R² 0.44
p 0.0006
IRmax (cAMP)
Emax (cAMP)
c
R² 0.07
p 0.2717
pIR50 (cAMP)
pk1 (cAMP)
d
R² 0.05
p 0.3886
pIR50 (cAMP)
pk2 (cAMP)
e
R² 0.64
p <0.0001
IRmax (cAMP)
pk1 (cAMP)
f
R² 0.01
p 0.6603
IRmax (cAMP)
pk2 (cAMP)
g
R² 0.09
p 0.1776
ΔEmax (cAMP)
pk1 (cAMP)
h
R² 0.18
p 0.1036
ΔEmax (cAMP)
pk2 (cAMP)
i
R² 0.90
p <0.0001
pIR50 (ß-arrestin)
pEC50 (ß-arrestin)
j
R² 0.80
p <0.0001
IRmax (ß-arrestin)
Emax (ß-arrestin)
k
R² 0.10
p 0.1791
pIR50 (ß-arrestin)
pk1 (ß-arrestin)
l
R² 0.14
p 0.1151
pIR50 (ß-arrestin)
pk2 (ß-arrestin)
m
R² <0.01
p 0.9130
IRmax (ß-arrestin)
pk1 (ß-arrestin)
n
R² 0.54
p 0.0003
IRmax (ß-arrestin)
pk2 (ß-arrestin)
o
R² 0.07
p 0.2346
ΔEmax (ß-arrestin)
pk1 (ß-arrestin)
p
R² 0.22
p 0.0444
ΔEmax (ß-arrestin)
pk2 (ß-arrestin)
q
R² 0.93
p <0.0001
pIR50 (ß-arrestin)
pIR50 (cAMP)
r
R² 0.53
p 0.0002
IRmax (ß-arrestin)
IRmax (cAMP)
s
R² <0.01
p 0.7044
pk1 (ß-arrestin)
pk1 (cAMP)
t
R² 0.04
p 0.4600
pk2 (ß-arrestin)
pk2 (cAMP)

← Figure 3.S13 Correlation plots between parameters from the multiplex cAMP production and ß-arrestin-2 recruitment assay on CB_2R for benchmark agonists, endocannabinoids and clinical agonists. Correlation plots with forskolin-induced cAMP production parameters from the multiplex assay comparing (a) potency pEC_{50} and kinetic potency pIR_{50}, (b) efficacy E_{max} and kinetic efficacy IR_{max} (c) signaling rate constant pk_1 and pIR_{50}, (d) signaling rate constant pk_2 and pIR_{50}, (e) pk_1 and IR_{max}, (f) pk_2 and IR_{max}, (g) pk_1 and ΔE_{max} from the time-dependent analysis and (h) pk_2 and ΔE_{max}. Correlation plots with ß-arrestin-2 recruitment parameters from the multiplex assay comparing (i) pEC_{50} and pIR_{50}, (j) E_{max} and IR_{max} (k) pk_1 and pIR_{50}, (l) pk_2 and pIR_{50}, (m) pk_1 and IR_{max}, (n) pk_2 and IR_{max}, (o) pk_1 and ΔE_{max} from time-dependent analysis and (p) pk_2 and ΔE_{max}. Correlation plots comparing cAMP production and ß-arrestin recruitment in terms of kinetic parameters from the two readouts (q) IR_{50}, (r) IR_{max}, signaling rate constants (s) pk_1 and (t) pk_2. Benchmark agonists are turquoise hexagons (⬢), endocannabinoids coral diamonds (◆) and clinical agonists black circles (●). Data are mean from at least three independent experiments performed in duplicate. The solid line represents a linear correlation between the parameters and the dotted lines indicate the 95% confidence interval. R^2 values represent a measure of goodness-of-fit of the simple linear regression and $p < 0.05$ indicate a slope statistically significant different from 0.

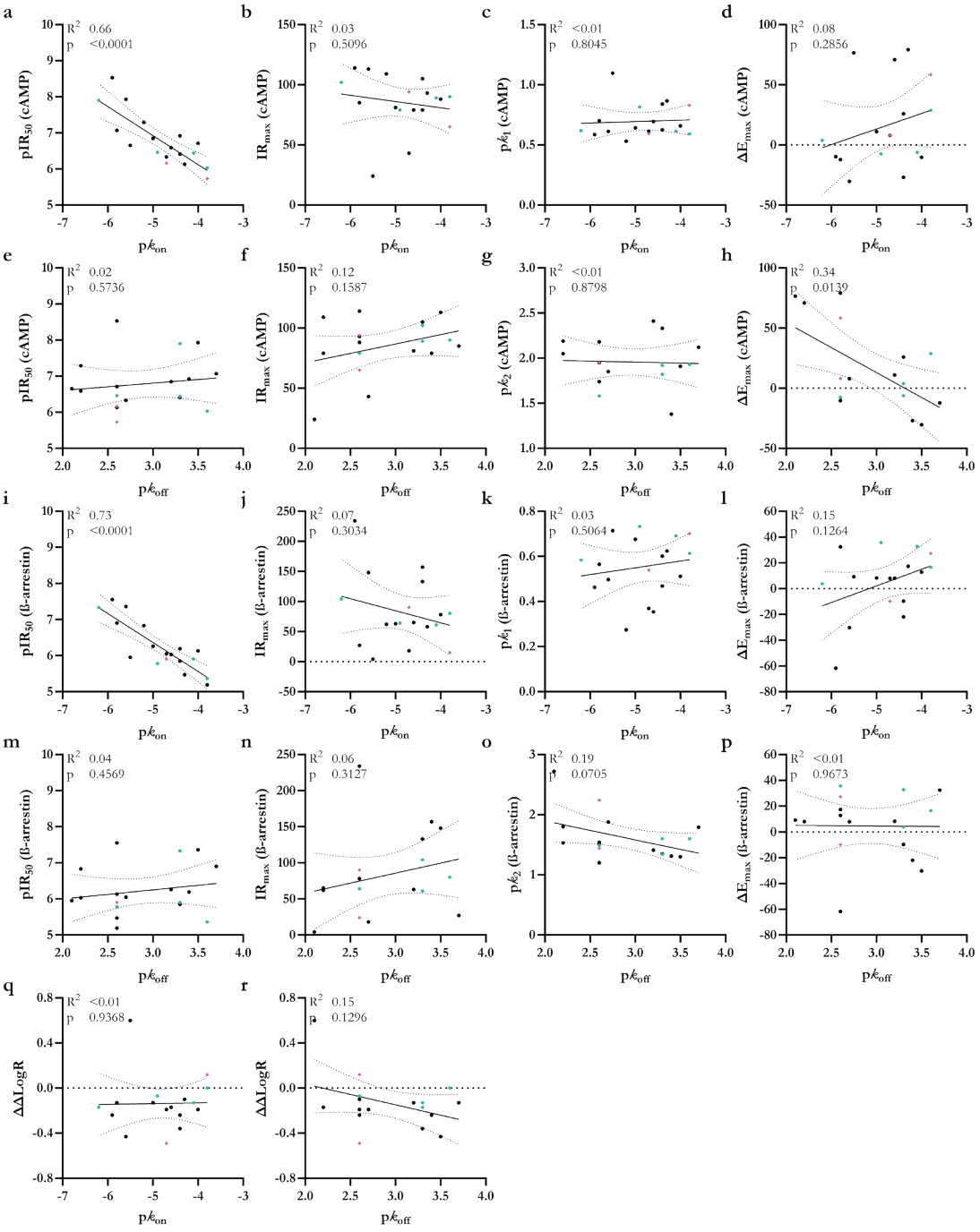
a
R² 0.66
p <0.0001
pIR50 (cAMP)
pkon
b
R² 0.03
p 0.5096
IRmax (cAMP)
pkon
c
R² <0.01
p 0.8045
pKi (cAMP)
pkon
d
R² 0.08
p 0.2856
ΔEmax (cAMP)
pkon
e
R² 0.02
p 0.5736
pIR50 (cAMP)
pkoff
f
R² 0.12
p 0.1587
IRmax (cAMP)
pkoff
g
R² <0.01
p 0.8798
pKi (cAMP)
pkoff
h
R² 0.34
p 0.0139
ΔEmax (cAMP)
pkoff
i
R² 0.73
p <0.0001
pIR50 (β-arrestin)
pkon
j
R² 0.07
p 0.3034
IRmax (β-arrestin)
pkon
k
R² 0.03
p 0.5064
pKi (β-arrestin)
pkon
l
R² 0.15
p 0.1264
ΔEmax (β-arrestin)
pkon
m
R² 0.04
p 0.4569
pIR50 (β-arrestin)
pkoff
n
R² 0.06
p 0.3127
IRmax (β-arrestin)
pkoff
o
R² 0.19
p 0.0705
pKi (β-arrestin)
pkoff
p
R² <0.01
p 0.9673
ΔEmax (β-arrestin)
pkoff
q
R² <0.01
p 0.9368
ΔΔLogR
pkon
r
R² 0.15
p 0.1296
ΔΔLogR
pkoff

← Figure 3.S14 Correlation plots between binding affinity, binding kinetic parameters and parameters from the multiplex assay on CB_2R for benchmark agonists, endocannabinoids and clinical agonists.
Correlation plots comparing association rate constant pk_{on} with cAMP production parameters from the multiplex assay (a) kinetic potency pIR_{50}, (b) kinetic efficacy IR_{max}, (c) signaling rate constant pk_1, (d) ΔE_{max} from the time-dependent analysis and dissociation rate constant pk_{off} with cAMP production parameters from the multiplex assay (e) pIR_{50}, (f) IR_{max}, (g) signaling rate constant pk_2 and (h) ΔE_{max}. Correlation plots comparing association rate constant pk_{on} with ß-arrestin-2 recruitment parameters from the multiplex assay (i) pIR_{50}, (j) IR_{max}, (k) signaling rate constant pk_1, (l) ΔE_{max} from the time-dependent analysis and dissociation rate constant pk_{off} with cAMP production parameters from the multiplex assay (m) pIR_{50}, (n) IR_{max}, (o) signaling rate constant pk_2 and (p) ΔE_{max}. Correlation plots between target binding kinetic parameters and bias parameters comparing (q) pk_{on} and $\Delta\Delta LogR$, and (r) pk_{off} and $\Delta\Delta LogR$. Benchmark agonists are turquoise hexagons (⬢), endocannabinoids coral diamonds (◆) and clinical agonists black circles (●). Data are mean from at least three independent experiments performed in duplicate. The solid line represents a linear correlation between the parameters and the dotted lines indicate the 95% confidence interval. R^2 values represent a measure of goodness-of-fit of the simple linear regression and $p < 0.05$ indicate a slope statistically significant different from 0.

Table 3.S1 Physicochemical properties and pharmacokinetic properties of benchmark agonists, endocannabinoids (eCB) and clinical agonists.

	Agonist	MW[a] (g/mol)	PSA[b] (Å)	LogD[c]	K_{ow}LogP[d]	Kinetic solubility[e] (µg/mL)	LIMBA LogDbrain[f]	PAMPA P_{eff}[g] ($\times 10^{-6}$ cm/s)	Human plasma protein binding (free fraction %)	hP-gp Efflux ratio
Benchmark	**HU308**	414.6	27.580	4.29	8.965	<0.5	N.D.	2.530 ± 1.460#	N.D.	1.266
	HU910	414.6	31.540	N.D.	9.001	<0.5	N.D.	0.315 ± 0.420#	<1.790	1.182
	JWH133	312.5	7.910	>3.00	8.458	<0.4	N.D.	0.930 ± 0.810#	0.070 ± 0.010	N.D.
	CP55,940	376.6	49.860	N.D.	7.498	1.4	0.7	N.D.	<1	0.950
eCB	**AEA**	347.5	41.910	N.D.	6.310	N.D.	N.D.	0.26 ± 0.16	N.D.	N.D.
	2-AG	378.5	51.250	N.D.	6.738	N.D.	N.D.	N.D.	N.D.	N.D.
Clinical	**Dronabinol**	314.5	22.240	N.A.	7.598	N.A.	N.A.	N.A.	N.A.	N.A.
	Nabilone	372.5	37.850	N.D.	7.069	<0.7	N.D.	N.D.	<0.1	N.D.
	Cannabidiol	314.5	31.120	N.D.	8.013	<0.2	N.D.	N.D.	N.D.	1.390
	Lenabasum	400.6	53.860	3.79	8.241	22.0	2.73	N.D.	<0.1	0.877
	Olorinab	357.4	85.780	1.77	1.244	368.0	-0.08	2.860 ± 0.298#	23.660 ± 0.428	1.220
	CMX-020	416.6	41.540	3.92	6.904	5.1	2.07	6.220 ± 2.250	<0.1	1.240
	Cannabinol	310.4	22.630	N.D.	7.232	<0.6	N.D.	N.D.	<1	1.18
	KN 387271	430.4	62.100	N.D.	4.881	<0.8	2.28	N.D.	<0.1	1.010
	GW-842166X	449.3	57.500	3.84	4.321	<0.2	2.40	3.540	0.620	0.980
	S-777469	414.5	60.940	0.21	4.857	45.0	0.27	3.520 ± 0.180	3.980 ± 0.078	1.310
	LY-2828360	426.9	50.310	2.82	3.979	>427.0	1.52	4.100 ± 0.220	5.810 ± 0.838	1.080
	PRS-211375	470.6	79.800	3.46	7.556	332.0	1.85	N.D.	N.D.	N.D.
	ART-27.13	413.5	53.860	3.07	5.913	4.6	1.56	4.390 ± 1.110	12.370 ± 0.270	2.150
	NTRX-07	335.4	26.520	3.75	5.184	N.D.	2.18	12.900	1.710 ± 0.134	1.220
	EHP-101	433.6	52.650	N.D.	7.862	N.D.	N.D.	N.D.	1.00 ± 0.095	N.D.
	Tedalinab	345.4	37.480	3.92	5.293	4.0	2.42	7.460 ± 1.640	1.240 ± 0.031	0.990
	TAK-937	423.6	42.520	N.D.	5.514	5.9	2.15	3.570 ± 0.070	1.230 ± 0.016	1.220

Table 3.S2 Assay characteristics of functional assays used in this study for investigation of agonist-mediated activation of CB_2R.

Assay	GloSensor™	NanoBiT®	[^{35}S]GTPγS binding
Transducer/Effector	cAMP	ß-arrestin-2	G protein
Endpoint or kinetic	Kinetic	Kinetic	Endpoint
Time point or span for data collection	54 – 150 min	54 – 150 min	90 min
System	Live cells	Live cells	Membrane fractions
Cell line	HEK293T CB_2R-SmBiT LgBiT-ß-arrestin-2		
Receptor expression levels[a]	11 ± 2 pmol/mg		
Measured process	Production	Recruitment	Binding
Measured molecule	cAMP	CB_2R-SmBiT	[^{35}S]GTPγS
Measured molecule 2 (if any)	N.A.	LgBiT-ß-arrestin-2	N.A.
Temperature	25 °C	25 °C	25 °C
Signal detection	Luminescence (Fluc)	Luminescence (NLuc)	Radioactivity
Reference ligand for bias	HU308		
Reference ligand for E_{max} per assay	CP55,940		
Multiplex possibilities	With NanoBiT	With GloSensor	N.A.

[a] Determined in [^{3}H]RO6957022 homologous displacement assays on HEK293T CB_2R-SmBiT LgBiT-ß-arrestin-2 membrane fractions. N.A. is not applicable.

Table 3.S3 Validation and characterization of the multiplexed cAMP production and ß-arrestin-2 recruitment assay on HEK293T CB_2R-SmBiT LgBiT-ß-arrestin-2 cells with full agonist CP55,940.

	cAMP channel	ß-arrestin channel
Reagent	**pEC_{50}**	**pEC_{50}**
cAMP reagent	8.86 (8.85; 8.86)	N.A.
Vivazine	N.A.	8.20 (8.28; 8.12)
Multiplex reagent	8.55 (8.58; 8.53)	8.16 (8.13; 8.20)

Potency values (pEC_{50} and pIR_{50}) of CP55,940 on inhibition of forskolin-induced cAMP production and ß-arrestin-2 recruitment obtained from the multiplex assay by quantification of AUC. Data are mean from two independent experiments performed in duplicate with individual values between brackets. N.A is not applicable.

← **Table 3.S1** *(continued legend)*

[a] Molecular weight (MW). [b] Polar surface area (PSA) calculated as surface sum of all polar atoms in the molecule. [c] Distribution coefficient (LogD) experimentally determined in 0.025 M phosphate/1-octanol buffer at pH 7.4. [d] Calculated partition coefficient value (cLogP) from experimentally determined octanol-water partition coefficient (K_{ow}). [e] Solubility of agonist in aqueous (0.05 M phosphate) buffer at pH 6.5 after lyophilization from DMSO stock. [f] Lipid Membrane Binding Assay (LIMBA) LogD to determine non-specific binding of agonists to brain lipids at pH 7.4. [g] Parallel artificial membrane permeability assay (PAMPA) for determination of membrane permeation coefficient values (P_{eff}) at pH 7.4 or 6.4 (#). [h] P-glycoprotein (P-gp) transport efflux ratio. Values represent the mean of a single experiment or the mean ± SD of at least two independent experiments. N.A. is not applicable due to restrictions. N.D. is not detectable due to intrinsic properties of agonists.

Table 3.S4 Inhibition of forskolin-induced cAMP production by benchmark agonists, endocannabinoids (eCB) and clinical agonists determined in the multiplex assay on CB_2R after 7.5 or 60 min.

		7.5 min		60 min	
	Agonist	**pEC_{50}**	**E_{max} or activation at 10 μM (%)**	**pEC_{50}**	**E_{max} or activation at 10 μM (%)**
Benchmark	**HU308**	6.75 ± 0.46	78 ± 4	7.03 ± 0.35	106 ± 7*
	HU910	8.19 ± 0.37	108 ± 11	8.59 ± 0.40	102 ± 8
	JWH133	6.76 ± 0.44	91 ± 6	7.96 ± 0.18	84 ± 4
	CP55,940	8.04 ± 0.22	104 ± 6	9.41 ± 0.08*	108 ± 8
eCB	**AEA**	5.37 ± 0.17	127 ±10	5.59 ± 0.13	185 ± 46
	2-AG	6.57 ± 0.38	101 ± 17	5.86 ± 0.19	109 ± 29
Clinical	**Dronabinol**	6.03 ± 0.15	27 ± 9	5.62 ± 0.04	103 ± 29
	Nabilone	6.64 ± 0.10	78 ± 11	7.95 ± 0.17*	90 ± 8
	Cannabidiol	N.D.	23 ± 4	N.D.	134 ± 61#
	Lenabasum	6.39 ± 0.24	160 ± 54	6.07 ± 0.11	240 ± 48
	Olorinab	6.83 ± 0.08	90 ± 31	8.05 ± 0.08*	63 ± 20
	CMX-020	N.D.	196 ± 28	5.49 ± 0.07	461 ± 114
	Cannabinol	6.35 ± 0.35	38 ± 13	5.49 ± 0.23	132 ± 35
	KN 387271	6.53 ± 0.37	109 ± 18	5.70 ± 0.17	272 ± 66
	GW-842166X	N.D.	146 ± 58	N.D.	183 ± 59#
	S-777469	6.75 ± 0.17	90 ± 22	7.14 ± 0.13	80 ± 13
	LY-2828360	N.D.	20 ± 7	7.45 ± 0.38	28 ± 6
	PRS-211375	6.44 ± 0.11	70 ± 7	7.33 ± 0.28*	96 ± 10
	ART-27.13	8.20 ± 0.17	131 ± 29	9.44 ± 0.26*	101 ± 16
	NTRX-07	6.31 ± 0.13	148 ± 45	5.84 ± 0.02*	219 ± 66
	EHP-101	N.D.	33 ± 9	N.D.	123 ± 22#*
	Tedalinab	9.01 ± 0.42	103 ± 10	9.53 ± 0.16	93 ± 7
	TAK-937	6.89 ± 0.12	105 ± 18	8.79 ± 0.19*	93 ± 11

Potency (pEC_{50}) and efficacy (E_{max}) values were determined from dose-response curves derived from the cAMP time traces in the multiplex assay analyzed at 7.5 and 60 min after agonist addition, respectively. #In the absence of a DRC, maximal activation (%) was determined at 10 μM of agonist. Multiple unpaired t-tests were performed to analyze differences in potency and efficacy at 60 min compared to 7.5 (* $p<0.05$). Data are mean from at least three independent experiments performed in duplicate. N.A is not applicable, N.D. is not detectable.

Table 3.S5 ß-arrestin-2 recruitment by benchmark agonists, endocannabinoids (eCB) and clinical agonists determined in the multiplex assay on CB_2R after 7.5 or 60 min.

		7.5 min		60 min	
	Agonist	pEC_{50}	E_{max} or activation at 10 µM (%)	pEC_{50}	E_{max} or activation at 10 µM (%)
Benchmark	**HU308**	5.66 ± 0.02	72 ± 4	6.08 ± 0.19	88 ± 8
	HU910	6.02 ± 0.02	72 ± 3	6.61 ± 0.04*	104 ± 6*
	JWH133	5.92 ± 0.07	76 ± 2	6.53 ± 0.06*	111 ± 3*
	CP55,940	7.62 ± 0.06	103 ± 0	8.97 ± 0.09*	107 ± 0*
eCB	**AEA**	5.57 ± 0.02	26 ± 0	6.02 ± 0.05	53 ± 3*
	2-AG	5.78 ± 0.16	93 ± 10	5.95 ± 0.11	83 ± 10
Clinical	**Dronabinol**	6.66 ± 0.08	5 ± 0	7.25 ± 0.08*	14 ± 2*
	Nabilone	6.51 ± 0.06	64 ± 9	7.80 ± 0.09*	72 ± 14
	Cannabidiol	N.A.	N.A.	N.A.	N.A.
	Lenabasum	5.79 ± 0.04	90 ± 7	6.57 ± 0.02*	107 ± 12
	Olorinab	6.47 ± 0.03	143 ± 12	7.47 ± 0.03*	121 ± 11
	CMX-020	6.59 ± 0.10	16 ± 0	7.06 ± 0.05*	27 ± 1*
	Cannabinol	6.28 ± 0.14	5 ± 1	6.99 ± 0.18*	17 ± 5
	KN 387271	7.38 ± 0.06	43 ± 1	7.90 ± 0.08*	61 ± 2*
	GW-842166X	N.D.	27 ± 8	N.D.	56 ± 11[#]
	S-777469	6.31 ± 0.06	65 ± 5	6.76 ± 0.08*	78 ± 8
	LY-2828360	6.37 ± 0.07	12 ± 0	7.22 ± 0.07*	20 ± 1*
	PRS-211375	6.09 ± 0.11	117 ± 7	7.11 ± 0.15*	107 ± 3
	ART-27.13	7.70 ± 0.13	154 ± 24	9.10 ± 0.22*	123 ± 16
	NTRX-07	6.35 ± 0.10	48 ± 14	6.88 ± 0.14*	56 ± 18
	EHP-101	N.A.	N.A.	N.A.	N.A.
	Tedalinab	7.87 ± 0.06	184 ± 8	8.85 ± 0.09*	122 ± 5*
	TAK-937	7.21 ± 0.12	32 ± 3	8.55 ± 0.09*	64 ± 10*

Potency (pEC_{50}) and efficacy (E_{max}) values were determined from dose-response curves derived from the ß-arrestin-2 time traces in the multiplex assay analyzed at 7.5 and 60 min after agonist addition, respectively. [#]In the absence of a DRC, maximal activation (%) was determined at 10 µM of agonist. Multiple unpaired t-tests were performed to analyze differences in potency and efficacy at 60 min compared to 7.5 (* $p<0.05$). Data are mean from at least three independent experiments performed in duplicate. N.A is not applicable, N.D. is not detectable.

Table 3.S6 **ΔΔLogR ratios and bias factors for benchmark agonists, endocannabinoids (eCB) and clinical agonists between forskolin-induced cAMP production and ß-arrestin-2 recruitment in the multiplex assay on CB_2R using an endpoint, semi-kinetic (AUC) or kinetic (IR) analysis.**

		7.5 min		60 min		AUC		IR	
	Agonist	ΔΔLogR[a]	Bias factor[b]	ΔΔLogR	Bias factor	ΔΔLogR	Bias factor	ΔΔLogR	Bias factor
Benchmark	**HU308**	0.00 ± 0.20	1.00	0.00 ± 0.13	1.00	0.00 ± 0.07	1.00	0.00 ± 0.21	1.00
	HU910	1.32 ± 0.40	20.78	1.24 ± 0.42	17.34	-0.40 ± 0.08	0.40	-0.13 ± 0.20	0.73
	JWH133	-0.16 ± 0.18	0.69	0.44 ± 0.22	2.78	-0.01 ± 0.09	0.98	-0.07 ± 0.19	0.86
	CP55,940	-0.28 ± 0.37	0.52	0.02 ± 0.21	1.05	0.09 ± 0.21	1.23	-0.17 ± 0.28	0.67
eCB	**AEA**	-0.07 ± 0.21	0.85	0.66 ± 0.17	4.55	0.16 ± 0.13	1.44	0.12 ± 0.25	1.33
	2-AG	0.17 ± 0.39	1.47	-0.23 ± 0.27	0.58	-0.10 ± 0.20	0.79	-0.49 ± 0.32	0.32
Clinical	**Dronabinol**	-1.10 ± 0.37	0.08	-0.61 ± 0.34	0.25	-1.07 ± 0.27	0.09	0.60 ± 0.29	3.95
	Nabilone	-0.46 ± 0.22	0.35	-0.12 ± 0.26	0.76	0.01 ± 0.14	1.03	-0.13 ± 0.21	0.74
	Cannabidiol	N.A.	N.A.	N.A.	N.A.	N.A.	N.A.	N.A.	N.A.
	Lenabasum	0.23 ± 0.38	1.68	0.01 ± 0.15	1.02	0.04 ± 0.13	1.10	-0.10 ± 0.20	0.80
	Olorinab	-0.23 ± 0.43	0.59	-0.24 ± 0.24	0.57	-0.15 ± 0.21	0.71	-0.24 ± 0.21	0.57
	CMX-020	N.D.	N.D.	0.74 ± 0.19	5.46	0.25 ± 0.44	1.76	0.02 ± 0.42	1.06
	Cannabinol	1.56 ± 1.05	36.48	-0.32 ± 0.37	0.48	-0.53 ± 0.21	0.30	N.D.	N.D.
	KN 387271	-1.15 ± 0.31	0.07	0.25 ± 0.42	1.77	-0.31 ± 0.38	0.49	0.06 ± 0.29	1.15
	GW-842166X	N.A.	N.A.	N.A.	N.A.	N.A.	N.A.	N.A.	N.A.
	S-777469	-0.23 ± 0.22	0.59	-0.02 ± 0.26	0.95	-0.10 ± 0.18	0.80	-0.19 ± 0.23	0.65
	LY-2828360	N.D.	N.D.	-0.29 ± 0.58	0.51	-0.69 ± 0.50	0.21	-0.19 ± 0.30	0.64
	PRS-211375	-0.79 ± 0.23	0.16	-0.16 ± 0.37	0.69	-0.21 ± 0.41	0.61	-0.36 ± 0.24	0.43
	ART-27.13	-0.14 ± 0.17	0.73	-0.14 ± 0.24	0.73	-0.02 ± 0.30	0.96	-0.43 ± 0.19	0.37
	NTRX-07	-0.05 ± 0.34	0.89	0.14 ± 0.32	1.39	-0.17 ± 0.15	0.68	-0.17 ± 0.29	0.67
	EHP-101	N.A.	N.A.	N.A.	N.A.	N.A.	N.A.	N.A.	N.A.
	Tedalinab	0.17 ± 0.40	1.48	0.07 ± 0.25	1.17	0.16 ± 0.26	1.43	-0.24 ± 0.23	0.57
	TAK-937	0.59 ± 0.42	3.88	0.03 ± 0.17	1.07	0.03 ± 0.14	1.08	-0.13 ± 0.20	0.75

[a] ΔΔLogR ratios were calculated to determine ligand bias between the cAMP and ß-arrestin-2 pathway using **Equation 3.10**. [b] The ligand bias factor for each ligand, relative to HU308, was determined following **Equation 3.11**. One-way ANOVA was performed to analyze differences in ΔΔLogR values of agonists compared to HU308 (* $p<0.05$). Values are presented as mean (± SEM) from at least three independent experiments performed in duplicate. N.D. is not determined. N.A. is not applicable.

Table 3.S7 G protein activation by benchmark agonists, endocannabinoids (eCB) and clinical agonists determined in [^{35}S]GTPγS assays on CB_2R.

	Agonist	pEC_{50}	E_{max} (%)
Benchmark	**HU308**	6.79 ± 0.10	72 ± 1
	HU910	7.01 ± 0.25	65 ± 1
	JWH133	7.02 ± 0.11	85 ± 6
	CP55,940	8.54 ± 0.11	91 ± 2
eCB	**AEA**	6.67 ± 0.17	25 ± 1
	2-AG	6.54 ± 0.15	67 ± 6
Clinical	**Dronabinol**	N.D.	-5 ± 7#
	Nabilone	7.31 ± 0.10	97 ± 8
	Cannabidiol	N.D.	-36 ± 5#
	Lenabasum	7.04 ± 0.08	71 ± 2
	Olorinab	7.87 ± 0.13	88 ± 2
	CMX-020	N.D.	3 ± 4#
	Cannabinol	N.D.	16 ± 5#
	KN 387271	7.46 ± 0.12	50 ± 3
	GW-842166X	N.D.	21 ± 3#
	S-777469	6.92 ± 0.06	83 ± 5
	LY-2828360	N.D.	9 ± 4#
	PRS-211375	7.50 ± 0.09	94 ± 2
	ART-27.13	9.06 ± 0.10	106 ± 3
	NTRX-07	6.66 ± 0.03	71 ± 5
	EHP-101	N.D.	-4 ± 15#
	Tedalinab	8.33 ± 0.20	105 ± 5
	TAK-937	8.73 ± 0.34	21 ± 2

Potency (pEC_{50}), efficacy (E_{max}) values were determined from dose-response curves. #In the absence of a DRC, maximal activation (%) was determined at 10 μM agonist. Data are mean from at least three independent experiments performed in duplicate. N.D. is not detectable

Chapter 4

Structural basis of selective cannabinoid CB_2 receptor activation

Xiaoting Li*, Hao Chang*, Jara Bouma*, Laura V. de Paus, Partha Mukhopadhyay, Janos Paloczi, Mohammed Mustafa, Cas van der Horst, Sanjay Sunil Kumar, Lijie Wu, Yanan Yu, Richard J. B. H. N. van den Berg, Antonius P.A. Janssen, Aron Lichtman, Zhi-Jie Liu, Pal Pacher, Mario van der Stelt, Laura H. Heitman, Tian Hua

Adapted from: *Nature Communications* (2023) **14**, 1447

* These authors contributed equally.

Abstract

Cannabinoid CB_2 receptor (CB_2R) agonists are investigated as therapeutic agents in the clinic. However, their molecular mode-of-action is not fully understood. Here, we report the discovery of LEI-102, a CB_2R agonist, used in conjunction with three other CBR ligands (APD371, HU308 and CP55,940), to investigate the selective CB_2R activation by binding kinetics, site-directed mutagenesis, and cryo-EM studies. We identify key residues for CB_2R activation. Highly lipophilic HU308 and the endocannabinoids, but not the more polar LEI-102, APD371 and CP55,940, reach the binding pocket through a membrane channel in TM1-TM7. Favorable physico-chemical properties of LEI-102 enable oral efficacy in a chemotherapy-induced nephropathy model. This chapter delineates the molecular mechanism of CB_2R activation by selective agonists and highlights the role of lipophilicity in CB_2R engagement. This may have implications for GPCR drug design and sheds light on their activation by endogenous ligands.

4.1 Introduction

Preparations of the plant *Cannabis sativa* have been used for centuries in the treatment of various diseases, including cancer and neuropathic pain[1]. The synthetic version of its psychoactive constituent, Δ^9-tetrahydrocannabinol (THC, **Figure 4.1**), is in FDA approved drugs Marinol® or Syndros® (dronabinol). The extracted version of THC is one of the active constituents of oromucosal spray Sativex® (nabiximols). These drugs are primarily used for the treatment of chemotherapy-induced nausea, enhancement of appetite in cachexic AIDS-patients, and to alleviate the spasticity and pain associated with multiple scleroses[2–6]. However, THC-based therapies are associated with clinically undesired psychotropic and cardiovascular adverse effects and challenging pharmacokinetic properties due to their high lipophilicity that may limit their therapeutic efficacy[7–10].

THC exerts its therapeutic effects mostly via the G protein-coupled receptors (GPCRs) cannabinoid CB_1 and CB_2 receptors (CB_1R and CB_2R), which have 68% sequence identity in their seven transmembrane (TM) domains[11]. Both receptors are activated by the endogenous signaling lipids anandamide (AEA) and 2-arachidonoylglycerol (2-AG) (**Figure 4.1**), the two main endocannabinoids. The CB_1R, which is the most abundantly expressed GPCR in the central nervous system (CNS) is responsible for the psychotropic side effects of THC[12–14]. It plays a role in memory, learning, neurogenesis, neuronal migration, and synaptogenesis. Furthermore, its presence in many organ tissues belies more non-neurological functions[15]. The CB_2R is mainly found on the cells of the immune system and is upregulated under pathophysiological conditions[16,17]. Its activation in general is associated with anti-inflammatory responses in tissue injury of the liver, heart, kidney, colon, and brain as determined in various preclinical models[18–22]. Based on preclinical studies it is thought that selective CB_2R agonists may retain and exceed certain therapeutic properties of THC without inducing psychotropic side effects[23].

Various academic and industrial groups have developed selective CB_2R ligands[24]. HU308 (**Figure 4.1**) was the first selective CB_2R agonist to be reported that displayed anti-inflammatory and analgesic properties in mouse models without inducing CNS-side effects[18].

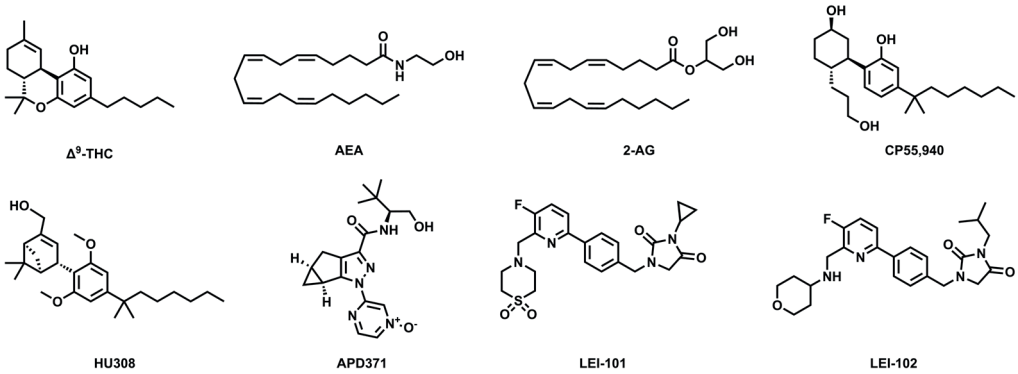

Figure 4.1 Chemical structures.

Shown are the main constituent of Cannabis sativa Δ^9-tetrahydrocannabinol (THC), and the two major endocannabinoids anandamide (AEA) and 2-arachidonoylglycerol (2-AG), as well as non-selective CBR agonist CP55,940 and CB_2R agonists HU308, APD371, LEI-101, and LEI-102.

However, poor physico-chemical properties (*e.g.* low solubility, high lipophilicity) of HU308, which has a calculated logarithm of octanol-water partition coefficient (cLogP) of 8.0[25], and its analogs prevented the successful clinical translation of this class of cannabinoid-based drugs.

A next generation of CB_2R ligands was developed with improved drug-like properties. For instance, Olorinab® (APD371, **Figure 4.1**) is the most polar CB_2R agonist reported to date with a cLogP of -0.4[26]. A phase 2a small-scale safety and tolerability trial in 14 patients with chronic abdominal pain associated with Crohn's disease showed mild-to-moderate adverse events and an improvement in abdominal pain scores[27]. We have previously disclosed pyridinylbenzylimidazolidine-2,4-dione derivatives as selective CB_2R agonists and studied their affinity, target binding kinetics and potency as a function of their lipophilicity, which resulted in the discovery of the orally available and peripherally restricted selective CB_2R agonist LEI-101 (**Figure 4.1**)[28–30]. It is intriguing that the CB_2R binding pocket tolerates a wide array of ligands with very different scaffolds and hydrophobicity. For example, HU308 has a 2-billion-fold higher lipophilicity than APD371. Despite the tremendous progress in the field of CB_2R drug discovery, we still do not have any molecular understanding on how these CB_2R agonists selectively activate CB_2R over CB_1R.

Recently, three-dimensional structures of the CB_1R and CB_2R have been elucidated in both the active and inactive states by crystallography or cryo-electron microscopy (cryo-EM) and the binding modes of diverse ligands and their activation mechanism were reported[31–35]. Remarkably, those structures revealed that CB_1R and CB_2R possess a highly similar, lipophilic orthosteric agonist binding pocket, which makes it challenging to explain the selective activation of CB_2R. To date, no structural studies with selective CB_2R agonists have been reported that could aid in understanding the molecular basis of CB_2R selectivity.

Here, we present the discovery of LEI-102, a potent and selective CB_2R agonist with good physicochemical and biological properties. LEI-102 is used in conjunction with CB_2R selective agonists APD371 and HU308, and nonselective agonist CP55,940 to investigate the activation mechanism of CB_2R. For this study, we combine ligand-target binding kinetics, site-directed mutagenesis, and cryo-EM methods. We find that CB_2R has a distinct activation mechanism compared to CB_1R. Additionally, we find that the physico-chemical properties of the ligands influence their entry pathway into the receptor. Highly lipophilic ligands, such as HU308 and the endocannabinoids, may reach the binding pocket through the membrane, whereas more polar ligands, such as LEI-102, APD371 and CP55,940, enter the receptor via an alternative route. Furthermore, we show that the favorable physico-chemical properties of LEI-102 and CB_2R selectivity underscore its promising *in vivo* efficacy via oral administration in a chemotherapy-induced nephropathy model without inducing CNS-mediated side effects. Together, these studies enhance our insights into how certain physicochemical properties of ligands translate to *in vivo* activity and changes their engagement to GPCRs.

4.2 Results

4.2.1 LEI-102 as a high affinity and potent CB_2R-selective agonist

To obtain a selective CB_2R agonist with beneficial physico-chemical properties, LEI-102, a pyridinylbenzylimidazolidine-2,4-dione derivative, was designed and synthesized (**Figure 4.S1**). LEI-102 combined an isobutyl substituent on the imidazolidine with an aminotetrahydropyran to replace the cyclopropyl and thiomorpholine 1,1-dioxide in LEI-101, respectively[30]. LEI-102 had a cLogP of 2.1 as calculated by ChemDraw 19.0 (**Table 4.S1**). The inhibitory constant (pK_i), potency (pEC_{50}) and intrinsic activity (E_{max}) of LEI-102 were determined in [^{3}H]RO6957022 displacement assays on stably expressing CB_2R membranes and [^{35}S]GTPγS G protein activation assays using HEK293T membranes transiently expressing recombinant hCB_2R or hCB_1R, respectively (**Table 4.S2**). APD371, HU308, CP55,940 and the endocannabinoids AEA and 2-AG were also explored. LEI-102 had a high binding affinity for CB_2R (pK_i 8.0 ± 0.1) and was more potent than the selective CB_2R agonists APD371 and HU308. LEI-102 did not bind CB_1R, thereby showing at least 1000-fold selectivity (**Table 4.S3**). In G protein activation assays, LEI-102 activated the receptor as a partial agonist (E_{max} 76 ± 1 %) with a pEC_{50} value of 6.9 ± 0.2 (**Table 4.S2**).

4.2.2 Distinct target binding kinetic profiles of CB_2R agonists

To quantify the ligand-target binding kinetic parameters of the agonists in more detail, we performed displacement and competition association assays with [^{3}H]RO6957022 on membranes stably expressing hCB_2R (**Table 4.S2**). The equilibrium K_i and kinetic K_D values were well correlated, validating the competition association assay. First, we determined the dissociation rate constants (k_{off}) of all agonists and converted these into a residence time (RT). LEI-102 had a RT of 16 min, which was around half that of APD371 (45 min) and CP55,940 (32 min), whereas HU308 had the longest RT at the receptor of 71 min (**Table 4.S2**). Endocannabinoids 2-AG and AEA had the shortest RT, both approximately 7 min. Of note, we found that the association rate constants (k_{on}) varied greatly between the different agonists, ranking from fast to slow engagement CP55,940 > LEI-102 > 2-AG > APD371 > HU308 = AEA. The calculated engagement time (ET) to CB_2R at 1 μM of each agonist further emphasized that CP55,940 arrived at CB_2R within one second, whereas APD371, LEI-102 and 2-AG needed between 16 and 40 s to reach the CB_2R binding site. Interestingly, HU308 and AEA took 143 and 152 s to bind CB_2R, respectively. In view of the distinct target-binding kinetic profiles of the four synthetic CB_2R agonists, we decided to elucidate their binding poses in the CB_2R using cryo-EM.

4.2.3 Overall similar structural comparison of CB_2R-G_i in complex with different agonists

To obtain the stable complex sample of CB_2R-G_i bound with LEI-102, APD371, HU308, or CP55,940, a similar procedure was used as for our previous AM12033-CB_2R-G_i complex preparation (PDB: 6KPF). Single particle analysis of the cryo-EM samples yielded a normal global map for CB_2R-LEI-102-G_i-scFv16, CB_2R-APD371-G_i-scFv16, CB_2R-HU308-

G_i-scFv16 and CB_2R-CP55,940-G_i-scFv16, complex, at 2.9 Å, 3.0 Å, 3.0 Å and 2.9 Å, respectively (**Figure 4.2**, **4.S2-4.S5**, **Table 4.S4**). The ligand, receptor and G protein in the isolated complex were clearly visible in the cryo-EM maps (**Figure 4.2**, **4.S6**). The overall structures of the four complexes were comparable, with root mean square deviation (RMSD) of the Cα atoms of the receptors are around 0.35 Å. The ligand binding interfaces of the four CB_2R and G_i complexes were similar to each other, and to those of the previous AM12033-CB_2R-G_i or WIN55212-2-CB_2R-G_i complex structures.

4.2.4 The binding mode of LEI-102 in CB_2R

A clear electron density in the orthosteric ligand binding pocket in the LEI-102-CB_2R-G_i complex resulted in the unambiguously defined binding pose of LEI-102 (**Figure 4.S6a**). LEI-102 predominantly interacted with the residues in the binding pocket via hydrophobic interactions (**Figure 4.3a**, **4.S7a**). The isobutyl substituent of LEI-102 showed interactions with residues $S90^{2.60}$ (Ballesteros-Weinstein numbering in superscript), $F106^{3.25}$, $K109^{3.28}$, and $I110^{3.29}$ in CB_2R. The imidazolidine-2,4-dione forms π-π interaction with $F94^{2.64}$ and showed further hydrophobic interactions with $F106^{3.25}$ and $P184^{ECL2}$. The benzyl formed an aromatic interaction with $F183^{ECL2}$, and hydrophobic interactions with $F87^{2.57}$ and $S285^{7.39}$. The phenyl ring in the core of LEI-102 formed a cationπ interaction with $F183^{ECL2}$ and T-shaped π-π interaction with $F281^{7.35}$. The pyridine had hydrophobic contacts with $F117^{3.36}$ and $W258^{6.48}$. The aminotetrahydropyran sidechain protruded into the long channel and formed hydrophobic interactions with residues $I110^{3.29}$, $T114^{3.33}$, $I186^{ECL2}$, $Y190^{5.39}$, $L191^{5.40}$, $W194^{5.43}$ and $M265^{6.55}$. Additionally, a hydrogen bond was formed with $T114^{3.33}$ (**Figure 4.S7a**).

4.2.5 The binding mode of APD371 in CB_2R

APD371 mainly formed hydrophobic and aromatic interactions with residues from ECL2, TM2, TM3, TM5, TM6 and TM7 (**Figure 4.3b**, **4.S7b**). The carbonyl group of APD371 formed a putative hydrogen bond with $S285^{7.39}$ and a hydrophobic interaction with $F87^{2.57}$. The pyrazole and pyrazine cores of APD371 formed aromatic interaction with $F183^{ECL2}$. Furthermore, the pyrazine core formed hydrophobic contacts with $T114^{3.33}$, $I186^{ECL2}$, $L191^{5.40}$ and $W194^{5.43}$. The (*S*)-1-hydroxy-3,3-dimethylbutyl head formed hydrophobic contacts with residues $M26^{N\text{-terminus}}$, $S90^{2.60}$, $F94^{2.64}$, $F106^{3.25}$, $I110^{3.29}$ and $V113^{3.32}$. The cyclopropyl group formed hydrophobic contacts with $F117^{3.36}$, $W194^{5.43}$, $W258^{6.48}$ and $V261^{6.51}$.

4.2.6 The binding mode of HU308 in CB_2R

The interactions between HU308 and CB_2R were hydrophobic, including residues from ECL2, TM2, TM3, TM5, TM6 and TM7 (**Figure 4.3c, 4.S7c**). The phenyl of 2,6-dimethoxyphenyl core formed hydrophobic interactions with $F87^{2.57}$, $F183^{ECL2}$ and $S285^{7.39}$, the C2-methoxy formed hydrophobic contacts with $A282^{7.36}$ and $S285^{7.39}$, and the C6-methoxy formed

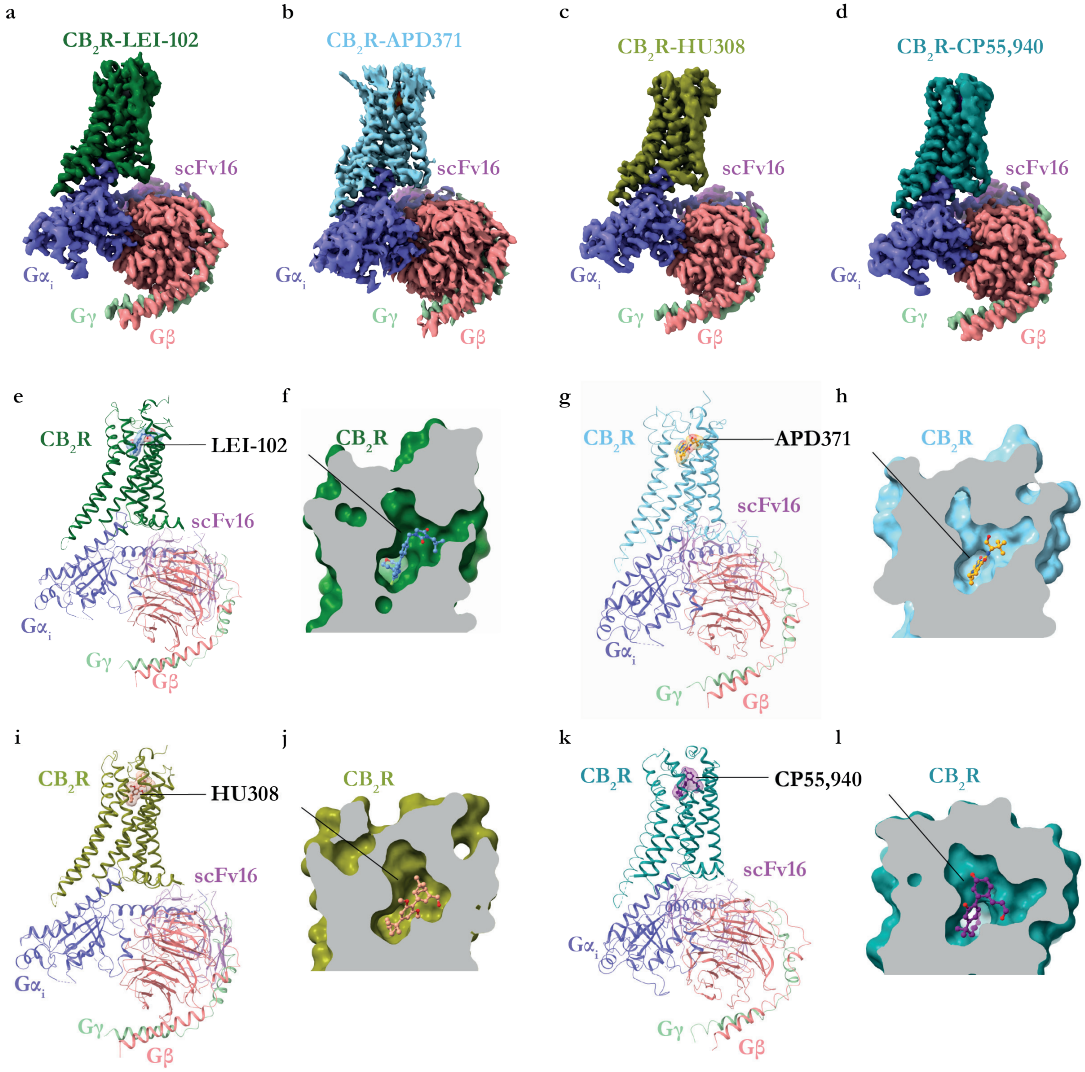

Figure 4.2 Cryo-EM structures of CB_2R-G_i complexes.
Cryo-EM density maps of (a) LEI-102 (Dark green), (b) APD371 (Sky blue), (c) HU308 (Olive), and (d) CP55,940 (Teal) bound CB_2R in complex with $G\alpha_i$ (Slate), Gβ (Salmon), Gγ (Pale green), scFv16 (Violet purple). (e–l) Overall structures of CB_2R-G_i complexes and enlarged view of orthosteric pocket of (f) LEI-102, (h) APD371, (j) HU308, and (l) CP55,940 using the same color codes as (a–d), with agonists shown as cornflower blue (LEI-102), orange (APD371), dark salmon (HU308) and purple (CP55,940) sticks, respectively.

hydrophobic contacts with $I110^{3.29}$, $V113^{3.32}$ and $T114^{3.33}$, respectively. The dimethylheptyl chain of HU308 extended into the long channel and formed hydrophobic interactions with residues from ECL2 ($F183^{ECL2}$), TM3 ($T114^{3.33}$, $F117^{3.36}$), TM5 ($W194^{5.43}$). The 1,1-dimethyl formed hydrophobic interactions with residues $F87^{2.57}$, $F117^{3.36}$, $F281^{7.35}$ and $S285^{7.39}$. The bicyclic head of HU308 formed hydrophobic interactions with $M26^{N\text{-terminus}}$, $F106^{3.25}$, $I110^{3.29}$, $S90^{2.60}$, $F94^{2.64}$, $P184^{ECL2}$ and the 2-methanol formed a hydrophobic interaction with $F94^{2.64}$ (**Figure 4.S7c**).

4.2.7 The binding mode of CP55,940 in CB_2R

CP55,940 adopted an L-shape conformation in the orthosteric binding pocket (**Figure 4.3d**, **4.S6d**). The cyclohexanol group formed hydrophobic interactions with F94$^{2.64}$, L182^{ECL2}, F183^{ECL2}, and P184^{ECL2}. The hydroxyl group established a hydrogen bond with L182^{ECL2} and the hydroxypropyl formed hydrophobic contacts with F87$^{2.57}$, S90$^{2.60}$, F91$^{2.61}$, I110$^{3.29}$, and V113$^{3.32}$. The phenol core formed hydrophobic interactions with F87$^{2.57}$, F183^{ECL2}, F281$^{7.35}$ and S285$^{7.39}$, and its hydroxyl additionally formed a hydrogen bond with S285$^{7.39}$. The dimethyl formed hydrophobic interactions with F183^{ECL2}, F281$^{7.35}$, M265$^{6.55}$, F87$^{2.57}$, F117$^{3.36}$ and C288$^{7.42}$. The dimethylheptyl alkyl chain of CP55,940 extended into the long channel and formed hydrophobic interactions with residues I110$^{3.29}$, F183^{ECL2}, I186^{ECL2}, W194$^{5.43}$, T114$^{3.33}$ and F117$^{3.36}$ (**Figure 4.S7d**).

4.2.8 LEI-102 and APD371 require H95$^{2.65}$ for G Protein activation in CB_2R

To study the mechanism of CB_2R activation, five residues in the binding pocket were further characterized based on the complex structures (**Figure 4.3**). Six CB_2R mutants were created, *i.e.* four residues (S285$^{7.39}$, H95$^{2.65}$, I110$^{3.29}$ and F117$^{3.36}$) were replaced by alanine, as these are conserved between CB_2R and CB_1R, and two others (I110$^{3.29}$, V261$^{6.51}$) were substituted by the hCB_1R reciprocal residue leucine. All mutants were sufficiently expressed at the cell surface as determined with an ELISA (**Figure 4.S8**, **Table 4.S5**). To characterize the binding mechanisms of LEI-102, APD371, HU308 and CP55,940, their responses were investigated by [^{3}H]CP55,940 displacement and [^{35}S]GTPγS binding assays. Of note, in the [^{3}H]CP55,940 displacement assay, only the CB_2R-I110$^{3.29}$L mutant showed a sufficient binding window (data not shown). This prevented the affinity determination of the four agonists on other mutant receptors. Five mutant receptors, except CB_2R-F117$^{3.36}$A, were still active in the [^{35}S]GTPγS functional assay, thereby allowing us to study the receptor activation mechanism (**Figure 4.4a-d**, **Table 4.S6**). All four synthetic agonists were unable to activate CB_2R-F117$^{3.36}$A, which indicated an important role of this residue in the activation of CB_2R.

The potency of LEI-102 was significantly increased at the CB_2R-I110$^{3.29}$L mutant to a pEC_{50} value of 7.8 ± 0.1 in the G protein activation assay, while the binding affinity remained similar to wild type (WT) receptor (**Figure 4.4a**, **Table 4.S6**, **4.S7**). Three mutations CB_2R-I110$^{3.29}$A, CB_2R-S285$^{7.39}$A and CB_2R-V261$^{6.51}$L had no significant effect on the potency of LEI-102 in the functional assay. In contrast, the potency on mutant receptor CB_2R-H95$^{2.65}$A was significantly reduced for LEI-102. No gain in binding affinity for the swap mutant in CB_1R-L359$^{6.51}$V was found with LEI-102 (**Table 4.S3**, **4.S8**).

APD371 acted as a full CB_2R agonist with a pEC_{50} value of 7.9 ± 0.1 and a higher maximal activation compared to that of CP55,940 in the functional assay (**Table 4.S2**). Mutant receptor CB_2R-I110$^{3.29}$L did not affect the G protein response of APD371 (**Figure 4.4b**, **Table 4.S6**), while the binding affinity was significantly reduced to a pK_i of 7.1 ± 0.0 (**Table 4.S7**). APD371 potency was not affected by mutant receptors CB_2R-I110$^{3.29}$A or CB_2R-S285$^{7.39}$A. The responses of APD371 for CB_2R-H95$^{2.65}$A and CB_2R-V261$^{6.51}$L were significantly impacted with 158-fold and 10-fold drop in potency, respectively (**Table 4.S6**).

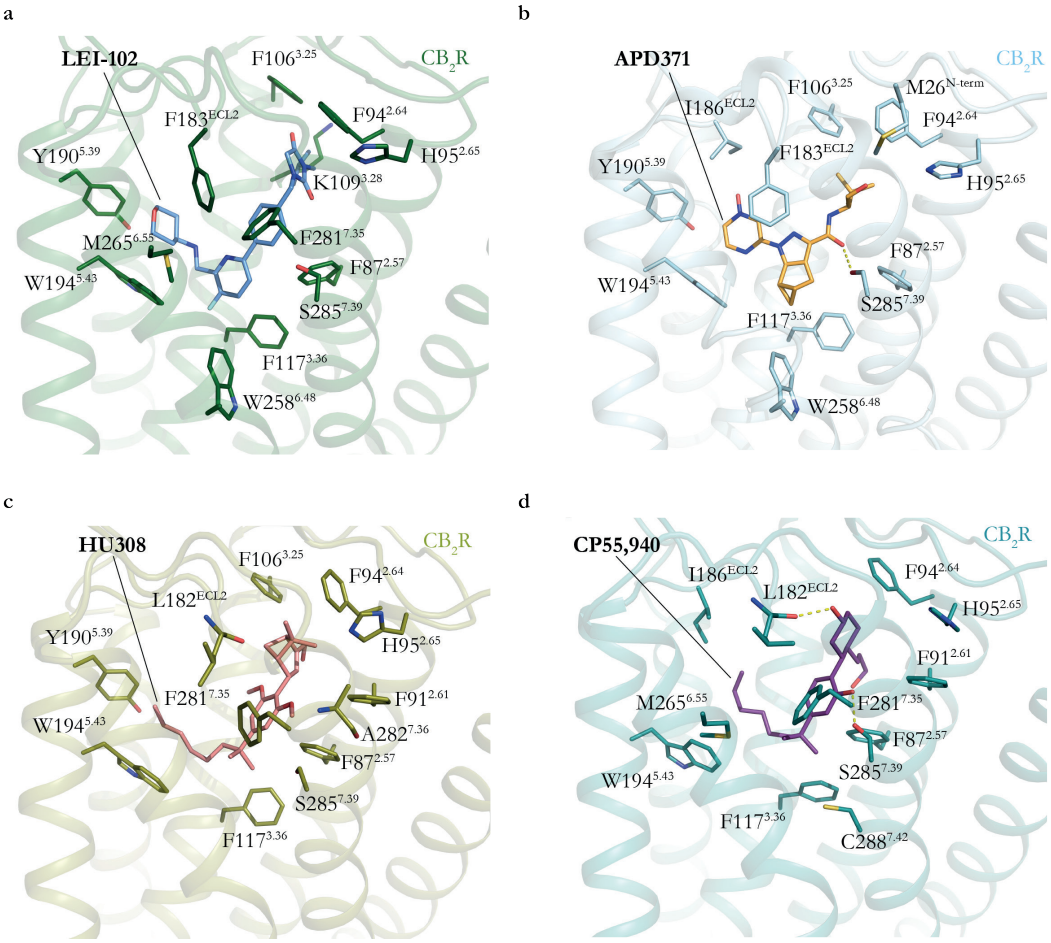

Figure 4.3 **Key interactions between CB_2R and agonists.**

Key residues involved in **a** LEI-102, **b** APD371, **c** HU308, and **d** CP55,940 binding in CB_2R-G_i complex structures. The amino acids involved in interactions are shown as sticks, hydrogen bonds are highlighted with yellow dashed lines. Same color codes as in **Figure 4.2**.

Thus, we uncovered a crucial role for CB_2R-H95$^{2.65}$ in G protein activation of CB_2R by LEI-102 and APD371. It's role in stabilizing Furthermore, LEI-102 activation was increased for the CB_2R-I110$^{3.29}$L mutant, while APD371 activation relied on CB_2R-V261$^{6.51}$.

4.2.9 An important role for S285$^{7.39}$ and V261$^{6.51}$ in CB_2R activation by HU308 and CP55,940

The potency and affinity of HU308 on CB_2R were not affected by the CB_2R-I110$^{3.29}$L swap mutant (**Figure 4.4c**, **Table 4.S6**, **4.S7**). In addition, activation of mutant receptors CB_2R-I110$^{3.29}$A and CB_2R-H95$^{2.65}$A by HU308 was not affected with pEC_{50} values of 6.4 ± 0.5 and 6.6 ± 0.6, respectively. The maximum activation level of mutant receptor CB_2R-S285$^{7.39}$A was unaffected compared to WT receptor, but a significant 15-fold loss in potency was

observed. Lastly, CB_2R-V261$^{6.51}$L had a significant loss of potency, *i.e.* more than 120-fold lower (**Figure 4.4c**, **Table 4.S6**).

Similar to HU308, the potency of CP55,940 on CB_2R was not affected by the CB_2R-I110$^{3.29}$ mutations compared to WT in the G protein activation assay, nor was its binding affinity for CB_2R-I110$^{3.29}$L (**Figure 4.4d**, **Table 4.S6**, **4.S7**). In response to CP55,940, mutant receptors CB_2R-S285$^{7.39}$A and CB_2R-V261$^{6.51}$L were significantly affected with decreased pEC_{50} values of 6.7 ± 0.1 and <5, respectively. Moreover, the potency of CP55,940 was significantly affected on the CB_2R-H95$^{2.65}$A with a 40-fold decrease compared to WT receptor (**Figure 4.4d**, **Table 4.S6**). No gain in potency or affinity was observed for the swap mutant CB_1R-L359$^{6.51}$V for either HU308 or CP55,940 (**Table 4.S3**, **4.S8**).

Taken together, this showed that CB_2R-S285$^{7.39}$ and CB_2R-V261$^{6.51}$ were crucial for HU308 and CP55,940 to activate the G protein at CB_2R, where CP55,940 additionally required an interaction with CB_2R-H95$^{2.65}$.

4.2.10 HU308 and endocannabinoids gain access via membrane entry

Our detailed ligand-target binding kinetic analysis revealed that the highly lipophilic HU308 and anandamide had a very slow on-rate compared to the other ligands. Since it has previously been postulated that ligands of lipid receptors may gain access to the binding pocket via a membrane channel, we examined two potential ligand entry pathways at CB_2R, *i.e.* either via ECL2 or via a membrane channel in TM1 and TM7. To this end, four additional mutant receptors were created. Three residues in the ECL2 of CB_2R, which were different from CB_1R, were mutated towards the reciprocal CB_1R residues, *i.e.* CB_2R-L185^{ECL2}H, CB_2R-L182^{ECL2}I and CB_2R-E181^{ECL2}D. In the fourth mutant receptor, four residues in TM1 and TM7 that align the potential membrane channel in CB_2R were mutated to the reciprocal CB_1R residues and combined as a quadruple mutant, *i.e.* CB_2R-K279$^{7.33}$T, CB_2R-K33$^{1.32}$Q, CB_2R-V36$^{1.35}$I and CB_2R-C40$^{1.39}$S (termed "CB_2R-Quadruple^{TM1,7}"). Next, we tested all four synthetic agonists and the two endocannabinoids on these four CB_2R mutant receptors in [^{3}H]CP55,940 and [^{35}S]GTPγS assays. Only CB_2R-L185^{ECL2}H and CB_2R-Quadruple^{TM1,7} were evaluated in the [^{3}H]CP55,940 displacement assays due to insufficient binding window for the other two mutant receptors (data not shown). The binding affinities of the agonists were not affected for mutant receptors CB_2R-L185^{ECL2}H and CB_2R-Quadruple^{TM1,7} (**Table 4.S7**). Interestingly, the potencies of LEI-102, APD371 and CP55,940 in the functional assay were not significantly affected for any of the mutant receptors, whereas HU308 and the endocannabinoids were less potent on CB_2R-L182^{ECL2}I (**Figure 4.4e-j**, **Table 4.S6**). Additionally, the endocannabinoids showed a decreased potency on CB_2R-L181^{ECL2}D, but not on CB_2R-L185^{ECL2}H. Of note, HU308 and both endocannabinoids completely lost their ability to activate CB_2R in the CB_2R-Quadruple^{TM1,7} mutant, suggesting that this may be an important access point to the receptor binding pocket for these agonists (**Figure 4.4g**,**i-j**).

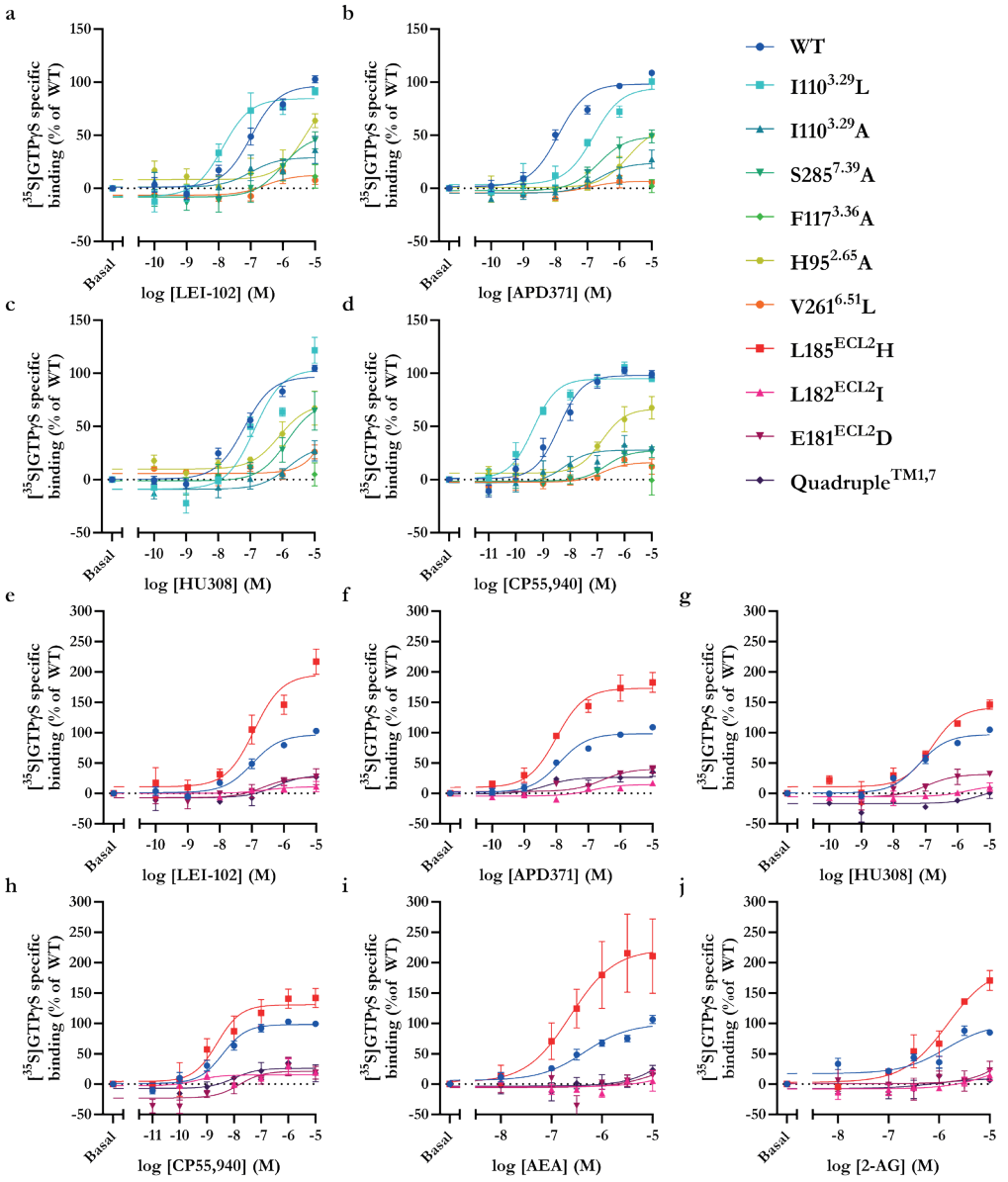

Figure 4.4 Characterization of G protein activation of wild type (WT) and mutant CB_2R by synthetic agonists and endocannabinoids.

Dose-response curves for G protein activation of WT and mutants that are located in the CB_2R binding pocket by (a) LEI-102, (b) APD371, (c) HU308, and (d) CP55,940. (e–j) Dose response curves for G protein activation of WT and mutants that are proposed to be involved in ligand entry of CB_2R via either the ECL2 or membrane access by (e) LEI-102, (f) APD371, (g) HU308, (h) CP55,940, (i) AEA and (j) 2-AG. (a–j) The maximum activation level of WT CB2R was set to 100% while the basal levels were set to 0%. Data are presented as mean ± SEM of at least three individual experiments performed in duplicate.

4.2.11 LEI-102 attenuates cisplatin-induced nephrotoxicity without CB_1R-mediated side effects

In view of the excellent physico-chemical properties of LEI-102 and its selective CB_2R agonist profile, we investigated the compound in a well-established *in vivo* model of kidney inflammation and injury induced by cisplatin. In this model CB_2R activation is associated with protective effects[29]. Cisplatin (25 mg/kg, i.p.) induced marked elevations of serum creatinine and blood urea nitrogen levels (functional markers of kidney injury) 72 h following cisplatin injection in wild type mice compared with vehicle-treated control animals. LEI-102 showed a dose-dependent attenuation of the functional markers of cisplatin-induced kidney injury both when administered p.o. (orally) or i.p. (**Figure 4.5a**). Renal dysfunction was also accompanied by morphological damage to the kidney tubules determined by histological examination following PAS staining. LEI-102 (10 mg/kg) significantly decreased tubular injury as determined by this staining (**Figure 4.5b**). Marked increases in oxidative and nitrative stress markers (4-HNE and 3-nitrotyrosine) were observed in kidneys of cisplatin-treated mice determined by immunostaining and quantitative ELISA. Furthermore, LEI-102 (10 mg/kg by i.p. or p.o.) decreased lipid peroxidation and protein nitration (**Figure 4.5c**,**d**). Additionally, the pro-inflammatory cytokines TNFα and IL1β that were elevated due to the cisplatininduced injury were attenuated in LEI102 treated mice (**Figure 4.5e**). Importantly, the protective effects of LEI-102 against cisplatin-induced renal dysfunction and tubular damage (**Figure 4.5f**), histopathological injury (**Figure 4.5g**) and markers of oxidative-nitrative stress (**Figure 4.5h,i**) were abolished in CB_2R knockout mice, which had enhanced kidney injury/dysfunction compared to their wild types.

To determine whether LEI-102 maintained its selectivity for CB_2R over CB_1R *in vivo*, LEI-102 was tested in the mouse tetrad assay for CB_1R activity[18]. In this assay, four consecutive behavioral tests, related to anti-nociception, hypothermia, catalepsy, and spontaneous activity, were performed 120 min after administration of the agonist. LEI-102 (25 mg/kg, p.o.) did not produce any effects in the tetrad assay as compared with vehicle. There were no effects on nociceptive behavior assessed in tail withdrawal test nor on body temperature

→ Figure 4.5 CB_2R agonist LEI-102 attenuates cisplatin-induced renal dysfunction, oxidative stress, and inflammation in a CB_2R-dependent manner.
(a) Cisplatin-induced renal dysfunction 72 h after administration to mice as evidenced by increased serum levels of blood urea nitrogen (BUN) and creatinine (CREA), which were attenuated by CB_2R agonist LEI-102 in a dose-dependent manner when administered either i.p. or p.o. (*$p < 0.001$ vs. vehicle group, #$p < 0.001$ vs. cisplatin group). (b) Periodic Acid-Schiff (PAS) staining in representative kidney sections from cisplatin treatment samples showing protein cast, vacuolation, and desquamation of epithelial cells in the renal tubules which are attenuated with LEI-102. Tubular damage score from kidney sections is shown (*$p < 0.001$ vs. vehicle group, #$p < 0.001$ vs. cisplatin group). (c) The cisplatin-induced nitrative and oxidative stress (nitrotyrosine staining (top row) and HNE staining (bottom row)) in representative kidney sections were also attenuated by LEI-102. (d) This was confirmed by quantitative determination of protein nitration and HNE adducts formation by ELISA (*$p < 0.001$ vs. vehicle group, #$p < 0.001$ vs. cisplatin group). (e) The cisplatin-induced kidney pro-inflammatory cytokine expressions were also attenuated by the CB2R agonist. (*$p < 0.001$ vs. vehicle group, #$p < 0.05$ vs. cisplatin group). (f) The protective effects of LEI-102 on cisplatin-induced kidney dysfunction (BUN and CREA) and tubular injury (tubular damage score) (*$p < 0.001$ vs. vehicle WT or KO group, #$p < 0.05$ vs. cisplatin WT group), histopathological injury (g), nitrative (h) and oxidative stress (i) were abolished in CB_2R knockout mice. All results are means ± SEM of $n = 6$/group for panels (a, b, d, e, f). Closed and open symbols are used for male and female mice respectively (4 males and 2 females/group). In panels (a, b, d), and (e) one-way ANOVA followed by Tukey's post hoc test for multiple comparisons were used, in panel f unpaired two-tailed t-test was used. $p < 0.05$ was considered statistically significant.

(**Figure 4.6 upper row**). No effect was found on locomotor behavior (**Figure 4.6 lower row**) in case of distance travelled, time spent mobile, or running speed of mice. Nor was catalepsy observed following administration of LEI-102. These results indicated that LEI-102 (or one of its metabolites) did not produce CB_1R-mediated CNS-side effects at doses up to 25 mg/kg (p.o.). Hence, the CB_2R agonist LEI-102 maintained its selectivity over CB_1R *in vivo*.

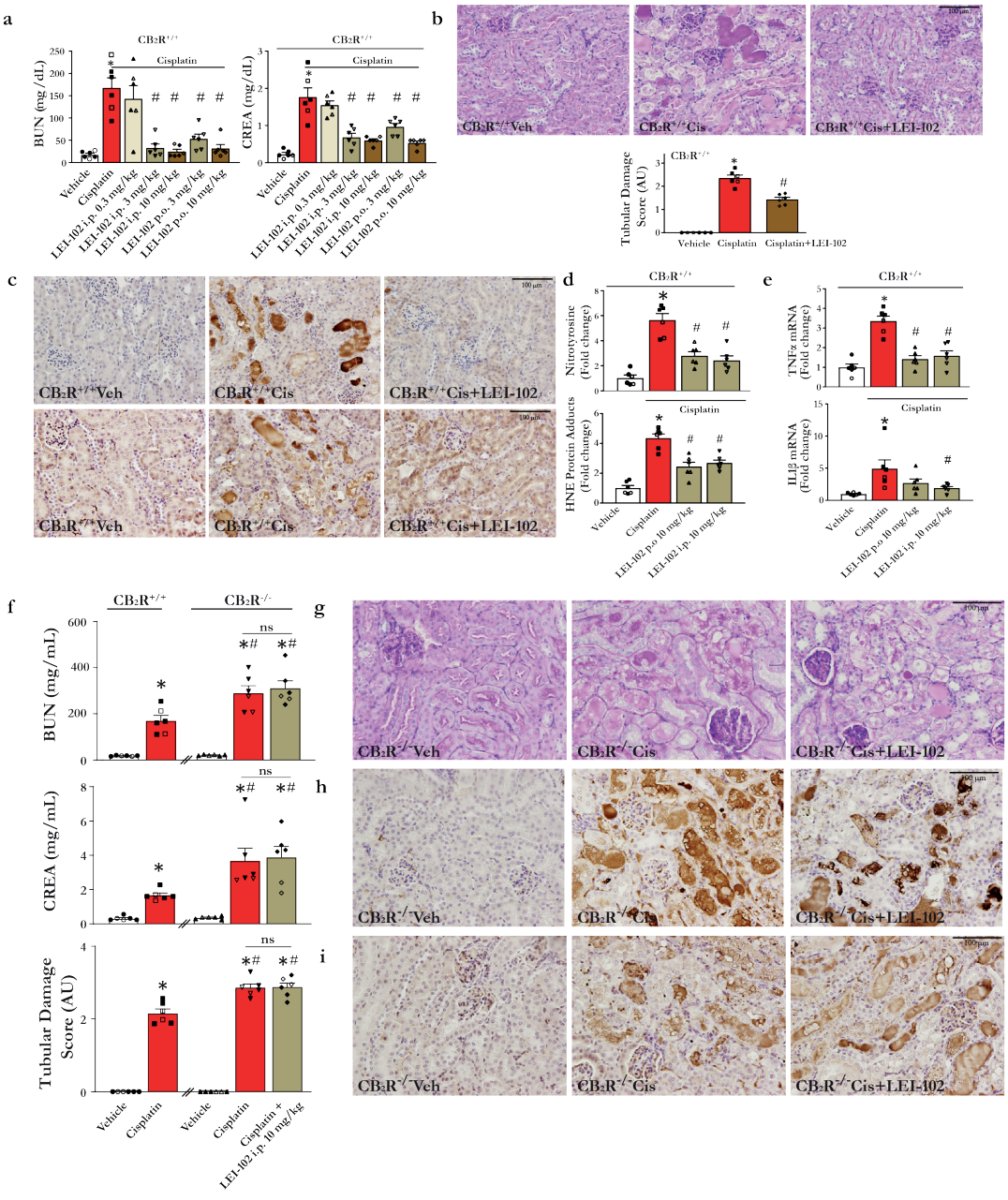

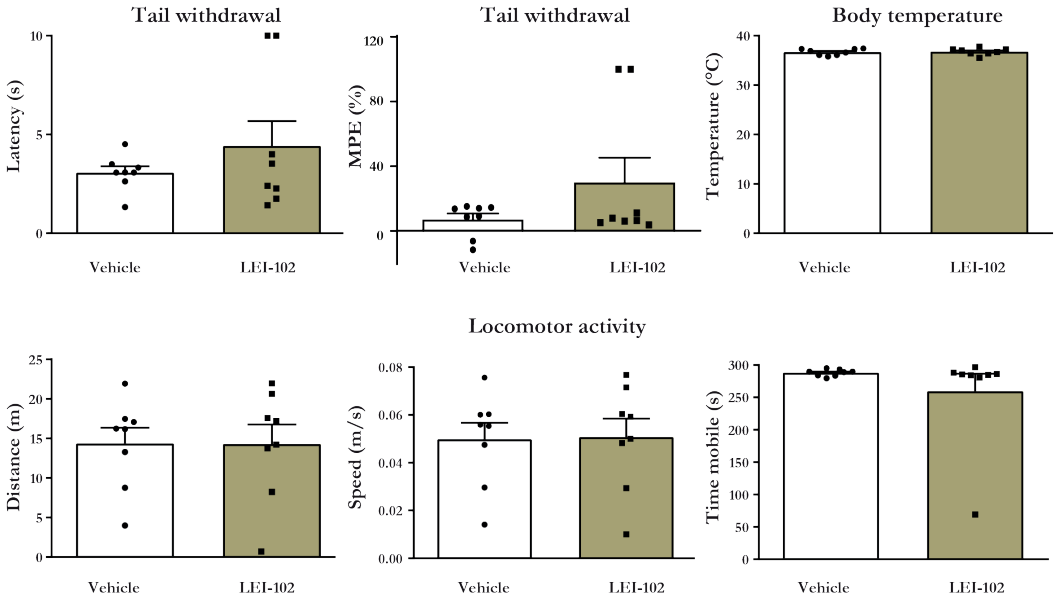

Figure 4.6 The CB_2R agonist LEI-102 does not induce cannabimimetic CB_1R-mediated effects (Tetrad assay) *in vivo*.
LEI-102 (25 mg/kg, p.o.) did not affect nociceptive behavior assessed in tail withdrawal test and body temperature, as compared with mice receiving vehicle (upper row). No effects on locomotor behavior were found (lower row). Results are means ± SEM; n = 8 per group.

4.3 Discussion

So far, several crystal and cryo-EM CBR structures have been resolved in which non-selective agonists adopt a nearly identical binding position in the orthosteric pocket, regardless of the receptor[34–38]. In this study, we aimed to generate a better understanding of the binding and activation mechanism of CB_2R-selective agonists. Therefore, we combined ligand-target binding kinetics, site-directed mutagenesis, and cryo-EM studies to investigate the activation mechanism of CB_2R for the introduced CB_2R selective agonist LEI-102 supplemented with agonists APD371, HU308 and CP55,940 on a molecular level. Furthermore, we investigated potential hotspots for CB_2R/CB_1R selectivity by creating swap mutants and discovered a ligand entry pathway for CBR agonists and endocannabinoids.

First, our data revealed a crucial role for CB_2R-F117$^{3.36}$ as replacement by alanine resulted in a complete loss of G protein activation by all tested agonists (**Figure 4.4a-d**, **Table 4.S6**). It has been shown that the CB_1R counterpart F200$^{3.36}$ plays an important regulatory role in activation as part of the "twin toggle switch" with CB_1R-W356$^{6.48}$ [39]. In contrast, CB_2R-W258$^{6.48}$ has been described to be solely responsible for activation as a toggle switch without the help of CB_2R-F117$^{3.36}$ in structural studies, since the conformation of CB_2R-F117$^{3.36}$ in agonist-bound structures is comparable to the conformation in the antagonist-bound CB_2R structure as well as the CB_1R agonist-bound structures[33,36]. Our mutational data further supports this hypothesis, as we do not see the same constitutive

activity pattern (**Table 4.S6**) as observed by McAllister *et al.* for the reciprocal CB_1R-F220$^{3.36}$ excluding CB_2R-F117$^{3.36}$ from a suppressive function[39]. Together, this data provides strong support for a different, but important, role for F117$^{3.36}$ in CB_2R activation.

In CB_1R, water-mediated interactions between CB_1R-H178$^{2.65}$, CB_1R-S383$^{7.39}$ and bound ligands have previously been shown with *in silico* modelling[40,41]. The importance of CB_1R-S383$^{7.39}$ for classical synthetic cannabinoids such as AM11542, AM841 and CP55,940 was further emphasized in CB_1R-S383$^{7.39}$A mutants[36]. This is in line with the observation that removal or methylation of the phenolic OH on classical cannabinoids, such as in L-759656, JWH-133 and HU308, always affords selectivity over CB_1R[18,42]. Non-classical agonists, such as WIN55,212-2, do not form a hydrogen bond with CB_1R-S383$^{7.39}$ and consequently are not affected by an alanine mutation[43]. This translates to our results that CP55,940 and HU308 are more affected by the CB_2R-S285$^{7.39}$A mutation than LEI-102 and APD371 (**Figure 4.4a-d**, **Table 4.S3**). The decrease in activation is at least 30-fold smaller for CB_2R than CB_1R[36]. The elucidated cryo-EM structures of our four agonists did not show direct interactions with CB_2R-H95$^{2.65}$, though we cannot rule out its role in stabilizing the surrounding residues. The large effect seen on G protein activation of CB_2R-H95$^{2.65}$A by LEI-102, APD371 and CP55,940 (**Figure 4.4a-d**, **Table 4.S6**) must therefore stem from an indirect interaction, supporting the polar network hypothesis between CB_2R-H95$^{2.65}$ and CB_2R-S285$^{7.39}$ in CB_2R.

Residues at position 6.51 have previously been described to be involved in the binding sites of μ, δ, and ϰ opioid receptors, the dopamine D2 receptor and adenosine receptors, and could play a role in ligand binding selectivity between different subtypes[44–46]. In our studies, introduction of the bulkier CB_1R leucine on this position in CB_2R-V261$^{6.51}$L reduced the G protein activation by APD371, HU308 and CP55,940, while LEI-102 could still be accommodated in the binding pocket (**Figure 4.4a-d**, **Table 4.S6**). Furthermore, with the swap mutant CB_1R-L359$^{5.61}$V we found a trend in partial recovery of displacement of [^{3}H]CP55,940 by the CB_2R selective agonists LEI-102, HU308 and APD371, although not significant (**Table 4.S3**). This supports a role of this residue in selectivity of agonists in CB_2R.

The ECL2 has frequently been implicated to be important for GPCR activation and some GPCRs even use their ECL2 as a ligand to auto-activation[47]. There are distinct differences between the conformations of ECL2 in CB_1R and CB_2R. In antagonist-bound CB_1R crystal structures, the ECL2 dips into the binding pocket, interacting with the ligand and inducing the inactive conformation[31,32]. The inactive state of CB_2R, however, does not expand like CB_1R and instead the ECL2 acts more as a lid on the binding pocket in active and inactive CB_2R, akin to active CB_1R[33]. A key distinction seen in the CB_1R crystal structures with AM6538 and taranabant, is the ionic lock formed by CB_1R-E100$^{N\text{-terminus}}$ (CB_2R-L17) and CB_1R-H270^{ECL2} (CB_2R-L185)[31,32]. We observed improved binding of [^{3}H]CP55,940 for LEI-102 and HU308 with the CB_1R-H270^{ECL2}L mutation, while the non-selective agonists showed no change (**Table 4.S3**). Through the loss of this ionic lock, selectivity over CB_1R is partially lost, showing that expulsion of ECL2 upon ligand entry may play an important role in selectivity.

In recent years, computational studies have suggested that lipophilic ligands for various GPCRs, such as the opsin receptor, sphingosine-1-phosphate receptor 1 ($S1P_1$) and cannabinoid receptors, might gain access to the binding pocket through lateral diffusion via a membrane channel between TM1 and TM7[32,41,48–51]. We experimentally examined this membrane entry pathway by creating a CB_2R quadruple mutant ($K33^{1.32}Q$, $V36^{1.35}I$, $C40^{1.39}S$ and $K279^{7.33}T$) for which we observed a significant loss of potency and a corresponding trend in reduced affinity, although not significant, for HU308 and the endocannabinoids (**Figure 4.4e-j**, **Table 4.S6**, **4.S7**). These compounds are more lipophilic than LEI-102 and APD371, making them more suitable to traverse the membrane to enter between TM1 and TM7. Notably, HU308 and anandamide also showed a substantially longer ET in our assays compared to the other agonists (**Table 4.S2**). This might suggest a possible relationship between a slower association and membrane channel entry at the CB_2R. Likewise, for a peptide GPCR a trend in reduced association rate was found with increasing lipophilicity[52]. Nevertheless, this is in contrast with the mechanism at the α_2-adrenoceptor at which lipophilic compounds had a faster association rate[53]. This shows the diversity in drug-target binding kinetics as receptor-specific properties and thus the importance of investigating these mechanisms for individual receptors[54].

The discovery of a membrane access channel for endocannabinoids on the CB_2R is also intriguing from a physiological perspective. Endocannabinoids are produced on demand and act as autocrine or paracrine effectors in the immune system regulating the migration of CB_2R-expressing immune cells[17]. Our results suggest that endocannabinoids first have to travel through the plasma membrane via lateral diffusion to reach the receptor. This may suggest that the trafficking and cellular uptake of endocannabinoids could be regulated through extracellular or intracellular vesicles that merge with the plasma membrane. Regardless of the exact mechanism of endocannabinoid trafficking, this study provides experimental evidence of a membrane channel located between TM1 and TM7 in CB_2R that is being used by the endocannabinoids to enter the receptor.

The ligands of the CB_2R, such as the phytocannabinoids and endocannabinoids, are typically very lipophilic, which comes at a cost of reduced solubility, increased off-target activity and poor pharmacokinetic properties[10,25]. Thus, balancing lipophilicity of a drug candidate is an important goal in medicinal chemistry. The first generation of experimental drugs targeting the CB_2R mimicked the plant-based cannabinoids. Consequently, they were highly lipophilic and suffered from poor clinical translation[10]. New generations of CB_2R agonists have optimized physico-chemical properties. For instance, LEI-102 and APD371 are orders of magnitude more hydrophilic than HU308. Remarkably, they can bind the same binding pocket in CB_2R as HU308. Our data revealed that LEI-102 and APD371 do not enter the receptor via the membrane channel like HU308, but gain access most likely via the extracellular space. LEI-102 and APD371 also form a specific (indirect) polar interaction network with $H95^{2.65}$ to activate CB_2R, which is not observed for HU308. This flexibility of the CB_2R binding pocket to be activated by a diverse set of chemotypes allows to select for a chemotype with more drug-like properties. This notion is supported by the oral efficacy of LEI-102 in the chemotherapy-induced nephropathy model and lack of CNS-adverse side effects (**Figure 4.5**, **4.6**).

Targeting CB_2R with agonists is a promising avenue for the treatment of autoimmune diseases, neuroinflammation and various forms of tissue injury/inflammation/fibrosis in the liver, heart, brain, and kidney[17]. In this study we show that LEI-102 protects against cisplatin-induced nephropathy in a CB_2R-dependent manner by attenuating kidney inflammation and injury (**Figure 4.5**). We also show that CB_2R knockout mice develop more severe nephropathy compared to their wild types suggesting protective role of endocannabinoid-CB_2R signaling during kidney injury. These results are consistent with protective effects of CB_2R agonists in various models of kidney injury/diseases and deleterious effect of CB_2R deletion in these models[29,55–63].

In conclusion, we have discovered LEI-102 as a selective CB_2R agonist that is efficacious in attenuating tissue injury in chemotherapy-induced nephropathy model without inducing CNS-mediated side effects. Using LEI-102 and five other CBR agonists we have shown that the physicochemical properties determine not only pharmacokinetic properties of ligands, but also how they engage with their target. Altogether, we elucidated several important molecular mechanisms for selective engagement and activation of the CB_2R, which may have implications for drug design and lipid signaling at GPCRs in general.

4.4 Materials and methods

4.4.1 General materials for functional assays

Monoclonal M2 mouse anti-FLAG primary antibody (#F3165) was purchased from Sigma-Aldrich (Zwijndrecht, the Netherlands), while secondary goat anti-mouse HRP-conjugated antibody (#115-035-003) was bought from Jackson ImmunoResearch Laboratories (West Grove, PA, USA). Bicinchoninic acid (BCA) ad BCA protein assay reagent was obtained from Pierce Chemical Company (Rockford, IL, USA). [^{3}H]RO6957022 (specific activity 82.83 Ci mmol^{-1}) was custom synthesized at F. Hoffman-La Roche Ltd (Basel, Switzerland). [^{35}S]GTPγS (specific activity 1250 Ci mmol^{-1} #NEG030H250UC), [^{3}H]CP55,940 (specific activity 108.5 Ci mmol^{-1} #NET1051250UC) and GF/C filter plates (#6055690) were purchased from Revvity (Waltham, MA, USA). CP55,940 (#C1112), AM630 (#SML0327) and DL-dithiothreitol (DTT, #646563) were obtained from Sigma-Aldrich, HU308 (#H800010) was from LKT Laboratories (St. Paul, MN, USA), APD371 was provided by F. Hoffmann-La Roche Ltd, anandamide (AEA, #1339), 2-Arachidonylglycerol (2-AG, #1298) and phenylmethylsulfonyl fluoride (PMSF, #4486) were purchased from Tocris Bioscience (Bristol, UK) and GDP (#J61646) was from Thermo Fisher Scientific (Waltham, MA, USA). All buffers and solutions were prepared using Millipore water (deionized using a MilliQ A10 Biocel with a 0.22 μm filter) and analytical grade reagents and solvents. Buffers are prepared at room temperature (rt) and stored at 4 °C, unless stated otherwise.

4.4.2 Cell lines

Spodoptera frugiperda (*Sf*9) cells were used for CB_2R-G_i co-expression for cryo-EM studies. *Sf*9 cells were grown in ESF 921 medium (Expression systems) at 27 °C and 125 rpm.

For transfections, human embryonic kidney 293 T (HEK293T; female, ATCC #CRL-3216) cells were grown as monolayers in culture medium i.e. Dulbecco's Modified Eagle's Medium (Sigma-Aldrich #6546), supplemented with 10% fetal calf serum (Sigma-Aldrich #F7524), 2 mM L-glutamine (Sigma-Aldrich #G8541), 100 IU/mL penicillin and 100 μg/mL streptomycin (Duchefa Biochemie #P0142 and #S0148) under a humidified atmosphere at 37 °C with 5% CO_2. Subculture was done twice a week at 80 - 90% confluence on 10 cm ø plates by trypsinization. CHO cells stably expressing hCB_2R (CHOK1_hCB_2bgal; PathHunter EA Parental Cell line, female, DiscoverX #93-0706C2) or hCB_1R (CHOK1_ hCB_1bgal; PathHunter EA Parental Cell line, female, DiscoverX #93-0959C2) were cultured in Ham's F12 Nutrient Mixture (Sigma-Aldrich #4888) supplemented with 10% fetal calf serum, 2 mM L-glutamine, 100 IU/mL penicillin, 100 μg/mL streptomycin, 300 μg/mL hygromycin (Bio-Connect #ANT-HG-5) and 800 μg/mL G418 (Bio-Connect #SC-29065B) in a humidified atmosphere at 37 °C with 5% CO_2. Cells were subcultured twice a week when reaching 80 - 90% confluence on 10 or 15 cm ø plates by trypsinization.

*4.4.3 Synthesis of LEI-102 (***Figure 4.S1***)*

All reagents and solvents were purchased from commercial sources and were of analytical grade (Sigma-Aldrich, BroadPharm®). Reagents and solvents were not further purified before use. All moisture sensitive reactions were performed under inert atmosphere. Solvents were dried using 4 Å molecular sieves prior to use when anhydrous conditions were required. Water used in reactions was always demineralized. Analytical Thin-layer Chromatography (TLC) was routinely performed to monitor the progression of a reaction and was conducted on Merck Silica gel 60 F254 plates. Reaction compounds on the TLC plates were visualized by UV irradiation (λ_{254}) and/or spraying with potassium permanganate solution (K_2CO_3 (40 g), $KMnO_4$ (6 g), and H_2O (600 mL)), ninhydrin solution (ninhydrin (1.5 g), n-butanol (100 mL) and acetic acid (3.0 mL)) or molybdenum solution ($(NH_4)_6MO_7{\cdot}4H_2O$ (25 g/L) and $(NH_4)_4Ce(SO_4)4{\cdot}H_2O$ (10 g/L) in sulfuric acid (10%)) followed by heating as appropriate. Purification by flash column chromatography was performed using Screening Devices B.V. silica gel 60 (40-63 μm, pore diameter of 60 Å). Solutions were concentrated using a Heidolph laborata W8 4000 efficient rotary evaporator with a Laboport vacuum pump.

Analytical purity was determined with Liquid Chromatography-Mass Spectrometry (LC-MS) using a Finnigan LCQ Advantage MAX apparatus with electrospray ionization (ESI), equipped with a Phenomenex Gemini 3 μm NX-C18 110Å column (50x4.6mm), measuring absorbance at 254 nm using a Waters 2998 PDA UV detector and the m/z ratio by using an Acquity Single Quad (Q1) detector. Injection was with the Finnigan Surveyor Autosampler Plus and pumped through the column with the Finnigan Surveyor LC pump plus to be analyzed with the Finnigan Surveyor PDA plus detector. Samples were analyzed using eluent gradient 10% → 90% ACN in MilliQ water (+ 0.1% TFA (v/v)).

For purification by mass guided preparative High-Performance Liquid Chromatography (Prep-HPLC) the Waters AutoPurification HPLC/MS apparatus was used with a Gemini prep column 5 μm 18C 110 Å (150x21.2mm), Waters 2767 Sample manager, Waters 2545 Binary gradient module, Waters SFO System fluidics organizer, Waters 515 HPLC pump M,

Waters 515 HPLC pump L attached to a Waters SQ detector Acquity Ultra performance LC.

^{1}H, ^{13}C, ^{1}H-COSY and HSQC Nuclear Magnetic Resonance (NMR) spectra were recorded on a Bruker AV 300 (300/75 MHz), AV 400 (400/100 MHz) or AV 500 (500/125 MHz) spectrometer at ambient temperature using $CDCl_3$ as solvent. Chemical shifts (δ) are referenced in parts per million (ppm) with tetramethylsilane (TMS) or $CDCl_3$ resonance as the internal standard peak ($CDCl_3$/TMS, δ 0.00 for ^{1}H (TMS), δ 77.16 for ^{13}C ($CDCl_3$)). Multiplicity is reported as s = singlet, d = doublet, dd = doublet of doublet, t = triplet, q = quartet, p = quintet, m = multiplet. Coupling-constants (*J*) are reported in Hertz (Hz).

(6-bromo-3-fluoropyridin-2-yl)methanol (2): To a solution of 6-bromo-3-fluoro-2-methylpyridine **(1**, 10.7 g, 56.3 mmol, 1 eq**)** under an inert atmosphere at 0 °C in DCM (370 mL) was added portion-wise *m*-CPBA (23.6 g, 70-75%, 100 mmol, 1.8 eq). The reaction mixture was stirred at room temperature (rt) for 4 days. Sat. $NaHCO_3$ and sat. $Na_2S_2O_3$ was added (1:1, v/v) and the layers were separated. The aqueous layer was extracted thrice with DCM. The combined organic layer was dried over $MgSO_4$, filtered, and concentrated under reduced pressure. To the residue was added TFAA (17 mL, 122 mmol, 2.2 eq) at 0 °C. After 15 minutes the temperature was increased to 55 °C for 3 h. The mixture was concentrated under reduced pressure, redissolved in DCM and sat. Na_2CO_3 was added. The layers were separated and the organic layer was washed with sat. $NaHCO_3$. The solvent was evaporated and the crude was dissolved in THF:MeOH (20:1, v/v) and K_2CO_3 (18.2 g, 132 mmol, 2.3 eq) was added. After 17 h H_2O was added and the layers were separated. The aqueous layer was extracted thrice with EtOAc. The combined organic layers were dried over $MgSO_4$, filtered, and the solvent evaporated under reduced pressure. The crude was purified with flash column chromatography (10-20% EtOAc in pentane) to yield 5.79 g (19.7 mmol, 35%) of a white solid. ^{1}H-NMR (500 MHz, $CDCl_3$) δ 7.42 (ddt, *J* = 8.5, 3.5, 0.7 Hz, 1H), 7.29 (t, *J* = 8.5 Hz, 1H), 4.80 (d, *J* = 3.3 Hz, 2H). ^{13}CNMR (126 MHz, $CDCl_3$) δ 156.10 (d, *J* = 256.2 Hz), 148.74 (d, *J* = 19.1 Hz), 135.01 (d, *J* = 2.9 Hz), 128.17 (d, *J* = 4.2 Hz), 126.09 (d, *J* = 19.8 Hz), 59.07.

(6-bromo-3-fluoropyridin-2-yl)methyl methanesulfonate (3): To a cooled (0 °C) mixture of (6-bromo-3-fluoropyridin-2-yl)methanol (1.6 g, 7.8 mmol, 1 eq) and Et_3N (2.5 mL, 17.9 mmol, 2.3 eq) in dry THF (40 mL) was added dropwise MsCl (1.0 mL, 12.9 mmol, 1.7 eq). After stirring at rt for 1 h the solution was concentrated under reduced pressure. DCM and H_2O were added and the layers were separated. The aqueous layer was extracted thrice with DCM. The combined organic layers were washed with brine, dried over $MgSO_4$, filtered, and the solvent evaporated under reduced pressure to yield 1.65 g (5.8 mmol, 75%) of an yellow solid. ^{1}H-NMR (500 MHz, $CDCl_3$) δ 7.52 (dd, *J* = 8.6, 3.5 Hz, 1H), 7.37 (t, *J* = 8.5 Hz, 1H), 5.33 (d, *J* = 2.1 Hz, 2H), 3.13 (s, 3H). ^{13}C-NMR (126 MHz, $CDCl_3$) δ 157.82 (d, *J* = 261.3 Hz), 142.15 (d, *J* = 16.0 Hz), 130.74 (d, *J* = 4.4 Hz), 127.06 (d, *J* = 20.4 Hz), 65.50 (d, *J* = 1.6 Hz), 38.39.

***N*-((6-bromo-3-fluoropyridin-2-yl)methyl)tetrahydro-2*H*-pyran-4-amine (4)**: (6-Bromo-3-fluoropyridin-2-yl)methyl methanesulfonate (1.49 g, 5.3 mmol, 1 eq), K_2CO_3 (1.6 g, 11.6 mmol, 2.2 eq) and tetrahydro-2*H*-pyran-4-amine (0.66 mL, 6.7 mmol, 1.3 eq) were suspended in acetonitrile and stirred at 50 °C for 6 h, then an additional 3 days at

rt. After dilution with DCM and H_2O the layers were separated. The aqueous layer was extracted thrice with DCM. The combined organic layers were dried over $MgSO_4$, filtered, and the solution evaporated under reduced pressure. The crude was purified with flash column chromatography (20-100% EtOAc in pentane) to yield 1.01 g (3.5 mmol, 67%) as a yellow oil. ^{1}H-NMR (300 MHz, $CDCl_3$) δ 7.40 (dd, *J* = 8.6, 3.6 Hz, 1H), 7.35 – 7.26 (m, 1H), 4.08 – 3.95 (m, 4H), 3.42 (td, *J* = 11.6, 2.2 Hz, 2H), 2.74 (tt, *J* = 10.5, 4.1 Hz 1H), 1.89 (ddd, *J* = 12.7, 4.5, 2.3 Hz, 2H), 1.52 (dtd, *J* = 13.1, 11.0, 4.5 Hz, 2H). ^{13}C-NMR (75 MHz, $CDCl_3$) δ 157.12 (d, *J* = 255.9 Hz), 149.21 (d, *J* = 17.0 Hz), 127.83 (d, *J* = 4.2 Hz), 125.97 (d, *J* = 21.2 Hz), 66.76, 53.64, 44.90, 33.59.

2-((4-bromobenzyl)amino)acetamide (6): To a mixture of 4-bromobenzaldehyde **(5**, 9.2 g (49.7 mmol, 1.1 eq**)** and 2-aminoacetamide hydrochloride (5.06 g, 45.8 mmol, 1.0 eq) in MeOH:H_2O (170 mL, 5:1, v/v) was added NaOH (2.06 g, 51.5 mmol, 1.1 eq) and left to stir at rt overnight. $NaBH_4$ (3.6 g, 95.2 mmol, 2.1 eq) was added and the solution was stirred overnight at rt. The solution was acidified to pH 3 with 2 M HCl, then neutralized with sat. aqueous $NaHCO_3$. Methanol was evaporated under reduced pressure and the resulting slurry was filtered to yield 11.0 g (45.2 mmol, 91%) of a white solid. ^{1}H-NMR (300 MHz, methanol-d_4) δ 7.69 – 7.59 (m, 2H), 7.47 – 7.38 (m, 2H), 4.22 (s, 2H), 3.81 (s, 2H).

1-(4-bromobenzyl)imidazolidine-2,4-dione (7): To a suspension of 2-((4-bromobenzyl)-amino)acetamide (10.0 g, 40.1 mmol, 1,0 eq) in acetonitrile (300 mL) were added CDI (13.86 g, 85.5 mmol, 2.1 eq) and DMAP (10.2 g, 83.5 mmol, 2.1 eq). The mixture was heated to 60 °C under inert atmosphere for 70 h. HCl (1 M, 250 mL) was added and the aqueous layer extracted thrice with EtOAc. The combined organic layers were washed with H_2O and brine, dried over $MgSO_4$, filtered, and the solvent evaporated under reduced pressure. The crude was purified with flash column chromatography with dry loading over Celite (5-10% acetone in DCM) to yield 3.95 g (14.7 mmol, 37%) of a yellow solid. ^{1}H-NMR (300 MHz, $CDCl_3$) δ 7.83 (bs, 1H), 7.56 – 7.45 (m, 2H), 7.20 – 7.10 (m, 2H), 4.49 (s, 2H), 3.79 (s, 2H). ^{13}C-NMR (75 MHz, $CDCl_3$) δ 132.41, 129.95, 77.58, 77.16, 76.74, 50.36, 46.01.

1-(4-bromobenzyl)-3-isobutylimidazolidine-2,4-dione (8): To solution of 1-(4-bromobenzyl)imidazolidine-2,4-dione (2.00 g, 7.4 mmol, 1,0 eq) in anhydrous DMF (18 mL) were subsequently added K_2CO_3 (3.08 g, 22.3 mmol, 3,0 eq) and 1-bromo-2-methylpropane (1.62 mL, 14.9 mmol, 2,0 eq) and the mixture was stirred for 20 h at rt. The mixture was filtered and the filtrate diluted with diethyl ether and washed thrice with water (3 x 50 mL). The combined organic layers were washed with brine, dried ($MgSO_4$), filtered, and concentrated under reduced pressure. The crude was purified with flash column chromatography (10-40% EtOAc in pentane) to yield 2.12 g (6.52 mmol, 88%) of a white solid. LCMS (LCQ Fleet, 10 90%): t_r = 7.00 min, m/z: 325.17 $[M+H]^+$, 327.08 $[M+H]^+$ (Br). ^{1}HNMR (300 MHz, $CDCl_3$) δ 7.47 (d, *J* = 8.3 Hz, 2H), 7.14 (d, *J* = 8.3 Hz, 2H), 4.52 (s, 2H), 3.74 (s, 2H), 3.33 (d, *J* = 7.4 Hz, 2H), 2.15 – 2.04 (m, 1H), 0.91 (d, *J* = 6.8 Hz, 6H). ^{13}C NMR (75 MHz, $CDCl_3$) δ 169.57, 156.78, 134.41, 131.79, 129.48, 121.77, 60.01, 48.61, 45.98, 45.71, 28.57, 19.70.

3-isobutyl-1-(4-(4,4,5,5-tetramethyl-1,3,2-dioxaborolan-2-yl)benzyl)imidazolidine-2,4-dione (9): A mixture of 1-(4-bromobenzyl)-3-isobutylimidazolidine-2,4-dione (0.50 g,

1.54 mmol, 1 eq), KOAc (0.66 g, 6.76 mmol, 4.4 eq) and bis(pinacolato)diboron (0.59 g, 2.31 mmol, 1.5 eq) in DMF (10 mL) was sonicated for 15 min under argon flow. Subsequently, $Pd(dppf)Cl_2$ (0.07 g, 0.09 mmol, 0.06 eq) was added and the mixture was stirred at 75 °C for 20 h. The mixture was cooled to rt, diluted with EtOAc (100 mL) and water (10 mL) and the layers were separated. The water layer was extracted thrice with EtOAc (3 × 20 mL). The combined organic layers were extracted with sat. aqueous $NaHCO_3$, water and brine, dried ($MgSO_4$), filtered, and concentrated under reduced pressure. The raw product was co-evaporated with $CHCl_3$ and used in the next step without further purification.

1-(4-(5-fluoro-6-(((tetrahydro-2*H*-pyran-4-yl)amino)methyl)pyridin-2-yl)benzyl)-3-isobutylimidazolidine-2,4-dione (LEI-102): To a degassed mixture of *N*-((6-bromo-3-fluoropyridin-2-yl)methyl)tetrahydro-2*H*-pyran-4-amine (**4**, 0.29 g, 1.0 mmol, 1,0 eq), 3-isobutyl-1-(4-(4,4,5,5-tetramethyl-1,3,2-dioxaborolan-2-yl)benzyl)imidazolidine-2,4-dione (**9**, 0.56 g, ~1.5 mmol, crude) and K_2CO_3 (1.29 g, 6.0 mmol, 6,0 eq) in toluene:ethanol (10 mL, 4:1, v/v) was added under argon atmosphere $Pd(PPh_3)_4$ (0.18 g, 0.10 mmol, 0.1 eq) . The resulting mixture was stirred for 18 h at 75 °C, subsequently cooled to rt and filtered. The filtrate was diluted with EtOAc and washed with water and brine, dried ($MgSO_4$), filtered, and concentrated under reduced pressure. The crude was purified with flash column chromatography (0-20% MeOH in EtOAc) to yield 0.24 g of a white solid (0.53 mmol, 53%). Further purification with preparative HPLC resulted in a yield of 0.204 g (0.45 mmol, 45%). LCMS (LCQ Advantage, 10 90%): t_r = 5.32 min, m/z: 455.27 $[M+H]^+$, 908.93 $[2M+H]^+$. HRMS (ESI+) m/z: calcd. for $C_{25}H_{32}FN_4O_3$ [M+H], 455.245; found, 455.245. ^{1}H NMR (400 MHz, CD_3CN) δ 8.05 (d, *J* = 8.3 Hz, 2H), 7.86 (dd, *J* = 8.7, 3.6 Hz, 1H), 7.61 (t, *J* = 9.0 Hz, 1H), 7.34 (d, *J* = 8.1 Hz, 2H), 4.53 (s, 2H), 4.45 (s, 2H), 3.93 (dd, J = 11.4, 4.4 Hz, 2H), 3.77 (s, 1H), 3.47 (tt, *J* = 11.8, 3.8 Hz, 2H), 3.30 (td, *J* = 11.9, 1.9 Hz, 2H), 3.24 (d, *J* = 7.3 Hz, 2H), 2.05 (br d, *J* = 13.3 Hz, 2H), 1.99 (dt, *J* = 13.2, 6.6 Hz, 1H), 1.83 (qd, *J* = 12.1, 4.5 Hz, 2H), 0.88 (d, *J* = 6.7 Hz, 6H). ^{13}C NMR (100 MHz, CD_3CN) δ 171.54, 157.25 (d, *J* = 226.6 Hz), 156.12, 153.03 (d, *J* = 4.5 Hz), 140.51 (d, *J* = 16.1 Hz), 138.83, 137.70, 129.13, 128.22, 125.56 (d, *J* = 18.8 Hz), 122.81 (d, *J* = 4.3 Hz), 118.38, 66.55, 55.55, 50.30, 46.81 (d, *J* = 7.9 Hz), 42.95, 30.02, 28.32, 20.32.

4.4.4 Constructs

The N-BRIL fused wild type (WT) human CB_2R construction and co-expression of G protein for cryo-EM study were performed using the similar procedure as described before[34]. In brief, the WT human CB_2R was modified to contain a fusion protein BRIL to improve the protein expression and thermostability, along with a 10×His-tag and a FLAG-tag at the N-terminal. The CB_2R, $G\alpha_{i1}$ and $G\beta_1\gamma_2$ subunits were cloned into the pFastBac vector separately using cloning kits.

4.4.5 Expression and purification of CB_2R-G_i-Scfv16 complexes

Methods of complex expression and purification in the current study have been described previously[34]. The CB_2R and G_i heterotrimer were co-expressed in *Sf9* insect cells using

the Bac-to-Bac Baculovirus Expression System (Invitrogen). Cells were infected with three separate virus preparations for CB_2R, $G\alpha_{i1}$ and $G\beta_1\gamma_2$ at a ratio of 1:2:2 at a cell density of 2.5×10^6 cells/mL. After 48 h, the cell culture was collected by centrifugation and the cell pellets were stored at -80 °C until use. The cell pellets were thawed and lysed in the hypotonic buffer of 10 mM HEPES (pH 7.5), 10 mM $MgCl_2$, 20 mM KCl with EDTA-free complete protease inhibitor cocktail tablets (Roche, #5056489001). The CB_2R-G_i complex was formed in membranes by addition of 25 μM agonist (LEI-102, APD371, HU308 and CP55,940, respectively) and 2 units of apyrase (NEB, #M0398S) in the presence 500 μg scFv16. The lysate was incubated for overnight at 4 °C and discard the supernatant by centrifugation at 186,000 × g for 30 min. Subsequently, the solubilization buffer containing 50 mM HEPES (pH 7.5), 100 mM NaCl, 0.75% (w/v) lauryl maltose neopentyl glycol (LMNG, Anatrace, #4216588), 0.15% (w/v) cholesterol hemisucinate (CHS, Sigma-Aldrich, #C6512) supplemented with 25 μM agonist and 2 units of apyrase (NEB) were added to solubilize complexes for 2 h at 4 °C. Insoluble material was removed by centrifugation at 186,000 × g for 30 min and the supernatant was immobilized by batch binding to TALON IMAC resin (Clontech, #635507) including 20 mM imidazole over 6 h at 4 °C. Then, the resin was packed and washed with 15 column volumes (CVs) of washing buffer I containing 25 mM HEPES (pH 7.5), 100 mM NaCl, 10% (v/v) glycerol, 0.1% (w/v) LMNG, 0.02% (w/v) CHS, 30 mM imidazole and 20 μM agonist, and 15 CVs of washing buffer II containing 25 mM HEPES (pH 7.5), 100 mM NaCl, 10% (v/v) glycerol, 0.03% (w/v) LMNG, 0.006% (w/v) CHS, 50 mM imidazole and 20 μM agonist. After that, the protein was eluted using 3 CVs of elution buffer containing 25 mM HEPES (pH 7.5), 100 mM NaCl, 10% (v/v) glycerol, 0.01% (w/v) LMNG, 0.002% (w/v) CHS, 250 mM imidazole and 25 μM agonist. Finally, the complex was concentrated using the centrifugal filter with 100 KD molecular weight cutoff and loaded onto a Superdex200 10/300 GL column (GE Healthcare) with buffer containing 20 mM HEPES (pH 7.5), 100 mM NaCl, 0.00075% (w/v) LMNG, 0.00025% GDN (Anatrace, #GDN101), 0.0001% (w/v) CHS, 100 μM TCEP. The fractions consisting of purified CB_2R-G_i complex were collected and concentrated to 0.8-1.0 mg/ml for electron microscopy experiments.

4.4.6 Cryo-EM grid preparation and data collection

For cryo-EM grids preparation of the CB_2R-G_i complexes, 3 μL of the concentrated protein was loaded to a glow-discharged holey carbon grid (CryoMatrix Amorphous alloy film R1.2/1.3, 300 mesh), and subsequently were plunge-frozen in liquid ethane using a Vitrobot Mark IV (Thermo Fisher Scientific). The chamber of Vitrobot was set to 100% humidity at 4 °C. The sample was blotted for 2.5 s with blot force 2. Cryo-EM images were collected on a Titan Krios microscope operated at 300 kV equipped with a Gatan Quantum energy filter, with a slit width of 20 eV, a Gatan K2 summit direct electron camera (Gatan). Images were taken at a dose rate of $8e^-/Å^2/s$ with a defocus range of -0.8 to -2.0 μm using SerialEM software[64] in EFTEM nanoprobe mode, with 50 μm C2 aperture, at a calibrated magnification of 130,000 corresponding to a magnified pixel size of 1.04 Å. The total exposure time was 8.1 s and 45 frames were recorded per micrograph.

4.4.7 Cryo-EM image processing

The cryo-EM data processing was performed with CryoSPARC[65]. For CB_2R-$G\alpha_i$-scFv16-APD371/LEI-102/HU308/CP55,940 dataset, a total of 7443, 5282, 7530 and 6473 movies were collected, respectively. For all datasets, patch motion correction was used for beam-induced motion correction. Contrast transfer function (CTF) parameters for each micrograph were determined by patch CTF estimation. Using Blob Picker in CryoSPARC to auto pick particles in the first 500 micrographs of CB_2R-$G\alpha_i$-scFv16-APD371 complex dataset and then 258347 particles were extracted to conduct 2D classification. 9277 particles in good 2D patterns were selected as templates to pick better particles. 5,239,870, 3,398,611, 4,653,294 and 3,595,875 particles extracted, respectively, in a 256 Å box were divided into three hundred two-dimensional (2D) class averages with a maximum alignment resolution of 6 Å. Then, 1,152,146, 762,471, 355,832 and 440,292 particles were selected from good 2D classification after two round 2D classification, individually. Following 2D classification, these particles were subjected for ab initio reconstruction into four classes. After heterogeneous refinement, homogeneous refinement, non-uniform refinement and local refinement of the best-looking dataset in CryoSPARC, the final map has an indicated global resolution of 3.08 Å, 2.98 Å, 2.97 Å and 2.84 Å at a Fourier shell correlation (FSC) of 0.143, respectively. Local resolution was determined using the Bsoft package with half maps as input maps[66].

4.4.8 Model building and refinement

For CB_2R-G_i-scFv16 complex, the CB_2R-AM12033 cryo-EM structure and G_i protein in CB_2R were used as the starting model. The model was docked into the EM density map using Chimera[67], followed by iterative manual adjustment and rebuilding in COOT[68] and phenix.real_space_refine in Phenix[69]. The model statistics were validates using MolProbity[70]. Structural figures were prepared in Chimera and PyMOL (http://www.pymol.org). The final refinement statistics are provided in **Table 4.S4**. The extent of any model overfitting during refinement was measured by refining the final model against one of the half-maps and by comparing the resulting map versus model FSC curves with the two half-maps and full model.

4.4.9 Generation of mutants

The WT CB_1R and CB_2R genes were subcloned into vector pcDNA3.1 with an N-terminal HA signal peptide and FLAG-tag. Mutations were introduced by QuikChange PCR (as described by supplier).

4.4.10 Transfection

24 h prior to transfection, HEK293T cells were seeded on 10 cm ø plates to reach approximately 50% confluence at the start of transfection. The cells were transfected

with 10 μg plasmid DNA of WT hCB_2R or hCB_1R receptor, or mutant receptor using the calcium phosphate precipitation method[71]. In short, a DNA-calcium mix was made containing 270 mM $CaCl_2$ and 10 μg plasmid DNA to which Hank's Balanced Salt Solution (HBSS; 280 mM NaCl, 10 mM KCl, 1.5 mM Na_2HPO_4 and 50 mM HEPES) was added in a 1:1 (v/v) ratio and mixed by aeration to create consistent calcium phosphate precipitates. For transfection, 1 mL DNA-calcium mix was added per 10 cm ø plate, followed by a 48 h incubation under a humidified atmosphere at 37 °C with 5% CO_2.

4.4.11 Enzyme-linked immunosorbent assay (ELISA)

Receptor expression after transfection was measured in an enzyme-linked immunosorbent assay (ELISA). After 24 h of transfection, HEK293T cells were detached with phosphate-buffered saline (PBS)/EDTA and seeded into a sterile 96-well poly-D-lysine coated plate at a density of 100,000 cells per well and kept under a humidified atmosphere at 37 °C with 5% CO_2. After an additional 24 h, cells were washed with PBS and fixed with 4% formaldehyde for 10 min at RT. Cells were washed twice with Tris-buffered saline (TBS) and were blocked with TBS supplemented with 0.1% TWEEN 20 (TBST) and 2% BSA (w/v)) for 30 min at rt while shaking. Subsequently, the cells were incubated with monoclonal M2 mouse anti-FLAG primary antibody (1:4000) for 2 h at rt while shaking. After removal of the antibody, the cells were washed three times with TBST and incubated with the secondary goat anti-mouse HRP-conjugated antibody (1:10,000) for 1 h at rt while shaking. After a final wash with TBS, the cells were treated with 3,3',5,5'-Tetramethylbenzidine (TMB, Sigma-Aldrich #T0440) in the dark for maximally 10 min at rt to visualize immunoreactivity. The reaction was quenched with 1 M H_3PO_4, and absorbance was read at 450 nm with a Wallac EnVision 2104 Multilabel reader (Revvity).

4.4.12 Membrane preparation

For membrane preparation, HEK293T cells were harvested 48 h after transfection. Cells were detached by scraping into 3 mL of PBS and subsequently centrifuged at 2000 × g for 5 min. Pellets were resuspended in ice-cold Tris buffer (50 mM Tris-HCl, pH 7.4) and homogenized with an Ultra Turrax homogenizer (IKA-Werke GmbH & Co. KG, Staufen, Germany). Cytosolic and membrane fractions were separated using a high-speed centrifugation step of 31,000 rpm in a Beckman Optima LE-80K ultracentrifuge with Ti70 Rotor for 20 min at 4 °C. After a second cycle of homogenization and centrifugation, the final pellets were resuspended in 50 mM Tris-HCl pH 7.4, 5 mM $MgCl_2$ and stored in 100 μL aliquots at -80 °C until use. CHOK1_hCB_2bgal and CHOK1_hCB_1bgal cells were harvested when reaching 90% confluence in 15 cm ø plates after one week subculture at a 1:6 ratio. Membrane preparation followed a similar procedure as described above. Final membrane pellets were resuspended in 50 mM Tris-HCl pH 7.4 and stored in 100 μL aliquots at -80 °C until use. Membrane protein concentrations were determined using a BCA protein determination assay as described by the manufacturer[72].

4.4.13 [^{3}H]RO6957022 competition association assays

For assessment of kinetic agonist binding at hCB_2R, [^{3}H]RO6957022 competition association assays were executed. These assays were previously described with the main difference of incubation at 25 °C compared to 10 °C for identification of more distinct kinetic differences[73]. In short, prior to kinetic assessment of agonist binding, the affinity (IC_{50}) of the agonists at the hCB_2R was determined in [^{3}H]RO6957022 displacement assays. CHOK1_hCB_2bgal were thawed, homogenized, and subsequently diluted to 1 µg protein per well. When studying endocannabinoids, membranes were preincubated with 50 µM PMSF for 30 min. Membranes were incubated with ~1.5 nM [^{3}H]RO6957022 and six increasing concentrations of competing agonists in a total volume of 100 µL assay buffer (50 mM Tris-HCl (pH 7.4), 0.1% (w/v) BSA). Incubations were done for 2 h at 10 °C to reach equilibrium. Subsequently, in competition association assays, agonists were incubated at their IC_{50} concentration in the presence of ~1.5 nM [^{3}H]RO6957022 in a total volume of 100 µL assay buffer at 10 °C. Competition was initiated by addition of membrane homogenates at different time points for 2 h. Nonspecific binding (NSB) was determined with 10 µM AM630 and organic solvent (DMSO or acetonitrile) concentrations were <1% in all samples. Total radioligand binding (TB) did not exceed 10% of the amount added to prevent ligand depletion. Incubations were terminated by rapid vacuum filtration with ice-cold 50 mM Tris-HCl (pH 7.4), 0.1% (w/v) BSA buffer through Whatman GF/C filters using a Filtermate 96-well harvester (Revvity). Filters were dried for at least 30 min at 55 °C and subsequently 25 µL MicroScint scintillation cocktail (Revvity #6013621) was added per well. Filter-bound radioactivity was measured by scintillation spectrometry using a Microbeta^2 2450 counter (Revvity).

4.4.14 [^{35}S]GTPγS binding assays

G protein activation by agonists LEI-102, APD371, HU308, CP55,940 AEA and 2-AG was measured by binding of radiolabeled [^{35}S]GTPγS to the cannabinoid receptors as previously described[25]. In short, transient HEK293T membrane homogenates (10 µg/well) were diluted in assay buffer (50 mM Tris-HCl (pH 7.4), 5 mM $MgCl_2$, 150 mM NaCl, 1 mM EDTA, 0.05% BSA (w/v) and 1 mM DTT, freshly prepared every day) and were pretreated with 10 µg saponin and 1 µM GDP. For endocannabinoid samples, the membranes were additionally pretreated for 30 minutes with 50 µM PMSF before agonist addition. To determine the G protein activation, the membranes were incubated with 10 µM or six increasing concentrations of agonist (ranging from 0.01 nM to 1 µM) for 30 minutes at rt. Basal receptor activity was determined in the presence of vehicle only (0.2% DMSO/acetonitrile). [^{35}S]GTPγS (0.3 nM) was added and the mixture was co-incubated for an additional 90 minutes at 25 °C while shaking at 400 rpm. Filtration was performed and filter-bound radioactivity was determined as described in section **4.4.13 [^{3}H]RO6957022 competition association assays** except for using ice-cold 50 mM Tris-HCl (pH 7.4), 5 mM $MgCl_2$ buffer.

4.4.15 [^{3}H]CP55,940 homologous and heterologous displacement assays

Agonist affinity (K_i) on WT and mutant receptors was determined in [^{3}H]CP55,940 displacement assays. The amount of transient HEK293T membrane, ranging from 0.75 μg to 10 μg protein per well, was chosen to obtain a specific [^{3}H]CP55,940 binding window of 1200-1500 disintegrations per minute (dpm) except for the CB_2R-Quadruple^{TM1,7} mutant, for which a window of ~500 dpm could be obtained using 20 μg protein per well. Membranes were thawed and subsequently homogenized using the Ultra Turrax homogenizer. For the endocannabinoid assays, the membranes were preincubated for 30 min with 50 μM PMSF. Homologous displacement assays were performed with 1.5 nM final concentration [^{3}H] CP55,940 and when necessary supplemented with an additional concentration of 0.55 nM [^{3}H]CP55,940 in the presence of competing CP55,940 (ranging from 0.01 nM to 1 μM) in assay buffer (50 mM Tris-HCl (pH 7.4), 5 mM $MgCl_2$, 0.1% (w/v) BSA). Heterologous displacement assays were executed for LEI-102, APD371, HU308, AEA and 2-AG using 1.5 nM final concentration [^{3}H]CP55,940 with one concentration (10 μM) or six increasing concentrations (ranging from 0.1 nM to 10 μM) in assay buffer. For both assays, binding was initiated by addition of membrane homogenates to reach a final volume of 100 μL. NSB was determined using 10 μM CP55,940 and organic solvent (DMSO or acetonitrile) concentrations were <1% in all samples. TB did not exceed 10% of the amount added to prevent ligand depletion. Incubation was done for 2 h at 25 °C to reach equilibrium. Filtration was performed and filter-bound radioactivity was determined as described in section **4.4.13 [^{3}H]RO6957022 competition association assays** except for using ice-cold 50 mM Tris-HCl (pH 7.4), 5 mM $MgCl_2$, 0.1% (w/v) BSA buffer.

4.4.16 Cisplatin-induced nephropathy

Ten to twelve-week-old male/female *C57BL/6J* mice were obtained from The Jackson Laboratory (Bar Harbor, ME, USA). CB_2 receptor knockout mice ($CB_2R^{-/-}$) and their wild-type littermates ($CB_2R^{+/+}$) were developed as described previously and had been backcrossed to a C57BL/6J background[74]. All animals were kept in a temperature-controlled environment with a 12 h light–dark cycle and were always allowed free access to food and water.

The well-established model of cisplatin-induced nephropathy was used[63]. Mice ($CB_2R^{-/-}$ and $CB_2R^{+/+}$) were sacrificed 72 h after a single injection of cisplatin (cis-diamine platinum (II) dichloride (Sigma#P4394) 25 mg/kg i.p.; freshly dissolved in physiological saline) by cervical dislocation under deep anesthesia with 5% isoflurane, for collection of blood and tissue samples. LEI-102 was given i.p. or by oral gavage (p.o.) at 0.3, 3.0 and 10 mg/kg every day, starting 1.5 h before the cisplatin exposure. The drug was dissolved in a vehicle of DMSO:Tween 80:saline, 1:1:18. After administration of LEI-102, mice were killed by cervical dislocation under deep anesthesia with 5% isoflurane, for collection of blood and tissue samples at the time described in the figure. All animal experiments were approved by the National Institute on Alcohol Abuse and Alcoholism Animal Care and Use Committee. The tetrad assay in mice has previously been described in detail[29].

4.4.17 *Biochemistry, Histopathology, Immunostaining, Real-Time PCR*

Markers of kidney dysfunction (BUN and CREA), histopathology (PAS staining), immunostaining or ELISA for 3-nitrotyrosine (3-NT; Cell Biolabs #STA-305) and 4-hydroxynonenal (4-HNE; Cell Biolabs#STA-838), and real-time PCR (Primers from Qiagen, SYBER Green Vita Scientific#MEIF01301, High-Capacity cDNA Reverse Transcription Kit, Thermo Fisher Scientific#4368813) for inflammatory cytokines were performed as previously described[63]. Tubular damage scores were determined based on the percentage of tubules showing epithelial necrosis where 0= normal; 1, < 10%; 2, 10–25%; 3, 26–75%; 4, > 75%. Tubular necrosis was defined as the loss of the proximal tubular brush border, blebbing of ff apical membranes, tubular epithelial cell detachment from the basement membrane, or intraluminal aggregation of cells and proteins. The morphometric examination was performed in a blinded manner. Ten fields were scored from each mouse kidneys at 200X magnification, and average scores were determined for each mouse. For final quantification graph, average tubular damage scores of six mice/group were plotted.

4.4.18 *Quantification and statistical analysis*

All experimental data were analyzed using GraphPad Prism 9.0 (GraphPad Software Inc., San Diego, CA). All values obtained are means ± standard error of the mean (SEM) of at least three independent experiments performed in duplicate, unless stated otherwise.

From [^{3}H]RO6957022 competition association assays, the k_{on} and k_{off} were determined by non-linear regression analysis, using the "kinetics of competitive binding" model as described by Motulsky and Mahan[75]:

$$K_a = k_1[L]\cdot 10^{-9} + k_2$$

$$K_b = k_3[I]\cdot 10^{-9} + k_4$$

$$S = \sqrt{(K_a - K_b)^2 + 4\cdot k_1\cdot k_3\cdot[L]\cdot[I]\cdot 10^{-18}}$$

$$K_f = 0.5(K_a + K_b + S)$$

$$K_s = 0.5(K_a + K_b - S)$$

$$Q = \frac{B_{max}\cdot k_1\cdot[L]\cdot 10^{-9}}{K_f - K_s}$$

$$[Y] = Q\left(\frac{k_4\cdot(K_f - K_s)}{K_f\cdot K_s} + \frac{k_4 - K_f}{K_f}\cdot e^{(-K_f\cdot X)} - \frac{k_4 - K_s}{K_s}\cdot e^{(-K_s\cdot X)}\right)$$

Where [L] is the radioligand concentration per experiment (~1.5 nM), I is the IC_{50} concentration of agonist (nM), X is the time (s), and Y is the specific binding of the radioligand (dpm). K_a and K_b are the observed association rate constants (k_{obs}) of the radioligand and the agonist of interest, respectively. k_1 and k_3 are the association rate constants (k_{on} in $M^{-1}s^{-1}$) of [^{3}H]RO6957022 (determined per experiment) and the agonist of interest, respectively. Similarly, k_2 and k_4 are the dissociation rate constants (k_{off} in s^{-1}) of [^{3}H]

RO6957022 (experimentally determined at 4.3×10^{-4} s^{-1}, data not shown) and the agonist of interest, respectively. The engagement time (ET in seconds) of the agonists of interest was determined at 1 μM of agonist using the equation $ET = 1/(k_{on} \cdot 10^{-6})$. The residence time (RT in min) was calculated using the equation $RT = 1/(k_{off} \cdot 60)$[76]. The association and dissociation rate constants were used to calculate the kinetic K_D using: $K_D = k_{off}/k_{on}$.

[^{35}S]GTPγS agonist responses on hCB_2R constructs were baseline-corrected for the individual mutant's basal activity. The responses were normalized to the basal activity of the construct (0%) and top of the CP55,940 (for WT responses only) or WT curve (for mutants, 100%). The potency (pEC_{50}) and efficacy (E_{max}) values were obtained by non-linear regression to a sigmoidal concentration-effect curve with a Hill slope of 1 by using the "log(agonist) vs response (three parameters)" model. [^{35}S]GTPγS data from hCB_1R constructs were expressed as fold over the mutant's basal activity to also quantify the effects of CB_2R selective agonists.

Displacement assays were baseline-corrected with NSB and normalized to this value (0%) and TB (100%). The equilibrium dissociation constants (K_D) of [^{3}H]CP55,940 on different mutants were calculated from homologous displacements by non-linear regression analysis, using the "one-site homologous" model. The half-maximal inhibitory concentrations (pIC_{50}) of the agonists in [^{3}H]CP55,940 and [^{3}H]RO6957022 assays were obtained by non-linear regression analysis of the homologous and heterologous displacement curves and further converted into inhibitory constant pK_i using the Cheng-Prusoff equation[77]. In which the experimentally determined K_D for each construct was used for [^{3}H]CP55,940 assays or 0.78 nM for [^{3}H]RO6957022 assays (data not shown).

Differences in pEC_{50}, E_{max}, pK_D and pK_i values for each mutant compared to WT were analyzed using a one-way Welch's ANOVA with Dunnett's T3 multiple comparisons test or an unpaired Student's t-test with Welch's correction. Significant differences are displayed as * $p < 0.05$; ** $p < 0.01$, *** $p < 0.001$ and **** $p < 0.0001$.

For the animal experiments all the values are represented as mean ± SEM. Statistical analysis of the data was performed by analysis of variance (ANOVA) followed by Tukey's post hoc test for multiple comparisons or t-test if appropriate. The analysis was conducted using GraphPad Prism 9 software. $p < 0.05$ was considered statistically significant.

4.4.19 Data and code availability

The atomic coordinates for CB_2R-LEI-102-G_i-scFv16, CB_2R-APD371-G_i-scFv16, CB_2R-HU308-G_i-scFv16 and CB_2R-CP55,940-G_i-scFv16 have been deposited in the Protein Data Bank with the accession codes 8GUT, 8GUQ, 8GUS and 8GUR. The EM maps for CB_2R-LEI-102-G_i-scFv16, CB_2R-APD371-G_i-scFv16, CB_2R-HU308-G_i-scFv16 and CB_2R-CP55,940-G_i-scFv16 have been deposited in EMDB with the codes EMD-34279, EMD-34276, EMD-34278 and EMD-34277, respectively.

References

1. Mechoulam, R., Hanuš, L. O., Pertwee, R. & Howlett, A. C. Early phytocannabinoid chemistry to endocannabinoids and beyond. *Nat Rev Neurosci* **15**, 757–764 (2014).
2. Pacher, P., Bátkai, S. & Kunos, G. The endocannabinoid system as an emerging target of pharmacotherapy. *Pharmacol Rev* **58**, 389–462 (2006).
3. Badowski, M. E. & Yanful, P. K. Dronabinol oral solution in the management of anorexia and weight loss in AIDS and cancer. *Ther Clin Risk Manag* **14**, 643–651 (2018).
4. Grimison, P. *et al.* Oral THC:CBD cannabis extract for refractory chemotherapy-induced nausea and vomiting: a randomised, placebo-controlled, phase II crossover trial. *Annals of Oncology* **31**, 1553–1560 (2020).
5. Inglet, S. *et al.* Clinical Data for the Use of Cannabis-Based Treatments: A Comprehensive Review of the Literature: *Annals of Pharmacotherapy* **54**, 1109–1143 (2020).
6. Jones, É. & Vlachou, S. A Critical Review of the Role of the Cannabinoid Compounds Δ^9-Tetrahydrocannabinol (Δ^9-THC) and Cannabidiol (CBD) and their Combination in Multiple Sclerosis Treatment. *Molecules* **25**, 4930 (2020).
7. Adams, I. B. & Martin, B. R. Cannabis: pharmacology and toxicology in animals and humans. *Addiction* **91**, 1585–1614 (1996).
8. Lucas, C. J., Galettis, P. & Schneider, J. The pharmacokinetics and the pharmacodynamics of cannabinoids. *Br J Clin Pharmacol* **84**, 2477–2482 (2018).
9. Pacher, P., Steffens, S., Haskó, G., Schindler, T. H. & Kunos, G. Cardiovascular effects of marijuana and synthetic cannabinoids: The good, the bad, and the ugly. *Nat Rev Cardiol* **15**, 151–166 (2018).
10. Riera, R., Pacheco, R. L., Bagattini, Â. M. & Martimbianco, A. L. C. Efficacy and safety of therapeutic use of cannabis derivatives and their synthetic analogs: Overview of systematic reviews. *Phytotherapy Research* **36**, 5–21 (2022).
11. Munro, S., Thomas, K. L. & Abu-Shaar, M. Molecular characterization of a peripheral receptor for cannabinoids. *Nature* **365**, 61–65 (1993).
12. Howlett, A. C. *et al.* International Union of Pharmacology. XXVII. Classification of cannabinoid receptors. *Pharmacol Rev* **54**, 161–202 (2002).
13. Pertwee, R. G. *et al.* International Union of Basic and Clinical Pharmacology. LXXIX. Cannabinoid Receptors and Their Ligands: Beyond CB_1 and CB_2. *Pharmacol Rev* **62**, 588–631 (2010).
14. Howlett, A. C. & Abood, M. E. CB_1 and CB_2 Receptor Pharmacology. in *Advances in Pharmacology* vol. 80 169–206 (Academic Press, 2017).
15. Howlett, A., Blume, L. & Dalton, G. CB1 Cannabinoid Receptors and their Associated Proteins. *Curr Med Chem* **17**, 1382–1393 (2010).
16. Galiègue, S. *et al.* Expression of Central and Peripheral Cannabinoid Receptors in Human Immune Tissues and Leukocyte Subpopulations. *Eur J Biochem* **232**, 54–61 (1995).
17. Pacher, P. & Mechoulam, R. Is lipid signaling through cannabinoid 2 receptors part of a protective system? *Prog Lipid Res* **50**, 193–211 (2011).
18. Hanuš, L. *et al.* HU-308: A specific agonist for CB_2, a peripheral cannabinoid receptor. *Proc Natl Acad Sci U S A* **96**, 14228–14233 (1999).
19. Guindon, J. & Hohmann, A. G. Cannabinoid CB_2 receptors: a therapeutic target for the treatment of inflammatory and neuropathic pain. *Br J Pharmacol* **153**, 319–334 (2008).
20. Hussain, M. T., Greaves, D. R. & Iqbal, A. J. The Impact of Cannabinoid Receptor 2 Deficiency on Neutrophil Recruitment and Inflammation. *DNA Cell Biol* **38**, 1025–1029 (2019).
21. Rizzo, M. D. *et al.* Targeting Cannabinoid Receptor 2 on Peripheral Leukocytes to Attenuate Inflammatory Mechanisms Implicated in HIV-Associated Neurocognitive Disorder. *Journal of Neuroimmune Pharmacology 2020 15:4* **15**, 780–793 (2020).
22. Liu, Q. R. *et al.* Anti-Inflammatory and Pro-Autophagy Effects of the Cannabinoid Receptor CB2R: Possibility of Modulation in Type 1 Diabetes. *Front Pharmacol* **12**, 809965 (2022).
23. Brennecke, B. *et al.* Cannabinoid receptor type 2 ligands: An analysis of granted patents since 2010. *Pharm Pat Anal* **10**, 111–163 (2021).
24. Whiting, Z. M., Yin, J., de la Harpe, S. M., Vernall, A. J. & Grimsey, N. L. Developing the Cannabinoid Receptor 2 (CB2) pharmacopoeia: past, present, and future. *Trends Pharmacol Sci* **43**, 754–771 (2022).
25. Soethoudt, M. *et al.* Cannabinoid CB_2 receptor ligand profiling reveals biased signalling and off-target activity. *Nat Commun* **8**, 1–14 (2017).

26. Han, S. *et al.* Discovery of APD371: Identification of a Highly Potent and Selective CB_2 Agonist for the Treatment of Chronic Pain. *ACS Med Chem Lett* **8**, 1309–1313 (2017).
27. Yacyshyn, B. R. *et al.* Safety, Pharmacokinetics, and Efficacy of Olorinab, a Peripherally Acting, Highly Selective, Full Agonist of the Cannabinoid Receptor 2, in a Phase 2a Study of Patients with Chronic Abdominal Pain Associated with Crohn's Disease. *Crohns Colitis 360* **3**, otaa089 (2021).
28. van der Stelt, M. *et al.* Discovery and Optimization of 1-(4-(Pyridin-2-yl)benzyl)-imidazolidine-2,4-dione Derivatives As a Novel Class of Selective Cannabinoid CB2 Receptor Agonists. *J Med Chem* **54**, 7350–7362 (2011).
29. Mukhopadhyay, P. *et al.* The novel, orally available and peripherally restricted selective cannabinoid CB_2 receptor agonist LEI-101 prevents cisplatin-induced nephrotoxicity. *Br J Pharmacol* **173**, 446–458 (2016).
30. Soethoudt, M. *et al.* Structure-kinetic relationship studies of cannabinoid CB_2 receptor agonists reveal substituent-specific lipophilic effects on residence time. *Biochem Pharmacol* **152**, 129–142 (2018).
31. Hua, T. *et al.* Crystal Structure of the Human Cannabinoid Receptor CB_1. *Cell* **167**, 750-762.e14 (2016).
32. Shao, Z. *et al.* High-resolution crystal structure of the human CB1 cannabinoid receptor. *Nature* **540**, 602–606 (2016).
33. Li, X. *et al.* Crystal Structure of the Human Cannabinoid Receptor CB2. *Cell* **176**, 459–467 (2019).
34. Hua, T. *et al.* Activation and Signaling Mechanism Revealed by Cannabinoid Receptor-G_i Complex Structures. *Cell* **180**, 655-665.e18 (2020).
35. Xing, C. *et al.* Cryo-EM Structure of the Human Cannabinoid Receptor CB2-G_i Signaling Complex. *Cell* **180**, 645-654.e13 (2020).
36. Hua, T. *et al.* Crystal structures of agonist-bound human cannabinoid receptor CB_1. *Nature* **547**, 468–471 (2017).
37. Shao, Z. *et al.* Structure of an allosteric modulator bound to the CB1 cannabinoid receptor. *Nat Chem Biol* **15**, 1199–1205 (2019).
38. Yang, X. *et al.* Molecular mechanism of allosteric modulation for the cannabinoid receptor CB1. *Nat Chem Biol* 1–10 (2022) doi:10.1038/s41589-022-01038-y.
39. McAllister, S. D. *et al.* Structural Mimicry in Class A G Protein-coupled Receptor Rotamer Toggle Switches: the importance of the F3.36(201)/W6.48(357) interaction in cannabinoid CB_1 receptor activation. *Journal of Biological Chemistry* **279**, 48024–48037 (2004).
40. Díaz, Ó., Dalton, J. A. R. & Giraldo, J. Revealing the Mechanism of Agonist-Mediated Cannabinoid Receptor 1 (CB1) Activation and Phospholipid-Mediated Allosteric Modulation. *J Med Chem* **62**, 5638–5654 (2019).
41. Krishna Kumar, K. *et al.* Structure of a Signaling Cannabinoid Receptor 1-G Protein Complex. *Cell* **176**, 448–458 (2019).
42. Bow, E. W. & Rimoldi, J. M. The structure-function relationships of classical cannabinoids: CB1/CB2 modulation. *Perspect Medicin Chem* **8**, 17–39 (2016).
43. Kapur, A. *et al.* Mutation Studies of Ser7.39 and Ser2.60 in the Human CB_1 Cannabinoid Receptor: Evidence for a Serine-Induced Bend in CB_1 Transmembrane Helix 7. *Mol Pharmacol* **71**, 1512–1524 (2007).
44. Javitch, J. A., Ballesteros, J. A., Weinstein, H. & Chen, J. A Cluster of Aromatic Residues in the Sixth Membrane-Spanning Segment of the Dopamine D2 Receptor Is Accessible in the Binding-Site Crevice. *Biochemistry* **37**, 998–1006 (1998).
45. Xu, W. *et al.* Comparison of the Amino Acid Residues in the Sixth Transmembrane Domains Accessible in the Binding-Site Crevices of μ, δ, and κ Opioid Receptors. *Biochemistry* **40**, 8018–8029 (2001).
46. Wang, X. *et al.* Identification of V6.51L as a selectivity hotspot in stereoselective A_{2B} adenosine receptor antagonist recognition. *Sci Rep* **11**, (2021).
47. Lin, X. *et al.* Structural basis of ligand recognition and self-activation of orphan GPR52. *Nature* **579**, 152–157 (2019).
48. Hanson, M. A. *et al.* Crystal structure of a lipid G protein-coupled receptor. *Science (1979)* **335**, 851–855 (2012).
49. Jakowiecki, J. & Filipek, S. Hydrophobic Ligand Entry and Exit Pathways of the CB1 Cannabinoid Receptor. *J Chem Inf Model* **56**, 2457–2466 (2016).
50. Stanley, N., Pardo, L. & Fabritiis, G. D. The pathway of ligand entry from the membrane bilayer to a lipid G protein-coupled receptor. *Sci Rep* **6**, 1–9 (2016).

51. Szlenk, C. T., GC, J. B. & Natesan, S. Does the Lipid Bilayer Orchestrate Access and Binding of Ligands to Transmembrane Orthosteric/Allosteric Sites of G Protein-Coupled Receptors? *Mol Pharmacol* **96**, 541 (2019).

52. Bokoch, M. P. *et al.* Entry from the Lipid Bilayer: A Possible Pathway for Inhibition of a Peptide G Protein-Coupled Receptor by a Lipophilic Small Molecule. *Biochemistry* **57**, 5748–5758 (2018).

53. Sykes, D. A. *et al.* Observed drug-receptor association rates are governed by membrane affinity: The importance of establishing 'micro-pharmacokinetic/pharmacodynamic relationships' at the β_2-adrenoceptor. *Mol Pharmacol* **85**, 608–617 (2014).

54. van der Velden, W. J. C., Heitman, L. H. & Rosenkilde, M. M. Perspective: Implications of Ligand−Receptor Binding Kinetics for Therapeutic Targeting of G Protein-Coupled Receptors. *ACS Pharmacol. Transl. Sci* **2020**, 179–189 (2020).

55. Swanson, M. L., Regner, K. R., Moore, B. M. & Park, F. Cannabinoid Type 2 Receptor Activation Reduces the Progression of Kidney Fibrosis Using a Mouse Model of Unilateral Ureteral Obstruction. *Cannabis Cannabinoid Res* **7**, 790–803 (2022).

56. Chafik, S. G., Michel, H. E. & El-Demerdash, E. The Cannabinoid-2 receptor agonist, 1-phenylisatin, protects against cisplatin-induced nephrotoxicity in mice. *Life Sci* **308**, 120928 (2022).

57. Trojnar, E. *et al.* Cannabinoid-2 receptor activation ameliorates hepatorenal syndrome. *Free Radic Biol Med* **152**, 540–550 (2020).

58. Çakır, M., Tekin, S., Doğanyiğit, Z., Çakan, P. & Kaymak, E. The protective effect of cannabinoid type 2 receptor activation on renal ischemia–reperfusion injury. *Mol Cell Biochem* **462**, 123–132 (2019).

59. Pressly, J. D. *et al.* Selective cannabinoid 2 receptor stimulation reduces tubular epithelial cell damage after renal ischemia-reperfusion injury. *Journal of Pharmacology and Experimental Therapeutics* **364**, 287–299 (2018).

60. Nettekoven, M. *et al.* Novel Triazolopyrimidine-Derived Cannabinoid Receptor 2 Agonists as Potential Treatment for Inflammatory Kidney Diseases. *ChemMedChem* **11**, 179–189 (2016).

61. Jenkin, K. A. *et al.* Renal effects of chronic pharmacological manipulation of CB2 receptors in rats with diet-induced obesity. *Br J Pharmacol* **173**, 1128–1142 (2016).

62. Barutta, F. *et al.* Deficiency of cannabinoid receptor of type 2 worsens renal functional and structural abnormalities in streptozotocin-induced diabetic mice. *Kidney Int* **86**, 979–990 (2014).

63. Mukhopadhyay, P. *et al.* Cannabinoid-2 receptor limits inflammation, oxidative/nitrosative stress and cell death in nephropathy. *Free Radic Biol Med* **48**, 467 (2010).

64. Mastronarde, D. N. Automated electron microscope tomography using robust prediction of specimen movements. *J Struct Biol* **152**, 36–51 (2005).

65. Punjani, A., Rubinstein, J. L., Fleet, D. J. & Brubaker, M. A. cryoSPARC: algorithms for rapid unsupervised cryo-EM structure determination. *Nat Methods* **14**, 290–296 (2017).

66. Heymann, J. B. Single particle reconstruction and validation using Bsoft for the map challenge. *J Struct Biol* **204**, 90–95 (2018).

67. Pettersen, E. F. *et al.* UCSF Chimera—A visualization system for exploratory research and analysis. *J Comput Chem* **25**, 1605–1612 (2004).

68. Emsley, P., Lohkamp, B., Scott, W. G. & Cowtan, K. Features and development of Coot. *Acta Crystallogr D Biol Crystallogr* **66**, 486–501 (2010).

69. Adams, P. D. *et al.* PHENIX: A comprehensive Python-based system for macromolecular structure solution. *Acta Crystallogr D Biol Crystallogr* **66**, 213–221 (2010).

70. Chen, V. B. *et al.* MolProbity: all-atom structure validation for macromolecular crystallography. *Acta Crystallogr D Biol Crystallogr* **66**, 12–21 (2010).

71. Chen, C. & Okayama, H. High-efficiency transformation of mammalian cells by plasmid DNA. *Mol Cell Biol* **7**, 2745–2752 (1987).

72. Smith, P. K. *et al.* Measurement of protein using bicinchoninic acid. *Anal Biochem* **150**, 76–85 (1985).

73. Martella, A. *et al.* A Novel Selective Inverse Agonist of the CB_2 Receptor as a Radiolabeled Tool Compound for Kinetic Binding Studies. *Mol Pharmacol* **92**, 389–400 (2017).

74. Batkai, S. *et al.* Cannabinoid-2 receptor mediates protection against hepatic ischemia/reperfusion injury. *The FASEB Journal* **21**, 1788–1800 (2007).

75. Motulsky, H. J. & Mahan, L. C. The kinetics of competitive radioligand binding predicted by the law of mass action. *Mol Pharmacol* **25**, 1–9 (1984).

76. Copeland, R. A., Pompliano, D. L. & Meek, T. D. Drug–target residence time and its implications for lead optimization. *Nat Rev Drug Discov* **5**, 730–739 (2006).

77. Cheng, Y.-C. & Prusoff, W. H. Relationship between the inhibition constant (K1) and the concentration of inhibitor which causes 50 per cent inhibition (I50) of an enzymatic reaction. *Biochem Pharmacol* **22**, 3099–3108 (1973).

4.S1 Supplementary figures

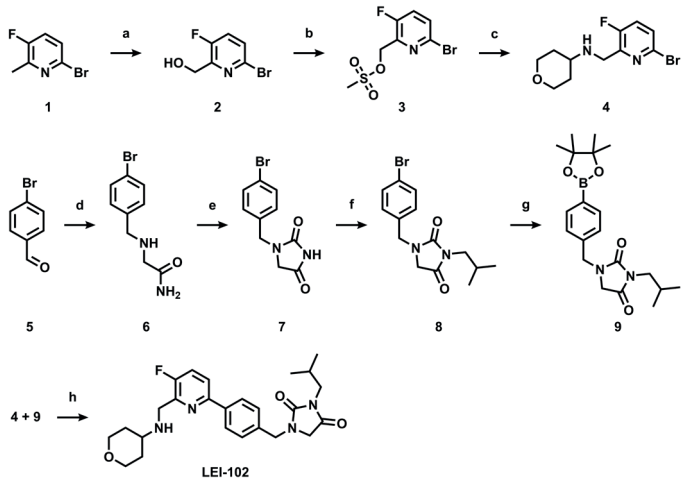

Figure 4.S1 Synthetic route of LEI-102.
Reagents and conditions: a) step 1: m-CPBA (1.8 eq), 0 °C-rt, DCM, 4 days; step 2: TFAA (2.2 eq), 55 °C, 3 h; step 3: K_2CO_3 (2.4 eq), THF:MeOH (20:1), 17 h, 35% (three steps); b) Et_3N (2.3 eq), MsCl (1.7 eq), THF, 0 °C-rt, 1 h, 75%; c) K_2CO_3 (2.2 eq), tetrahydro-2H-pyran-4-amine (1.3 eq), ACN, 50 °C, 3 h, 67%; d) step 1: 2-aminoacetamide hydrochloride (1.0 eq), NaOH (1.1 eq), MeOH:H_2O (5:1), rt, 18 h; $NaBH_4$ (2.1 eq), 18 h, 91% (two steps); e) CDI (2.1 eq), DMAP (2.1 eq), ACN, 60 °C, 70 h, 37%; f) K_2CO_3 (3.0 eq), 1-bromo-2-methylpropane (2.0 eq), DMF, rt, 20 h, 88%; g) KOAc (4.4 eq), bis(pinacolato)diboron (1.5 eq), Pd(dppf)Cl2 (0.06 eq), DMF, 75 °C, 20 h; h) 4 (1.0 eq), 9 (1.5 eq), K_2CO_3 (6.0 eq), $Pd(PPh_3)_4$ (0.1 eq), toluene:EtOH (4:1), 75 °C, 18 h, 45% (two steps).

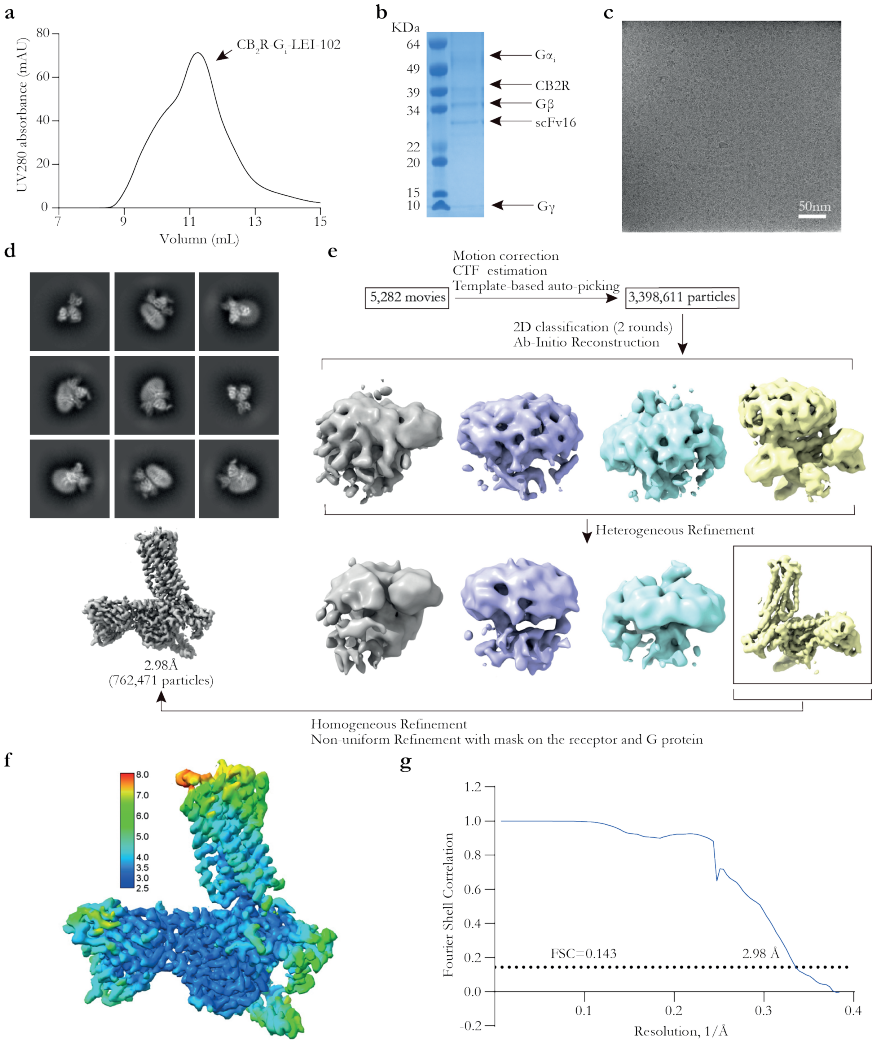

Figure 4.S2 CB_2R-G_i-Scfv16-LEI-102 complex preparation and cryo-EM data processing.
(a) Representative size-exclusion chromatography elution profile of CB_2R complex. Fractions corresponding to the main peak of monomers are indicated. (b) Coomassie blue staining of the CB_2R-G_i-scFv16 complex. (c) Representative cryo-EM micrograph of the CB_2R-G_i-scFv16 complex. Scale bar: 50 nm. (d) Representative 2D averages (box size: 256 Å) showing diverse secondary structure features. (e) Flow chart of cryo-EM single particle analysis of the CB_2R-G_i-scFv16 complex. (f) Local resolution map of the CB_2R-Gi-scFv16 complex. (g) Fourier shell correlation curves of the CB_2R-G_i-scFv16 complex.

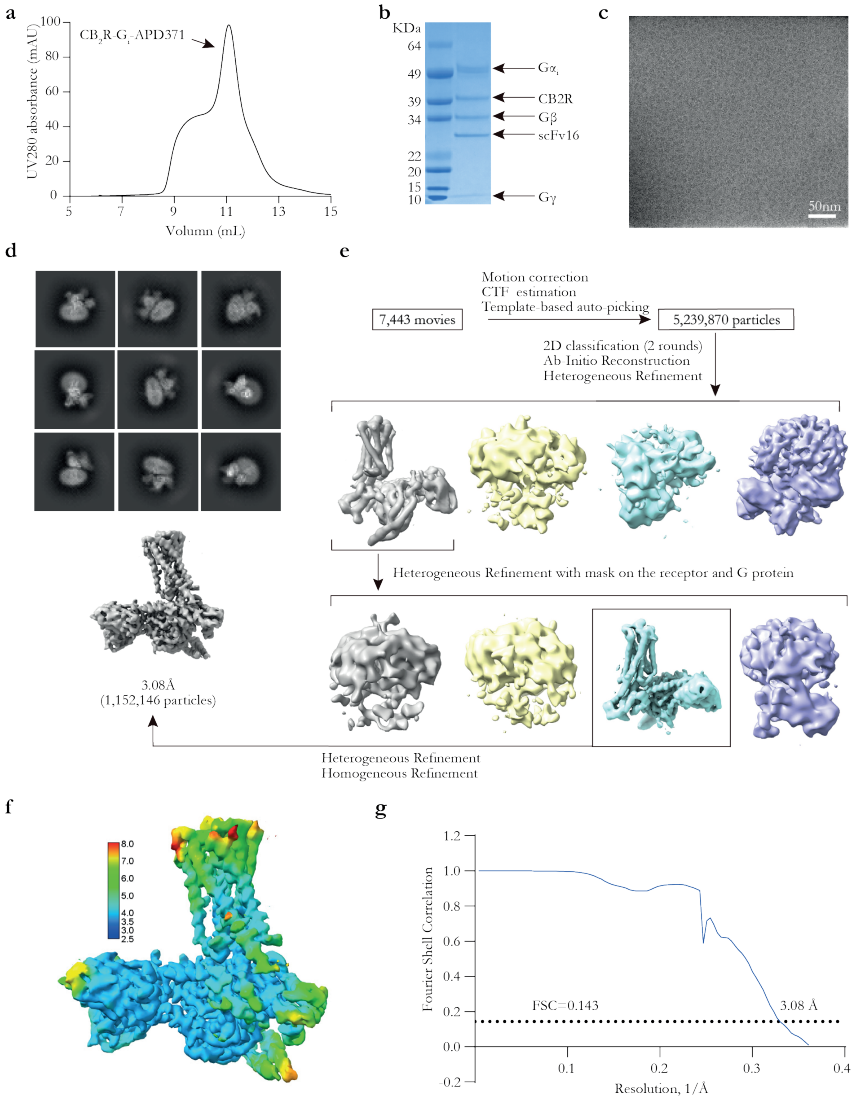

Figure 4.S3 **CB_2R-G_i-Scfv16-APD371 complex preparation and cryo-EM data processing.**
(a) Representative size-exclusion chromatography elution profile of CB_2R complex. Fractions corresponding to the main peak of monomers are indicated. (b) Coomassie blue staining of the CB_2R-G_i-scFv16 complex. (c) Representative cryo-EM micrograph of the CB_2R-G_i-scFv16 complex. Scale bar: 50 nm. (d) Representative 2D averages (box size: 256 Å) showing diverse secondary structure features. (e) Flow chart of cryo-EM single particle analysis of the CB_2R-G_i-scFv16 complex. (f) Local resolution map of the CB_2R-Gi-scFv16 complex. (g) Fourier shell correlation curves of the CB_2R-G_i-scFv16 complex.

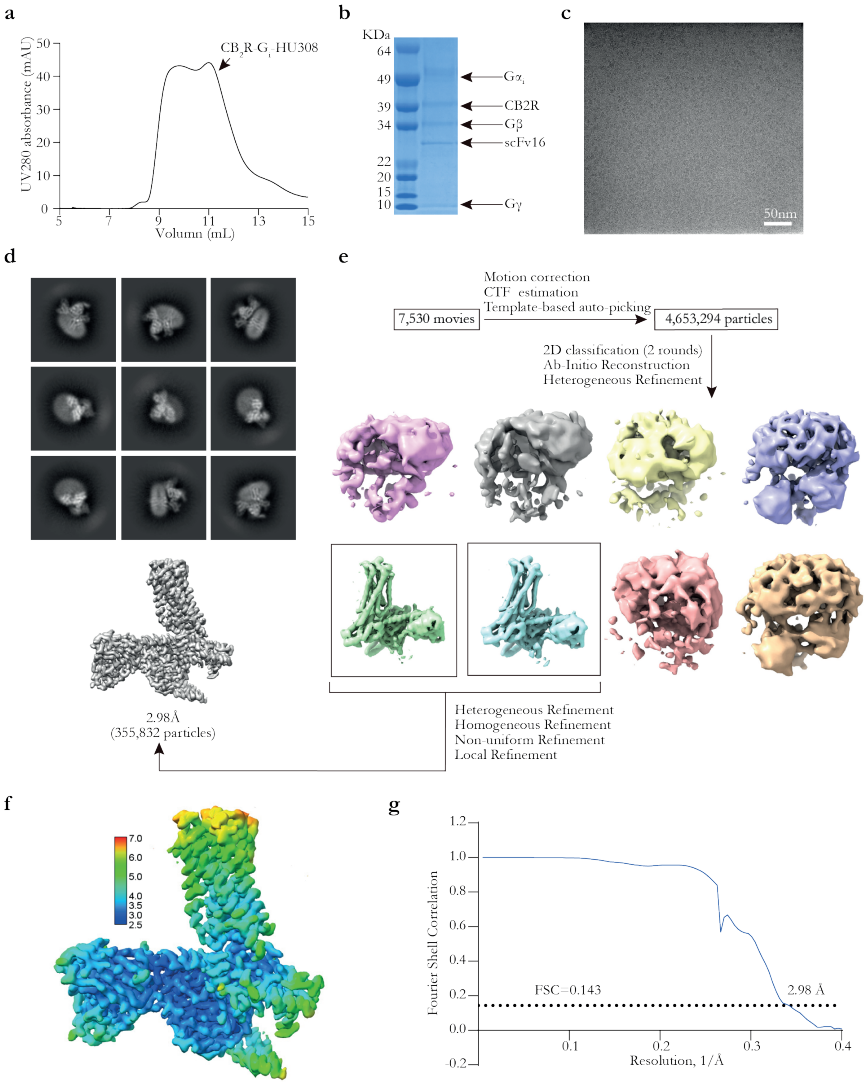

Figure 4.S4 **CB_2R-G_i-Scfv16-HU308 complex preparation and cryo-EM data processing.**
(a) Representative size-exclusion chromatography elution profile of CB_2R complex. Fractions corresponding to the main peak of monomers are indicated. (b) Coomassie blue staining of the CB_2R-G_i-scFv16 complex. (c) Representative cryo-EM micrograph of the CB_2R-G_i-scFv16 complex. Scale bar: 50 nm. (d) Representative 2D averages (box size: 256 Å) showing diverse secondary structure features. (e) Flow chart of cryo-EM single particle analysis of the CB_2R-G_i-scFv16 complex. (f) Local resolution map of the CB_2R-Gi-scFv16 complex. (g) Fourier shell correlation curves of the CB_2R-G_i-scFv16 complex.

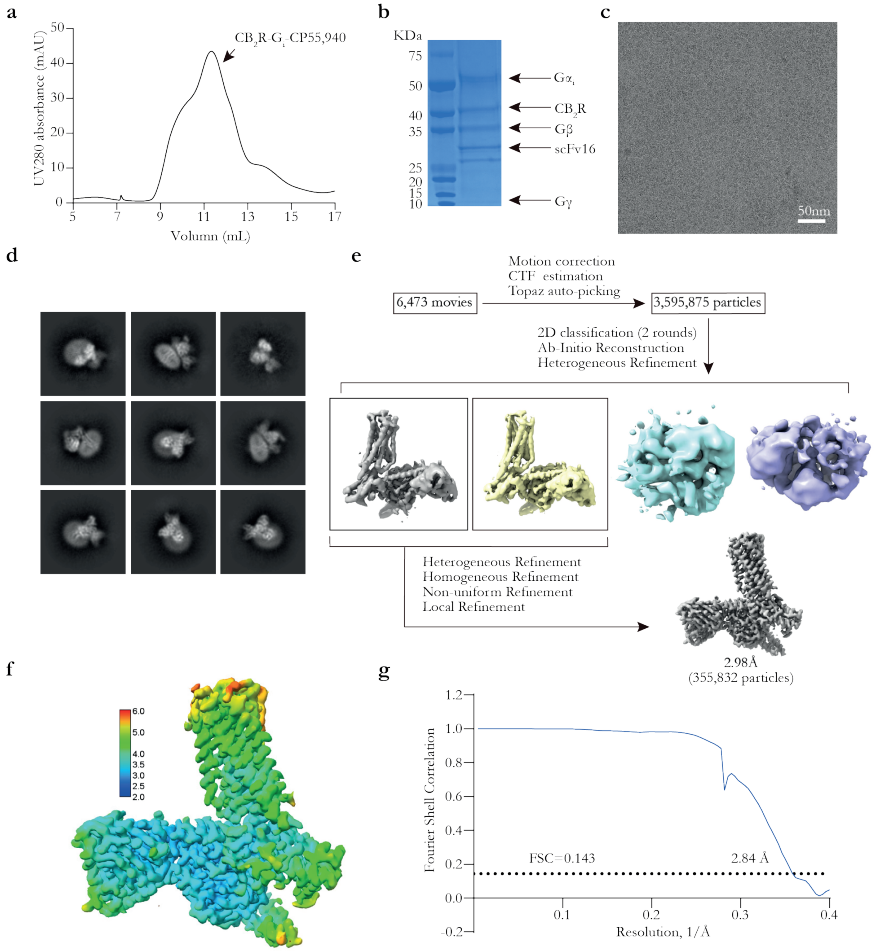

Figure 4.S5 **CB_2R-G_i-Scfv16-CP55,940 complex preparation and cryo-EM data processing.**
(a) Representative size-exclusion chromatography elution profile of CB_2R complex. Fractions corresponding to the main peak of monomers are indicated. (b) Coomassie blue staining of the CB_2R-G_i-scFv16 complex. (c) Representative cryo-EM micrograph of the CB_2R-G_i-scFv16 complex. Scale bar: 50 nm. (d) Representative 2D averages (box size: 256 Å) showing diverse secondary structure features. (e) Flow chart of cryo-EM single particle analysis of the CB_2R-G_i-scFv16 complex. (f) Local resolution map of the CB_2R-Gi-scFv16 complex. (g) Fourier shell correlation curves of the CB_2R-G_i-scFv16 complex.

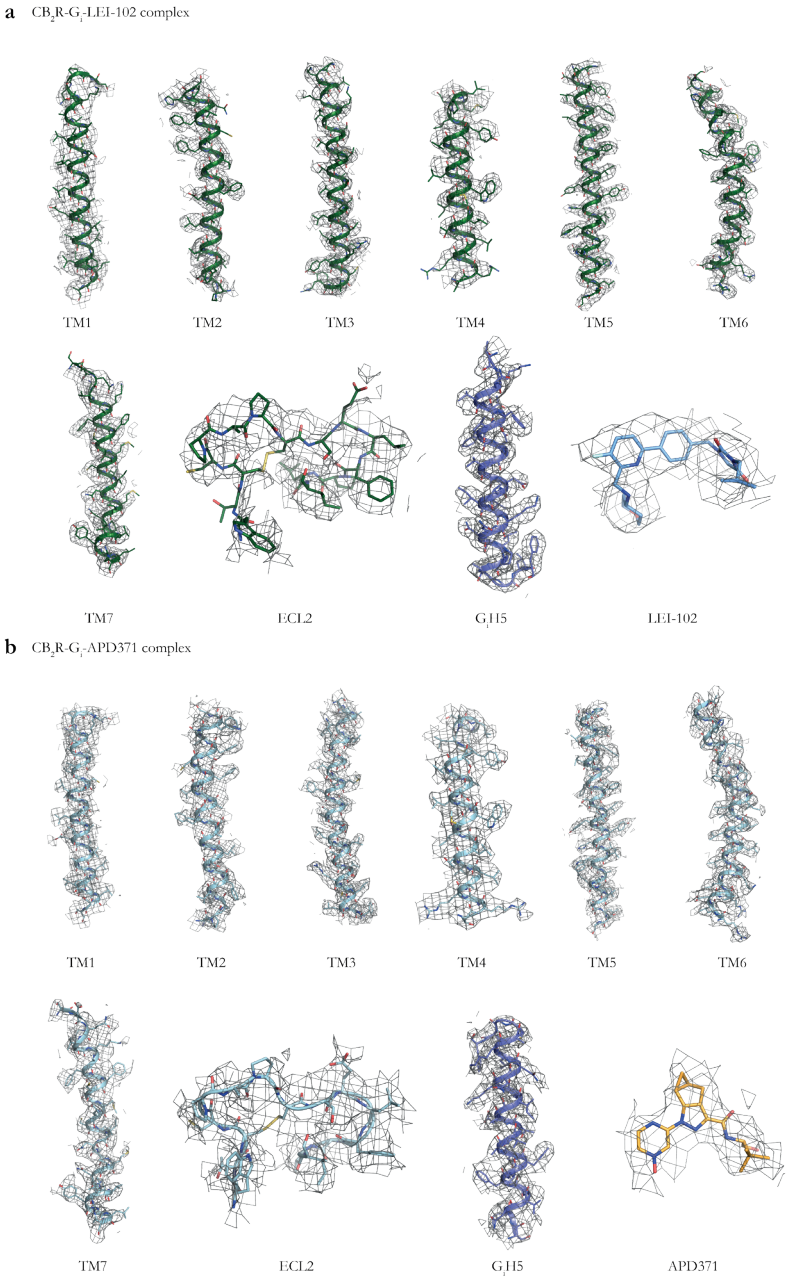
a CB2R-Gi-LEI-102 complex
TM1
TM2
TM3
TM4
TM5
TM6
TM7
ECL2
GiH5
LEI-102
b CB2R-Gi-APD371 complex
TM1
TM2
TM3
TM4
TM5
TM6
TM7
ECL2
GiH5
APD371

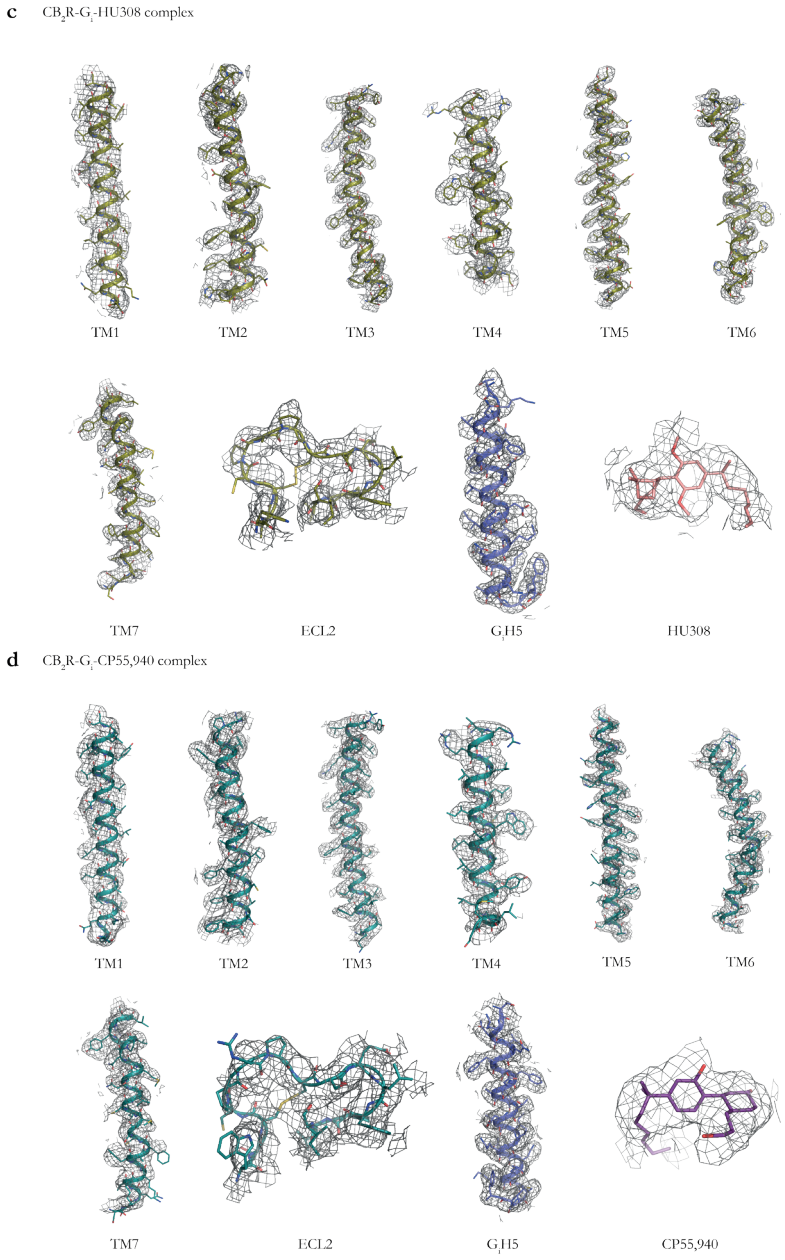

Figure 4.S6 **Representative cryo-EM density map of the CB_2R-G_i-scFv16 complex.**
(a-d) EM density map and models are shown for all transmembrane helices, ECL2, ligand and α5 helix of $G\alpha_i$ (G_iH5) in (a) LEI-102, (b) APD371, (c) HU308 and (d) CP55,940 bound CB_2R-G_i-scFv16 complex. Same color codes as in **Figure 4.2**.

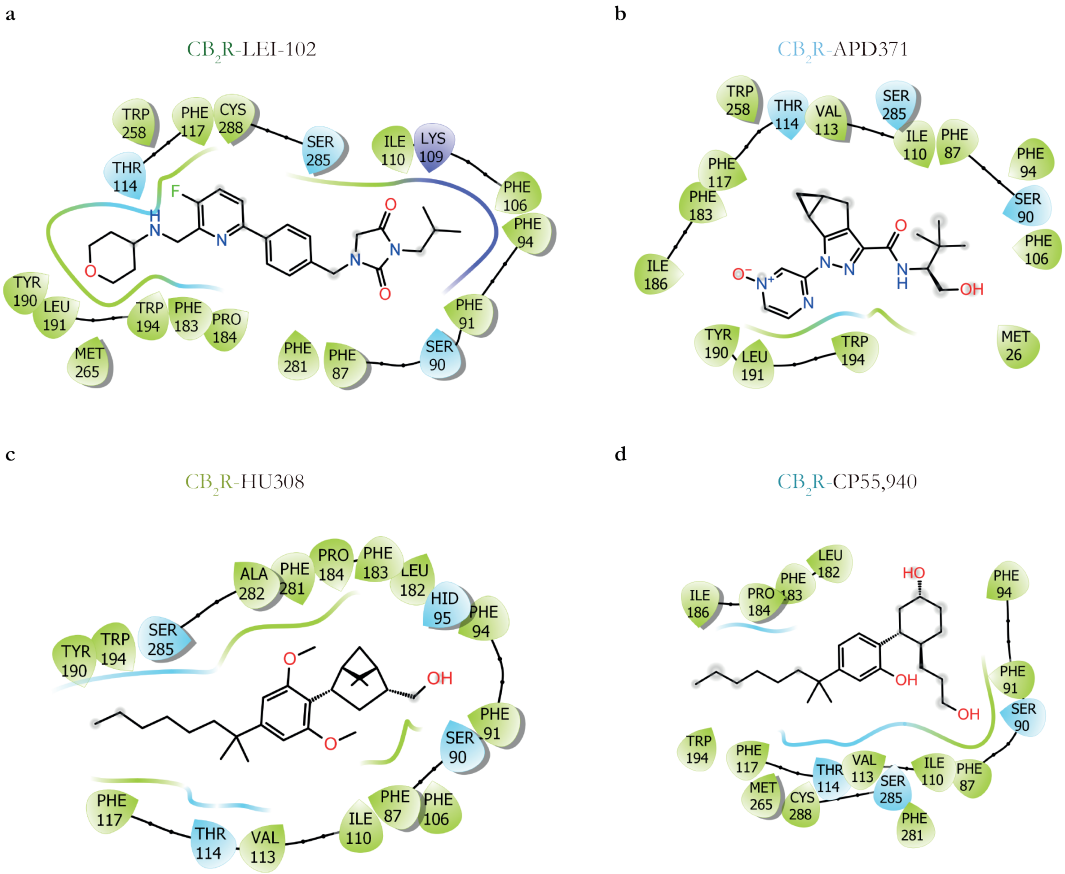

Figure 4.S7 Schematic representation of interactions between CB_2R and agonists.
(a-d) Schematic 2D representation of the binding pocket of agonist (a) LEI-102, (b) APD371, (c) HU308 and (d) CP55,940. Hydrophobic amino acids are colored in green, polar amino acids are colored in cyan, basic amino acids are colored in purple.

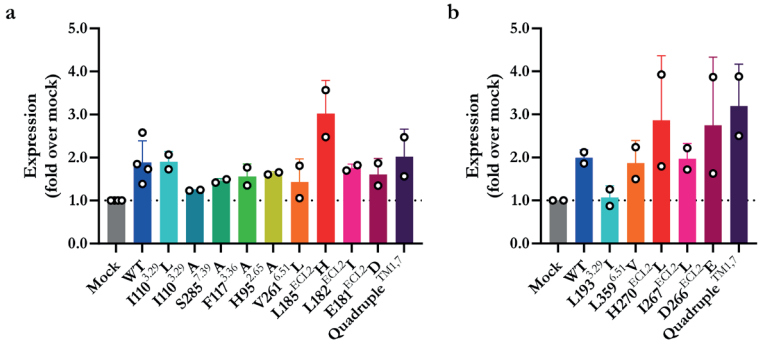

Figure 4.S8 **Cell surface receptor expression.**
Receptor expression as determined by ELISA for (a) CB_2R and (b) CB_1R WT and mutants. Data are expressed as mean ± SD of at least two experiments performed in quintuplicate.

4.S2 Supplementary tables

Table 4.S1 **Physico-chemical properties of the investigated ligands.**

Compound	cLogP	sLogP	TPSA (Å)	MW (g/mol)	Number Rotatable Bonds	Number HBD	Number HBA
Δ^9-THC	7.24	5.74	29.5	314.5	4	1	2
2-AG	6.89	5.03	66.8	378.6	17	2	4
AEA	6.18	5.24	49.3	347.5	16	2	2
CP55,940	5.82	5.66	60.7	376.6	10	3	3
HU308	8.00	6.63	38.7	414.6	10	1	3
APD371	-0.35	0.70	107.0	357.4	4	2	6
LEI-102	2.07	3.58	74.8	454.5	8	1	5

All values were calculated using RDKit KNIME nodes version 4.5.0.v202207051536, apart from cLogP which was calculated using ChemDraw 19.0.

Table 4.S2 **Functional activity, affinity and kinetic parameters of synthetic agonists and endocannabinoids on hCB_2R.**

Compound	pEC_{50}[a]	E_{max} (%)[b]	pK_i (K_i, nM)[c]	k_{on} ($M^{-1}s^{-1}$)[d]	ET (s)[e]	k_{off} (s^{-1})[f]	RT (min)[g]	K_D (nM)[h]
LEI-102	6.9 ± 0.2	76 ± 1	8.0 ± 0.1 (9.7)	(6.3 ± 1.1) × 10^4	16.0 ± 2.82	(1.0 ± 0.2) × 10^{-3}	16 ± 3.3	16.5
APD371	7.9 ± 0.1	134 ± 12	7.5 ± 0.1 (35.3)	(2.5 ± 0.4) × 10^4	40.1 ± 5.90	(3.7 ± 0.5) × 10^{-4}	45 ± 6.6	14.9
HU308	7.1 ± 0.2	91 ± 8	7.0 ± 0.1 (92.4)	(7.0 ± 2.3) × 10^3	143 ± 47.9	(2.3 ± 0.4) × 10^{-4}	71 ± 11	33.7
CP55,940	8.5 ± 0.3	98 ± 4	8.9 ± 0.1 (1.4)	(1.8 ± 0.4) × 10^6	0.57 ± 0.13	(5.2 ± 0.9) × 10^{-4}	32 ± 5.5	0.3
AEA	6.3 ± 0.2	60 ± 5	6.3 ± 0.1 (484.5)	(6.6 ± 0.5) × 10^3	152 ± 10.4	(2.4 ± 0.1) × 10^{-3}	6.8 ± 0.4	371.7
2-AG	5.9 ± 0.1	93 ± 22	7.0 ± 0.1 (97.3)	(5.3 ± 1.0) × 10^4	18.8 ± 3.61	(2.3 ± 0.3) × 10^{-3}	7.4 ± 1.0	42.7

[a, b] Potency (pEC_{50}) and efficacy (E_{max}) values were obtained from [^{35}S]GTPγS assays on HEK293T membranes transiently expressing CB_2R WT. The percentage maximum effect (E_{max} in %) was calculated compared to CP55,940. [c, d, f] Binding affinities (pK_i), association (k_{on}) and dissociation (k_{off}) rate constants were determined in [^{3}H]RO6957022 binding assays on CHOK1_hCB_2bgal membranes at 10 °C. [e] Engagement time (ET) of the compound to the receptor at 1 μM agonist was determined by $ET = 1/(k_{on} \cdot 1 \times 10^{-6})$ and is expressed in seconds (s), whereas k_{on} is expressed in $M^{-1}s^{-1}$. [g] Residence time (RT) was determined by $RT = 1/(60 \cdot k_{off})$ and is expressed in min, whereas k_{off} is expressed in s^{-1}. [h] Kinetic K_D values, defined by $K_D = k_{off}/k_{on}$. Values represent the mean ± SEM of at least three independent experiments performed in duplicate .

Table 4.S3 Characterization of cannabinoid CB_1 receptor mutations in [^{3}H]CP55,940 displacement assays.

	Construct	pK_D (K_D, nM)	LEI-102	APD371	HU308	CP55,940	AEA	2-AG
			Displacement (%)[a]			pK_i[b]	pK_i[b]	pK_i[b]
BP	**WT**	8.3 ± 0.1 (5.24)	17 ± 7	-19 ± 17	6 ± 7	8.3 ± 0.1	6.3 ± 0.1	5.6 ± 0.2
BP	**L193$^{3.29}$I**	N.D.	N.D.	N.D.	N.D.	N.D.	N.D.	N.D.
BP	**L359$^{6.51}$V**	8.6 ± 0.2 (2.80)	25 ± 6	18 ± 9	41 ± 10	8.5 ± 0.1	6.3 ± 0.1	5.9 ± 0.1
Ligand entry	**H270^{ECL2}L**	8.4 ± 0.2 (3.70)	47 ± 5	8 ± 3	46 ± 3	8.4 ± 0.1	6.3 ± 0.0	5.5 ± 0.2
Ligand entry	**I267^{ECL2}L**	8.6 ± 0.1 (2.57)	25 ± 3	-24 ± 17	-7 ± 19	8.6 ± 0.1	6.4 ± 0.1	6.1 ± 0.2
Ligand entry	**D266^{ECL2}E**	8.7 ± 0.2 (1.91)	38 ± 10	12 ± 7	34 ± 5	8.7 ± 0.1	6.7 ± 0.1	5.9 ± 0.1
Ligand entry	**Quadruple^{TM1,7}**	8.1 ± 0.2 (8.36)	26 ± 10	0 ± 25	-13 ± 22	8.1 ± 0.2	6.4 ± 0.0	5.3 ± 0.0

Mutations are shown in the numbering of the cannabinoid CB_1 receptor (CB_1R) amino acid sequence, as well as the Ballesteros and Weinstein GPCR numbering system. [a,b] Percentage of [^{3}H]CP55,940 displacement by 10 μM compound or binding affinity (pK_i) were determined in [^{3}H]CP55,940 displacement assays on HEK293T membranes transiently expressing CB_1R constructs. All values are presented as the mean ± SEM of at least three independent experiments performed in duplicate. One-way Welch ANOVA with Dunnett's T3 posthoc test was used to analyze differences in pK_D or pK_i values compared to WT. N.D. is not determined. BP is binding pocket.

Table 4.S4 **Cryo-EM Data collection, model refinement, and validation statistics.**

	CB_2R-LEI-102-G_i	**CB_2R-APD371-G_i**	**CB_2R-HU308-G_i**	**CB_2R-CP55,940-G_i**
Data collection and processing				
Magnification	105,000	105,000	105,000	105,000
Voltage (kV)	300	300	300	300
Electron exposure (e–/Å^2)	60	60	60	60
Defocus range (μm)	-1.0~-2.0	-1.0~-2.0	-1.0~-2.0	-1.0~-2.0
Pixel size (Å)	0.52	0.52	0.52	0.52
Symmetry imposed	C1	C1	C1	C1
Images (no.)	5,282	7,443	7,530	6,473
Initial particle images (no.)	3,398,611	5,239,870	4,653,294	3,595,875
Final particle images (no.)	762,471	1,152,146	355,832	440,292
Map resolution (Å)	2.98	3.08	2.97	2.84
FSC threshold	0.143	0.143	0.143	0.143
Map resolution range (Å)	2.9~6.0	2.9~6.0	2.9~6.0	2.7~5.0
Refinement				
Initial model used (PDB code)	6KPF	6KPF	6KPF	6KPF
Map sharpening *B* factor (Å^2)	-104.2	-118.6	110.8	-100.9
Model composition				
Non-hydrogen atoms	8,812	8,801	8,817	8,888
Protein residues	1,137	1,137	1,137	1,139
Ligands	1	1	1	1
B factors (Å^2)				
Protein	68.00	61.04	68.91	68.22
Ligand	76.90	104.87	67.91	85.48
R.m.s. deviations				
Bond lengths (Å)	0.003	0.009	0006	0.010
Bond angles (°)	0.57	1.24	0.69	1.80
Validation				
MolProbity score	1.82	1.64	1.83	1.46
Clashscore	12.29	5.04	12.11	7.74
Poor rotamers (%)	0.00	0.32	0.00	0.00
Ramachandran plot				
Favored (%)	96.60	94.46	96.43	97.86
Allowed (%)	3.40	5.54	3.57	2.14
Disallowed (%)	0.00	0.00	0.00	0.00

Table 4.S5 **Cell surface expression levels of cannabinoid receptor constructs in ELISA.**

	CB_2R	Expression (fold over mock)	CB_1R	Expression (fold over mock)
Binding pocket	**WT**	1.9 ± 0.5	**WT**	2.0 ± 0.2
	I110$^{3.29}$L	1.9 ± 0.2	**L193$^{3.29}$I**	1.1 ± 0.3
	I110$^{3.29}$A	1.2 ± 0.0	**L193$^{3.29}$A**	N.D.
	S285$^{7.39}$A	1.5 ± 0.1	**S383$^{7.39}$A**	N.D.
	F117$^{3.36}$A	1.6 ± 0.3	**F200$^{3.36}$A**	N.D.
	H95$^{2.65}$A	1.6 ± 0.0	**H178$^{2.65}$A**	N.D.
	V261$^{6.51}$L	1.4 ± 0.5	**L359$^{6.51}$V**	1.9 ± 0.5
Ligand entry	**L185^{ECL2}H**	3.0 ± 0.8	**H270^{ECL2}L**	2.9 ± 1.5
	L182^{ECL2}I	1.8 ± 0.1	**I267^{ECL2}L**	2.0 ± 0.4
	E181^{ECL2}D	1.6 ± 0.4	**D266^{ECL2}E**	2.7 ± 1.6
	Quadruple^{TM1,7}	2.0 ± 0.6	**Quadruple^{TM1,7}**	3.2 ± 1.0

Mutations are shown in the numbering of the cannabinoid CB_2 (CB_2R) or CB_1 receptor (CB_1R) amino acid sequence as well as the Ballesteros and Weinstein GPCR numbering system. Data are presented as fold over mock (empty pcDNA3.1 vector) and are mean ± SD of at least two individual experiments performed in. N.D. is not determined.

Table 4.S6 **Characterization of cannabinoid CB_2 receptor mutations in G protein activation assays.**

			LEI-102		APD371		HU308	
	Construct	**Basal[a]**	**pEC_{50}[b]**	**E_{max} (%)[c]**	**pEC_{50}**	**E_{max} (%)**	**pEC_{50}**	**E_{max} (%)**
Binding pocket	**WT**	1.0 ± 0.0	6.9 ± 0.2	103 ± 3	7.9 ± 0.1	109 ± 3	7.1 ± 0.2	105 ± 3
	$I110^{3.29}L$	1.0 ± 0.0	7.8 ± 0.1**	91 ± 3	6.7 ± 0.3	101 ± 7	6.7 ± 0.4	122 ± 12
	$I110^{3.29}A$	1.0 ± 0.1	7.0 ± 0.6	36 ± 13	6.6 ± 0.6	28 ± 9**	6.4 ± 0.5	27 ± 10**
	$S285^{7.39}A$	0.9 ± 0.0	6.3 ± 0.3	45 ± 8*	6.5 ± 0.3	49 ± 6*	5.9 ±0.1***	65 ± 18
	$F117^{3.36}A$	0.8 ± 0.1	N.D.	11 ± 11	N.D.	2 ± 6**	N.D.	5 ± 11*
	$H95^{2.65}A$	0.9 ± 0.0	<5	64 ± 7	5.7 ± 0.2**	50±1****	6.6 ± 0.6	67 ± 16
	$V261^{6.51}L$	0.8 ± 0.0	6.4 ± 0.0	8 ± 4****	6.9 ± 0.2*	6 ± 2****	<5	26 ± 7**
Ligand entry	**$L185^{ECL2}H$**	1.2 ± 0.1	6.9 ± 0.1	217 ± 21	8.0 ± 0.1	183 ± 16	6.8 ± 0.2	146 ± 8
	$L182^{ECL2}I$	0.8 ± 0.0*	7.4 ± 0.8	11 ± 8*	6.6 ± 0.4	17 ± 4***	<5	10 ± 7**
	$E181^{ECL2}D$	0.9 ± 0.0	6.9 ± 0.6	28 ± 13	6.9 ± 0.6	39 ± 6**	7.0 ± 0.7	32 ± 3****
	$Quadruple^{TM1,7}$	0.9 ± 0.0	6.2 ± 0.2	27 ± 5**	8.4 ± 0.1	35 ± 7*	N.D.	1 ± 9*

← **Table 4.S6** *(continued)*

		CP55,940		AEA		2-AG	
	Construct	**pEC_{50}**	**E_{max} (%)**	**pEC_{50}**	**E_{max} (%)**	**pEC_{50}**	**E_{max} (%)**
Binding pocket	**WT**	8.5 ± 0.3	99 ± 3	6.3 ± 0.2	106 ± 7	5.9 ± 0.1	85 ± 2
	$I110^{3.29}L$	9.4 ± 0.2	96 ± 3	N.D.	N.D.	N.D.	N.D.
	$I110^{3.29}A$	8.7 ± 0.4	30 ± 2****	N.D.	N.D.	N.D.	N.D.
	$S285^{7.39}A$	6.7 ± 0.1**	25 ± 5**	N.D.	N.D.	N.D.	N.D.
	$F117^{3.36}A$	N.D.	-1 ± 14	N.D.	N.D.	N.D.	N.D.
	$H95^{2.65}A$	6.9 ± 0.2**	68 ± 11	N.D.	N.D.	N.D.	N.D.
	$V261^{6.51}L$	<5	12 ± 7**	N.D.	N.D.	N.D.	N.D.
Ligand entry	**$L185^{ECL2}H$**	8.9 ± 0.4	142 ± 16	6.6 ± 0.0	210 ± 61	5.9 ± 0.2	171 ± 16
	$L182^{ECL2}I$	8.8 ± 0.8	19 ± 2****	<5	5 ± 17*	<5	15 ± 9*
	$E181^{ECL2}D$	7.9 ± 0.5	19 ± 10	<5	14 ± 5**	<5	22 ± 15
	$Quadruple^{TM1,7}$	8.1 ± 0.2	18 ± 14	<5	24 ± 7**	<5	6 ± 4***

Mutations are shown in the numbering of the cannabinoid CB_2 receptor (CB_2R) amino acid sequence as well as the Ballesteros and Weinstein GPCR numbering system. [a,b,c] Basal activity, potency (pEC_{50}) and efficacy (E_{max}) values were obtained from [^{35}S]GTPγS assays on HEK293T membranes transiently expressing CB_2R constructs. The percentage maximum effect at 10 μM (E_{max} in %) and the fold basal activity values were calculated compared to WT. pEC_{50} <5 was reported when the curve fit was not finished. Binding pocket mutations were not assessed for endocannabinoids. Values are presented as the mean ± SEM of at least three independent experiments performed in duplicate. One-way Welch ANOVA with Dunnett's T3 posthoc test or Welch's t-test was used to analyze differences in pEC_{50} and E_{max} values compared to WT (*p < 0.05, ** p < 0.01, *** p < 0.001, **** p < 0.00001). N.D. is not determined.

Table 4.S7 **Characterization of cannabinoid CB_2 receptor mutations in [^{3}H]CP55,940 displacement assays.**

	Construct	pK_D (K_D, nM)[a]	LEI-102 pK_i[b]	APD371 pK_i[b]	HU308 pK_i[b]	CP55,940 pK_i[b]	AEA pK_i[b]	2-AG pK_i[b]
BP	**WT**	9.1 ± 0.0 (0.77)	7.5 ± 0.1	8.0 ± 0.0	7.8 ± 0.2	9.2 ± 0.2	6.2 ± 0.1	5.8 ± 0.1
BP	**I110$^{3.29}$L**	9.2 ± 0.2 (0.66)	7.9 ± 0.0	7.1 ± 0.0***	7.3 ± 0.1	9.1 ± 0.1	6.1 ± 0.1	5.8 ± 0.1
Ligand entry	**L185^{ECL2}H**	9.2 ± 0.1 (0.60)	7.3 ± 0.1	7.7 ± 0.1	7.2 ± 0.0	9.4 ± 0.1	6.3 ± 0.1	6.4 ± 0.2
Ligand entry	**Quadruple^{TM1,7}**	9.0 ± 0.1 (1.08)	6.8 ± 0.2	6.7 ± 0.3	7.1 ± 0.4	9.2 ± 0.1	5.6 ± 0.3	<5

Mutations are shown in the numbering of the cannabinoid CB_2 receptor (CB_2R) amino acid sequence as well as the Ballesteros and Weinstein GPCR numbering system. [a,b] Binding affinities (pK_D, pK_i) were determined in [^{3}H]CP55,940 displacement assays on HEK293T membranes transiently expressing CB_2R constructs. pK_i <5 was reported when the curve fit was not finished. All values are presented as the mean ± SEM of at least three independent experiments performed in duplicate. One-way Welch ANOVA with Dunnett's T3 posthoc test was used to analyze differences in pK_i values compared to WT (*$p < 0.05$, ** $p < 0.01$, *** $p < 0.001$). Mutations I110$^{3.29}$L, S285$^{7.39}$A, F117$^{3.36}$A, H95$^{2.65}$A, V261$^{6.51}$L, L185^{ECL2}I and E181^{ECL2}D could not be assessed due to lack of specific binding window. BP is binding pocket.

Table 4.S8 **Characterization of cannabinoid CB_1 receptor mutations in G protein activation assays.**

	Construct	Basal[a]	LEI-102	APD371	HU308	CP55,940	AEA	2-AG
BP	**WT**	1.0 ± 0.0	1.0 ± 0.1	1.0 ± 0.0	0.8 ± 0.0	1.2 ± 0.1	1.2 ± 0.1	1.3 ± 0.1
BP	**L193$^{3.29}$I**	N.D.	N.D.	N.D.	N.D.	N.D.	N.D.	N.D.
BP	**L359$^{6.51}$V**	0.7 ± 0.0*	1.1 ± 0.1	1.1 ± 0.1	0.9 ± 0.1	1.4 ± 0.2	1.4 ± 0.2	1.4 ± 0.2
Ligand entry	**H270^{ECL2}L**	0.7 ± 0.0**	1.2 ± 0.0	1.1 ± 0.0	1.2 ± 0.1*	1.6 ± 0.1	1.4 ± 0.1	1.5 ± 0.1
Ligand entry	**I267^{ECL2}L**	1.1 ± 0.0	1.0 ± 0.0	0.9 ± 0.0	0.8 ± 0.0	1.0 ± 0.0	1.0 ± 0.1	1.1 ± 0.0
Ligand entry	**D266^{ECL2}E**	0.7 ± 0.0**	1.1 ± 0.1	0.9 ± 0.1	0.8 ± 0.1	1.4 ± 0.1	1.3 ± 0.1	1.5 ± 0.2
Ligand entry	**Quadruple^{TM1,7}**	0.6 ± 0.1**	1.2 ± 0.1	1.1 ± 0.0	0.9 ± 0.0	1.8 ± 0.1*	1.6 ± 0.1	1.8 ± 0.1*

Mutations are shown in the numbering of the cannabinoid CB_1 receptor (CB_1R) amino acid sequence as well as the Ballesteros and Weinstein GPCR numbering system. [a] Basal activity is expressed as fold over WT. Agonist-mediated activation values were obtained from [^{35}S]GTPγS assays on HEK293T membranes transiently expressing CB_1R constructs using 10 μM agonist, and are expressed as fold over its basal. Values are presented as the mean ± SEM of three independent experiments performed in duplicate (*n* indicates the number of biological replicates). One-way Welch ANOVA with Dunnett's T3 posthoc test was used to analyze differences in activation values compared to WT (*$p < 0.05$, ** $p < 0.01$, *** $p < 0.001$, **** $p < 0.00001$). Exact p values are given between square brackets. N.D. is not determined. BP is binding pocket.

Chapter 5

Dual allosteric and orthosteric pharmacology of synthetic analog cannabidiol-dimethylheptyl, but not cannabidiol, on the cannabinoid CB_2 receptor

Jara Bouma, Jeremy D. Broekhuis, Cas van der Horst, Poulami Kumar, Alessia Ligresti, Mario van der Stelt, Laura H. Heitman

Adapted from: *Biochemical Pharmacology* (2023) **218**, 115924

Abstract

Cannabinoid CB_2 receptor (CB_2R) is a class A G protein-coupled receptor (GPCR) involved in a broad spectrum of physiological processes and pathological conditions. For that reason, targeting CB_2R might provide therapeutic opportunities in neurodegenerative disorders, neuropathic pain, inflammatory diseases, and cancer. The main components from Cannabis sativa, such as Δ^9-tetrahydrocannabinol (Δ^9-THC) and cannabidiol (CBD), have been therapeutically exploited and synthetically-derived analogs have been generated. One example is cannabidiol-dimethylheptyl (CBD-DMH), which exhibits anti-inflammatory effects. Nevertheless, its pharmacological mechanism of action is not yet fully understood and is hypothesized for multiple targets, including CB_2R. The aim of this study was to further investigate the molecular pharmacology of CBD-DMH on CB_2R while CBD was taken along as control. These compounds were screened in equilibrium and kinetic radioligand binding studies and various functional assays, including G protein activation, inhibition of cAMP production and ß-arrestin-2 recruitment. In dissociation studies, CBD-DMH allosterically modulated the radioligand binding. Furthermore, CBD-DMH negatively modulated the G protein activation of reference agonists CP55,940, AEA and 2-AG, but not the agonist-induced ß-arrestin-2 recruitment. Nevertheless, CBD-DMH also displayed competitive binding to CB_2R and partial agonism on G protein activation, inhibition of cAMP production and ß-arrestin-2 recruitment. CBD did not exhibit such allosteric behavior and only very weakly bound CB_2R without activation. This chapter shows a dual binding mode of CBD-DMH, but not CBD, to CB_2R with the suggestion of two different binding sites. Altogether, it encourages further research into this dual mechanism which might provide a new class of molecules targeting CB_2R.

5.1 Introduction

The cannabinoid CB_1 and CB_2 receptors (CB_1R and CB_2R) are class A G protein-coupled receptors (GPCRs) that are responsible for signal transduction of the endocannabinoid system (ECS)[1]. Both receptors couple primarily to $G\alpha_{i/o}$ proteins and recruit ß-arrestin upon stimulation by agonists, such as the endocannabinoids anandamide (AEA) and 2-arachidonoylglycerol (2-AG)[2,3]. However, due to the distinct localization of these receptors, they regulate different processes. CB_1R is the most abundant GPCR in the central nervous system and involved in the regulation of cognition and memory. On the contrary, CB_2R is primarily expressed on cells of the immune system and modulates (neuro)inflammatory processes[4]. Therefore, specific targeting of CB_2R might provide opportunities in the treatment of a variety of pathological conditions characterized by low-grade inflammation, such as neuropathic pain, inflammatory bowel disease, neurodegenerative disorders, and cancer[5].

The main components of *Cannabis sativa* Δ^9-tetrahydrocannabinol (Δ^9-THC) and cannabidiol (CBD), and synthetically-derived analogs have been therapeutically exploited to target CB_2R[6]. Over the years, CBD has received increasing attention due to its variety of therapeutic effects, including antiepileptic, anti-inflammatory, analgesic, and anti-cancer properties as well as neuroprotective and neuromodulatory functions in Parkinson's disease[7,8]. Currently, Epidiolex® (CBD) and Sativex® (1:1 CBD: Δ^9-THC) are approved for the treatment of Dravet syndrome, Lennox-Gastaut syndrome and multiple sclerosis-associated spasticity[9]. Additionally, CBD has been brought to the attention of the public as component of oils or infused beverages that can be obtained without a prescription[10]. However, the pharmacological mechanism of action of CBD is not yet fully understood and has been linked to interactions with various targets via contradicting mechanisms[8,11–13].

In view of the promising therapeutic possibilities of CBD, various derivatives have been synthesized over the years. One such derivative is cannabidiol-dimethylheptyl (CBD-DMH) in which the pentyl side chain of CBD is replaced for a dimethylheptyl chain (**Figure 5.1**)[14]. Similar to CBD, CBD-DMH is devoid of any psychotropic activity and has been shown to possess anti-inflammatory effects by reducing the levels of various pro-inflammatory genes and key inflammatory mediators, such as nitric oxide and reactive oxygen intermediates[14–17]. Additionally, CBD-DMH induced apoptosis in myeloblastic cells, but not healthy control cells[18]. Fride *et al.* further demonstrated efficacy and anti-inflammatory activity of CBD-DMH *in vivo*[19]. These beneficial effects of CBD-DMH have been hypothesized to be mediated via various proteins, such as CB_2R, CB_1R, adenosine A_{2A} receptor and an anandamide transporter[15–17,19–22]. Interestingly, low (orthosteric) affinity of CBD-DMH to CB_2R has been found, but also allosteric modulation of downstream signaling pathways has been speculated[20–22]. Nevertheless, the exact molecular mechanisms remain unknown.

In view of the therapeutic possibilities, we aimed to investigate the molecular pharmacological effect of CBD-DMH on CB_2R, while close analog CBD was taken along. The possibility of an allosteric interaction with CB_2R was explored in equilibrium and kinetic radioligand binding studies in which all commercially available proclaimed allosteric modulators of the ECS were screened for validation (**Figure 5.1**)[23]. Of these, only CBD-DMH displayed

allosteric properties on CB_2R and was further characterized in radioligand binding assays and functional studies. CBD-DMH demonstrated competitive binding to CB_2R and (partial) agonism on G protein activation, inhibition of cAMP production and ß-arrestin-2 recruitment. Additionally, CBD-DMH negatively impacted the affinity of a set of reference ligands. Furthermore, in the presence of CBD-DMH the G protein activation of CP55,940 and 2-AG was impaired, which was not observed in ß-arrestin-2 recruitment assays to CB_2R. This chapter shows that CBD-DMH has allosteric interactions with CB_2R, but also competitively binds to the receptor with orthosteric ligands. It therefore invites further research into this dual mechanism of CBD-DMH to CB_2R which might provide a new class of molecules targeting CB_2R.

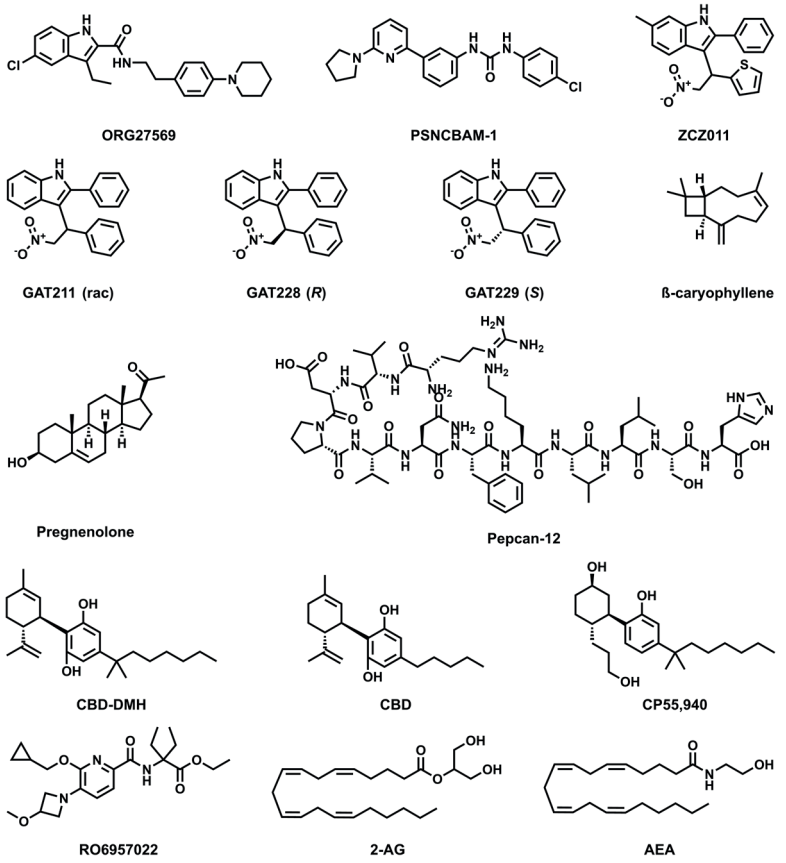

Figure 5.1 **Chemical structures of reported allosteric modulators and references ligands of the endocannabinoid system.**

5.2 Results

5.2.1 *Screening of CBD-DMH and proclaimed allosteric modulators of ECS on CB_2R*

To explore the molecular pharmacological profile of CBD-DMH on CB_2R, it was screened in single point displacement assays using inverse agonist [^{3}H]RO6957022 and agonist [^{3}H]CP55,940 along with ten proclaimed ECS modulators for reference (**Figure 5.1**, **5.2a**, **Table 5.1**). ZCZ011, GAT211, GAT228, GAT229 and CBD-DMH displaced [^{3}H]RO6957022 between 18 and 42% when tested at 10 µM, whereas ORG27569 and CBD displaced the radioligand more than 50% at this concentration. PSNCBAM-1, ß-caryophyllene and pregnenolone did not displace [^{3}H]RO6957022 at all and pepcan-12 slightly increased the specific binding of [^{3}H]RO6957022. Using [^{3}H]CP55,940, six compounds displaced the radioligand between 17 and 45%, but only 10 µM CBD and CBD-DMH displaced the agonistic radioligand for 65% and 105%, respectively. Compounds ß-caryophyllene, pregnenolone and pepcan-12 did not influence [^{3}H]CP55,940 binding.

To investigate allosteric effects of CBD-DMH and the ECS modulators, radioligand dissociation assays were executed. For a quick screening of all compounds, a single point

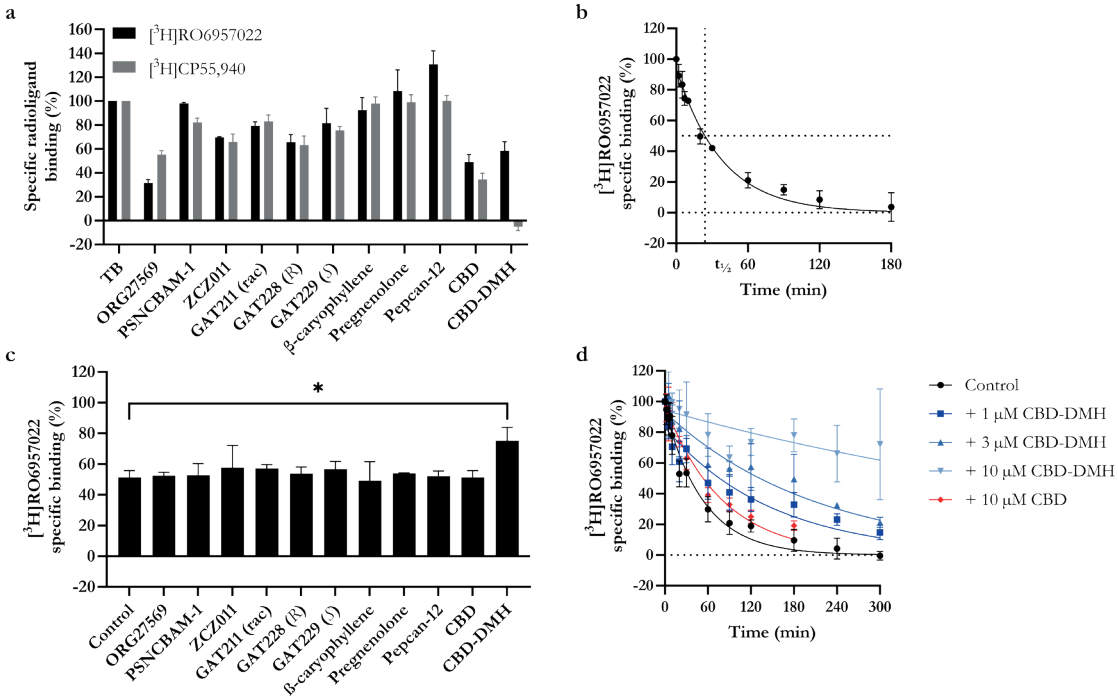

Figure 5.2 Screening of reported allosteric modulators of the ECS in radioligand binding assays on hCB_2R.

(a) Displacement of [^{3}H]RO6957022 or [^{3}H]CP55,940 by 10 µM compound. (b) Dissociation of [^{3}H]RO6957022 from hCB_2R at 10 °C with indicated half life time ($t_{½}$). (c) Binding of [^{3}H]RO6957022 after 27 min of dissociation ($t_{½}$) from hCB_2R induced by 10 µM AM630 in the absence (control) or presence of 10 µM of compound. (d) Dissociation curves of [^{3}H]RO6957022 from hCB_2R induced by 10 µM AM630 in the absence (control) or presence of increasing concentrations of CBD-DMH or 10 µM CBD. Total binding (TB) of specific radioligand was set to 100%. Data are shown as mean ± SD from at least (a,c) two or (b,d) three independent experiments performed in duplicate.

Table 5.1 Screening of reported allosteric modulators of the ECS in radioligand binding assays on hCB_2R.

Compound	[^{3}H]RO6957022 displacement (%)[a]	[^{3}H]CP55,940 displacement (%)[b]	[^{3}H]RO6957022 binding (%)[c]
Control	N.A.	N.A.	51 ± 5
ORG27569	68 ± 3	45 ± 3	52 ± 2
PSNCBAM-1	2 ± 1	18 ± 4	53 ± 8
ZCZ011	30 ± 1	34 ± 7	58 ± 14
GAT211 (rac)	21 ± 3	17 ± 5	57 ± 2
GAT228 (*R*)	34 ± 6	37 ± 8	54 ± 4
GAT229 (*S*)	18 ± 12	25 ± 3	57 ± 5
β-caryophyllene	8 ± 11	2 ± 6	49 ± 12
Pregnenolone	-8 ± 18	1 ± 6	54 ± 0
Pepcan-12	-31 ± 11	0 ± 4	52 ± 3
CBD	51 ± 6	65 ± 5	51 ± 5
CBD-DMH	42 ± 8	105 ± 3	75 ± 9*

Values represent the mean ± SD of at least two individual experiments performed in duplicate. [a] Percentage [^{3}H]RO6957022 displacement from hCB_2R in the presence of 10 μM compound after 2 h. [b] Percentage [^{3}H]CP55,940 displacement from hCB_2R in the presence of 10 μM compound after 2 h. [c] Percentage [^{3}H]RO6957022 binding after 27 minutes of dissociation from hCB_2R induced by 10 μM AM630 in absence (control) or presence of 10 μM compound. One-way ANOVA with Dunnett's multiple comparisons test was used to analyze differences in specific binding compared to control (*$p < 0.05$). N.A. is not applicable.

[^{3}H]RO6957022 dissociation assay was designed. In the presence of 10 μM AM630, dissociation of [^{3}H]RO6957022 followed a monophasic decay until full dissociation was reached after approximately 180 min, where its dissociation half-life ($t_{½}$) was 27 minutes, i.e., the point where 50% of the radioligand was still bound (**Figure 5.2b**). Subsequently, all eleven compounds were screened in a single point [^{3}H]RO6957022 dissociation assay at $t_{½}$ of 27 minutes of dissociation, i.e., the time point that equally allows for the observation of an increase or decrease in radioligand dissociation rate (**Figure 5.2c**). Only CBD-DMH significantly increased the specific binding of [^{3}H]RO6957022 to 75 ± 9% compared to 51 ± 5% of control (**Figure 5.2c**, **Table 5.1**). Interestingly, close analog CBD did not change the specific binding (51 ± 5%). To further quantify these effects, a full curve dissociation in the presence of CBD-DMH and CBD was performed (**Figure 5.2d**, **Table 5.2**). CBD-DMH drastically altered the dissociation of [^{3}H]RO6957022, which could not be quantified in the three hour timeframe. Therefore, the incubation time was extended to five hours and time points were distributed to capture the full response. The dissociation rate constant (k_{off}) of [^{3}H]RO6957022 was significantly reduced in the presence of 1 and 3 μM CBD-DMH with k_{off} values of 0.007 ± 0.002 min^{-1} and 0.005 ± 0.001 min^{-1}, respectively, compared to 0.019 ± 0.005 min^{-1} in the control condition. Furthermore, even after 5 h incubation in the presence of 10 μM CBD-DMH this parameter could no longer be quantified, as the radioligand's dissociation was extremely impaired. The k_{off} of [^{3}H]RO6957022 in the presence of 10 μM CBD was also significantly reduced to 0.013 ± 0.001 min^{-1}, but this was less than 2-fold from control and is therefore not considered biologically relevant (**Figure 5.2d**, **Table 5.2**).

Table 5.2 Dissociation rate constants in the absence and presence of increasing concentrations of CBD-DMH or 10 μM CBD in [^{3}H]RO6950722 dissociation assays.

Modulator	k_{off} (min^{-1})
Control	0.019 ± 0.005
+ 1 μM CBD-DMH	0.007 ± 0.002***
+ 3 μM CBD-DMH	0.005 ± 0.001***
+ 10 μM CBD-DMH	N.D.
+ 10 μM CBD	0.013 ± 0.001*

Values represent the mean ± SD of at least three individual experiments performed in duplicate. One-way ANOVA with Dunnett's multiple comparisons test was used to analyze differences in k_{off} compared to vehicle (*p < 0.05, ** p < 0.01, *** p < 0.001, **** p < 0.00001). N.D. is not determined.

Together, the results from the screening assays suggest a weak competitive interaction of ORG27569 and CBD with [^{3}H]CP55,940 at CB_2R, while CBD weakly and CBD-DMH more potently displaced [^{3}H]RO6957022. Interestingly, CBD-DMH is also an allosteric enhancer of [^{3}H]RO6957022 binding at CB_2R, indicating a second possible binding site. Notably, none of the other compounds exhibit evident allosteric enhancement or inhibition. Therefore, the binding mechanism of CBD-DMH is further explored, while taking CBD along as control.

5.2.2 Affinity of orthosteric reference ligands in the absence or presence of CBD-DMH and CBD

The competitive behavior of CBD-DMH and CBD was further investigated in full curve displacement assays with [^{3}H]RO6957022. CBD-DMH displayed a pK_i value of 6.46 ± 0.20, while a remaining 20% of [^{3}H]RO6957022 was not displaced (**Figure 5.3a**, **Table 5.3**). CBD only showed weak displacement at 10 μM, as such its affinity for CB_2R could not be determined (**Figure 5.3a**).

As allosteric modulation can be probe-dependent, the modulating effect of CBD-DMH and CBD was investigated on the binding of various reference ligands. Specifically, modulation of CP55,940 (which was also used as a radioligand in the screen, **Figure 5.2a**), and two endogenous agonists, i.e., 2-AG and AEA, was evaluated and compared to their effect on unlabeled RO6957022. To this end, [^{3}H]RO6957022 displacement assays in the absence or presence of increasing concentrations of CBD-DMH or 3 μM CBD were performed (**Figure 5.3**, **Table 5.3**). The control conditions reflected the increased displacement of [^{3}H]RO6957022 in the presence of increasing concentrations of CBD-DMH from 0% up to 80% and 20% displacement in the presence of 3 μM CBD, which corresponded well to their values in the displacement curves (**Figure 5.3**).

For both inverse agonist RO6957022 and agonist CP55,940 a trend in decreased apparent affinity (pIC_{50}) was found in the presence of increasing concentrations of CBD-DMH (**Figure 5.3c**,**d**, **Table 5.3**). Specifically, their apparent affinities were significantly decreased

Table 5.3 Apparent affinity (pK_i) of CBD-DMH or apparent affinity (pIC_{50}) of orthosteric ligands in the absence or presence of CBD-DMH and CBD as determined in [^{3}H]RO6957022 displacement assays.

Modulator	CBD-DMH	RO6957022	CP55,940	2-AG	AEA
Control	6.46 ± 0.20	8.39 ± 0.49	8.78 ± 0.28	6.20 ± 0.16	5.58 ± 0.16
+ 0.03 μM CBD-DMH	N.A.	8.30 ± 0.32	8.62 ± 0.26	6.14 ± 0.06	5.49 ± 0.17
+ 0.3 μM CBD-DMH	N.A.	7.97 ± 0.12	8.52 ± 0.63	6.06 ± 0.21	5.57 ± 0.25
+ 3 μM CBD-DMH	N.A.	6.99 ± 0.55**	7.04 ± 0.92*	5.01 ± 0.20****	4.47 ± 0.50**
+ 3 μM CBD	N.A.	8.04 ± 0.45	8.60 ± 0.36	5.88 ± 0.05	5.45 ± 0.14

Values represent the mean ± SD of at least three individual experiments performed in duplicate. pK_i (CBD-DMH) and pIC_{50} values of orthosteric reference ligands in the absence (control) or presence of increasing concentrations of CBD-DMH or 3 μM CBD were obtained from [^{3}H]RO6957022 displacement assays on membranes stably expressing hCB_2R. One-way ANOVA with Dunnett's multiple comparisons test was used to analyze differences in pIC_{50} compared to control (*p < 0.05, ** p < 0.01, *** p < 0.001, **** p < 0.00001). N.A. is not applicable.

in the presence of the highest concentration of 3 μM CBD-DMH by 25- and 54-fold, respectively. Similarly, the apparent affinities of endogenous agonists 2-AG and AEA were significantly reduced in the presence of 3 μM CBD-DMH by 15- and 13-fold compared to control condition. However, 3 μM CBD did not statistically significant affect the apparent affinity of any orthosteric ligand (**Figure 5.3c-f**, **Table 5.3**). This further confirms the lack of allosteric modulation by CBD at CB_2R, whereas CBD-DMH impaired the apparent affinity of the inverse agonist, synthetic agonist, and endogenous agonists at CB_2R. Nevertheless, CBD-DMH also competes with RO6957022 for binding to CB_2R.

5.2.3 Ga_i protein activation by CBD-DMH and modulation of orthosteric reference agonists in the absence or presence of CBD-DMH and CBD

[^{35}S]GTPγS binding assays were performed to investigate $G\alpha_i$ protein activation by CBD-DMH and CBD. CBD-DMH behaved as a partial agonist with a pEC_{50} value of 7.42 ± 0.14 and E_{max} value of 69 ± 5% compared to full agonist CP55,940 (**Figure 5.4a**, **Table 5.4**). CBD did not induce any $G\alpha_i$ protein activation on CB_2R. Furthermore, this agonistic effect of CBD-DMH was also observed in a cAMP assay with a potency of 8.05 ± 0.28, i.e., cAMP production was inhibited by CBD-DMH at CB_2R (**Table 5.4**).

To evaluate the modulatory effect of CBD-DMH and CBD on $G\alpha_i$ protein activation induced by orthosteric agonists CP55,940, 2-AG and AEA, functional [^{35}S]GTPγS binding assays were performed in the absence and presence of increasing concentrations of CBD-DMH and 0.3 μM CBD (**Figure 5.4**, **Table 5.4**). Firstly, the basal conditions reflected the partial agonistic behavior of CBD-DMH for $G\alpha_i$ protein activation, which was not observed for CBD (**Figure 5.4**). Secondly, a dose-dependent negative modulation of CP55,940-incuded $G\alpha_i$ protein activation was observed in the presence of CBD-DMH (**Figure 5.4b**). Specifically, pEC_{50} values were significantly decreased from 8.90 ± 0.45 to 7.01 ± 0.46 in the presence of 0.3 μM CBD-DMH (**Table 5.4**). On the other hand, CBD did not modulate CP55,940 activation of CB_2R. Neither CBD-DMH nor CBD affected the maximum activation level by CP55,940. Although not statistically significant, a trend was observed that CBD-DMH dose-dependently decreased the potency of 2-AG, without affecting its

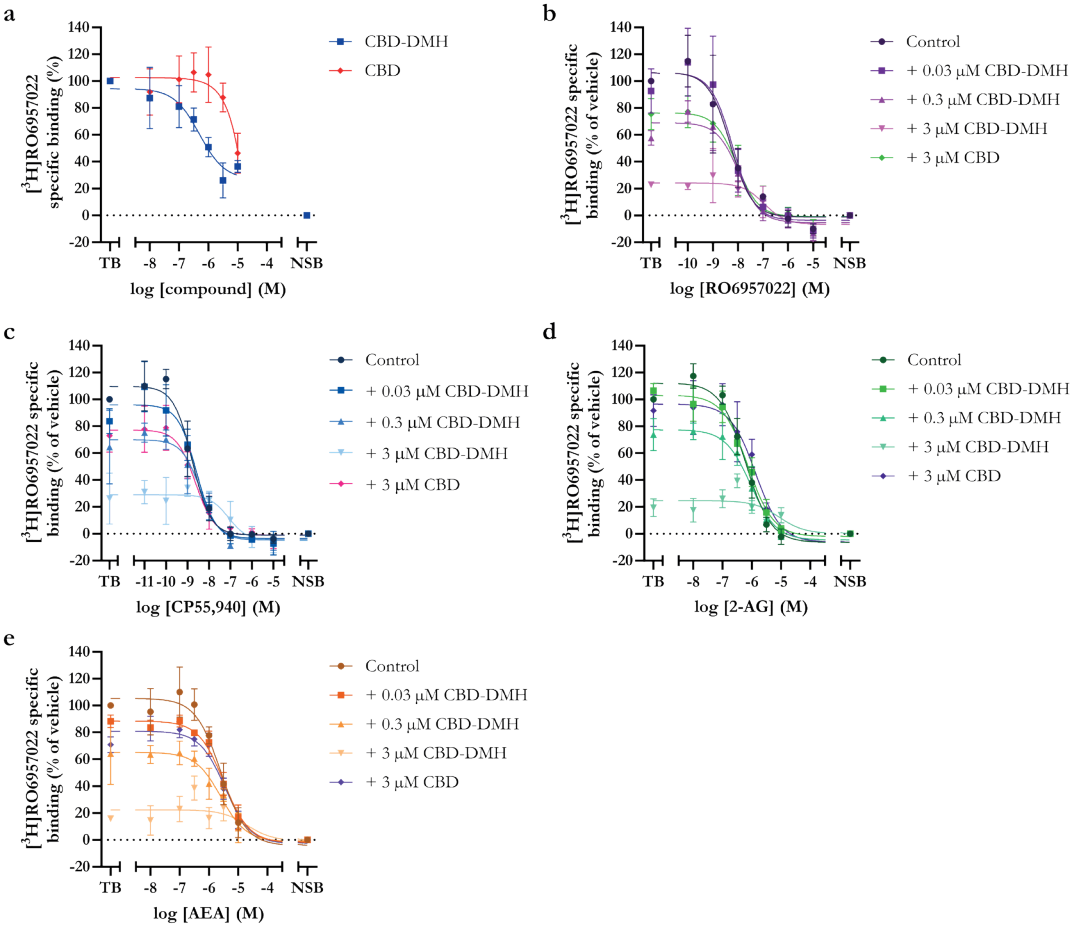

Figure 5.3 **Affinity and modulation of affinity of orthosteric ligands by CBD-DMH and CBD.** (a) [^{3}H]RO6957022 displacement by CBD-DMH and CBD. [^{3}H]RO6950722 displacement by (b) orthosteric inverse agonist RO6957022, orthosteric agonists (c) CP55,940, (d) 2-AG and (e) AEA in the absence (control) or presence of increasing concentrations of CBD-DMH or 3 µM CBD. Data are shown as mean ± SD from at least three independent experiments performed in duplicate.

maximum activation (**Figure 5.4c**, **Table 5.4**). CBD did neither statistically significant affect the potency of 2-AG nor AEA (**Figure 5.4c**,**d**, **Table 5.4**). Finally, AEA-induced G protein activation was differently impacted by CBD-DMH compared to the other agonists, as the level of activation induced by CBD-DMH was higher than AEA efficacy (**Figure 5.4a**). Hence, the increasing concentrations of AEA caused the level of CBD-DMH activation to be brought back to the maximal AEA activation level. Noteworthy, the lowest CBD-DMH concentration tested (0.03 µM) resulted in a level of G protein activation equal to AEA's efficacy, i.e., resulting in a flat dose-response curve.

Table 5.4 Potency (pEC_{50}) and maximum activation (E_{max}) of orthosteric ligands in the absence or presence of CBD-DMH and CBD determined in functional assays.

Assay	Modulator	CBD-DMH		CP55,940		2-AG		AEA	
		pEC_{50}	E_{max} (%)	pEC_{50}	E_{max} (%)	pEC_{50}	E_{max} (%)	pEC_{50}	E_{max} (%)
[^{35}S]GTPγS binding	Control	7.42 ± 0.14	69 ± 5	8.90 ± 0.45	106 ± 10	6.39 ± 0.26	105 ± 6	7.03 ± 0.34	123 ± 11
	+ 0.03 μM CBD-DMH	N.A.	N.A.	8.42 ± 0.01	99 ± 13	6.30 ± 0.41	102 ± 7	N.D.	100 ± 34$^{\#}$
	+ 0.1 μM CBD-DMH	N.A.	N.A.	8.01 ± 0.02*	94 ± 4	6.18 ± 0.83	98 ± 16	N.D.	84 ± 29$^{\#}$
	+ 0.3 μM CBD-DMH	N.A.	N.A.	7.01 ± 0.46****	98 ± 3	5.63 ± 0.32	100 ± 20	N.D.	83 ± 27$^{\#}$
	+ 0.3 μM CBD	N.A.	N.A.	9.00 ± 0.47	110 ± 12	6.27 ± 0.46	89 ± 16	6.52 ± 0.14	86 ± 20
cAMP	Control	8.05 ± 0.28	N.A.	N.A.	N.A.	N.A.	N.A.	N.A.	N.A.
ß-arrestin-2 recruitment	Control	6.92 ± 0.13	47 ± 15	8.35 ± 0.12	99 ± 3	5.68 ± 0.09	100 ± 17$^{\#}$	6.53 ± 0.13	98 ± 3
	+ 0.1 μM CBD-DMH	N.A.	N.A.	8.50 ± 0.11	115 ± 9	5.32 ± 0.76	104 ± 13$^{\#}$	6.51 ± 0.32	102 ± 8
	+ 0.3 μM CBD-DMH	N.A.	N.A.	8.46 ± 0.06	100 ± 5	5.58 ± 0.40	111 ± 29$^{\#}$	6.41 ± 0.82	103 ± 14
	+ 1 μM CBD-DMH	N.A.	N.A.	8.28 ± 0.32	115 ± 13	5.64 ± 0.28	104 ± 14$^{\#}$	N.D.	105 ± 21
	+ 1 μM CBD	N.A.	N.A.	8.43 ± 0.12	72 ± 11	5.54 ± 0.16	103 ± 23$^{\#}$	6.48 ± 0.31	107 ± 18

Values represent the mean ± SD of at least three individual experiments performed in duplicate. Potency (pEC_{50}) and maximum effect (E_{max}) or effect at 10 μM values of orthosteric reference ligands (#) in the absence (control) or presence increasing concentrations of CBD-DMH or CBD were obtained from [^{35}S]GTPγS binding, cAMP or ß-arrestin-2 recruitment assays on membranes or cells stably expressing hCB_2R, respectively. The percentage maximum effect at 10 μM was calculated compared to the top of the control curves. One-way ANOVA with Dunnett's multiple comparisons test was used to analyze differences in pEC_{50} compared to control (*$p < 0.05$, ** $p < 0.01$, *** $p < 0.001$, **** $p < 0.00001$). N.D. is not determined. N.A. is not applicable.

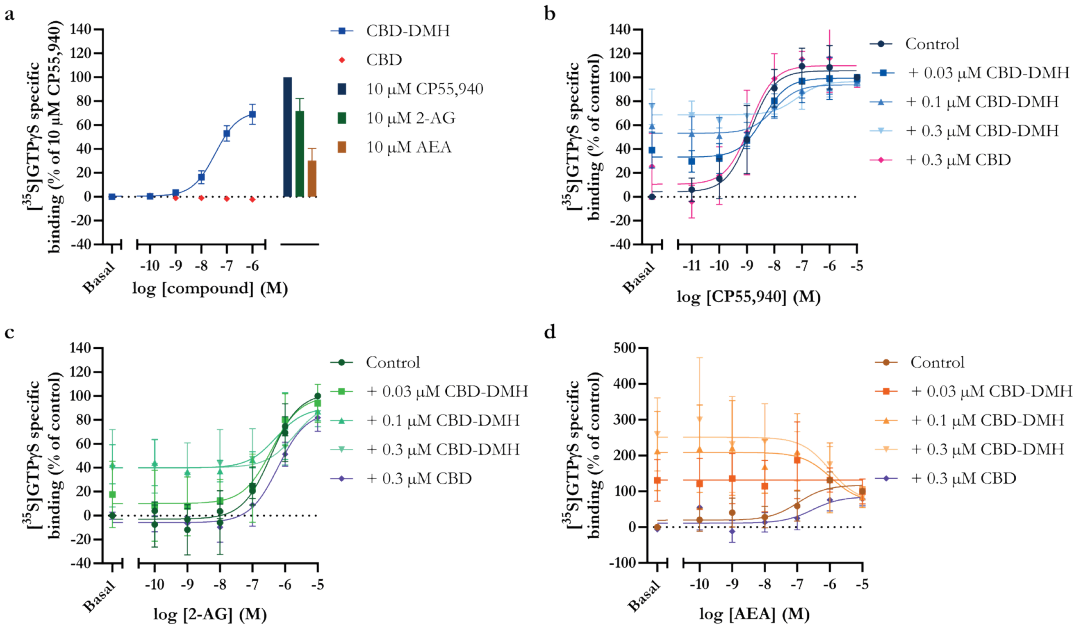

Figure 5.4 G protein activation and modulation thereof by CBD-DMH and CBD.
(a) [^{35}S]GTPγS binding by CBD-DMH and CBD compared to full agonist CP55,940. Modulation of orthosteric agonists (b) CP55,940, (c) 2-AG and (d) AEA-induced [^{35}S]GTPγS binding in the absence (control) or presence of increasing concentrations of CBD-DMH or 0.3 μM CBD. Data are shown as mean ± SD from at least three independent experiments performed in duplicate.

In conclusion, we observed partial agonism of CBD-DMH, but not CBD, in G protein activation and cAMP assays on CB_2R. Moreover, CBD-DMH, but not CBD, also negatively modulated agonist-induced $G\alpha_i$ protein activation.

5.2.4 ß-arrestin-2 recruitment by CBD-DMH and modulation of orthosteric reference agonists in the absence or presence of CBD-DMH and CBD

Another functional assay was performed to investigate the effect of CBD-DMH and CBD on ß-arrestin-2 recruitment to CB_2R. CBD-DMH behaved as a partial agonist on ß-arrestin-2 recruitment with a pEC_{50} value of 6.92 ± 0.13 and 47 ± 15% activation compared to CP55,940 (**Figure 5.5a**, **Table 5.4**). Furthermore, CBD did not induce ß-arrestin-2 recruitment to CB_2R.

The modulatory effect of CBD-DMH and CBD on ß-arrestin-2 recruitment by CP55,940, 2-AG and AEA to CB_2R was further examined in this assay (**Figure 5.5**, **Table 5.4**). As expected, the basal conditions reflected the partial agonism of CBD-DMH on ß-arrestin-2 recruitment to CB_2R (**Figure 5.5a**). Similar to the G protein activation results, no statistically significant modulation by CBD was detected for CP55,940, 2-AG or AEA-induced ß-arrestin-2 recruitment (**Figure 5.5b-d**, **Table 5.4**). CBD-DMH did not induce a dose-dependent negative modulation of CP55,940, 2-AG or AEA-induced ß-arrestin-2

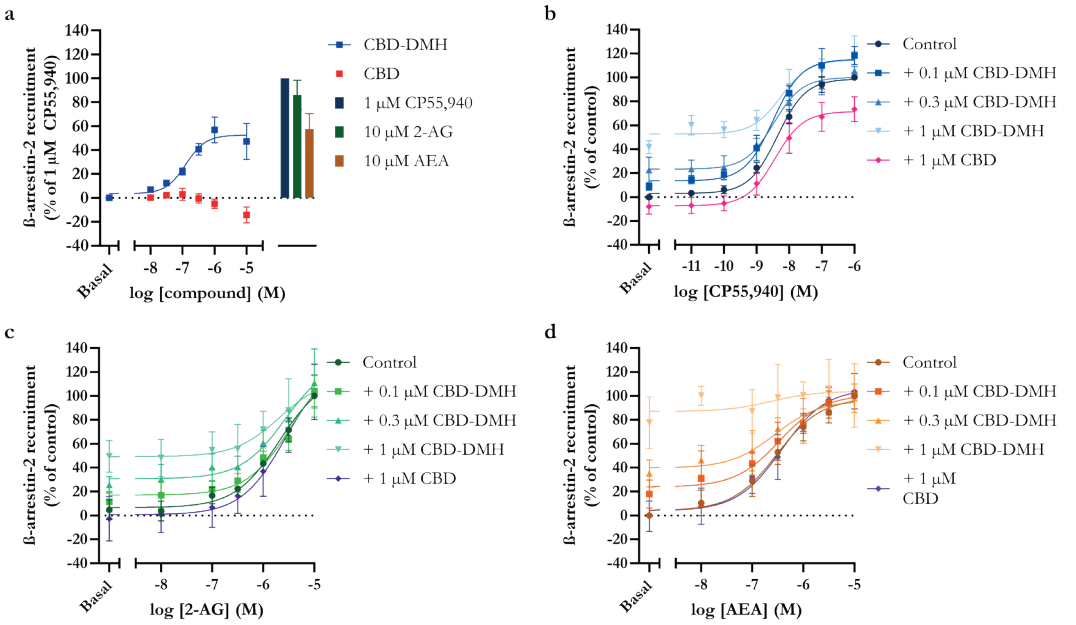

Figure 5.5 ß-arrestin-2 recruitment and the modulation thereof by CBD-DMH and CBD.
(a) ß-arrestin-2 recruitment by CBD-DMH and CBD compared to full agonist CP55,940. Modulation of agonists (b) CP55,940, (c) 2-AG and (d) AEA-induced ß-arrestin-2 recruitment in the absence (control) or presence of increasing concentrations of CBD-DMH or 1 µM CBD. Data are shown as mean ± SD from at least three independent experiments performed in duplicate.

recruitment, in contrast to G protein activation results (**Figure 5.5b-d**, **Table 5.4**). Interestingly, modulation of AEA-induced ß-arrestin-2 recruitment by highest concentration of 1 µM CBD-DMH could not be determined due to an already maximal activation of the receptor by CBD-DMH.

Altogether, we found partial agonism of CBD-DMH, but not CBD, in ß-arrestin-2 recruitment assays similar to the G protein activation assays. However, unlike in G protein activation assays, no modulation of CBD-DMH or CBD was observed on any agonist-induced ß-arrestin-2 recruitment to CB_2R.

5.3 Discussion

For centuries, components from *Cannabis sativa*, such as CBD, have been used for medicinal purposes[6]. Recently, the FDA approved Epidiolex®, a pure CBD solution, for the treatment of severe pediatric seizure disorders[5,9]. Furthermore, CBD has attracted the attention of the general public as a wonder drug that can be obtained over the counter. However, its pharmacological profile is still not fully understood and seems to be attributed to polypharmacology, i.e., activity at multiple targets[10–13,24]. Meanwhile, synthetic CBD derivates have been synthesized including CBD-DMH[14]. CBD-DMH showed anti-inflammatory effects in various in vitro models, and furthermore showed efficacy in an in

vivo arachidonic acid-induced inflammation model[15–17,19]. Nevertheless, the exact molecular mechanism of CBD-DMH remains unknown but has been hypothesized to be mediated by various proteins including CB_2R[20–22]. Therefore, we aimed to further characterize the molecular pharmacological effect of CBD-DMH on this receptor. One of the proposed mechanisms of CBD-DMH on CB_2R has been attributed to allosteric modulation[22]. Allosteric modulation, i.e., binding of a ligand at a binding site distinct from the orthosteric site, presents several advantages over orthosteric targeting of receptors[25]. This includes the lack of intrinsic agonistic properties indicating allosteric modulators can only modify the binding or signaling of a second ligand, e.g., the endogenous ligand. Furthermore, allosteric modulators bear the possibility of a higher subtype selectivity[25,26]. This class of molecules might present a different strategy for targeting CB_2R.

To investigate the allosteric behavior of CBD-DMH, radioligand binding dissociation assays were performed in which commercially available proclaimed ECS modulators were taken along for reference (**Figure 5.1**)[23]. Alteration of the dissociation rate constant (k_{off}) of an orthosteric ligand has been described as a typical hallmark of allosteric interactions and can consequently lead to altered affinity and/or potency of the orthosteric ligand at the receptor[25,27]. We screened CBD-DMH and the proclaimed modulators of the ECS in a single point dissociation assay at CB_2R for a quick insight into their dissociation modulating properties (**Figure 5.2c**, **Table 5.1**)[28]. CB_1R allosteric modulators ORG27569, PSNCBAM-1, ZCZ011, GAT211 (rac), GAT229 (*S*), and pregnenolone did not alter radioligand binding in these assays, which confirmed their lack of allosteric interaction with CB_2R[23]. Previously reported CB_2R negative allosteric modulators (NAMs) ß-caryophyllene and CBD, and positive allosteric modulator (PAM) pepcan-12 did not change the binding profile in our assays[29–31]. To the best of our knowledge, dissociation experiments to identify the allosteric mechanism have only been performed for ß-caryophyllene and pepcan-12 using [^{3}H]CP55,940[30,31]. The use of a biphasic radioligand such as [^{3}H]CP55,940 may complicate the determination of accurate kinetic parameters for unlabeled ligands due to the preference for different binding states[32]. This issue is circumvented in our assays by using the monophasic [^{3}H]RO6957022. Furthermore, pepcan-12 did not induce a statistically significant shift in agonist potency in [^{35}S]GTPγS or cAMP assays[31]. Intriguingly, several studies report agonistic behavior of ß-caryophyllene by showing affinity for CB_2R and G protein mediated signaling[33,34]. As we aimed to investigate allosterism in this project (which we did not observe), this compound was not taken along in sequential functional studies.

The only compound allosterically affecting the binding of the radioligand on CB_2R was CBD-DMH (**Figure 5.2c**, **Table 5.1**). Therefore, the allosteric modulation by CBD-DMH was further investigated in a full curve dissociation assay (**Figure 5.2d**, **Table 5.2**). A dose-dependent decrease of [^{3}H]RO6957022 binding was observed in the presence of CBD-DMH and further quantified by significantly reduced k_{off} values, which corroborates an allosteric enhancing effect on inverse agonist RO6957022 at CB_2R[25,28]. Of note, CBD was included in this and all consecutive assays as control compound next to CBD-DMH. Examination of CBD showed no statistically significant allosteric modulation (**Figure 5.2a**), very weak competitive binding (**Figure 5.3a**) but no potency on CB_2R (**Figure 5.4a**, **5.5a**, **Table 5.3**, **5.4**). Evidently, CBD might bind orthosteric to CB_2R, but with a very low, non-detectable potency in all our assays, which contrasts with previous assumptions that

CBD acts as a partial agonist or allosteric modulator at CB_2R[22,35].

The modulating effect of CBD-DMH was further investigated on the affinity and potency of reference orthosteric ligands in various binding and functional assays. The orthosteric ligands used in this study were inverse agonist RO6957022, reference orthosteric agonist CP55,940 and endogenous agonists 2-AG and AEA to account for potential probe dependence of CBD-DMH, i.e., differential effects on different (types of) ligands (**Figure 5.1**)[26]. The inclusion of the endocannabinoids to our study is a valuable addition since this reflects physiological conditions and provides insight into how physiological effects might be altered[25]. A negative allosteric modulation phenotype of CBD-DMH was found in G protein activation assays in which the potency of CP55,940 was significantly reduced with increasing concentrations of CBD-DMH (**Figure 5.4b**, **Table 5.4**). Although not statistically significant, a similar effect by CBD-DMH was observed on the potency of 2-AG (**Figure 5.4c**, **Table 5.4**). The modulation of AEA-mediated G protein activation was less apparent due to the higher level of partial agonism of CBD-DMH compared to AEA, which probably overshadows the allosteric action on potency (**Figure 5.4a**,**d**, **Table 5.4**). However, in the presence of various concentrations of CBD-DMH, we observed a higher G protein activation than by AEA alone, where in combination with higher concentrations of AEA the maximal AEA level was observed (**Figure 5.4d**). Together, this suggests that CBD-DMH is a NAM for G protein activation by CB_2R agonists.

Nonetheless, this allosteric effect of CBD-DMH was not sustained in ß-arrestin-2 recruitment assays (**Figure 5.4b-d**, **Table 5.4**), which might indicate that CBD-DMH behaves as a biased allosteric modulator, i.e., demonstrating preference for modulating one pathway over another[36]. In the study by Tham *et al.*, CBD-DMH was described as a PAM of CP55,940-dependent cAMP inhibition in contrast to the NAM effect on upstream G protein activation found in our study[22]. Secondly, pathway-specific allostery was described with a NAM effect on CP55,940-dependent ß-arrestin-1 recruitment. It is important to note that in this specific study, recruitment of ß-arrestin-1 was investigated in contrast to ß-arrestin 2 in our study. It has been previously described that ß-arrestin-1 has a weaker affinity for CB_2R than ß-arrestin-2, which might suggest different signaling mechanisms and could therefore be differently impacted by binding of CBD-DMH[37]. Even though we did not find a pronounced effect on ß-arrestin-2 recruitment to CB_2R, we also found a pathway-specific allostery between the G protein and ß-arrestin-2 signaling. Importantly, our experiments also highlight the importance of including different chemotypes and types of agonists, i.e., agonists and inverse agonists, for investigating probe dependency[38]. Namely, G protein activation by agonists CP55,940 and 2-AG was negatively impacted by CBD-DMH, whereas inverse agonist RO6957022 binding was positively modulated in dissociation studies. Furthermore, these results might be a first indication towards transducer dependency and a biased allosteric effect of CBD-DMH towards G protein activation over ß-arrestin-2 recruitment[36].

While studying the allosteric behavior of CBD-DMH, we also observed competitive or agonistic behavior in several assays. We found competitive displacement of the highest concentration of CBD-DMH with both [^{3}H]RO6957022 and [^{3}H]CP55,940 (**Figure 5.2a**, **Table 5.1**). This was further quantified by a low affinity of CBD-DMH for CB_2R in

displacement studies, which suggests that CBD-DMH competes with [^{3}H]RO6957022 for the orthosteric binding site (**Figure 5.3a**, **Table 5.3**). Although, not further analyzed, Tham *et al.* also found this competitive binding of CBD-DMH with [^{3}H]CP55,940 and a similar low affinity is previously reported with [^{3}H]-HU-243 to CB_2R[20,22]. Interestingly, the binding could not be fully inhibited in our studies (**Figure 5.3a**, **Table 5.3**), which is indicative of the formation of a ternary complex of binding of [^{3}H]RO6957022 to the orthosteric site, while CBD-DMH occupies the allosteric site[28,39].

For all tested reference ligands, a decreased apparent affinity was observed in presence of the highest concentration (3 μM) of CBD-DMH (**Figure 5.3b-e**, **Table 5.3**), which further highlights the competitive interaction at the orthosteric binding site. The different conclusions obtained from the [^{3}H]RO6957022 dissociation and displacement assays with regard to CBD-DMH's mechanism of action highlight the importance of employing both these assays, as these expose the allosteric and competitive interactions by CBD-DMH, respectively.

The agonistic effect of CBD-DMH was further observed in the various functional assays, where CBD-DMH elicited partial G protein activation and ß-arrestin-2 recruitment compared to full agonist CP55,940 with moderate pEC_{50} values and hill slopes close to unity (**Figure 5.4a**, **5.5a**, **Table 5.4**). No agonistic effect of CBD-DMH on cAMP inhibition was described in the study by Tham *et al.,* but the apparent upward shift of the CP55,940 curve in the presence of increasing concentrations of CBD-DMH would compare to the agonistic effect we also observed and quantified for CBD-DMH on NKH477-induced inhibition of cAMP levels (**Table 5.4**)[20]. Our results together stress the duality of CBD-DMH, which is not a pure allosteric modulator, but rather a NAM-agonist due to having two different interactions with CB_2R from which it modulates and activates the receptor[40].

Ligands with two different binding interactions have previously been described for the muscarinic M_2 receptor, where bitopic ligands might adopt a dualsteric binding mode, bridging the orthosteric and allosteric site or purely bind to the allosteric binding site[39]. This allosteric binding pocket has been crystallized for the muscarinic M_2 receptor and sits directly above the orthosteric site[41]. Recently, a study by Yuan *et al.* identified seven potential allosteric sites for CB_2R of which 'site H' was the most promising binding site, which resembles the allosteric site from the M_2 receptor and is close to the orthosteric binding pocket of CB_2R[42]. This site located just above the orthosteric pocket has also been referred to as the extracellular vestibule, ligand entry site or outer vestibule. It is a region in which ligands might pre-engage before moving deeper into the orthosteric binding pocket. Nevertheless, allosteric ligands could bind here without continuing to the orthosteric pocket and execute allosteric actions such as changing the orthosteric ligand-binding kinetics[27,43]. The duality of CBD-DMH described in this paper can be well explained by it having interactions at a yet to be identified allosteric binding site, but also by its binding to the orthosteric site. These orthosteric interactions might be directed by the dimethylheptyl moiety that CBD-DMH has opposed to CBD's pentyl chain. These side chain substitutions generally enhance the activity of cannabinoids[18]. Evidently, it is a common structural feature for CB_2R agonists such as CP55,940, HU308 and HU910 and is described to interact with various amino acids in the orthosteric binding pocket in **Chapter 4**[44]. To dive further into the exact

binding mechanism of CBD-DMH at CB_2R, structural elucidation of CB_2R in conjunction with CBD-DMH by docking and molecular dynamic studies could be performed. These should be supported with *in vitro* mutagenesis studies for validation of resultant predicated positions. Together this might aid in obtaining a better idea of the dual pharmacology of CBD-DMH at CB_2R.

In conclusion, this chapter provides a dual profile of CBD-DMH with both allosteric and orthosteric effects on CB_2R, although it does not identify the exact binding site(s) of CBD-DMH. Interestingly, CBD-DMH partially activates both G protein and ß-arrestin-2 recruitment, while it is a PAM for an inverse agonist, and a NAM for synthetic and endogenous agonists. In case of the latter, it only modulates G protein activation and not ß-arrestin-2 recruitment suggesting a biased allosteric mechanism. Furthermore, in these robust fundamental assays we could not confirm any potent interaction of CBD with CB_2R. Hence, the beneficial effects of CBD can still be attributed to polypharmacology, but most likely not via CB_2R. Together, this study invites further research into identifying the dual molecular pharmacology of CBD-DMH at CB_2R, which might provide a new class of molecules targeting CB_2R.

5.4 Materials and methods

5.4.1 Chemicals and reagents

Compounds AM630, CP55,940, GAT228, GAT229, GAT211, pregnenolone and PSNCBAM-1 were obtained from Sigma-Aldrich (St. Louis, MO, USA). Pepcan-12 (RVD-HPα), (-)-cannabidiol (CBD), anandamide (AEA), 2-arachidonoylglycerol (2-AG) and phenylmethylsulfonyl fluoride (PMSF) were bought from Tocris Bioscience (Bristol, United Kingdom). ZCZ011 was received from Axon Medchem (Groningen, the Netherlands), while ß-caryophyllene was obtained from Bio-Connect (Huissen, the Netherlands), and (-)-5'-cannabidiol-dimethylheptyl (CBD-DMH) was from Bio-Techne Ltd (Abingdon, United Kingdom). RO6957022 and [^{3}H]RO6957022 (specific activity 82.8 Ci/mmol) were custom-synthesized and custom-labeled, respectively, by F. Hoffmann-La Roche Ltd (Basel, Switzerland). [^{3}H]CP55,940 (specific activity 108.5 Ci/mmol), guanosine 5'-O-[γ-thio]triphosphate ([^{35}S]GTPγS, specific activity 1250 Ci/mmol) and GF/C filter plates were purchased from Revvity (Waltham, MA, USA). The PathHunter and cAMP Hunter detection kits were obtained from DiscoverX (Fremont, CA, USA). Bicinchoninic acid (BCA) and BCA protein assay reagent were purchased from Pierce Chemical Company (Rockford, IL, USA). All other chemicals were of analytical grade and obtained from standard commercial sources. Buffers and solutions were prepared at room temperature (rt) using Millipore water (deionized using a MilliQ A10 Biocel™, with a 0.22 μm filter).

5.4.2 Cell culture

CHO cells stably expressing hCB_2R (CHOK1_hCB_2bgal, DiscoverX) were cultured in Ham's F12 Nutrient Mixture supplemented with 10% (v/v) fetal calf serum (FCS), 2 mM

Glutamax, 100 IU/mL penicillin, 100 µg/mL streptomycin, 300 µg/mL hygromycin and 800 µg/mL G418 in a humidified atmosphere at 37 °C and 5% CO_2. Cells were subcultured twice-weekly when reaching 80-90% confluence on 10 or 15 cm ø plates by trypsinization. All experiments were done within 20 passages.

5.4.3 Membrane preparation

CHOK1_hCB$_2$bgal cells were harvested when reaching 90% confluence in 15 cm ø plates after one week subculture at a 1:6 ratio. The cells were detached by scraping into 5 mL phosphate-buffered saline (PBS) and subsequently centrifuged at 2000 × g for 5 min. Pellets were resuspended in ice-cold Tris buffer (50 mM Tris-HCl, pH 7.4) and homogenized with an Ultra Turrax homogenizer (IKA-Werke GmbH & Co. KG, Staufen, Germany). Cytosolic and membrane fractions were separated using an Optima LE-80 K ultracentrifuge (Beckman Coulter, Inc., Fullerton, CA) at 100,000 × g for 20 min at 4 °C. This homogenization and centrifugation cycle were repeated a second time. The final pellet was resuspended and homogenized in ice-cold Tris buffer and subsequently aliquoted and stored in 100 µL aliquots at -80 °C. Membrane protein concentrations were determined using a BCA protein determination assay, as described by the manufacturer (Pierce BCA protein assay kit)[45].

5.4.4 [^{3}H]RO6957022 binding assays

[^{3}H]RO6957022 binding assays have previously been described with the main difference that the incubation temperature was changed to 10 °C for improved separation of kinetic differences[46]. In short, CHOK1_hCB$_2$bgal membranes were thawed and subsequently homogenized using the Ultra Turrax homogenizer. For experiments with endocannabinoids, membranes were preincubated for 30 min with 50 µM phenylmethylsulfonyl fluoride (PMSF). The reactions were carried out in 100 µL assay buffer (50 mM Tris-HCl (pH 7.4), 0.1% (w/v) bovine serum albumin (BSA)) containing 1 µg of membrane protein and 1.5 nM [^{3}H] RO6957022. Incubations were performed at 10 °C. Therefore, assay buffer, (radio)ligands and membranes were precooled to 10 °C prior to the experiment. Nonspecific binding (NSB) was determined using 10 µM AM630 and vehicle (i.e., acetonitrile for endocannabinoids, and DMSO for all other compounds) concentrations were constant and kept < 1% in all samples unless stated otherwise. Total radioligand binding (TB) did not exceed 10% of the amount added to prevent ligand depletion. For all assays, incubations were terminated by rapid vacuum filtration with ice-cold 50 mM Tris-HCl (pH 7.4), 0.1% (w/v) BSA buffer through Whatman GF/C filters using a Filtermate 96-well harvester (Revvity). Filters were dried for at least 30 min at 55 °C and subsequently 25 µL MicroScint scintillation cocktail was added per well. Filter-bound radioactivity was measured by scintillation spectrometry using a Microbeta^2 2450 counter (Revvity).

5.4.4.1 Dissociation assays

For all dissociation assays, membranes were pre-incubated with radioligand for 2 h at 10 °C. [^{3}H]RO6957022 dissociation was initiated by addition of 10 µM AM630 as displacer at

different time points for 3 h. The allosteric screen was performed in single point dissociation assays by addition of displacer in the absence (control) or presence of 10 μM (f.c.) compound for a total incubation of 27 minutes (i.e., dissociation half-life of the radioligand in this assay). In full curve modulatory dissociation assays, the amount of receptor-bound radioligand was determined at different time points up to 3 h (CBD) or 5 h (CBD-DMH) upon addition of the displacer in the absence (control) or presence of increasing concentrations of CBD-DMH or 10 μM CBD. Final DMSO concentrations were increased to 1.5% to improve solubility. Incubations were terminated and receptor-bound radioactivity was determined as described in section **5.4.4 [^{3}H]RO6957022 binding assays**.

5.4.4.2 Displacement assays

For displacement assays, membranes were incubated with 10 μM or six increasing concentrations of competing ligand (ranging from 0.01 nM to 10 μM) in the absence (control) or presence of increasing concentrations of CBD-DMH or 3 μM CBD. To prevent precipitation in the assay, the maximum modulatory concentrations of CBD-DMH and CBD were set to 3 μM and all other CBD-DMH concentrations were chosen to be evenly distributed over its displacement curve. The reaction mixture was incubated for 2 h at 10 °C after which incubations were terminated and receptor-bound radioactivity was determined as described in section **5.4.4 [^{3}H]RO6957022 binding assays**.

5.4.5 [^{3}H]CP55,940 displacement assays

For single point [^{3}H]CP55,940 displacement assays, CHOK1_hCB$_2$bgal membranes were homogenized and diluted to 1.5 μg of membrane protein per well in assay buffer (50 mM Tris-HCl (pH 7.4), 5 mM $MgCl_2$, 0.1% (w/v) BSA). Membranes were incubated with 10 μM of competing ligand in the presence of 1.5 nM [^{3}H]CP55,940. Incubations were for 2 h at 25 °C. NSB was determined using 10 μM AM630 and DMSO concentrations were constant and kept < 1% in all samples. TB did not exceed 10% of the amount added to prevent ligand depletion. Incubations were terminated as described in section **5.4.4 [^{3}H] RO6957022 binding assays** except using ice-cold wash buffer containing 50 mM Tris-HCl, 5 mM $MgCl_2$ and 0.1% BSA.

5.4.6 [^{35}S]GTPγS binding assays

G protein activation of CB_2R was measured by binding of [^{35}S]GTPγS as previously described in **Chapter 4**[44]. In short, CHOK1_hCB$_2$bgal membrane homogenates (5 μg) were diluted in assay buffer (50 mM Tris-HCl, 5 mM $MgCl_2$, 150 mM NaCl, 1 mM EDTA, 0.05% BSA (w/v) and 1 mM DTT, freshly prepared each day) and supplemented with 5 μg saponin and 1 μM GDP to a total volume of 100 μL. For endocannabinoid samples, the membranes were additionally preincubated for 30 min with 50 μM PMSF. To determine pEC_{50} and E_{max} values, increasing concentrations of ligand of interest (ranging from 0.01 nM to 10 μM) in absence (control) or presence of increasing concentrations of CBD-DMH or 0.3 μM CBD were preincubated for 30 min at rt. To prevent precipitation in the assay, the maximum

modulatory concentrations of CBD-DMH and CBD were set to 0.3 μM and all other CBD-DMH concentrations were chosen to be evenly distributed over its displacement curve. Basal activity was determined in the presence of vehicle (i.e., acetonitrile for endocannabinoids, and DMSO for all other compounds) or specific CBD-DMH/CBD concentration only and the maximal response was determined by 10 μM CP55,940 or specific ligand of interest. [^{35}S]GTPγS (0.3 nM) was added, and the samples were incubated for 90 min at 25 °C while shaking at 400 rpm. Incubations were terminated as described in section **5.4.4 [^{3}H] RO6957022 binding assays** except using ice-cold wash buffer containing 50 mM Tris-HCl and 5 mM $MgCl_2$.

5.4.7 cAMP Hunter™ assays

Inhibition of cAMP production by CB_2R stimulation in CB_2R-overexpressing cell lines was measured using the cAMP Hunter™ assay enzyme fragment complementation chemiluminescent detection kit as described before and following the manufacturer's protocol (DiscoveRx, Fremont, CA)[47]. Briefly, CHO-K1 cells overexpressing human CB_2R were plated into a 96 well plate (10,000 cells/well) and incubated overnight at 37 °C and 5% CO_2. Media were aspirated and replaced with 30 μL of cell assay buffer. Cells were treated for 30 min at 37 °C with 15 μL of 3× dose-response solutions of samples prepared in presence of cell assay buffer containing a 3× 25 μM NKH477 solution (a water soluble analog of forskolin) to stimulate adenylate cyclase and enhance basal cAMP levels. Following stimulation, cell lysis and cAMP detection were performed as per the manufacturer's protocol. Luminescence was measured using a GloMax Multi Detection System (Promega, Italy).

5.4.8 PathHunter ß-arrestin-2 recruitment assays

ß-arrestin-2 recruitment to CB_2R was measured using the PathHunter ß-arrestin recruitment assay kit as described in **Chapter 2**[48]. In short, CHOK1_hCB_2bgal cells were seeded at a density of 5,000 cells/well in solid white-walled 384-wells plates in culture medium as described in section 2.2 and incubated overnight at 37 °C and 5% CO_2. For experiments with endocannabinoids, the cells were preincubated for 30 min at 37 °C and 5% CO_2 with 50 μM PMSF. To determine pEC_{50} and E_{max} values, cells were stimulated with increasing concentrations of ligand of interest (ranging from 0.01 nM to 10 μM) in absence (control) or presence of increasing concentrations of CBD-DMH or 1 μM CBD for 90 min at 37 °C and 5% CO_2. To prevent precipitation in the assay, the maximum modulatory concentrations of CBD-DMH and CBD were set to 1 μM and all other CBD-DMH concentrations were chosen to be evenly distributed over its displacement curve. Basal activity was determined in the presence of vehicle or specific CBD-DMH/CBD concentration only and the maximal response was determined by 10 μM CP55,940 or specific ligand of interest. Vehicle (i.e., acetonitrile for endocannabinoids, and DMSO for all other compounds) concentrations were constant and kept < 1% in all samples. Subsequently, cells were loaded with 12.5 μL detection reagent prepared according to suppliers protocol[49] and incubated for 1 h in the

dark at rt to detect ß-galactosidase enzyme activity. Luminescence was measured on an Envision multilabel plate reader (Revvity).

5.4.9 Data analysis

All experimental data were analyzed using GraphPad Prism 9.0 (GraphPad Software Inc., San Diego, CA). All values obtained are means ± standard deviation (SD) of at least three independent experiments performed in duplicate, unless stated otherwise.

[^{3}H]RO6957022 and [^{3}H]CP55,940 assays were baseline-corrected with NSB and normalized to this value (0%) and TB (100%). Dissociation rate constants (k_{off}) were determined by the 'one-phase decay exponential decay' analysis. The half-maximal inhibitory concentrations (pIC_{50}) of the agonists in [^{3}H]RO6957022 displacement assays were obtained by non-linear regression analysis of the displacement curves. Values from direct competition curves were further converted into inhibitory constant pK_i using the Cheng-Prusoff equation[50] with the experimentally determined dissociation constant (K_D) value 0.78 nM (data not shown). The modulation in apparent affinities was investigated on the level of the pIC_{50} values and the Cheng-Prusoff equation was not applied due to the possibility of CBD-DMH altering the K_D crucial for the analysis.

Functional agonist responses from the [^{35}S]GTPγS binding assays and ß-arrestin-2 recruitment assays were baseline-corrected with the basal activity and normalized to 10 μM of CP55,940 (orthosteric effect) or control response (allosteric modulation). pEC_{50} and E_{max} values were determined using non-linear regression curve fitting 'log(agonist) vs. response'. On reference agonist data the 'three parameters' fit was used, whereas for CBD-DMH and CBD the variable slope (four parameter) fit was applied. This gave freedom to observe both agonistic and allosteric mechanisms of these unknown compounds. Data from the cAMP assay were normalized to NKH477 stimulus alone as 100%. The percentage of response was calculated using the following formula:

$$\% \text{ response} = 100 \cdot 1 - \frac{\text{mean RLU}_{\text{test sample}} - \text{mean RLU}_{\text{NKH477}}}{\text{mean RLU}_{\text{vehicle}} - \text{mean RLU}_{\text{NKH477}}}$$

pEC_{50} values were determined using non-linear regression curve fitting 'log(agonist) vs. response (three parameters)'.

Differences in pIC_{50} and pEC_{50} values were analyzed using an ordinary one-way ANOVA with Dunnett's multiple comparisons test or an unpaired Student's t-test with Welch's correction. Significant differences are displayed as * $p < 0.05$, ** $p < 0.01$, *** $p < 0.001$ and **** $p < 0.0001$.

References

1. Howlett, A. C. *et al.* International Union of Pharmacology. XXVII. Classification of cannabinoid receptors. *Pharmacol Rev* **54**, 161–202 (2002).
2. di Marzo, V., Bifulco, M. & de Petrocellis, L. The endocannabinoid system and its therapeutic exploitation. *Nat Rev Drug Discov* **3**, 771–784 (2004).
3. Ibsen, M. S., Connor, M. & Glass, M. Cannabinoid CB_1 and CB_2 Receptor Signaling and Bias. *Cannabis Cannabinoid Res* **2**, 48–60 (2017).
4. Pertwee, R. G. *et al.* International Union of Basic and Clinical Pharmacology. LXXIX. Cannabinoid Receptors and Their Ligands: Beyond CB_1 and CB_2. *Pharmacol Rev* **62**, 588–631 (2010).
5. Brennecke, B. *et al.* Cannabinoid receptor type 2 ligands: An analysis of granted patents since 2010. *Pharm Pat Anal* **10**, 111–163 (2021).
6. Mechoulam, R., Hanuš, L. O., Pertwee, R. & Howlett, A. C. Early phytocannabinoid chemistry to endocannabinoids and beyond. *Nat Rev Neurosci* **15**, 757–764 (2014).
7. Patricio, F., Morales-Andrade, A. A., Patricio-Martínez, A. & Limón, I. D. Cannabidiol as a Therapeutic Target: Evidence of its Neuroprotective and Neuromodulatory Function in Parkinson's Disease. *Front Pharmacol* **11**, 595635 (2020).
8. Peng, J. *et al.* A narrative review of molecular mechanism and therapeutic effect of cannabidiol (CBD). *Basic Clin Pharmacol Toxicol* **130**, 439–456 (2022).
9. Talwar, A., Estes, E., Aparasu, R. & Reddy, D. S. Clinical efficacy and safety of cannabidiol for pediatric refractory epilepsy indications: A systematic review and meta-analysis. *Exp Neurol* **359**, 114238 (2022).
10. Miller, O. S., Elder, E. J., Jones, K. J. & Gidal, B. E. Analysis of cannabidiol (CBD) and THC in nonprescription consumer products: Implications for patients and practitioners. *Epilepsy & Behavior* **127**, 108514 (2022).
11. Vitale, R. M., Iannotti, F. A. & Amodeo, P. The (Poly) Pharmacology of Cannabidiol in Neurological and Neuropsychiatric Disorders: Molecular Mechanisms and Targets. *Int. J. Mol. Sci* **22**, 4876 (2021).
12. Peltner, L. K. *et al.* Cannabidiol acts as molecular switch in innate immune cells to promote the biosynthesis of inflammation-resolving lipid mediators. *Cell Chem Biol* **30**, 1508–1524 (2023).
13. Rosenberg, E. C. *et al.* Cannabidiol modulates excitatory-inhibitory ratio to counter hippocampal hyperactivity. *Neuron* **111**, 1282-1300.e8 (2023).
14. Cordova, T. *et al.* The ovulation blocking effect of cannabinoids: Structure-activity relationships. *Psychoneuroendocrinology* **5**, 53–62 (1980).
15. Juknat, A., Kozela, E., Kaushansky, N., Mechoulam, R. & Vogel, Z. Anti-inflammatory effects of the cannabidiol derivative dimethylheptyl-cannabidiol - Studies in BV-2 microglia and encephalitogenic T cells. *J Basic Clin Physiol Pharmacol* **27**, 289–296 (2016).
16. Silva, R. L. *et al.* DMH-CBD, a cannabidiol analog with reduced cytotoxicity, inhibits TNF production by targeting NF-kB activity dependent on A_{2A} receptor. *Toxicol Appl Pharmacol* **368**, 63–71 (2019).
17. Ben-Shabat, S., Hanuš, L. O., Katzavian, G. & Gallily, R. New cannabidiol derivatives: Synthesis, binding to cannabinoid receptor, and evaluation of their antiinflammatory activity. *J Med Chem* **49**, 1113–1117 (2006).
18. Gallily, R. *et al.* γ-Irradiation enhances apoptosis induced by cannabidiol, a non-psychotropic cannabinoid, in cultured HL-60 myeloblastic leukemia cells. *Leuk Lymphoma* **44**, 1767–1773 (2003).
19. Fride, E., Ponde, D., Breuer, A. & Hanuš, L. Peripheral, but not central effects of cannabidiol derivatives: Mediation by CB1 and unidentified receptors. *Neuropharmacology* **48**, 1117–1129 (2005).
20. Bisogno, T. *et al.* Molecular targets for cannabidiol and its synthetic analogues: Effect on vanilloid VR1 receptors and on the cellular uptake and enzymatic hydrolysis of anandamide. *Br J Pharmacol* **134**, 845–852 (2001).
21. Hanuš, L. O. *et al.* Enantiomeric cannabidiol derivatives: Synthesis and binding to cannabinoid receptors. *Org Biomol Chem* **3**, 1116–1123 (2005).
22. Tham, M. *et al.* Allosteric and orthosteric pharmacology of cannabidiol and cannabidiol-dimethylheptyl at the type 1 and type 2 cannabinoid receptors. *Br J Pharmacol* **176**, 1455–1469 (2019).
23. Gado, F. *et al.* Allosteric modulators targeting cannabinoid cb1 and cb2 receptors: implications for drug discovery. *Future Med Chem* **11**, 2019–2037 (2019).
24. Martinez Naya, N. *et al.* Molecular and Cellular Mechanisms of Action of Cannabidiol. *Molecules* **28**, 5980 (2023).

25. Christopoulos, A. & Kenakin, T. G protein-coupled receptor allosterism and complexing. *Pharmacol Rev* **54**, 323–374 (2002).
26. Kenakin, T. P. Biased signalling and allosteric machines: new vistas and challenges for drug discovery. *Br J Pharmacol* **165**, 1669 (2012).
27. Lane, J. R., May, L. T., Parton, R. G., Sexton, P. M. & Christopoulos, A. A kinetic view of GPCR allostery and biased agonism. *Nat Chem Biol* **13**, 929–937 (2017).
28. Leach, K., Sexton, P. M. & Christopoulos, A. Quantification of allosteric interactions at G protein-coupled receptors using radioligand binding assays. *Current protocols in pharmacology / editorial board, S.J. Enna (editor-in-chief) ... [et al.]* Chapter 1, (2011).
29. Pandey, P., Roy, K. K. & Doerksen, R. J. Negative allosteric modulators of cannabinoid receptor 2: protein modeling, binding site identification and molecular dynamics simulations in the presence of an orthosteric agonist. *J Biomol Struct Dyn* **38**, 32–47 (2020).
30. Rajasekaran, M. Characterization of allosteric modulators of CB2 receptors as novel therapeutics for inflammatory diseases. (University of Arkansas for Medical Sciences, 2011).
31. Petrucci, V. *et al.* Pepcan-12 (RVD-hemopressin) is a CB2 receptor positive allosteric modulator constitutively secreted by adrenals and in liver upon tissue damage. *Sci Rep* **7**, 1–14 (2017).
32. Guo, D. *et al.* A two-state model for the kinetics of competitive radioligand binding. *Br J Pharmacol* **175**, 1719–1730 (2018).
33. Gertsch, J. *et al.* Beta-caryophyllene is a dietary cannabinoid. *PNAS* **105**, 9099–9104 (2008).
34. Chicca, A. *et al.* Functionalization of β-Caryophyllene Generates Novel Polypharmacology in the Endocannabinoid System. *ACS Chem. Biol* **9**, 30 (2014).
35. Navarro, G. *et al.* Design of Negative and Positive Allosteric Modulators of the Cannabinoid CB $_2$ Receptor Derived from the Natural Product Cannabidiol. *J Med Chem* **64**, 9354–9364 (2021).
36. Slosky, L. M., Caron, M. G. & Barak, L. S. Biased Allosteric Modulators: New Frontiers in GPCR Drug Discovery. *Trends Pharmacol Sci* **42**, 283–299 (2021).
37. Ibsen, M. S. *et al.* Cannabinoid CB1 and CB2 Receptor-Mediated Arrestin Translocation: Species, Subtype, and Agonist-Dependence. *Front Pharmacol* **10**, (2019).
38. Kenakin, T. The quantitative characterization of functional allosteric effects. *Curr Protoc Pharmacol* **76**, 9.22.1-9.22.10 (2017).
39. Bock, A. *et al.* Ligand binding ensembles determine graded agonist efficacies at a G protein-coupled receptor. *Journal of Biological Chemistry* **291**, 16375–16389 (2016).
40. Kenakin, T. P. *A Pharmacology Primer: Techniques for More Effective and Strategic Drug Discovery*. (Academic Press, 2014).
41. Kruse, A. C. *et al.* Activation and allosteric modulation of a muscarinic acetylcholine receptor. *Nature* **504**, 101–106 (2013).
42. Yuan, J. *et al.* In Silico Prediction and Validation of CB2 Allosteric Binding Sites to Aid the Design of Allosteric Modulators. *Molecules* **27**, 453 (2022).
43. Congreve, M., Oswald, C. & Marshall, F. H. Applying Structure-Based Drug Design Approaches to Allosteric Modulators of GPCRs. *Trends Pharmacol Sci* **38**, 837–847 (2017).
44. Li, X. *et al.* Structural basis of selective cannabinoid CB_2 receptor activation. *Nat Commun* **14**, 1–16 (2023). **(Chapter 4)**
45. Smith, P. K. *et al.* Measurement of protein using bicinchoninic acid. *Anal Biochem* **150**, 76–85 (1985).
46. Martella, A. *et al.* A Novel Selective Inverse Agonist of the CB_2 Receptor as a Radiolabeled Tool Compound for Kinetic Binding Studies. *Mol Pharmacol* **92**, 389–400 (2017).
47. Tonelli, M. *et al.* Exploring the effectiveness of novel benzimidazoles as CB2 ligands: synthesis, biological evaluation, molecular docking studies and ADMET prediction. *Medchemcomm* **9**, 2045–2054 (2018).
48. Bouma, J. *et al.* Cellular Assay to Study β-Arrestin Recruitment by the Cannabinoid Receptors 1 and 2. in *Endocannabinoid Signaling. Methods in Molecular Biology* (ed. Maccarrone, M.) vol. 2576 189–199 (Humana, New York, NY, 2022). **(Chapter 2)**
49. DiscoverX. User Manual PathHunter® Detection Kit. https://www.discoverx.com/DiscoveRx/media/ContentFiles/DataSheets/93-0001L.pdf.

50. Cheng, Y.-C. & Prusoff, W. H. Relationship between the inhibition constant (K1) and the concentration of inhibitor which causes 50 per cent inhibition (I50) of an enzymatic reaction. *Biochem Pharmacol* **22**, 3099–3108 (1973).

Chapter 6

Impact of cancer-associated mutations on receptor function and drug targeting of cannabinoid CB_2 receptor

Jara Bouma, Xuesong Wang, Ikram el Miloudi, Silke Cornelissen, Marina Gorostiola González, Antonius P.A. Janssen, Mario van der Stelt, Laura H. Heitman

Abstract

Cannabinoid CB_2 receptor (CB_2R) activation has shown beneficial effects as a potential anticancer treatment strategy. Nevertheless, mutations in CB_2R are found in patient-derived tumor samples, which might affect the protective effects mediated via CB_2R. Therefore, we aimed to investigate the effect of cancer-associated CB_2R mutations on endocannabinoid binding and activation, as well as the druggability of these mutant receptors. To this end, receptor expression of ten mutant CB_2Rs was assessed in an ELISA, followed by a G protein activation screen with an inverse agonist as tool compound to assess receptor state, i.e., basal activity. Furthermore, G protein activation by endogenous and synthetic reference or clinical agonists was assessed and radioligand binding assays were executed to investigate the impact on binding of the radioligand, an endogenous agonist and two clinical agonists. Expression levels of receptors with mutations in the transmembrane domains were similar to wild type (WT), whereas mutations in the flexible regions altered expression levels and receptor state. Furthermore, mutations in the binding pocket and structurally close to a conserved motif markedly affected receptor activation, while mutations in the N- and C-termini were less likely to alter activation. Radioligand binding was reduced for the majority of mutant CB_2Rs. Affinity of the other agonists was only moderately affected on mutant receptors $N11^{N\text{-}term}K$, $D24^{N\text{-}term}N$, $A282^{7.36}T$ and $P348^{C\text{-}term}S$. Overall, our results indicate that cancer-associated mutations in CB_2R can impact the expression, agonist binding and activation of the receptor. This highlights the importance of precision medicine and patient genome screening prior to administration of cannabinoid-based therapies.

6.1 Introduction

Cancer is an extraordinarily complex disease due to the diversity in cancer genotypes and phenotypes[1]. A large cancer genome mutation analysis revealed that in 20% of all human cancers G protein-coupled receptors (GPCRs) were found to be mutated and specific conserved motifs were more prone to mutations[2–4]. Furthermore, GPCRs are involved in cancer-relevant signaling pathways and are therefore hypothesized to be interesting targets for anticancer drugs[5,6]. Nevertheless, the effect of GPCR mutations on cancer progression or druggability is largely unknown[2,5]. Previous studies on cancer-associated mutations for adenosine A_1, A_{2A} and A_{2B} receptors, as well as CC chemokine receptor 2 (CCR2) showed the impact of such mutations on receptor functionality and druggability, underlining the importance to study them[7–11]. Moreover, a recent large investigation on GPCR mutations from patient-derived cancer samples revealed novel GPCRs implicated in cancer development, including the cannabinoid CB_2 receptor (CB_2R)[3].

CB_2R is part of the endocannabinoid system (ECS) along with the cannabinoid CB_1 receptor (CB_1R), the endocannabinoids 2-arachidonoylglycerol (2-AG) and anandamide (AEA), and their metabolizing enzymes[12]. CB_2R is primarily located on immune cells and as such is involved in the regulation of inflammatory processes[13,14]. Nevertheless, dysregulation or altered expression levels of CB_2R have been described for a variety of diseases, including cancer[15,16]. In various cancer types, such as gliomas, human epidermal growth factor 2 (HER2) positive breast tumors and non-small-cell lung cancer, elevated CB_2R levels have been reported[17–20]. It was shown that these increased levels were correlated with a poor patient prognosis and tumor malignancy, as well as a higher probability to develop metastases. Moreover, endogenous CB_2R expression has also been shown to suppress colon tumorigenesis[21].

Nevertheless, this also provides the opportunity to therapeutically exploit CB_2R, which is substantiated by previously described antitumor effects of cannabinoids that have been extensively reviewed[22–25]. The protective effects of cannabinoids via CB_2R activation are regulated through a large variety of pathways and proteins. In HER2 positive breast cancer, non-selective cannabinoid Δ^9-tetrahydrocannabinol (Δ^9-THC) disrupted the heteromerization of HER2 with CB_2R, which consequently triggered antitumor responses in both *in vitro* and *in vivo* models[19]. Moreover, Δ^9-THC has been shown to downregulate matrix metalloproteinase-2 expression in gliomas, which in turn inhibited glioma cell invasion[26]. These effects were mimicked by CB_2R selective agonist JWH133 to further support the protective effect via CB_2R activation[26]. The antitumor effects of JWH133 have been further described in various cancer types, including breast, colon, lung, brain, and skin cancer by inhibition of tumor cell proliferation and migration as well as attenuation of angiogenesis[18,25,27]. Similarly, WIN55,212-2 has been reported to inhibit growth of malignant skin tumor cells and increased the number of apoptotic cells, while impairing tumor vascularization[28]. Recently, a phase II trial with Sativex®, an oromucosal spray with Δ^9-THC and cannabidiol (CBD), showed promising results on the overall survival of patients with recurrent glioblastoma and follow-up clinical trails will focus on the improvement of disease outcomes after treatment with Sativex®[29]. However currently, cannabinoid-based therapies are prescribed to cancer patients experiencing chemotherapy-induced nausea and

vomiting (CINV) or cancer-related anorexia as palliative strategies[30]. Hereto, Dronabinol (Δ^9-THC) and Nabilone are approved drugs and ART-27.13 has completed clinical phase I studies for cancer-related anorexia[13].

In view of the therapeutic potential of CB_2R agonists and the CB_2R mutations found in cancer patient samples, we aimed to investigate the impact of CB_2R cancer-associated mutations on the functionality of the receptors as well as the implications for drug targeting. CB_2R mutations from the Genomic Data Commons (GDC) were collected and narrowed down based on occurrence and proximity to the orthosteric binding pocket. Expression and G protein activation on ten mutant CB_2Rs was investigated by screening a variety of CB_2R ligands in [^{35}S]GTPγS assays. The endocannabinoids 2-AG and AEA were screened to investigate the endogenous implications of mutant CB_2Rs (**Figure 6.1**). Furthermore, structurally diverse reference agonists CP55,940, WIN55,212-2 and JWH133 and clinically relevant agonists Δ^9-THC, Nabilone and ART-27.13 were included in this screen to determine the effect of mutations on potential drug treatment (**Figure 6.1**). Agonists 2-AG, CP55,940, Δ^9-THC and Nabilone were further investigated in binding affinity assays. We found that mutations in the binding pocket or structurally close to a conserved motif were detrimental for receptor activation or binding by all tested agonists. This effect was less pronounced on mutations located in the N- or C-terminus. Furthermore, activation and binding were differentially affected dependent on the combination of CB_2R mutant and agonist. Altogether, this shows the importance of precision medicine, i.e., investigating patient CB_2R genotype, prior to administration of cannabinoid-based therapies.

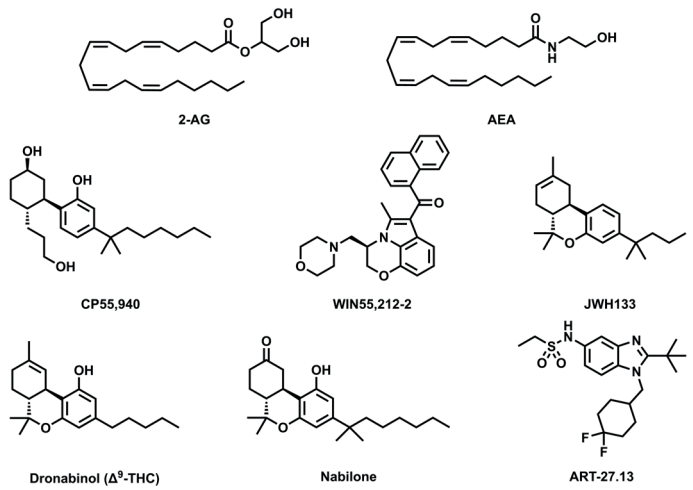

Figure 6.1 Chemical structures of cannabinoid CB_2 receptor agonists used in this study.
Endocannabinoids (2-AG and AEA), reference agonists (CP55,940, WIN55,212-2 and JWH133) and clinical agonists (Dronabinol, Nabilone and ART-27.13). CP55,940, WIN55,2121-2, Nabilone and ART-27.13 are full agonists on CB_2R, whereas 2-AG, AEA, JWH133 are partial agonist (described in **Chapter 3** and Soethoudt *et al.*)[55].

6.2 Results

6.2.1 Selection of cancer-associated CB_2R mutations

Mutations found in CB_2R in patient solid tumors were retrieved from the GDC, which resulted in a total of 85 CB_2R mutations of which 60 missense mutations. The selection was narrowed down by applying three inclusion criteria. First, nine amino acids that were mutated more than once were included. This yielded CB_2R mutations $N11^{N\text{-}term}K/S$, $D24^{N\text{-}term}N$, $E50^{1.49}D$, $R136^{3.55}H/C$, $S161^{4.53}L$, $A199^{5.48}T$, $R236^{ICL3}Q$, $A282^{7.36}T/S$ and $P348^{C\text{-}term}S/L$ (Ballesteros-Weinstein numbering in superscript). Second, presence of mutations in known conserved GPCR residues or motifs was investigated for inclusion, but no mutations were found in any of these residues or motifs. Third, mutations in the binding pocket were included. To this end, all amino acids in a 5 Å radius around the ligands, i.e., one antagonist/inverse agonist and seven agonists, in all available X-ray and cryo-EM CB_2R structures were cross-examined with the mutation list (**Figure 6.2a**). This resulted in the inclusion of five mutations $F87^{2.57}L$, $H95^{2.65}L$, $A282^{7.36}T/S$ and $L182^{ECL2}P$ in the extracellular loop 2 (ECL2) that were in close proximity to the ligand and therefore deemed part of the orthosteric binding pocket. Finally, the resulting list of mutations was compared to the natural variants reported for CB_2R in the GPCRdb, which resulted in the exclusion of six mutations ($N11^{N\text{-}}$

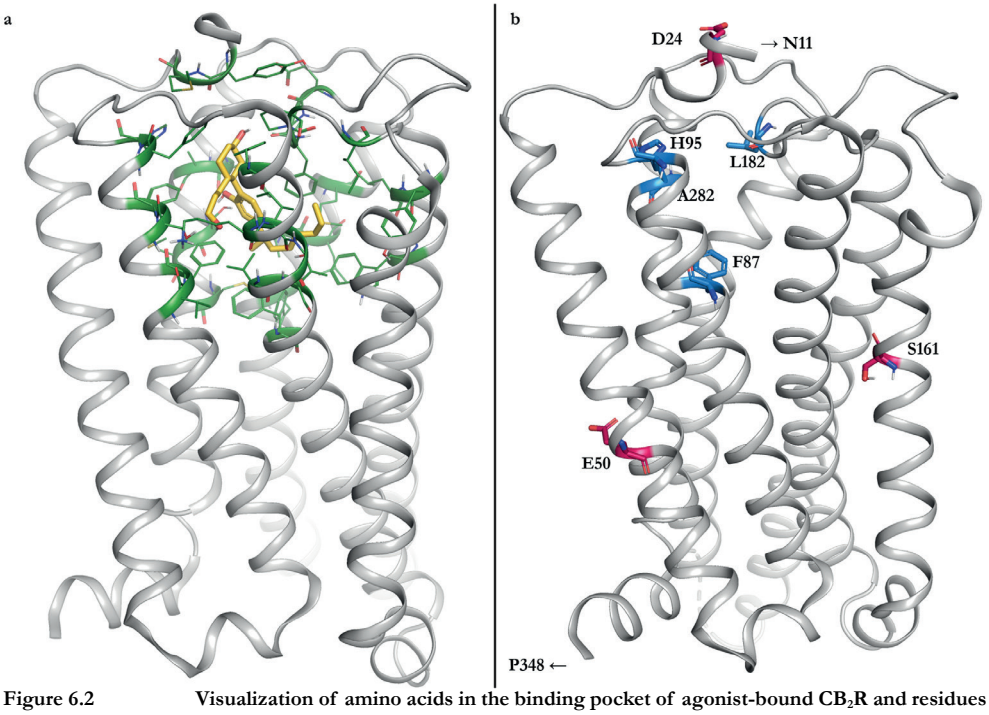

Figure 6.2 Visualization of amino acids in the binding pocket of agonist-bound CB_2R and residues bearing cancer-associated CB_2R mutations included in this study.
(a) Representative visualization of amino acids in the binding pocket of active CB_2R cryo-EM structure (8GUR) with agonist CP55,940 (yellow), showing amino acids in a 5 Å radius around the agonist (green). (b) Overview of residues investigated in this study mapped on active structure of CB_2R (8GUR). Note: Residues $N11^{N\text{-}term}$ and $P348^{C\text{-}term}$ could not be mapped, since these regions were not resolved in the structure. The colors correspond to the inclusion criteria, i.e., frequency >1 (magenta) or proximity to the orthosteric binding pocket (blue).

Table 6.1 List of selected cancer-associated mutations in CB_2R in our study identified from different cancer types.

Mutation	Primary site	Frequency	Inclusion criteria
$N11^{N\text{-}term}K$	Bronchus and lung	1	Frequency >1
$D24^{N\text{-}term}N$	Skin	2	Frequency >1
$E50^{1.49}D$	Corpus uteri, thyroid gland	2	Frequency >1
$F87^{2.57}L$	Corpus uteri	1	Binding pocket
$H95^{2.65}L$	Kidney	1	Binding pocket
$S161^{4.53}L$	Cervix uteri, bladder	2	Frequency >1
$L182^{ECL2}P$	Brain	1	Binding pocket
$A282^{7.36}T$	Corpus uteri	1	Frequency >1, binding pocket
$A282^{7.36}S$	Thyroid gland	1	Frequency >1, binding pocket
$P348^{C\text{-}term}S$	Brain, skin	2	Frequency >1

Mutations are shown in numbering of the cannabinoid CB_2 receptor (CB_2R) amino acid sequence as well as the Ballesteros-Weinstein GPCR numbering system.

^{term}S, $R136^{3.55}$H/C, $A199^{5.48}$T, $R236^{ICL3}$Q, and $P348^{C\text{-}term}$L), as they represent genetic variance and not perse a correlation to cancer. This yielded a final selection of ten mutations on nine residues due to two mutations ($A282^{7.36}$T/S) applying to two criteria (**Table 6.1**).

Seven of the nine amino acids investigated in this study were mapped on the active G protein-bound CB_2R structure with agonist CP55,940 (8GUR) (**Figure 6.2b**). Residues $N11^{N\text{-}term}$ and $P348^{C\text{-}term}$ could not be mapped on this structure, since these flexible regions were not resolved in this, or any other, CB_2R structure. Most mutations in the selected set are located in the top half of the receptor, close to the binding pocket. Mutations on $E50^{1.49}$ and $S161^{4.53}$ (and $P348^{C\text{-}term}$) are found in the bottom half of the receptor, i.e., away from the orthosteric binding pocket. Of note, the selected mutations were found in a variety of cancer types, including primary tumor sites in skin, corpus uteri and brain (**Table 6.1**).

6.2.2 Expression and receptor state of CB_2R mutants

Plasmids of all ten CB_2R mutations were generated and transiently transfected into HEK293T cells that do not endogenously express CB_2R. Wild type (WT) CB_2R was taken along as a control in all assays, which resulted in a total test set of eleven CB_2R constructs. The expression of WT and mutants CB_2R on the cell surface after transfection was examined with an ELISA and quantified as fold over mock, i.e., empty vector (**Figure 6.3a**, **Table 6.2**). The level of WT CB_2R expression was 1.6 ± 0.4 over mock and almost all mutant receptor constructs were expressed to a similar extend as WT. The expression level of mutant $D24^{N\text{-}term}N$, 2.2 ± 0.4, appeared slightly higher compared to WT, although not statistically significant. Notably, $L182^{ECL2}P$ was not expressed on the cell surface evident by a fold expression similar to mock.

To investigate whether the transiently expressed receptors were still functional, G protein activation assays were performed (**Figure 6.3b-j**, **Table 6.2**). The basal activity of all

receptor constructs was investigated and compared to WT (**Figure 6.3b**, **Table 6.2**). The basal activity of D24$^{N\text{-term}}$N was significantly increased compared to WT, whereas all other mutant receptors had a similar basal activity to WT. Potential constitutive activity of the receptors was studied by incubation with the known inverse agonist AM630 (**Figure 6.3c**, **Table 6.2**). As expected, decreased levels of activity were observed on WT which was set to -100%. D24$^{N\text{-term}}$N, the mutant with increased constitutive activity, was inhibited to a greater extent compared to WT, although not statistically significant. Activity of all other mutants was inhibited to a similar extent compared to WT (**Figure 6.3c**, **Table 6.2**). No inhibition of the constitutive activity of L182^{ECL2}P was observed, which reflected the lack of expression as determined by ELISA (**Figure 6.3a**,**c**).

Overall, most mutant receptors were expressed, and they maintained similar levels of constitutive activity compared to WT. Only mutant receptor D24$^{N\text{-term}}$N showed increased expression on the cell surface compared to WT, and also exhibited a higher level of constitutive activity.

6.2.3 Activation of CB_2R mutants by agonists

G protein activation of all CB_2R mutants was investigated for a large set of agonists with different chemotypes and partial to full agonism (**Figure 6.1**). Activation of mutant receptors was compared (and normalized) to WT activation by the specific studied agonist. To determine the physiological effect of CB_2R mutations, activation by endocannabinoids 2-AG and AEA was assessed (**Figure 6.3d**,**e**). The endocannabinoids 2-AG and AEA were able to activate D24$^{N\text{-term}}$N to a greater extent with activation levels of 144 ± 18% and 151 ± 41%, respectively, compared to their activation on WT. These activation levels corresponded to full agonism of WT CB_2R by CP55,940 (data not shown). 2-AG activation was significantly reduced on all other mutant receptors. Specifically, mutant receptors A282$^{7.36}$T and P348$^{C\text{-term}}$S were activated for 35% relative to WT, whereas all other receptors were activated less than 17% relative to WT (**Figure 6.3d**, **Table 6.2**). AEA activation on N11$^{N\text{-term}}$K, A282$^{7.36}$T and P348$^{C\text{-term}}$S was between 44% and 66% relative to WT. All other receptors were activated less than 21% by AEA (**Figure 6.3e**, **Table 6.2**).

Furthermore, activation by synthetic CB_2R agonists that have been reported in literature to attenuate cancer progression was studied, which included full agonists CP55,940 and WIN55,212-2, and partial agonist JWH133 (**Figure 6.1**, **6.3f-h**). For CP55,940, the level of activation was only similar to WT for H95$^{2.65}$L (108 ± 23%), while it was significantly decreased on mutant receptors N11$^{N\text{-term}}$K, E50$^{1.49}$D, F87$^{2.65}$L, S161$^{4.53}$L, L182^{ECL2}P, A282$^{7.36}$T, A282$^{7.36}$S and P348$^{C\text{-term}}$S and no activation was observed on mutant receptors E50$^{1.49}$D, F87$^{2.65}$L, S161$^{4.53}$L, L182^{ECL2}P (**Figure 6.3f**, **Table 6.2**). Interestingly, D24$^{N\text{-term}}$N was partially activated by CP55,940 compared to WT with a remaining 64 ± 24% activation. WIN55,212-2-mediated G protein activation was observed for all mutant CB_2R except for L182^{ECL2}P (**Figure 6.3g**, **Table 6.2**). In this case, all receptors were activated to partial levels compared to WT with activation levels between 17 ± 8% for S161$^{4.53}$L and 87 ± 7% for P348$^{C\text{-term}}$S. Finally, no JWH-133-mediated activation was observed on CB_2R mutant receptors F87$^{2.65}$L, S161$^{4.53}$L and L182^{ECL2}P and only low activation was found on E50$^{1.49}$D

(14 ± 6%) (**Figure 6.3h**, **Table 6.2**). All other mutant receptors were activated for at least 30% relative to WT yet remained partial compared to WT (**Table 6.2**).

Finally, G protein activation by the structurally diverse clinically relevant agonists Nabilone and ART-27.13 was investigated (**Figure 6.1**). No Nabilone-mediated G protein activation was observed on mutant receptors $E50^{1.49}D$, $F87^{2.57}L$ and $L182^{ECL2}P$ (**Figure 6.3i**, **Table 6.2**). Low activation of 16 ± 5% and 15 ± 11% compared to WT was found on $N11^{N\text{-}term}K$ and $S161^{4.53}L$, respectively. All other receptors were partially activated compared to WT, with activation levels between 27 ± 3% for $A282^{7.36}S$ and 81 ± 13% for $D24^{N\text{-}term}N$. ART-27.13 did not induce any G protein activation on $E50^{1.49}D$, $S161^{4.53}L$ and $L182^{ECL2}P$, while ART-27.13-mediated activation of mutant receptors $N11^{N\text{-}term}K$, $F87^{2.57}L$ and $H95^{2.65}L$ was statistically significant reduced compared to WT with activation levels of 21 ± 2 %, 17 ± 4% and 45 ± 5%, respectively, (**Figure 6.3i,j**, **Table 6.2**). $D24^{N\text{-}term}N$, $A282^{7.36}T$, $A282^{7.36}S$ and $P348^{C\text{-}term}S$ were activated at least 49% relative to WT, whereas only $A282^{7.36}T$ could be fully activated.

Screening of G protein activation by a structurally diverse set of agonists on CB_2R mutants highlighted differences between endocannabinoids, synthetic reference and clinically relevant agonists. Specifically, CB_2R receptors bearing the $H95^{2.65}L$ mutation were not activated by endocannabinoids but were partially activated by all synthetic agonists compared to WT. Mutations in N- and C-termini moderately impacted receptor activation by all agonists, whereas mutations in the binding pocket differently impacted receptor activation dependent on the agonist at hand.

6.2.4 Expression levels (B_{max}) and binding affinity (K_D) of CB_2R mutants

To investigate the binding of various agonists on the mutant receptors, binding experiments with orthosteric agonist [^{3}H]CP55,940 and inverse agonist [^{3}H]RO6957022 were performed (**Figure 6.4**). Initial binding experiments with a high concentration of membranes (20 μg membrane/well) showed that for seven mutant receptors ($E50^{1.49}D$, $F87^{2.57}L$, $H95^{2.65}L$, $S161^{4.53}L$, $L182^{ECL2}P$, $A282^{7.36}T$, $A282^{7.36}S$) low levels of [^{3}H]CP55,940 binding were detected, if any, and thus affinity of the ligands could no longer be determined on these mutant receptors (**Figure 6.4a**). However, sufficient binding of [^{3}H]CP55,940 was found for

→ Figure 6.3 Expression, receptor state and G protein activation of wild type (WT) and mutant CB_2Rs by an inverse agonist, endocannabinoids, reference and clinical agonists.
(a) Expression levels of transiently transfected WT and mutant CB_2Rs on HEK293T cells. Mock cells were transfected with empty pcDNA3.1 vector and expression data is calculated as fold over mock. Data are expressed as mean ± SD of at least two independent experiments performed in quintuplicate. (b) Basal G protein activation of WT and mutant CB_2Rs and (c) inverse agonism by 10 μM AM630. G protein activation by 10 μM of endocannabinoids (d) 2-AG and (e) AEA, 10 μM of reference agonists (f) CP55,940, (g) WIN55,212-2 and (h) JWH133, and 10 μM of clinical compounds (i) Nabilone and (j) ART-27.13. The maximum activation level of WT by the specific ligand was set to 100% while specific mutant basal activation levels were set to 0%. Data are presented as mean ± SEM of three individual experiments performed in duplicate.

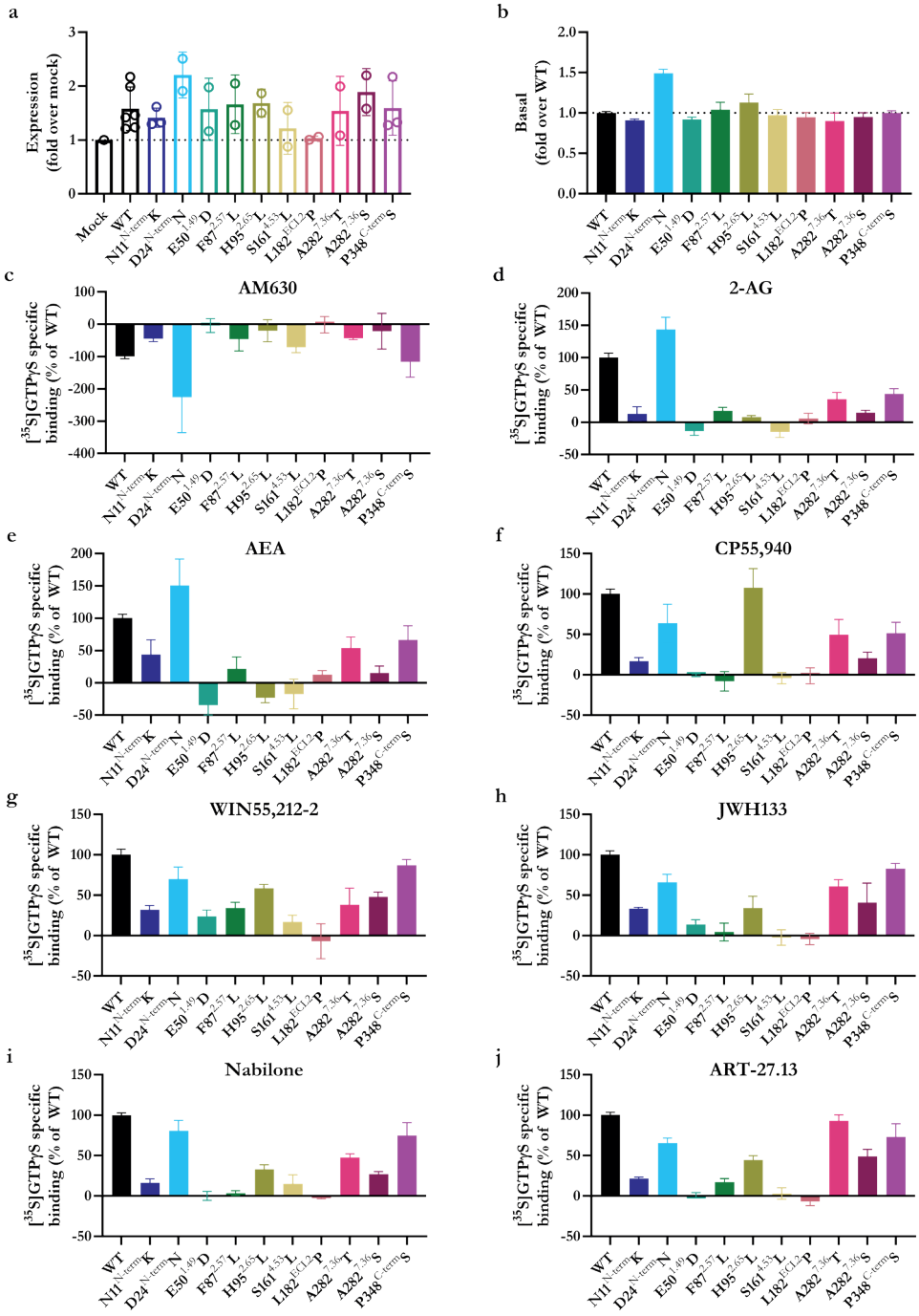
a
Expression (fold over mock)
Mock
WT
N11 N-term K
D24 N-term N
E50 1.49 D
F87 2.57 L
H95 2.65 L
S161 4.53 L
L182 ECL2 P
A282 7.36 T
A282 7.36 S
P348 C-term S
b
Basal (fold over WT)
c
AM630
[35S]GTPγS specific binding (% of WT)
d
2-AG
e
AEA
f
CP55,940
g
WIN55,212-2
h
JWH133
i
Nabilone
j
ART-27.13

Table 6.2 Expression, receptor state and G protein activation of WT and mutant CB_2Rs by 10 μM of inverse agonist, endocannabinoids, reference and clinical agonists.

Mutation	Expression (fold over mock)[a]	Basal[b] (fold over WT)	AM630[c] (%)	2-AG[c] (%)	AEA[c] (%)	CP55,940[c] (%)	WIN55,212-2[c] (%)	JWH133[c] (%)	Nabilone[c] (%)	ART-27.13[c] (%)
WT	1.6 ± 0.4	1.0 ± 0.0	-100 ± 6	100 ± 6	100 ± 5	100 ± 5	100 ± 6	100 ± 3	100 ± 3	100 ± 3
N11$^{N\text{-term}}$K	1.4 ± 0.2	0.9 ± 0.0	-45 ± 9	13 ± 11*	44 ± 22	17 ± 5*	32 ± 5*	33 ± 2*	16 ± 5*	21 ± 2*
D24$^{N\text{-term}}$N	2.2 ± 0.4	1.5 ± 0.1*	-226 ± 110	144 ± 18*	151 ± 41	64 ± 24	70 ± 15	66 ± 10	81 ± 13*	65 ± 6
E50$^{1.49}$D	1.6 ± 0.6	0.9 ± 0.0	-4 ± 22	-14 ± 6*	-34 ± 21*	0 ± 2*	24 ± 8*	14 ± 6*	0 ± 6*	1 ± 3*
F87$^{2.57}$L	1.7 ± 0.5	1.0 ± 0.1	-46 ± 36	17 ± 6*	21 ± 18*	-8 ± 12*	34 ± 7*	4 ± 11*	3 ± 3*	17 ± 4*
H95$^{2.65}$L	1.7 ± 0.3	1.1 ± 0.1	-20 ± 34	8 ± 2*	-23 ± 8*	108 ± 23	59 ± 5	34 ± 14*	33 ± 6*	45 ± 5*
S161$^{4.53}$L	1.2 ± 0.5	1.0 ± 0.1	-72 ± 16	-15 ± 9*	-17 ± 23*	-4 ± 7*	17 ± 8*	-2 ± 10*	15 ± 11*	3 ± 7*
L182^{ECL2}P	1.0 ± 0.0	0.9 ± 0.1	-2 ± 25	6 ± 8*	13 ± 6*	-1 ± 10*	-7 ± 22*	-4 ± 7*	-3 ± 1*	-7 ± 5*
A282$^{7.36}$T	1.5 ± 0.6	0.9 ± 0.1	-44 ± 4	36 ± 10*	54 ± 17	49 ± 19*	38 ± 20*	61 ± 8*	47 ± 5	93 ± 8
A282$^{7.36}$S	1.9 ± 0.4	0.9 ± 0.1	-22 ± 55	15 ± 4*	15 ± 11*	21 ± 7*	48 ± 6*	41 ± 24*	27 ± 3*	49 ± 9
P348$^{C\text{-term}}$S	1.6 ± 0.5	1.0 ± 0.0	-116 ± 48	44 ± 8*	66 ± 22	51 ± 14*	87 ± 7	83 ± 6	75 ± 16*	73 ± 16

Mutations are shown in numbering of the cannabinoid CB_2 receptor (CB_2R) amino acid sequence as well as the Ballesteros-Weinstein GPCR numbering system. [a] Expression level of WT and mutant CB_2Rs are presented as fold over mock (empty pcDNA3.1 vector) and are mean ± SD of at least two individual experiments performed in quintuplicate. [b] Basal activity expressed as fold change over WT in [^{35}S]GTPγS assays. [c] Percentage of G protein activation by 10 μM compound compared to WT. Values are mean ± SEM of three independent experiments performed in duplicate. One-way ANOVA with Dunnett's posthoc test was used to analyze differences in activation compared to WT (*$p < 0.05$).

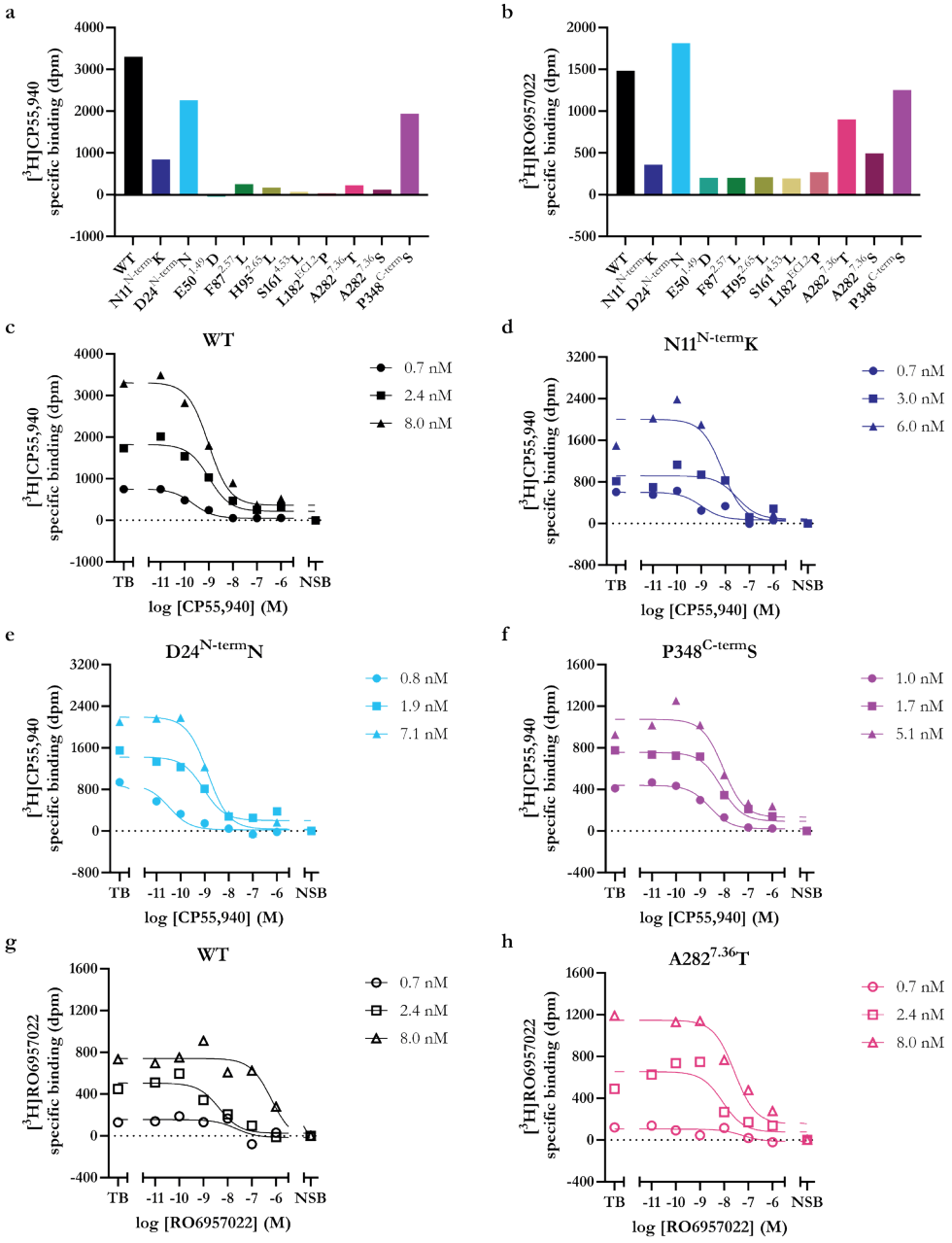

Figure 6.4 Specific binding of agonist [^{3}H]CP55,940 and inverse agonist [^{3}H]RO6957022 on WT and mutant CB_2Rs.

Specific binding of (a) agonist [^{3}H]CP55,940 and (b) inverse agonist [^{3}H]RO6957022 to membranes expressing WT or mutant CB_2R (20 µg/well). Homologous displacement experiment with (c) WT, (d) N11$^{N\text{-term}}$K, (e) D24$^{N\text{-term}}$N and (f) P348$^{C\text{-term}}$S CB_2R using [^{3}H]CP55,940. Homologous displacement experiments with (g) WT and (h) A282$^{7.36}$T CB_2R using [^{3}H]RO6957022. Total binding (TB) of the radioligand is set to 100% and non-specific binding (NSB) of radioligand was determined the presence of cold ligand and set to 0%. Data shown are specific radioligand binding of a representative experiment of at least two (a, b) or three (c-h) experiments performed in duplicate.

mutant receptors $N11^{N\text{-}term}K$, $D24^{N\text{-}term}N$ and $P348^{C\text{-}term}S$, which were further characterized in homologous displacement assays. Similarly, all mutant receptors were screened at the same high membrane concentration in [^{3}H]RO6957022 binding assays (**Figure 6.4b**). This resulted in low levels of [^{3}H]RO6957022 binding for seven mutant receptors ($N11^{N\text{-}term}K$, $E50^{1.49}D$, $F87^{2.57}L$, $H95^{2.65}L$, $S161^{4.53}L$, $L182^{ECL2}P$, $A282^{7.36}S$). Similar to the screen with [^{3}H]CP55,940, sufficient binding of [^{3}H]RO6957022 was found for mutant receptors $D24^{N\text{-}term}N$ and $P348^{C\text{-}term}S$. However, sufficient binding of the radioligand was also found on $A282^{7.36}S$ with this radioligand. Therefore, binding to this mutant was further characterized in [^{3}H]RO6957022 binding assays.

Homologous displacements with CP55,940 on WT, $N11^{N\text{-}term}K$, $D24^{N\text{-}term}N$ and $P348^{C\text{-}term}S$ yielded affinities of CP55,940 on these mutants similar to WT with pK_D values between 8.4 ± 0.2 and 8.8 ± 0.1 (**Figure 6.4c-f**, **Table 6.3**). Likewise, the affinity of inverse agonist RO6957022 on CB_2R was not statistically significant impacted by the $A282^{7.36}T$ mutation (**Figure 6.4g**,**h**, **Table 6.3**). Homologous displacement experiments with CP55,940 and RO6957022 also yielded B_{max} values for receptor expression in the membranes used. B_{max} values were slightly reduced for $N11^{N\text{-}term}K$ and $D24^{N\text{-}term}N$ compared to WT, whereas it was significantly reduced for $P348^{C\text{-}term}S$ to 1.0 ± 0.2 compared to 2.3 ± 0.5 for WT (**Table 6.3**). The expression level of $A282^{7.36}T$ was 2-fold higher than on WT, but not statistically significant different (**Table 6.3**).

Altogether, binding of both radioligands [^{3}H]CP55,940 and [^{3}H]RO6957022 was negatively impacted for six mutant receptors $E50^{1.49}D$, $F87^{2.57}L$, $H95^{2.65}L$, $S161^{4.53}L$, $L182^{ECL2}P$ and $A282^{7.36}S$. Nevertheless, binding of [^{3}H]CP55,940 could still be detected on $N11^{N\text{-}term}K$, $D24^{N\text{-}term}N$ and $P348^{C\text{-}term}S$, while sufficient binding of [^{3}H]RO6957022 was observed on mutant receptors $D24^{N\text{-}term}N$, $A282^{7.36}T$ and $P348^{C\text{-}term}S$. The affinity of CP55,940 for $N11^{N\text{-}term}K$, $D24^{N\text{-}term}N$ and $P348^{C\text{-}term}S$ and RO6957022 for $A282^{7.36}T$ was not significantly altered compared to WT and expression levels were similar to WT, except for $P348^{C\text{-}term}S$ which was reduced.

6.2.5 Binding affinity of reference agonists at CB_2R mutants

Binding affinity at $N11^{N\text{-}term}K$, $D24^{N\text{-}term}N$, $A282^{7.36}T$ and $P348^{C\text{-}term}S$, i.e., the mutants that still showed sufficient binding, was investigated for a selection of agonists. Since endocannabinoids 2-AG and AEA behaved similarly on all mutant receptors in G protein activation assays, only 2-AG was selected for further profiling (**Figure 6.3d**,**e**, **6.5a,b**). Similarly, affinity of only Nabilone was examined as activation by Nabilone and ART-27.13 was similarly impacted by all mutant receptors (**Figure 6.3i,j**). This was supplemented with affinity determination of clinical agonist Δ^9-THC, which did not yield detectable G protein activation levels (**Chapter 3**). The affinity of 2-AG was significantly, yet moderately, increased on mutant receptors $D24^{N\text{-}term}N$ and $P348^{C\text{-}term}S$ to 5.8 ± 0.1 and 5.6 ± 0.1, respectively, compared to 5.1 ± 0.1 on WT (**Figure 6.5a**, **Table 6.3**). Mutation $N11^{N\text{-}term}K$ did not influence the binding affinity of 2-AG on CB_2R. The affinity of 2-AG on mutant CB_2R $A282^{7.36}T$, as detected in [^{3}H]RO6957022 binding assays, was slightly, yet significantly reduced compared to WT with pK_i values of 5.6 ± 0.1 and 6.1 ± 0.1, respectively (**Figure**

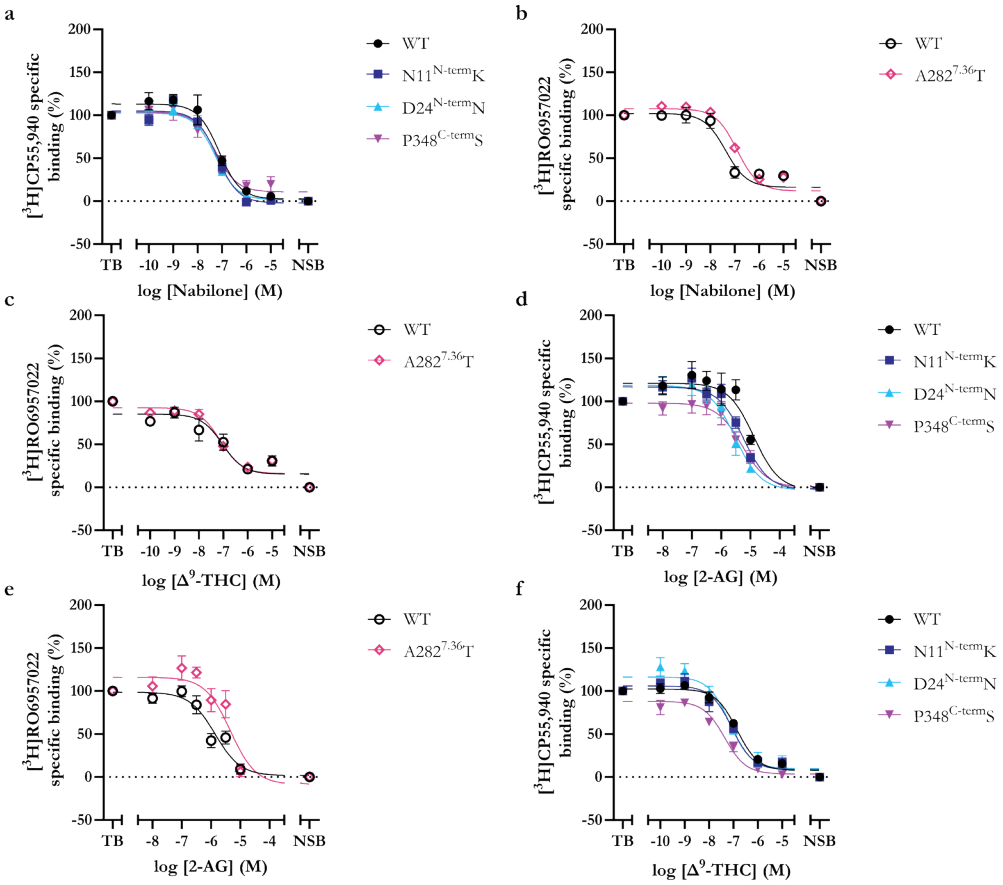

Figure 6.5 Affinity of endogenous agonist and clinical agonists on WT and mutant CB_2Rs.
Displacement of [^{3}H]CP55,940 (WT, N11$^{N\text{-term}}$K, D24$^{N\text{-term}}$N and P348$^{C\text{-term}}$S) or [^{3}H]RO6957022 (WT and A282$^{7.36}$T) with (a,b) endogenous agonist 2-AG, and (c,d) clinical agonists Δ^9-THC and (e,f) Nabilone. Total binding (TB) of the radioligand is set to 100% and non-specific binding (NSB) of radioligand was determined the presence of cold ligand and set to 0%. Data are the mean ± SEM of at least three experiments performed in duplicate.

6.5b, **Table 6.3**). Furthermore, the binding affinity of Δ^9-THC and Nabilone was not affected by mutations N11$^{N\text{-term}}$K, D24$^{N\text{-term}}$N or P348$^{C\text{-term}}$S (**Figure 6.5c**,**e**, **Table 6.3**). Similarly, the affinity of Δ^9-THC was not affected on A282$^{7.36}$T (**Figure 6.5d**, **Table 6.3**). However, binding affinity of Nabilone was significantly reduced to 7.1 ± 0.1 on A282$^{7.36}$T compared to 7.6 ± 0.1 for WT (**Figure 6.5f**, **Table 6.3**). In conclusion, the impact of the investigated CB_2R mutations on binding affinity of reference agonists 2-AG, Δ^9-THC and Nabilone was agonist-dependent, and if any, only moderate effects were observed.

6.2.6 Structural mapping of cancer-associated CB_2R mutations

Most of the mutations in the CB_2R binding pocket negatively affected the activation or binding by agonists. Strikingly, mutant H95$^{2.65}$L responded differently to the endocannabinoids

Table 6.3 Expression levels (B_{max}) and affinities of CP55,940, RO6957022, 2-AG, Δ^9-THC and Nabilone for WT and mutant CB_2R determined from radioligand binding assays.

	[^{3}H]CP55,940 binding assays			[^{3}H]RO6957022 binding assays		
Mutation	**B_{max} (pmol/mg)**	**pK_D (K_D (nM))**		**B_{max} (pmol/mg)**	**pK_D (K_D (nM))**	
WT	2.3 ± 0.5	8.6 ± 0.0 (2.6)		0.5 ± 0.0	8.8 ± 0.1 (1.5)	
N11$^{N\text{-term}}$K	1.1 ± 0.2	8.4 ± 0.2 (4.1)		N.A.	N.A.	
D24$^{N\text{-term}}$N	1.9 ± 0.3	8.8 ± 0.1 (1.7)		N.A.	N.A.	
A282$^{7.36}$T	N.A.	N.A.		1.0 ± 0.2	8.8 ± 0.2 (1.7)	
P348$^{C\text{-term}}$S	1.0 ± 0.2*	8.8 ± 0.1 (1.7)		N.A.	N.A.	
	pK_i 2-AG	**pK_i Δ^9-THC**	**pK_i Nabilone**	**pK_i 2-AG**	**pK_i Δ^9-THC**	**pK_i Nabilone**
WT	5.1 ± 0.1	7.1 ± 0.1	7.4 ± 0.1	6.1 ± 0.1	7.2 ± 0.4	7.6 ± 0.1
N11$^{N\text{-term}}$K	5.4 ± 0.0	7.3 ± 0.2	7.3 ± 0.1	N.A.	N.A.	N.A.
D24$^{N\text{-term}}$N	5.8 ± 0.1***	7.5 ± 0.1	7.5 ± 0.2	N.A.	N.A.	N.A.
A282$^{7.36}$T	N.A.	N.A.	N.A.	5.6 ± 0.1†	7.4 ± 0.2	7.1 ± 0.1††
P348$^{C\text{-term}}$S	5.6 ± 0.1**	7.6 ± 0.1	7.6 ± 0.1	N.A.	N.A.	N.A.

Values are mean ± SEM of three independent experiments performed in duplicate. No affinity and expression values were determined for mutants E50$^{1.49}$D, F87$^{2.57}$L, H95$^{2.65}$L, S161$^{4.53}$L, L182^{ECL2}P, A282$^{7.36}$S due to no or too low levels of specific radioligand binding. One-way ANOVA with Dunnett's multiple comparisons test or an unpaired t-test was performed to analyzed differences in pK_D, B_{max} or pK_i values compared to WT ($^{*}p<0.05$, $^{**}p<0.01$, $^{***}p<0.001$ in [^{3}H] CP55,940 assays or $^{\dagger}p<0.05$, $^{\dagger\dagger}p<0.01$ in [^{3}H]RO6957022 assays).

compared to synthetic agonists, i.e., activation by 2-AG and AEA was completely abolished compared to WT, while partial activation remained for all synthetic agonists (**Figure 6.3**, **Table 6.2**). Further structural investigation of this residue demonstrated that H95$^{2.65}$ is in close proximity to the cyclohexanol group of CP55,940 (5.7 Å) and as such might interact with agonists (**Figure 6.6a**).

Furthermore, differences in activation levels of the A282$^{7.36}$T and A282$^{7.36}$S CB_2Rs, i.e., receptors with two different mutations on the same residue, were observed and these also differently impacted affinity of inverse agonist RO6957022 (**Figure 6.3**, **6.4**). From the cryo-EM structure with CP55,940, it can be observed that the carbonyl of this residue is located near the agonist and the hydroxyl on the phenol core of CP55,940 (4.4 Å) (**Figure 6.6a**). The cyclohexanol group of CP55,940 is moved away from the methyl group at a distance of 6.4-6.7 Å.

Finally, mutation E50$^{1.49}$D significantly impacted receptor activation by all agonists and the binding of [^{3}H]CP55,940 and [^{3}H]RO69557022 was greatly reduced, while the expression level remained similar to WT (**Figure 6.3**, **6.4**). Closer examination of this residue in the cryo-EM structure indicated that E50$^{1.49}$ is structurally close to P296$^{7.50}$ in the conserved NPxxY motif (4.4 Å), which might aid in the stabilization of the receptor (**Figure 6.6b**). As such, reduction of the amino acid side chain by the E50$^{1.49}$D mutation might destabilize the receptor and alter its function.

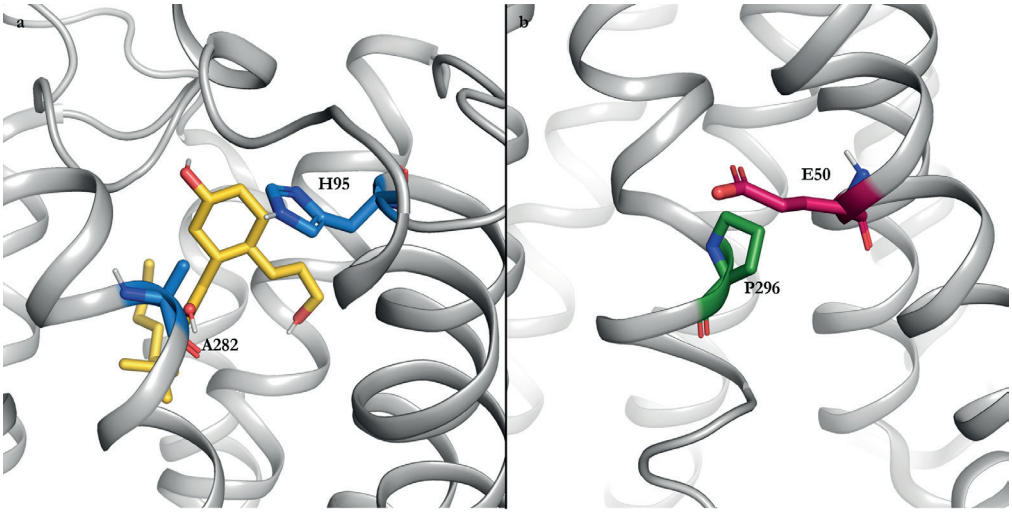

Figure 6.6 Structural visualization of residues H95$^{2.65}$, A282$^{7.36}$ and E50$^{1.49}$ in CB_2R structure with agonist CP55,940.
Overview of specific residues investigated in this study mapped on active structure of CB_2R (grey; 8GUR). (a) Zoom in on binding pocket with CP55,940 (yellow) and residues H95$^{2.65}$ and A282$^{7.36}$ (blue). (b) Zoom in on residue E50$^{1.49}$ (magenta) and structurally close NPxxY motif residue P296$^{7.50}$ (green).

6.3 Discussion

Cancer is the second leading cause of death globally and research to more efficacious and safer therapies is constantly ongoing[31]. Recently, the role of GPCRs in cancer development and progression is becoming more acknowledged since GPCR-mediated cell signaling pathways have been associated with cell migration, survival, and growth[5]. As such a small number of GPCR drugs and antibodies are in clinical trials as cancer therapies[6]. Various *in vitro* and *in vivo* studies on different cancer types have also specifically shown the beneficial effects of CB_2R activation[22–25]. Nevertheless, in 20% of all cancers GPCRs are mutated, which might interfere with endogenous signaling or targeting of these receptors[2,3,7–11]. In this chapter, we investigated the impact of cancer-associated CB_2R mutations on endogenous binding and activation, as well as the druggability of these mutant receptors by a variety of CB_2R agonists.

Mutations in CB_2R were extracted from the GDC and narrowed down to include the most frequently mutated locations as well as mutations in vicinity to the binding pocket (**Figure 6.2**, **Table 6.1**). The resulting ten mutations were transiently transfected into HEK293T cells (**Figure 6.3a**, **Table 6.2**). Of these, only CB_2R with the L182^{ECL2}P mutation was not expressed on the cell membrane and as such no responses were observed in functional or binding assays (**Figure 6.3**, **6.4**, **Table 6.2**). We, in **Chapter 4**, and others previously showed that L182^{ECL2} is involved in binding of diverse agonists since a mutation to isoleucine (L182^{ECL2}I) reduced the potency of agonists but not expression of the receptor[32–35]. Nevertheless, mutations to or from proline (P) are more often described to have a detrimental effect on receptor activity and trafficking to the cell membrane as the rigid backbone of proline provokes a forced turn in the protein sequence[9,36]. The swap to

proline in the ECL2, and close to the binding pocket, thus most likely interferes with the trafficking of the receptor to the cell membrane and as such is detrimental. This suggests that patients bearing the CB_2R $L182^{ECL2}P$ mutation will no longer benefit from endogenous protection or respond to cannabinoid-based therapies.

On the other hand, the exchange of proline for serine (S) in the C-terminus ($P348^{C\text{-}term}S$), distant from the binding pocket, did not prevent receptor trafficking to the cell membrane, but significantly reduced the expression level of this mutant receptor in binding assays (**Figure 6.3a**, **Table 6.2**, **6.3**). Furthermore, we observed reduced G protein activation levels by this mutant receptor for various agonists compared to WT (**Figure 6.3d-j**, **Table 6.2**). The swap from proline to serine introduces an extra site on the C-terminus for a post-translational modifications (PTM), which are involved in control of the dynamics of signaling[37,38]. Specifically, serine residues, opposed to proline, on the C-terminus are prone to phosphorylation, which might initiate the recruitment of ß-arrestins and desensitization or internalization of the receptor[37,38]. Similarly, PTMs on the N-terminus of GPCRs have been described to be involved in the receptor folding, trafficking and regulation of binding and signaling[37,38]. Asparagines (N) are prone to *N*-glycosylation and specifically, CB_2R $N11^{N\text{-}term}$ was described to be glycosylated in mammalian cell lines, which contributed to a higher protein stability[39]. As such, the reduced agonist-mediated G protein activation on CB_2R mutant $N11^{N\text{-}term}K$ might be due to losing a glycosylation site (**Figure 6.3**, **Table 6.2**)[40]. In contrast, the increased basal activity and levels of G protein activation of mutant receptor $D24^{N\text{-}term}N$ might be attributed to the gain of a glycosylation site (**Figure 6.3b**,**c**, **Table 6.2**).

In **Chapter 4** and other studies, hydrophobic interactions in the orthosteric pocket of CB_2R between $F87^{2.57}$ and/or $H95^{2.65}$ and various (inverse) agonists are described[32,33,35]. Interestingly, CP55,940-mediated inhibition of cAMP accumulation was investigated on CB_2R $F87^{2.57}A$ and $H95^{2.65}A$ mutants, which revealed a decrease in agonist potency with a small or no effect on its efficacy[33]. This contrasts with the loss of or reduced G protein activation by CP55,940 and other agonists in our studies on $F87^{2.57}L$ and $H95^{2.65}L$ (**Figure 6.3**, **Table 6.2**). Pathway amplification by measurement of downstream second messengers, such as cAMP, might explain these contrasting results[41]. Furthermore, $H95^{2.65}$ has been postulated to maintain a polar network with $S285^{7.39}$ around orthosteric ligands, which might be disturbed in our studies by switching to hydrophobic leucine (L) (**Figure 6.6a**). Interestingly, the endocannabinoids were not able to activate $H95^{2.65}L$ CB_2R, whereas synthetic agonists still activated the receptor albeit partially (**Figure 6.3**). Different functional effects of endocannabinoids compared to synthetic agonists were previously also reported by Hillger *et al.* on lymphoblastoid cell lines (LCLs) from individuals with different CB_2R genotypes[42]. This emphasizes the importance of including various chemotypes to explore the effects of disease-associated mutations on receptor behavior.

One amino acid in the patient data set was mutated twice, namely $A282^{7.36}$, which was located close to the binding pocket (**Figure 6.6a**). Although structurally-related, we found profound differences between the $A282^{7.36}T$ and $A282^{7.36}S$ mutations. Consistently higher activation by the different agonists on the $A282^{7.36}T$ mutant was found compared to $A282^{7.36}S$ (**Figure 6.3**, **Table 6.2**). Furthermore, in binding studies only CB_2R $A282^{7.36}T$ could be bound by an inverse agonist, whereas binding to $A282^{7.36}S$ could not be quantified

(**Figure 6.4**, **6.5**, **Table 6.3**). Hydrophobic interactions between A282$^{7.36}$ and HU308 have been postulated in **Chapter 4**, which may be disturbed by the polar residues serine and threonine (T) in our studies[32]. Furthermore, this specific residue has previously been described to shape the ligand entry pathway to the CB_2R orthosteric pocket and a mutation towards phenylalanine (F) occluded the entry pathway for JWH133[43]. We hypothesize that the two studied mutations might also interfere with the shaping of the ligand entry pathway. However, the differences between the two mutants requires more experimental validation. Nevertheless, it becomes evident that mutations near the orthosteric binding pocket have a substantial impact on the physiological function and druggability of CB_2R.

Mutations E50$^{1.49}$D and S161$^{4.53}$L were structurally distant from the binding pocket, yet they significantly affected G protein activation and binding of agonists to the receptors (**Figure 6.3**, **6.4a**,**b**, **Table 6.2**). Two independent cancer genome analysis studies revealed a high mutational frequency amongst GPCRs of residues at position 1.49 and 4.53[3,4]. A key role for tight packing of transmembrane helices is attributed to S$^{4.53}$ in several class A GPCRs and mutations to leucine have been shown to disrupt the structure or activation patterns of these receptors[10,44,45]. Furthermore, in the ß$_2$-adrenoceptor residue 1.49 appeared to be structurally proximal to the conserved NPxxY motif, which is involved in receptor folding, localization and regulation of signaling[4]. Upon closer examination of this region in the CB_2R active cryo-EM structure from **Chapter 4** (8GUR), we observed that NPxxY residue P296$^{7.50}$ was structurally close to E50$^{1.49}$ (**Figure 6.6b**)[32]. This suggests that the specific orientations of E50$^{1.49}$ and S161$^{4.53}$ are important for the structural stability and functionality of CB_2R and reduction of the amino acid side chain by the E50$^{1.49}$D mutation might destabilize and alter receptor function.

It should be noted that conclusions from this study are based on functional screening results. Therefore, the functional investigation of these mutations should be expanded to determine the potency of different agonists. As such, the [^{35}S]GTPγS assays that were used in this screen could be continued or a switch to another G protein-dependent assay could be made. However, it may be of interest to also include ß-arrestin-2 recruitment assays since we hypothesize that PTMs may differ on the P348$^{C\text{-term}}$S mutation compared to WT and consequently could alter ß-arrestin-2 recruitment. Furthermore, to investigate whether mutations introduce or remove PTMs, SDS-page and mass spectrometry-based quantitative proteomic experiments might be executed on mutant receptors N11$^{N\text{-term}}$K, D24$^{N\text{-term}}$N and P348$^{C\text{-term}}$S[38,48]. The recently developed a multiplex assay to simultaneously investigate the inhibition of cAMP production and ß-arrestin-2 recruitment (**Chapter 3**) may serve as a platform to screen functional responses of mutant receptors. This assay can be easily adapted to transiently express CB_2R mutants, opposed to the ß-arrestin-2 recruitment assay in **Chapter 2**, and investigate simultaneously their effect on two different pathways. The kinetic context in this assay might highlight further kinetic differences between the mutants, which was previously shown for A_{2A} receptor mutation that affected a ligand's dissociation[46]. Moreover, most mutations caused a decrease in sensitivity to agonist stimulation, which may aid the tumor cells to evade the antitumor effects of CB_2R activation. As such these mutations might be driver mutations, but more research is required to examine whether they are actually driver or passenger mutations[47]. Ultimately, experiments focusing on cancer processes, such as migration and proliferation, might be executed with CB_2R mutants to

investigate the impact on cancer development and progression. These experiments could be extended to cancer relevant cell lines making use of the CRISPR-Cas9 technology[49,50].

In conclusion, our results indicate that cancer-associated mutations in CB_2R can impact the expression, agonist binding and activation of the receptor. Binding of agonists and subsequent activation of CB_2R was reduced or completely abolished for CB_2Rs with mutations in the binding pocket. Unexpectedly, mutations distant from the binding pocket also affected the receptor behavior most likely by interfering with conserved motifs or transmembrane packaging. Ultimately, mutations in the N- and C-terminus altered the CB_2R expression levels possibly due to the introduction or removal of post-translational modifications. Interestingly, there might be differences between the activation of the mutant receptors by endogenous and synthetic agonists as we found clear differences on specifically the $H95^{2.65}L$ mutant. Altogether, this study emphasizes the importance of personalized medicine by examination of the patient's genetic composition of CB_2R prior to treatment with cannabinoid-based therapeutics. Follow-up experimentation is required to further investigate the implications of the selected cancer-associated CB_2R mutations on cancer development and progression. Furthermore, the mutant selection can be expanded to include more mutations from the GDC to obtain a broad understanding of targeting CB_2R in cancer.

6.4 Materials and methods

6.4.1 Chemicals and reagents

Primary rabbit anti-HA tag polyclonal antibody was obtained from ThermoFisher (Waltham, MA, USA) and secondary goat anti-rabbit HRP-conjugated antibody was from Jackson ImmunoResearch (Cambridgeshire, UK). Compounds 2-arachidonoylglycerol (2-AG), anandamide (AEA), WIN55,212-2, JWH133 and phenylmethylsulfonyl fluoride (PMSF) were bought from Tocris Bioscience (Bristol, UK). CP55,940 was obtained from Sigma-Aldrich (St. Louis, MO, USA), while Nabilone and ART-27.13 were provided by F. Hoffmann-La Roche Ltd (Basel, Switzerland). RO6957022 and [^{3}H]RO6957022 (specific activity 82.8 Ci/mmol) were custom-synthesized and custom-labeled, respectively, by F. Hoffmann-La Roche Ltd. [^{3}H]CP55,940 (specific activity 108.5 Ci/mmol), guanosine 5'-O-[γ-thio]triphosphate ([^{35}S]GTPγS, specific activity 1250 Ci/mmol) and GF/C filter plates were purchased from PerkinElmer (Waltham, MA, USA). Bicinchoninic acid (BCA) and BCA protein assay reagent were purchased from Pierce Chemical Company (Rockford, IL, USA). All other chemicals were of analytical grade and obtained from standard commercial sources. Buffers and solutions were prepared at room temperature (rt) using Millipore water (deionized using a MilliQ A10 Biocel™, with a 0.22 μm filter).

6.4.2 Data mining and mutation selection

Cancer-associated mutations in CB_2R were retrieved from Genomic Data Commons (GDC) (version 21.0). A selection of missense mutations was made based on a mutation frequency

>1 or mutation towards two different amino acids. Furthermore, structural importance was investigated by inclusion of mutations in conserved GPCR regions (x.50, Ballesteros-Weinstein numbering) or motifs (DRY, CWxP, NPxxY), and mutations in the orthosteric binding pocket. The orthosteric binding pocket residues were defined in all eight CB_2R X-ray or cryo-EM structures (6KPC, 6KPF, 6PT0, 5ZTY, 8GUQ, 8GUR, 8GUS, 8GUT) by direct interactions of the ligand with amino acids or amino acids in a 5 Å radius around the ligand. The respective receptor structures were retrieved from the Protein Data Bank (PDB) using the fetch function in PyMOL Molecular Graphics System version 2.4 (Schrödinger, LLC., NY, USA) and hydrogen atoms were added. Using built-in functionality, the selection of the ligand was expanded to all residues around it within 5 Å. All mutations that were reported as natural variants in the GPCRdb (release Oct. 25, 2019) were excluded from our study[51].

6.4.3 Plasmid design and isolation

Primers were designed using the QuikChange® Primer Design feature from Agilent Technologies (Santa Clara, CA, USA) and ordered via Integrated DNA Technologies (Coralville, IA, USA). An N-terminal 3×HA-tagged human wild type cannabinoid CB_2 receptor (WT hCB_2R) (cDNA Resource Center; Bloomsburg, PA, USA) cloned into pcDNA3.1(+) was used as a template for mutations. Mutations were generated with the QuikChange II Site-Directed Mutagenesis Kit (Agilent Technologies) according to the protocol. In short, 50 ng of the template was mixed with 10 µM forward and reverse primer, 1 µL of deoxyribonucleotide triphosphate (dNTP) mix, 2.5 µL of 10× reaction buffer and 2.5 U *PfuUltra* HF DNA polymerase in a total volume of 20 µL. The PCR reaction was performed in a T100™ Thermal Cycler (Biorad; Irvine, CA, USA) for 22 cycles consisting of 30 s at 98 °C, 1 min at 55 °C and 10 min at 68 °C. The template DNA was then removed by incubating the mixture with 5 U of *Dpn I* restriction enzyme for 2 h at 37 °C before transforming the plasmids into XL-1 Blue supercompetent cells according to the kit's protocol. The plasmids were isolated with the QIAprep mini and midi plasmid purification kits (Qiagen; Germantown, MD, USA). All mutations were confirmed by double-strain DNA sequencing (Leiden Genome Technology Center; Leiden, the Netherlands).

6.4.4 Cell culture, transfection, and membrane preparation

Human embryonic kidney 293 T (HEK293T) cells were grown as monolayers in culture medium i.e., Dulbecco's Modified Eagle's Medium, supplemented with 10% fetal calf serum, 2 mM L-glutamine, 100 IU/mL penicillin and 100 µg/mL streptomycin under a humidified atmosphere at 37 °C with 5% CO_2. Subculture was done twice a week at 80 – 90% confluence on 10 cm ø plates by trypsinization.

HEK293T were transfected with WT or mutant hCB_2R as previously described in **Chapter 4**[32]. In short, cells were seeded on 10 cm ø plates 24 h prior to transfection to reach approximately 50% confluence at the start of transfection. The cells were transfected with 10 µg plasmid DNA of WT or mutant hCB_2R using the calcium phosphate precipitation

method. To this end, a DNA-calcium mix was made containing 270 mM $CaCl_2$ and 10 μg plasmid DNA to which Hank's Balanced Salt Solution (HBSS; 280 mM NaCl, 10 mM KCl, 1.5 mM Na_2HPO_4 and 50 mM HEPES) was added in a 1:1 (v/v) ratio and mixed by aeration to create consistent calcium phosphate precipitates. For transfection, 1 mL DNA-calcium mix was added per 10 cm ø plate, followed by a 48 h incubation under a humidified atmosphere at 37 °C with 5% CO_2.

For membrane preparation, transient HEK293T cells were harvested 48 h after transfection. Cells were detached by scraping into 3 mL of PBS and subsequently centrifuged at 2000 × g for 5 min. Pellets were resuspended in ice-cold Tris buffer (50 mM Tris-HCl, pH 7.4) and homogenized with an Ultra Turrax homogenizer (IKA-Werke GmbH & Co. KG; Staufen, Germany). Cytosolic and membrane fractions were separated using a high-speed centrifugation step of 31,000 rpm (100,000 × g) in a Beckman Optima LE-80K ultracentrifuge with Ti70 Rotor for 20 min at 4 °C. After a second cycle of homogenization and centrifugation, the final pellets were resuspended in 50 mM Tris-HCl (pH 7.4) and stored in 100 μL aliquots at -80 °C until use. Membrane protein concentrations were determined using a BCA protein determination assay as described by the manufacturer[52].

6.4.5 ELISA

Receptor expression after transfection was measured in an enzyme-linked immunosorbent assay (ELISA). After 24 h of transfection, HEK293T cells were detached with PBS/EDTA and seeded into a sterile 96-well poly-D-lysine coated plate at a density of 100,000 cells per well. After an additional 24 h incubation under a humidified atmosphere at 37 °C with 5% CO_2, cells were washed with PBS and fixed with 4% formaldehyde for 10 min at rt. Cells were washed twice with tris-buffered saline (TBS) and were blocked with TBS supplemented with 0.1% TWEEN 20 (TBST) and 2% BSA (w/v) for 1 h at rt while shaking. Subsequently, the cells were incubated with rabbit anti-HA tag polyclonal antibody (1:2500) for 1 h at rt while shaking. After removal of the antibody, the cells were washed three times with TBST and incubated with the secondary goat anti-rabbit HRP-conjugated antibody (1:6000) for 30 min at rt while shaking. After a final wash with TBS, the cells were treated with 3,3',5,5'-tetramethylbenzidine (TMB) in the dark for maximally 10 min at rt to visualize immunoreactivity. The reaction was quenched with 1 M H_3PO_4, and absorbance was read at 450 nm with a Wallac EnVision 2104 Multilabel reader (Revvity; Waltham, MA, USA).

6.4.6 [^{35}S]GTPγS binding assays

G protein activation by agonists 2-AG, AEA, CP55,940, WIN55,212-2, JWH133, Nabilone, ART-27.13 and inverse agonist AM630 was measured by binding of radiolabeled [^{35}S] GTPγS to WT and mutant CB_2R as previously described in **Chapter 4**[32]. In short, transiently transfected HEK293T membrane homogenates (10 μg/well) were diluted in assay buffer (50 mM Tris-HCl (pH 7.4), 5 mM $MgCl_2$, 150 mM NaCl, 1 mM EDTA, 0.05% BSA (w/v) and 1 mM DTT, freshly prepared every day) and were pretreated with 10 μg saponin and 1 μM GDP for 30 minutes at rt. For endocannabinoid samples, the membranes were additionally

preincubated with 50 μM PMSF before agonist addition. To determine G protein activation, the membranes were incubated with 10 μM agonist and [^{35}S]GTPγS (0.3 nM) for 90 minutes at 25 °C while shaking at 400 rpm. Basal receptor activity was determined in the presence of vehicle (i.e., acetonitrile for endocannabinoids, and DMSO for all other compounds). Incubations were terminated by rapid vacuum filtration with ice-cold 50 mM Tris-HCl (pH 7.4) and 5 mM $MgCl_2$ wash buffer through Whatman GF/C filters using a Filtermate 96-well harvester (Revvity). Filters were dried for at least 30 min at 55 °C and subsequently 25 μL MicroScint scintillation cocktail was added per well. Filter-bound radioactivity was measured by scintillation spectrometry using a Microbeta^2 2450 counter (Revvity).

6.4.7 [^{3}H]CP55,940 binding assays

Agonist affinity (K_D, K_i) on WT and mutant CB_2R ($N11^{N\text{-term}}K$, $D24^{N\text{-term}}N$, $P348^{C\text{-term}}S$) was determined in [^{3}H]CP55,940 displacement assays. The amount of transiently transfected HEK293T membranes ranged from 2.5 μg to 20 μg protein per well, i.e., optimized to obtain a specific [^{3}H]CP55,940 binding window of ~1000 disintegrations per minute (dpm). Membranes were thawed and subsequently homogenized using the Ultra Turrax homogenizer. For experiments with endocannabinoids, the membranes were preincubated for 30 min with 50 μM PMSF. Homologous displacement assays were performed with three concentrations of [^{3}H]CP55,940 of ~0.7 nM, ~1.5 nM and ~7.0 nM in the presence of competing CP55,940 (ranging from 0.01 nM to 1 μM) in assay buffer (50 mM Tris-HCl (pH 7.4), 5 mM $MgCl_2$, 0.1% BSA (w/v)). Heterologous displacement assays were performed using ~1.5 nM final concentration of [^{3}H]CP55,940 with six increasing concentrations of 2-AG, Δ^9-THC and Nabilone (ranging from 0.1 nM to 10 μM) in assay buffer. In both assays, binding was initiated by addition of membrane homogenates to reach a final volume of 100 μL. Non-specific binding (NSB) was determined using 10 μM CP55,940. Organic solvent, i.e., acetonitrile for 2-AG, and DMSO for all other compounds, concentrations were <1% in all samples. Total binding (TB) did not exceed 10% of the amount added to prevent ligand depletion. Incubation was done for 2 h at 25 °C to reach equilibrium. Filtration was performed and filter-bound radioactivity was determined as described in section **6.4.6 [^{35}S] GTPγS binding assays** except for using ice-cold 50 mM Tris-HCl (pH 7.4), 5 mM $MgCl_2$, 0.1% BSA (w/v) as wash buffer.

6.4.8 [^{3}H]RO6957022 binding assays

Agonist affinity (K_D, K_i) on WT and mutant CB_2R ($A282^{7.36}T$) was determined in [^{3}H] RO6957022 displacement assays as described in **Chapter 5**[53]. The amount of transiently transfected HEK293T membranes ranged from 9 μg to 20 μg protein per well, i.e., optimized to obtain a specific [^{3}H]RO6957022 binding window of ~1000 dpm. Membranes were thawed and subsequently homogenized using the Ultra Turrax homogenizer. For experiments with endocannabinoids, the membranes were preincubated for 30 min with 50 μM PMSF. Incubations were performed at 10 °C. Therefore, assay buffer, (radio)ligands and membranes were precooled to 10 °C prior to the experiment. Homologous displacement

assays were performed with three concentrations of [^{3}H]RO6957022 of ~0.7 nM, ~2.4 nM and ~8.0 nM in the presence of competing RO6957022 (ranging from 0.01 nM to 1 μM) in assay buffer (50 mM Tris-HCl (pH 7.4), 0.1% BSA (w/v)). Heterologous displacement assays were executed using ~1.5 nM final concentration [^{3}H]RO6957022 with six increasing concentrations of 2-AG, Δ^9-THC and Nabilone (ranging from 0.1 nM to 10 μM) in assay buffer. For both assays, binding was initiated by addition of membrane homogenates to reach a final volume of 100 μL. NSB was determined using 10 μM RO6957022. Organic solvent, i.e., acetonitrile for 2-AG, and DMSO for all other compounds, concentrations were <1% in all samples. TB did not exceed 10% of the amount added to prevent ligand depletion. Incubation was done for 2 h at 10 °C to reach equilibrium. Filtration was performed and filter-bound radioactivity was determined as described in **6.4.6 [^{35}S]GTPγS binding assays** except for using ice-cold 50 mM Tris-HCl (pH 7.4), 0.1% BSA (w/v) as wash buffer.

6.4.9 Structural mapping

Figures were created based on the experimentally determined cryo-EM structure of G protein-bound CB_2R with agonist CP55,940 in **Chapter 4** (PDB: 8GUR)[32]. Figures were generated using PyMOL Molecular Graphics System version 2.4.

6.4.10 Data analysis and statistics

All experimental data were analyzed using GraphPad Prism 9.0 (GraphPad Software Inc.; San Diego, CA, USA). All values obtained are means ± standard error of the mean (SEM) of at least three independent experiments performed in duplicate, unless stated otherwise.

[^{35}S]GTPγS agonist responses on hCB_2R constructs were baseline-corrected for the individual mutant's basal activity and the responses were normalized to the basal activity of the specific construct (0%) and maximal activation on WT (100%). Basal activity was represented as fold over WT.

Displacement assays were baseline-corrected with NSB and normalized to this value (0%) and TB (100%). The equilibrium dissociation constants (K_D) of [^{3}H]CP55,940 or [^{3}H]RO6957022 on different mutants were calculated from homologous displacements by non-linear regression analysis, using the "one-site homologous" model. The half-maximal inhibitory concentrations (pIC_{50}) of the agonists in [^{3}H]CP55,940 and [^{3}H]RO6957022 assays were obtained by non-linear regression analysis of the heterologous displacement curves and further converted into inhibitory constant pK_i using the Cheng-Prusoff equation[54]. For this conversion, the experimentally determined K_D for each construct in [^{3}H]CP55,940 or [^{3}H]RO6957022 assays was used.

Differences in activation, pK_D and pK_i values for each mutant compared to WT were analyzed using a one-way ANOVA with Dunnett's multiple comparisons test or an unpaired t-test. Significant differences in activation are displayed as * $p< 0.05$ and differences in affinity are displayed as * $p < 0.05$; ** $p < 0.01$, *** $p < 0.001$ and **** $p < 0.0001$.

6.5 Acknowledgements

We thank Mea Abani, Jenny Lam, Lynn H. Somsen and Yasmine S.O. Jamani for their experimental support.

References

1. Hanahan, D. Hallmarks of Cancer: New Dimensions. *Cancer Discov* **12**, 31–46 (2022).
2. O'Hayre, M. *et al.* The Emerging Mutational Landscape of G-proteins and G-protein Coupled Receptors in Cancer. *Nat Rev Cancer* **13**, 424 (2013).
3. Bongers, B. J. *et al.* Pan-cancer functional analysis of somatic mutations in G protein-coupled receptors. *Sci Rep* **12**, 1–15 (2022).
4. Huh, E. *et al.* Recurrent high-impact mutations at cognate structural positions in class A G protein-coupled receptors expressed in tumors. *Proc Natl Acad Sci U S A* **118**, (2021).
5. Chaudhary, P. K. & Kim, S. An Insight into GPCR and G-Proteins as Cancer Drivers. *Cells* **10**, 3288 (2021).
6. Usman, S., Khawer, M., Rafique, S., Naz, Z. & Saleem, K. The current status of anti-GPCR drugs against different cancers. *J Pharm Anal* **10**, 517–521 (2020).
7. Wang, X. *et al.* Cancer-Related Somatic Mutations in Transmembrane Helices Alter Adenosine A1 Receptor Pharmacology. *Molecules* **27**, 3742 (2022).
8. Wang, X. *et al.* Cancer-related somatic mutations alter adenosine A1 receptor pharmacology - A focus on mutations in the loops and C-terminus. *The FASEB Journal* **36**, e22358 (2022).
9. den Hollander, L. S. *et al.* Impact of cancer-associated mutations in CC chemokine receptor 2 on receptor function and antagonism. *Biochem Pharmacol* **208**, 115399 (2023).
10. Feng, C. *et al.* Cancer-Associated Mutations of the Adenosine A_{2A} Receptor Have Diverse Influences on Ligand Binding and Receptor Functions. *Molecules* **27**, 4676 (2022).
11. Wang, X. *et al.* Characterization of cancer-related somatic mutations in the adenosine A2B receptor. *Eur J Pharmacol* **880**, 173126 (2020).
12. Howlett, A. C. & Abood, M. E. CB_1 and CB_2 Receptor Pharmacology. in *Advances in Pharmacology* vol. 80 169–206 (Academic Press, 2017).
13. Brennecke, B. *et al.* Cannabinoid receptor type 2 ligands: An analysis of granted patents since 2010. *Pharm Pat Anal* **10**, 111–163 (2021).
14. Pertwee, R. G. *et al.* International Union of Basic and Clinical Pharmacology. LXXIX. Cannabinoid Receptors and Their Ligands: Beyond CB_1 and CB_2. *Pharmacol Rev* **62**, 588–631 (2010). Fraguas-Sánchez, A. I., Martín-Sabroso, C. & Torres-Suárez, A. I. Insights into the effects of the endocannabinoid system in cancer: a review. *Br J Pharmacol* **175**, 2566–2580 (2018).
15. Pagano, C., Navarra, G., Coppola, L., Bifulco, M. & Laezza, C. Molecular mechanism of cannabinoids in cancer progression. *Int J Mol Sci* **22**, (2021).
16. Pérez-Gómez, E. *et al.* Role of Cannabinoid Receptor CB_2 in HER2 Pro-oncogenic Signaling in Breast Cancer. *J Natl Cancer Inst* **107**, 77 (2015).
17. Sánchez, C. *et al.* Inhibition of Glioma Growth in Vivo by Selective Activation of the CB_2 Cannabinoid Receptor. *Cancer Res* **61**, 5784–5789 (2001).
18. Blasco-Benito, S. *et al.* Therapeutic targeting of HER2–CB_2R heteromers in HER2-positive breast cancer. *Proc Natl Acad Sci U S A* **116**, 3863–3872 (2019).
19. Xu, S., Ma, H., Bo, Y. & Shao, M. The oncogenic role of CB2 in the progression of non-small-cell lung cancer. *Biomedicine & Pharmacotherapy* **117**, 109080 (2019).
20. Iden, J. A. *et al.* The Anti-Tumorigenic Role of Cannabinoid Receptor 2 in Colon Cancer: A Study in Mice and Humans. *Int J Mol Sci* **24**, (2023).
21. Hinz, B. & Ramer, R. Anti-tumour actions of cannabinoids. *Br J Pharmacol* **176**, 1384–1394 (2019).
22. Mangal, N. *et al.* Cannabinoids in the landscape of cancer. *J Cancer Res Clin Oncol* **147**, 2507–2534 (2021).
23. Ladin, D. A., Soliman, E., Griffin, L. T. & Van Dross, R. Preclinical and clinical assessment of cannabinoids as anti-cancer agents. *Front Pharmacol* **7**, 361 (2016).
24. Hashiesh, H. M., Sharma, C., Goyal, S. N., Jha, N. K. & Ojha, S. Pharmacological Properties, Therapeutic Potential and Molecular Mechanisms of JWH133, a CB2 Receptor-Selective Agonist. *Front Pharmacol* **12**, 1818 (2021).
25. Blázquez, C. *et al.* Cannabinoids inhibit glioma cell invasion by down-regulating matrix metalloproteinase-2 expression. *Cancer Res* **68**, 1945–1952 (2008).
26. Qamri, Z. *et al.* Synthetic cannabinoid receptor agonists inhibit tumor growth and metastasis of breast cancer. *Mol Cancer Ther* **8**, 3117–3129 (2009).
27. Casanova, M. L. *et al.* Inhibition of skin tumor growth and angiogenesis in vivo by activation of cannabinoid receptors. *Journal of Clinical Investigation* **111**, 43–50 (2003).

28. Bhaskaran, D. *et al.* A randomised phase II trial of temozolomide with or without cannabinoids in patients with recurrent glioblastoma (ARISTOCRAT): protocol for a multi-centre, double-blind, placebo-controlled trial. *BMC Cancer* **24**, 83 (2024).

29. Rock, E. M. & Parker, L. A. Cannabinoids As Potential Treatment for Chemotherapy-Induced Nausea and Vomiting. *Front Pharmacol* **7**, (2016).

30. Wild, C. P., Weiderpass, E. & Stewart. B.W. *World Cancer Report: Cancer Research for Cancer Prevention*. (International Agency for Research on Cancer, Lyon, France, 2020).

31. Li, X. *et al.* Structural basis of selective cannabinoid CB_2 receptor activation. *Nat Commun* **14**, 1–16 (2023). **(Chapter 4)**

32. Li, X. *et al.* Crystal Structure of the Human Cannabinoid Receptor CB2. *Cell* **176**, 459–467 (2019).

33. Hua, T. *et al.* Activation and Signaling Mechanism Revealed by Cannabinoid Receptor-G_i Complex Structures. *Cell* **180**, 655-665.e18 (2020).

34. Xing, C. *et al.* Cryo-EM Structure of the Human Cannabinoid Receptor CB2-G_i Signaling Complex. *Cell* **180**, 645-654.e13 (2020).

35. Ulloa-Aguirre, A., Zariñán, T., Dias, J. A. & Conn, P. M. Mutations in G protein-coupled receptors that impact receptor trafficking and reproductive function. *Mol Cell Endocrinol* **382**, 411–423 (2014).

36. Zhang, B., Li, S. & Shui, W. Post-Translational Modifications of G Protein-Coupled Receptors Revealed by Proteomics and Structural Biology. *Front Chem* **10**, (2022).

37. Patwardhan, A., Cheng, N. & Trejo, J. Post-Translational Modifications of G Protein–Coupled Receptors Control Cellular Signaling Dynamics in Space and Time. *Pharmacol Rev* **73**, 120–151 (2021).

38. Yeliseev, A. *et al.* Thermostability of a recombinant G protein-coupled receptor expressed at high level in mammalian cell culture. *Sci Rep* **10**, 16805 (2020).

39. Cabral, G. A. & Griffin-Thomas, L. T. Emerging role of the cannabinoid receptor CB_2 in immune regulation: Therapeutic prospects for neuroinflammation. *Expert Rev Mol Med* **11**, (2009).

40. Kolb, P. *et al.* Community guidelines for GPCR ligand bias: IUPHAR review 32. *Br J Pharmacol* **179**, 3651–3674 (2022).

41. Hillger, J. M. *et al.* Phenotypic screening of cannabinoid receptor 2 ligands shows different sensitivity to genotype. *Biochem Pharmacol* **130**, 60–70 (2017).

42. Casajuana-Martin, N. *et al.* A Single Point Mutation Blocks the Entrance of Ligands to the Cannabinoid CB_2 Receptor via the Lipid Bilayer. *J Chem Inf Model* **62**, 5771–5779 (2022).

43. Sanchez-Reyes, O. B. *et al.* G Protein-Coupled Receptors Contain Two Conserved Packing Clusters. *Biophys J* **112**, 2315–2326 (2017).

44. Chelikani, P. *et al.* Role of group-conserved residues in the helical core of β_2-adrenergic receptor. *Proc Natl Acad Sci U S A* **104**, 7027–7032 (2007).

45. Guo, D. *et al.* Molecular basis of ligand dissociation from the adenosine A_{2A} receptor. *Mol Pharmacol* **89**, 485–491 (2016).

46. Arang, N. & Gutkind, J. S. G Protein-Coupled receptors and heterotrimeric G proteins as cancer drivers. *FEBS Lett* **594**, 4201–4232 (2020).

47. Soethoudt, M. *et al.* Selective Photoaffinity Probe That Enables Assessment of Cannabinoid CB_2 Receptor Expression and Ligand Engagement in Human Cells. *J Am Chem Soc* **140**, 6067–6075 (2018).

48. Ng, S. K. *et al.* The protective effect of cannabinoids against colorectal cancer cachexia through modulation of inflammation and immune responses. *Biomedicine and Pharmacotherapy* **161**, (2023).

49. Chen, G. & Obal, D. Detecting and measuring of GPCR signaling – comparison of human induced pluripotent stem cells and immortal cell lines. *Front Endocrinol (Lausanne)* **14**, (2023).

50. Pándy-Szekeres, G. *et al.* GPCRdb in 2018: Adding GPCR structure models and ligands. *Nucleic Acids Res* **46**, D440–D446 (2018).

51. Smith, P. K. *et al.* Measurement of protein using bicinchoninic acid. *Anal Biochem* **150**, 76–85 (1985).

52. Bouma, J. *et al.* Dual allosteric and orthosteric pharmacology of synthetic analog cannabidiol-dimethylheptyl, but not cannabidiol, on the cannabinoid CB_2 receptor. *Biochem Pharmacol* **218**, 115924 (2023). **(Chapter 5)**

53. Cheng, Y.-C. & Prusoff, W. H. Relationship between the inhibition constant (K1) and the concentration of inhibitor which causes 50 per cent inhibition (I50) of an enzymatic reaction. *Biochem Pharmacol* **22**, 3099–3108 (1973).

54. Soethoudt, M. *et al.* Cannabinoid CB_2 receptor ligand profiling reveals biased signalling and off-target activity. *Nat Commun* **8**, 1–14 (2017).

Chapter 7

Discussion and future perspectives

7.1 Conclusions

At least one third of all marketed pharmaceutical drugs interacts with G protein-coupled receptors[1,2]. Nevertheless, a major challenge in the extensive drug discovery and development process is a high attrition rate of drug candidates in clinical trials[3]. Almost half of the failures are due to lack of clinical efficacy, but also toxicity is a major cause for attrition[4]. To this end, novel concepts and approaches in preclinical development are gaining recognition to provide a more successful translational perspective[5]. In this thesis, we focused on the investigation of drug-target binding kinetics, allosteric modulation and biased signaling on the cannabinoid CB_2 receptor (CB_2R), an interesting GPCR for the treatment of inflammatory conditions. Here, the findings from the different chapters are combined and future perspectives and opportunities for drug discovery on CB_2R and other GPCRs are discussed.

7.1.1 Assay development: continuous improvements to provide novel insights on receptor pharmacology

To improve the preclinical to clinical translational perspective, it is important to develop and properly use biologically, physiologically, and pharmacologically relevant *in vitro* assays. Additionally, continuous adaptation of these assays and data analyses may provide novel insights beyond the initial application[6].

In **Chapter 2**, we provided a comprehensive protocol for the recruitment of ß-arrestin-2 to activated cannabinoid receptors (CBRs). In this chapter, we used the PathHunter® technology, which relies on the complementation of two enzyme fragments for the generation of an active ß-galactosidase that emits a luminescent signal relative to the amount of complementation. Agonist-mediated activation of CB_1R or CB_2R induced the recruitment of ß-arrestin-2 to the receptors, which resulted in complementation of the active ß-galactosidase and a luminescent signal (**Figure 2.1**). Furthermore, this assay could be used for the investigation of antagonists and inverse agonists by co-incubation with an agonist or prolongation of the incubation time, respectively. Altogether, the PathHunter® technology provided an easy-to-use and high-throughput assay for a quick screening of ligand-induced ß-arrestin-2 recruitment to CBRs. As such, we successfully used this assay in **Chapter 5** for a set of ligands to investigate orthosteric and allosteric activation of CB_2R.

In **Chapter 3**, we continued the development of a ß-arrestin-2 recruitment assay for CB_2R by the use of the NanoLuc Binary Technology (NanoBiT®). This technology also relies on the complementation of two enzyme fragments, but in this case an active NanoLuc luciferase (NLuc) is generated. The advantage of this system is that the complementation is reversible, in contrast to the irreversible complementation of the ß-galactosidase, and as such kinetic, real-time analysis of protein-protein interactions is possible. In our assay, CB_2R was C-terminally fused to a small complimentary peptide (SmBiT) and ß-arrestin-2 was N-terminally fused to the large peptide (LgBiT) (**Figure 7.1**). After agonist-mediated ß-arrestin-2 recruitment to CB_2R the two subunits interact and form the active NLuc. We combined this technology with the GloSensor™ technology for the detection of real-time

inhibition of cAMP production after CB_2R activation (**Figure 7.1**). This biosensor was developed by circularly permuting a firefly luciferase (Fluc) and inserting a cAMP binding domain[7]. Binding of cAMP to the sensor will cause a conformational shift to the active Fluc. In the presence of the two different substrates both luciferases generate a luminescent signal with different emission wavelengths. The combination of these two technologies presented, for the first time, a multiplex assay for the simultaneous and kinetic detection of cAMP production and ß-arrestin-2 recruitment in one well. In this assay, the influence of system or observation bias was reduced, i.e., all results were obtained at the same time and under the same conditions. The applicability of the multiplex assay was shown by screening a diverse panel of benchmark and clinically tested CB_2R agonists. The results were

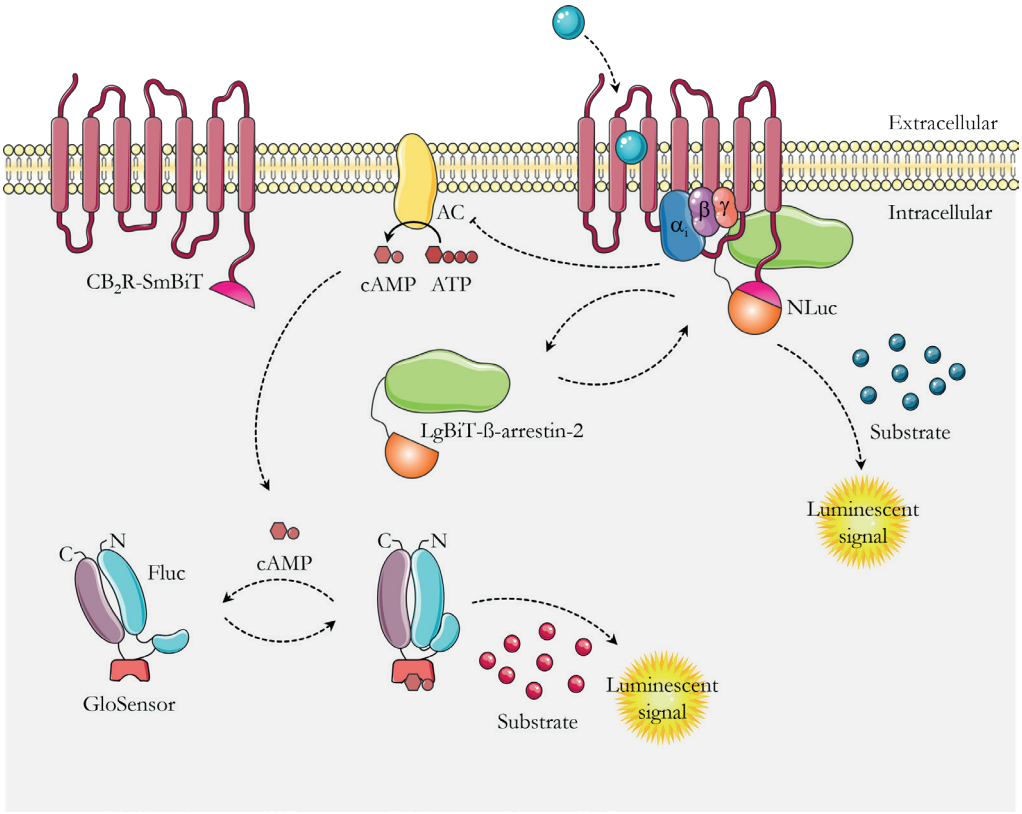

Figure 7.1 Schematic representation of the novel multiplex assay for ß-arrestin-2 recruitment and cAMP production.

Upon activation of SmBiT-tagged CB_2R by a ligand the LgBiT-ß-arrestin-2 is recruited to the receptor. This induces complementation to the active NanoLuc luciferase (NLuc), which results in a luminescent signal upon substrate addition. This process is reversible, and the LgBiT-ß-arrestin-2 can uncouple from the receptor, which will reduce the luminescent signal. Activation of CB_2R can also activate the $G\alpha_i$ pathway and subsequently inhibit the adenylyl cyclase, which will reduce the cAMP levels in the cytosol. These levels can be monitored by the GloSensor technology. Binding of cAMP to the sensor will cause a conformational shift to the active firefly luciferase (Fluc), which results in a luminescent signal upon substrate addition. The resulting two luciferases require a different substrate and as such emit light at different wavelengths, which allows combining them in the multiplex assay for the simultaneous and kinetic measurement of inhibition of cAMP production and ß-arrestin-2 recruitment after CB_2R activation. This figure incorporates drawings from Servier Medical Art (smart.servier.com).

interpreted via the use of an endpoint, semi-kinetic and kinetic analysis to investigate time-dependency of agonist-mediated activation as well as the determination of kinetic signaling parameters. Interestingly, the activation by certain agonists was time sensitive and the potency increased over time, whereas activation by other agonists was not affected over time. Time-dependency of activation was further highlighted in the bias determination, which indicated that agonists such as 2-AG may be (slightly) biased towards cAMP production at early time points but switch to ß-arrestin-2 recruitment bias after a longer incubation time. On the other hand, clinically relevant agonists Olorinab, S-777469 and ART-27.13 did not display changes in their bias profiles at different time points. Furthermore, novel mathematical models were applied to analyze the full time course and calculate kinetic parameters. Agonists Olorinab, PRS-211375, ART-27.13 and Tedalinab displayed higher efficacy in ß-arrestin-2 recruitment than commonly used full agonist CP55,940, classifying them as superagonists. These superagonists were characterized by faster signaling rate constants (k_1) than CP55,940, but not all agonists with faster k_1 values demonstrated superagonism. Nevertheless, independently of the analysis, none of the benchmark or clinically relevant agonists induced significant signaling bias in cAMP production or ß-arrestin-2 recruitment in our cellular system. This may suggest that the lack of detectable signaling bias could be the reason for the high attrition rate of CB_2R selective agonists in clinical trials. However, the mechanism of therapeutic effects at CB_2R and the potential importance of biased signaling is still largely unknown. Incorporation of the novel kinetic multiplex assay in early drug discovery programs may aid in a better and more extensive profiling of agonists prior to selection for (pre)-clinical models. Altogether, we hypothesize that combining the kinetic signaling parameters with target binding kinetics could provide a holistic overview of kinetic context for agonist-mediated receptor activation, which may be a better prediction for *in vivo* efficacy as they capture the early signaling responses.

7.1.2 Association rate constant: more than just diffusion

The investigation of drug-target binding kinetics gained attention over two decades ago when Copeland and colleagues presented it as a better predictor of drug efficacy and safety *in vivo*[8]. The initial focus has been on the investigation and optimization of target residence time (RT), calculated as the reciprocal of the dissociation rate constant (k_{off})[9]. Specifically since the association rate constant (k_{on}) was initially thought to be diffusion controlled and as such would be unaffected by the ligand. Nevertheless, this assumption has been rejected and the role of the association rate constant has become increasingly more important[10].

In **Chapter 3** a large and diverse panel of CB_2R agonists was screened in radioligand competition association assays. This yielded k_{on} and k_{off} values, which were converted into target engagement time (ET) at 1 μM of agonist and RT, respectively. The agonists displayed diverse kinetic profiles in which ETs ranged by 260-fold. It appeared that a fast agonist association was the driving factor for high affinity on CB_2R. Subsequently, all agonists were screened in the newly developed multiplex assay and kinetic signaling parameters were determined to obtain a complete overview of agonist-mediated CB_2R activation in a kinetic context. A fast engagement, i.e., k_{on} value, was significantly correlated with high kinetic

potency. Altogether, this indicates that high affinity and kinetic potency for CB_2R is driven by fast agonist engagement with the receptor.

In **Chapter 4**, we utilized the k_{on} value to predict a novel ligand entry mechanism for lipophilic agonists. In this chapter, we combined *in silico*, *in vitro* and *in vivo* methods to characterize the potent and selective CB_2R agonist LEI-102. Four cryo-electron microscopy (cryo-EM) structures were elucidated with LEI-102, CB_2R-selective agonists APD371 (Olorinab) and HU308, and non-selective agonist CP55,940. Based on these structures, the influence of several amino acids in agonist activation was explored via site-directed mutagenesis in functional [^{35}S]GTPγS binding assays. Although the overall structures of the CB_2R-$G\alpha_i$ bound complexes with LEI-102, APD371, HU308 or CP55,940 were similar, the agonists interacted with different amino acids in the orthosteric binding pocket. Furthermore, two potential ligand entry pathways at CB_2R, i.e., either via the extracellular loop 2 (ECL) or via a membrane channel between transmembrane domains 1 and 7 (TM1 and TM7), were investigated. By combining results from site-directed mutagenesis studies and the association rate constants of the agonists, we suggest that highly lipophilic agonist HU308 and the endocannabinoids (eCBs) may reach the binding pocket via a membrane channel, whereas more polar ligands LEI-102, APD371 and CP55,940 use an alternative route. Ultimately, the promising *in vivo* efficacy of oral administration of LEI-102 was shown in a chemotherapy-induced nephropathy model without inducing central nervous system (CNS)-mediated side effects.

7.1.3 Dissociation rate constant: more than residence time and efficacy

Additionally in **Chapter 3** and **4**, the k_{off} values of all benchmark and clinically tested CB_2R agonists were determined. Residence times ranged from 2.1 min in our assays for Dronabinol (Δ^9-tetrahydrocannabinol, Δ^9-THC) to 93 min for TAK-937. Nevertheless, the RTs only differed 44-fold in our assays, opposed to the 260-fold difference in k_{on} values. We observed no statistically significant correlation between k_{off} values and affinity, potency or efficacy. However, we found that slowly dissociating agonists exhibited slow deactivation of ß-arrestin-2 recruitment, which may suggest that extended agonist binding results in a longer receptor interaction with ß-arrestin-2. This clearly indicates that optimization of the dissociation rate constants as well as optimization of the association rate constants is valuable for CB_2R agonists. Together, these results emphasize the importance of understanding drug-target binding kinetics of CB_2R agonists and quantification of these kinetic parameters could be a valuable addition to drug discovery efforts for CB_2R.

In **Chapter 5** we described an alternative use of the dissociation rate constant to reveal allosteric interactions with CB_2R. All commercially available proclaimed allosteric modulators of the endocannabinoid system (ECS) were screened in a single point radioligand dissociation assay to reveal allosteric interactions. This suggested allosteric properties of cannabidiol-dimethylheptyl (CBD-DMH), but not for structural analog cannabidiol (CBD) or other compounds. CBD-DMH was further investigated in dissociation assays and was found to significantly reduce the k_{off} value of radioligand [^{3}H]RO6957022 in a dose-dependent manner. To this end, CBD-DMH was characterized as a positive allosteric modulator (PAM)

for an inverse agonist. In functional assays, it behaved as a negative allosteric modulator (NAM) for synthetic and endogenous agonists in G protein activation assays, but not in ß-arrestin-2 recruitment. Moreover, in these assays CBD-DMH itself behaved as orthosteric agonist and partially activated both the G protein and ß-arrestin-2 recruitment. Together, this suggests dual allosteric and orthosteric molecular pharmacology of CBD-DMH at CB_2R, which may provide a new class of molecules targeting CB_2R.

7.1.4 Precision medicine: keeping the patient in mind

Chapters 2, **3**, **4**, and **5** focused on assay development and targeting of wild type (WT) CB_2R. Yet, in several diseases, including cancer, GPCRs may contain somatic point mutations[11–13]. Despite this, the effect of GPCR mutations on cancer progression or druggability is largely unknown[14]. While targeting of WT CB_2R may provide a great therapeutic potential in cancer, mutations have been observed in cancer patient samples. Therefore, in **Chapter 6**, we aimed to investigate the impact of CB_2R cancer-associated mutations on the functionality of the receptor as well as the implications for drug targeting. We selected ten single point mutations in CB_2R from the Genomic Data Commons based on occurrence and proximity to the orthosteric binding pocket. Receptor expression and G protein activation by endogenous, synthetic and clinically tested CB_2R agonists was investigated for all ten mutant receptors. Binding affinity of a subselection of these agonists was further tested in radioligand displacement assays. We found that mutations in the binding pocket or structurally close to a conserved motif markedly affected receptor activation. Although the activation and binding were differentially affected dependent on the combination of CB_2R mutant and agonist. This effect was less pronounced on mutations located in the N- or C-termini. Altogether, this emphasized the importance of precision medicine, i.e., investigating patient CB_2R genotype, prior to administration of cannabinoid-based therapies.

In conclusion, by the development and application of a variety of assays we have increased the molecular pharmacological understanding of targeting CB_2R. The work presented in this thesis highlights the potential and importance of studying kinetic binding and signaling parameters for the elucidation of novel ligand entry pathways, allosteric interactions and the overall agonist-mediated CB_2R activation. Moreover, by combining and developing different biochemical and cellular assays along with the implementation of new methods of analysis, this thesis presents comprehensive procedures to improve agonist profiling during the initial phases of drug discovery. These findings could proof valuable for future drug discovery endeavors on CB_2R as well as other GPCRs.

7.2 Future perspectives

7.2.1 Kinetic traces as indication for mechanism of signaling regulation

The novel multiplex assay that we designed and validated in **Chapter 3** provided an elegant system for the simultaneous assessment of two signaling events after agonist-mediated CB_2R activation. Furthermore, the kinetic nature of this assay offered the opportunity to trace and analyze the full dynamics of agonist-mediated receptor activation. Equations to fit the time-trace data have been developed that enable the determination of kinetic parameters, which could display kinetic differences between agonists[15]. It has been hypothesized that the shape of the trace represents the complexity of signaling and regulatory mechanisms. Therefore, kinetic parameters could potentially shed light on the different regulation events. However, a good understanding of the regulation of signaling is crucial, which may vary depending on the target, agonist or cellular background. Utilizing specific inhibitors of certain processes or complementary assays may offer more insights into these signaling mechanisms, as further outlined below.

The best-known regulators of cAMP signaling are phosphodiesterases (PDEs), which belong to a superfamily consisting of eight different families[16]. PDEs play a role in the rapid degradation of cAMP to AMP[16]. PDE inhibitors prevent the degradation of cAMP, resulting in accumulation of cAMP. Often, competitive non-selective PDE inhibitor 3-isobutyl-1-methylxanthine (IBMX) or selective PDE inhibitors rolipram and cilostamide are used in (endpoint) cAMP assays since an accumulation of the cAMP signal is required for quantification of the effect[17,18]. Our kinetic assay does not require this accumulation and we therefore deliberately omitted PDE inhibitors from our setup to limit artificial modification of the system. Nonetheless, addition of IBMX or subtype-selective PDE inhibitors could be beneficial for studying agonist-mediated effects of G protein activation and subsequent adenylate cyclase activity independently of cAMP metabolism[7,19].

Alternatively, ß-arrestin recruitment to the receptor is only the first step in initiation of potential signaling or regulation mechanisms. As described in **Chapter 1**, this could terminate G protein signaling or cause internalization and trafficking of the receptor to endosomes prior to different receptor fates such as recycling or degradation. Complementary assays could shed light on the specific receptor fate after agonist-mediated ß-arrestin recruitment to CB_2R, and the difference between ß-arrestin isoforms. Investigation of trafficking to endosomes can be done by use of endosomal markers from the Rab-GTPase (Rab) family. Specially, Rab5 is a marker for early endosomes, Rab4 or Rab11 for the recycling endosome and Rab7 is used as marker for the late endosome[20]. Bioluminescence resonance energy transfer (BRET) assays have been developed to measure relative distances between a luciferase-tagged GPCR and green or yellow fluorescent protein (GFP or YFP)-tagged Rab5, Rab4 or Rab7[20,21]. These assays have already been described for CB_2R and could be used to investigate whether agonists, like the data set in **Chapter 3**, promote the same receptor fate or if there could be bias in internalization. Nevertheless, caution should be taken to check whether this process is actually ß-arrestin-dependent, and not G protein-dependent, since it was recently demonstrated that GPCRs may differentially rely on ß-arrestins or G proteins for internalization[22].

Additionally, ß-arrestin recruitment could trigger signaling cascades via mitogen-activated protein kinase (MAPK) and extracellular signal-related kinase 1 and 2 (ERK1/2)[23,24]. Activation of the ERK1/2 signaling cascade can be measured in a variety of endpoint assays, or a kinetic assay by the use of a BRET-based sensor[25–27]. However, whether this activation is ß-arrestin-dependent and G protein-independent, or if recruitment of ß-arrestin is nonessential requires a more thorough examination. To this end, CRISPR/Cas9 genome-edited cell lines with genetic ablation of ß-arrestins or G proteins, or in combination with pharmacological inhibition of G proteins by, for example, Pertussis Toxin (PTX) could help to discriminate whether there is a dependence on a specific pathway[25].

These strategies could be applied to the agonists studied in **Chapter 3** to investigate whether parts of the signaling time traces, and corresponding signaling rate constants, can be assigned to specific mechanisms. Furthermore, it would be highly interesting to investigate whether there is bias on another signaling level, which will be expanded upon in the following paragraphs. Eventually, a comprehensive understanding of signaling and regulatory mechanisms after agonist-mediated receptor activation is of the utmost importance to better exploit CB_2R, and other GPCRs, for therapeutic purposes. This becomes particularly valuable if a biased signaling approach has been confirmed as a therapeutic strategy. Alternatively, better profiling of agonists targeting novel receptors could contribute to a deeper understanding of the necessity for biased signaling. This may benefit from the inclusion of agonists with diverse bias profiles in *in vivo* studies to predict the most therapeutically relevant profile.

7.2.2 Alternative technologies to expand and further develop multiplex assays

In the multiplex assay from **Chapter 3**, we combined two luminescent technologies to measure cAMP production and ß-arrestin-2 recruitment after CB_2R activation. We employed the GloSensor™, a permuted firefly luciferase (Fluc) utilizing D-luciferin as substrate, and the NanoBiT®, which relies on complementation of two parts (BiTs) to form an active NanoLuc luciferase (NLuc) that requires furimazine as substrate (**Figure 7.1**). The luminescent signals could be distinguished due to the distinct emission spectra of the luciferases. We demonstrated, for the first time, that simultaneous and kinetic detection of two luminescent readouts was possible without the need for signal quenching or lysis of the cells. This encourages the exploration of adding more biosensors to expand the current multiplex assay or develop other new multiplex assays, which is explored in more detail in the following paragraphs. Ultimately, this could contribute to a more efficient and better screening of compounds and biased signaling for GPCRs.

7.2.2.1 Luciferase-based biosensors

Luciferase-based biosensors are widely employed in biochemical research due to their high signal-to-background ratio as they do not require excitation light energy like fluorescent assays[28]. Various luciferases have been used in biochemical assays, each requiring a specific substrate devoid of cross-reactions with other substrates (**Table 7.1**)[29]. Consequently,

Table 7.1 Examples of luciferases used in biochemical assays with associated substrate and emission wavelengths (λ_{em}), and the possibility to be used as split luciferase.

Luciferase	Substrate	Peak emission wavelength (λ_{em})	Split luciferase?	Ref.
Click beetle Green (CBGluc)	D-luciferin/ATP	540 nm	Yes	[28,34,35]
Click beetle Red (CBRluc)	D-luciferin/ATP	615 nm	Yes	[28,34,35]
Cypridina (Cluc)	Vargulin	465 nm	No	[29]
Firefly (Fluc)	D-luciferin/ATP	560 nm	Yes	[7,28,36]
Gaussia (Gluc)	Coelenterazine	460 nm	Yes	[28,37]
NanoLuc (NLuc)	Furimazine	453 nm	Yes	[30,32,38]
Renilla (Rluc)	Coelenterazine	480 nm	Yes	[28,39]

luciferases emit light at different wavelengths[28]. While the use of intact luciferase-based biosensors such as the GloSensor™ has been limited in GPCR research, split luciferase assays such as the NanoBiT® are gaining popularity. In **Chapter 3** we used the NanoBiT® for recruitment of ß-arrestin-2 to CB_2R. Moreover, this technology has been employed to investigate other signaling processes like G protein dissociation or GRK recruitment following agonist-mediated GPCR activation[30,31]. In the development of the split segments of NLuc, BiTs with different affinities for the LgBiT have been designed. For instance, the NanoBiT® LgBiT and SmBiT segments have a low intrinsic affinity (K_D 190 μM) for one another and consequently, complementation is driven by interaction of the tagged proteins. Conversely, the HiBiT segment exhibits a very high affinity for LgBiT (K_D 700 pM), and this complementation is used to monitor internalization of GPCRs (**Figure 7.2a**)[32,33]. In this case, a GPCR is N-terminally tagged with a HiBiT segment, which automatically complements with the extracellularly present LgBiT that is cell impermeable. Upon internalization of the receptor, a decreased NLuc signal is observed due to loss of GPCRs on the cell surface[31,33].

A similar approach was undertaken with click beetle luciferases (CBluc), which were split into C- and N-terminal segments[34]. Because of the overlap of the green and red CBluc (CBGluc and CBRluc) C-terminal segments and their distinct N-terminal segments, the CBGluc C-terminus could serve as a contact point for both CBGluc and CBRluc N-terminal segments. Consequently, mixing CBGluc and CBRluc fragments enabled simultaneous quantification of two pairs of interacting proteins or the interaction of two proteins with a shared protein[34]. The latter approach was recently successfully applied to monitor the simultaneous recruitment of ß-arrestin-1 and 2 to the δ-opioid receptor, which could be distinguished based on the different wavelengths (**Figure 7.2b**,**c**, **Table 7.1**)[35].

While split luciferases of Renilla luciferase (Rluc), Fluc and Gaussia luciferase (Gluc) have not yet been utilized in GPCR pharmacology, they have been designed and applied in research fields for other targets[37,39,40]. The complementation assays have been employed for the detection of a variety of protein-protein interactions proving their applicability across diverse systems. For instance, Rluc complementation assays have been conducted with Rluc segments tagged to heat shock protein 90 (Hsp90) and ATPase homologue 1 (Aha1), respectively, to monitor the disruption of these interactions[39]. On the other hand, a split firefly luciferase complementation assay has been explored for interactions between virus

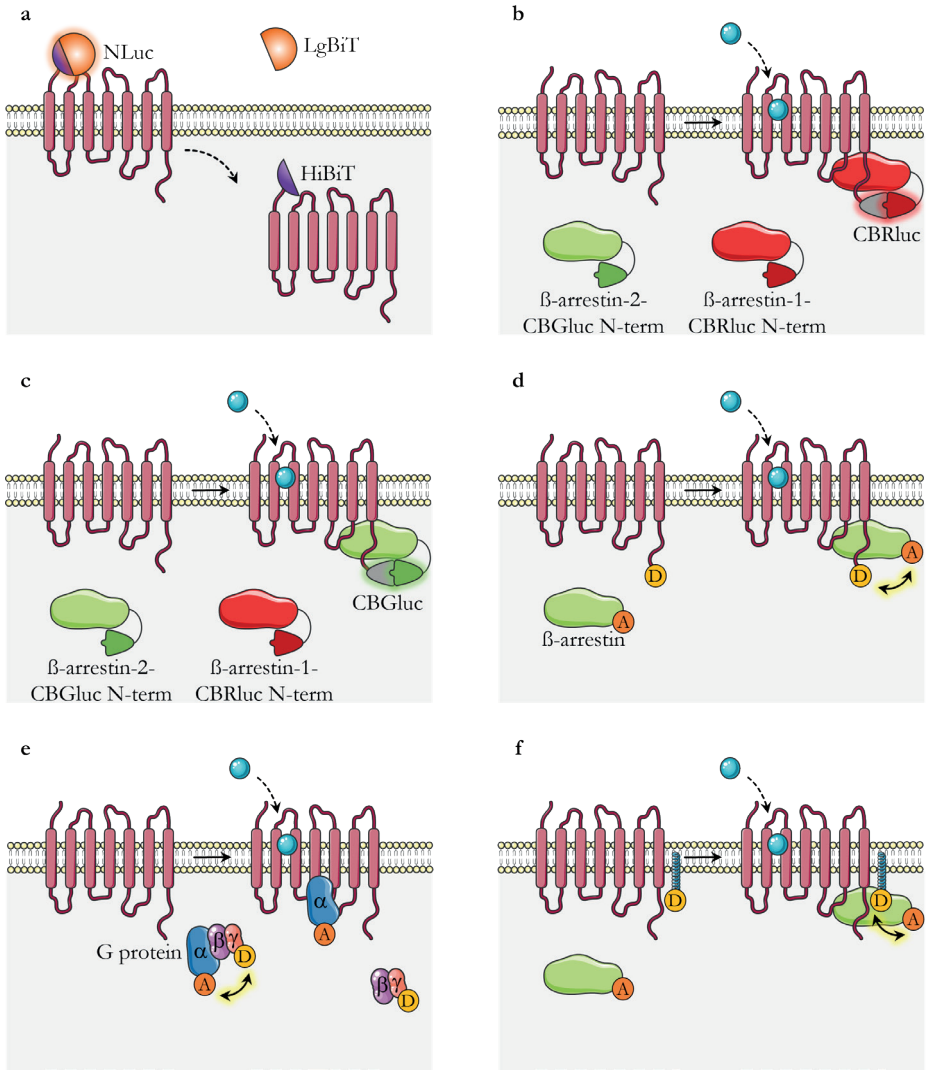

Figure 7.2 Schematic representation of currently available GPCR split luciferase-based and BRET-based biosensors.

(a) Split luciferase HiBiT to monitor the internalization of a GPCR. Extracellular LgBiT and a N-terminally HiBiT-tagged GPCR complement to an active NLuc. Upon internalization of the receptor, the NLuc signal will decrease. (b) Click beetle red luciferase (CBRluc) and (c) click beetle green luciferase (CBGluc) to simultaneously quantify the interaction of two proteins, in this case ß-arrestin-1 and 2, with a third protein, the GPCR. (d) BRET to measure the proximity between the donor (D)-tagged GPCR and acceptor (A)-tagged transducer, in this case ß-arrestin. BRET signal will increase upon recruitment of ß-arrestin to the GPCR. (e) BRET to measure the dissociation of the heterotrimeric G protein with donor-tagged Gα and acceptor-tagged Gγ, which will result in a decreased BRET signal. (f) Enhanced bystander BRET (ebBRET) to measure the proximity between the donor (D)-tagged membrane anchor and acceptor (A)-tagged transducer, in this case ß-arrestin. BRET signal will increase upon recruitment of ß-arrestin to the GPCR and thus membrane anchor. Luciferases (BRET donors) only emit light in the presence of substrate, but this is not shown for clarity reasons. This figure incorporates drawings from Servier Medical Art (smart.servier.com).

and host proteins in plant leaves[40].

Split luciferase assays may present an interesting strategy for multiplexing due to their high sensitivity for the quantification of protein-protein interactions. Complementation of NLuc and click beetle segments have already proven useful in GPCR pharmacology, while split luciferases of Rluc, Fluc and Gluc could open up new avenues for GPCR signaling. Moreover, novel substrates are developed to shift emission peaks and gain more distinct spectra. For instance, a new luciferin analogue, AkaLumine-HCl, was synthesized to shift the emission peak of Fluc to the near-infrared wavelengths (λ_{em} 677 nm)[41]. Nevertheless, multiplexing split luciferases may require some optimization to ensure no interference of the split luciferase segments with the GPCR of interest and the protein partner, such as G proteins or ß-arrestins.

7.2.2.2 BRET-based assays

Over the years, bioluminescence resonance energy transfer (BRET)-based assays have been widely used in GPCR research. BRET assays rely on the principle of energy transfer between a luminescent donor and a fluorophore acceptor, both fused to proteins or protein fragments of interest[42]. This energy transfer occurs when the donor and acceptor are brought into close proximity by ligand-binding, protein-protein interactions, or conformational changes. The resulting ratio between acceptor and donor emission is then used to quantify the effect[43].

A wide array of BRET donor and acceptor pairs have been documented in literature (**Table 7.2**). Initially, commonly used donors were Rluc variants (RlucII, Rluc8, Rluc8.6), which emit light between 400 and 535 nm in the presence of the required substrate[44,45]. These were typically combined with fluorescent proteins like enhanced yellow fluorescent protein (EYFP), green fluorescent protein (GFP) or its mutant variants (e.g., GFP2 or GFP10)

Table 7.2 Examples of BRET donor and acceptor pairs with associated substrate and excitation and emission wavelengths (λ_{ex} and λ_{em}) found in literature.

Luciferase (donor)	Substrate	λ_{em}	Fluorophore (acceptor)	λ_{ex}	λ_{em}	Ref.
RlucII	Coelenterazine h	480 nm	EYFP	511 nm	530 nm	[42]
RlucII	Coelenterazine 400a	400 nm	GFP2 or GFP 10	400 nm	510 nm	[42]
RlucII	Prolume Purple	405 nm	GFP2 or GFP 10	400 nm	510 nm	[42]
RlucII	Coelenterazine 400a	400 nm	rGFP	480 nm	508 nm	[44,45]
RlucII	Prolume Purple	405 nm	rGFP	480 nm	508 nm	[44,45]
Rluc8	Coelenterazine 400a	400 nm	GFP2	400 nm	510 nm	[46]
Rluc8	Coelenterazine	480 nm	mOrange	548 nm	562 nm	[47]
Rluc8.6	Coelenterazine	535 nm	TurboFP635	588 nm	635 nm	[48]
NLuc	Furimazine	453 nm	Venus	515 nm	528 nm	[50,52]
NLuc	Furimazine	453 nm	mVenus	515 nm	527 nm	[31,51]
NLuc	Vivazine	453 nm	mKATE2	588 nm	633 nm	[49]
NLuc	Vivazine	453 nm	EGFP	488 nm	507 nm	[49]

serving as acceptors with emission peaks around 510-530 nm[42,46]. However, enhanced energy transfer efficiency has been achieved by combining Rluc with other fluorophores such as rGFP, mOrange and TurboFP635[42,44,45,47,48]. Similarly, improvements on the luciferase donor have been made by introducing the brighter intact NLuc for NanoBRET assays[38]. This allowed pairing with red-shifted fluorophores, thereby enhancing the signal-to-noise ratio compared to early BRET pairs due to better spectral separation between donor and acceptor emission[31,49–52].

The possibilities for BRET-based biosensors to study different components of GPCR pharmacology are endless and continuous development of BRET-based biosensors has led to the development of multiple generations, which have been reviewed previously[42,43,53–55]. For example, the earliest biosensors used donor-tagged GPCRs while transducers, such as ß-arrestins or G proteins, were tagged with an acceptor (BRET^1, BRET^2). Depending on the mechanism studied, BRET signals could either increase after agonist-mediated receptor activation, e.g., ß-arrestin recruitment, or decrease, e.g., dissociation of Gα and Gβγ subunits as a proxy for G protein activation (**Figure 7.2d**,**e**)[25]. The latter has been upscaled in the TRUPATH platform, which enables the detection of fourteen G protein pathways by tagging various Gα, Gβ and Gγ subunits with donor and acceptor pairs in separate assays with the same cellular background[46]. Enhanced bystander BRET (ebBRET) is the improved BRET-based biosensor technology, which does not require modification of the GPCR (**Figure 7.2f**). In this case, the BRET donor is tethered to a cellular compartment and the translocation of an accepter-fused protein to this compartment can be measured[42]. The ebBRET can be used for characterization of trafficking or localization of GPCRs and/or transducers, as the donor-anchors can be targeted to the plasma membrane but also endosomal or other membranes[44,45]. This offers the opportunity to explore agonist-mediated signaling across different cellular compartments, a phenomenon referred to as 'location bias' by activation of distinct signaling pathways in various subcellular locations[56,57]. Altogether, BRET-based biosensors have facilitated the study of numerous events following GPCR activation including G protein activation, GRK and ß-arrestin recruitment, desensitization, internalization, recycling and dimer formation[31,43].

The versatility of BRET-based biosensors renders them highly appealing tools for studying GPCR pharmacology. Nonetheless, multiplexing of BRET-based biosensors in cellular assays remains unexplored. This could prove very challenging given that two different emission spectra are measured in BRET-based assays. Incorporating a second biosensor would require meticulous optimization of donor and acceptor pairs to effectively distinguish between the different emission spectra.

7.2.2.3 Expanding the multiplex assay

Expanding the multiplex assay as described in **Chapter 3** by addition of a biosensor for dissociation of the heterotrimeric G protein, serving as proxy for G protein activation, may be a valuable strategy. However, incorporating more biosensors poses various significant challenges due to the emission spectra of the luciferases. First, no luciferase and substrate pairs with emission spectra >700 nm have been discovered, which would be required

since NLuc and Fluc signals range from approximately 380 to 580 nm and 500 to 700 nm, respectively. Secondly, switching the substrate for Fluc from D-luciferin to AkaLumine-HCl shifts the light emission to between 600 and 800 nm, and as such creates a small opportunity for integration of a third biosensor. In this case, integration of a CBGluc (λ_{max} 540 nm) biosensor may be the only possibility. However, CBGluc requires D-luciferin as substrate, which will move the Fluc emission spectrum back to 500 to 700 nm (**Table 7.1**). Thirdly, using complemented NLuc as donor for a BRET-based G protein dissociation biosensor renders challenges as this would require constant interaction of CB_2R with ß-arrestin for complementation to the active luciferase. Furthermore, this would require ß-arrestin recruitment to occur prior to G protein dissociation and remain at a constant level to prevent reduction of BRET signals due to reduced NLuc emission. Altogether, expanding the current multiplex presents various limitations. Consequently, exploring novel biosensor combinations may offer more opportunities for enhancing our understanding of GPCR pharmacology with particular regard to biased signaling. Moreover, this approach holds promise for elucidating multiprotein interactions or unraveling the sequence of signaling/trafficking events for which a few examples are outlined below.

To capture the effect of agonist-mediated GPCR activation on the ß-arrestin level and G protein level, opposed to the downstream cAMP in our multiplex, one potential strategy may involve multiplexing the CBluc complementation biosensors CBGluc (λ_{max} 540 nm) and CBRluc (λ_{max} 615 nm, **Figure 7.2b**,**c**) with NanoBiT® (λ_{max} 460 nm). In this case, ß-arrestin-1 and 2 could be tagged by CBGluc and CBRluc, respectively, which would show the preferred isoform recruitment after activation since either ß-arrestin-1 or ß-arrestin-2 can complement the CBGluc C-term segment. The LgBiT segment could be fused to the Gα subunit and the SmBiT segment to the Gβγ subunit consequently dissociation of the heterotrimeric G protein, and thus attenuated luminescence, can serve as proxy for G protein activation[35,58].

Alternatively, to better comprehend the effect of isoform-specific ß-arrestin recruitment and subsequent receptor internalization, the ß-arrestin CBluc complementation biosensors as described above could be combined with the HiBiT complementation assay by N-terminal fusion of the HiBiT to the GPCR (**Figure 7.2a**). This would capture the internalization of the GPCR and may be correlated to the recruitment of a specific ß-arrestin isoform.

In addition to multiplexing split luciferase assays, exploring the potential for multiplexing two BRET-based biosensors presents an intriguing avenue. While this approach may not be suitable for simultaneous detection of two transducer proteins, like the G protein and ß-arrestin, due to their likely proximity to one another and to the GPCR, it may hold promise for determining receptor localization after activation over time. A combination of NLuc with EGFP and mKATE2 may be a promising starting point due to the far-red shifted emission spectrum of mKATE2 (**Table 7.2**). However, careful consideration is required to prevent that the emission of EGFP causes excitation of mKATE2. In this case, the trafficking of a NLuc-tagged GPCR to the early endosome could be followed by increased BRET signals for EGFP if in close proximity to Rab5-EGFP. Subsequently, increased mKATE2 BRET signals would indicate proximity to mKATE2-tagged Rab7 and thus receptor trafficking to the late endosome (**Figure 7.3**).

Nevertheless, multiplexing of biosensors may remain very challenging, and technical and biological considerations should be made. On the technical side, this would require careful optimization of protein constructs to prevent interference of (split) luciferase or fluorophore tags on the intrinsic protein function. Moreover, consideration of the appropriate substrate or combinations of substrates is essential and spectral overlap should be minimized via the proper use of suitable equipment to separate the detection of different excitation and emission wavelengths. Currently, most split luciferase and BRET-based assays are not applied to physiologically relevant systems as they require modification of proteins and the modified proteins need to be expressed in large excess to prevent interactions of native proteins. The competition between modified and native proteins may shield or reduce the luminescent or BRET signals[52]. Additionally, endogenous signaling may be altered by overexpression of these proteins and loss of biased signaling at GPCRs has been reported in overexpressed systems[59]. Solutions are presented in the form of endogenous protein modification by the CRISPR/Cas9 technology, which maintains the endogenous expression levels and stoichiometry[60]. For instance, NLuc fragments have been introduced on native proteins like ß-arrestin-2 in HEK293 cells or atypical chemokine receptor 3 in HeLa cells for

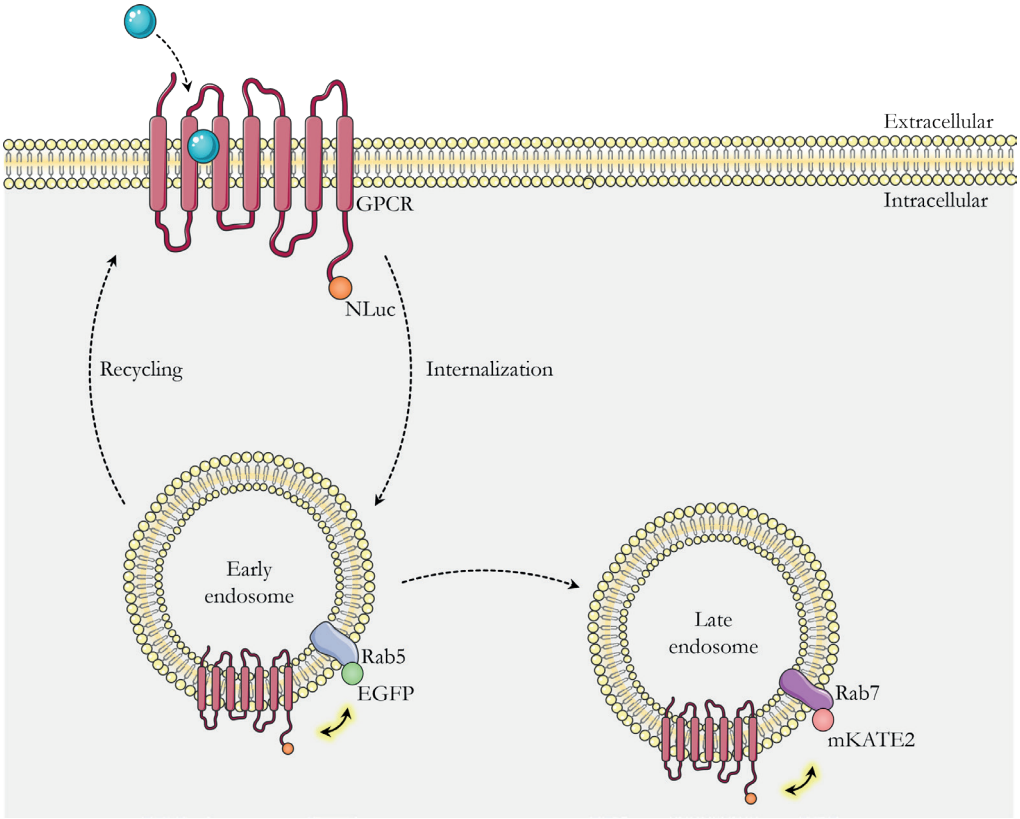

Figure 7.3 **Possibility for multiplexing two BRET-based biosensors.**
Possible multiplex assay setup with NLuc-tagged GPCR, which upon internalization in the early endosome may increase BRET signals with EGFP-tagged Rab5. Transition to the late endosome would be reflected by increased BRET signaling with mKATE2-tagged Rab7. This figure incorporates drawings from Servier Medical Art (smart.servier.com).

NanoBRET/NanoBiT purposes[61,62]. While endogenous expression levels and stoichiometry are maintained in these engineered cell lines, it does not always reflect the heterogeneity of the human population or the relevant disease tissue. The use of human induced pluripotent stem cells (hiPSCs) in GPCR pharmacology research is emerging to further increase the physiological relevance [60]. The use of biosensors in hiPSCs was first demonstrated by Avet and colleagues, where ebBRET was used to detect the translocation of (heterologous) $G\alpha_i$ proteins to the endogenous sphingosine 1 phosphate receptor-1 ($S1P_1$) in hiPSC-derived cardiomyocytes[63]. Nonetheless, in case of successful implementation of these technical and biological challenges, multiplex assays could contribute greatly to novel insights into agonist-induced GPCR pharmacology and concepts such as biased signaling.

7.2.3 Intertwining novel concepts to improve drug discovery

As described in **Chapter 1** there is great potential for integrating novel concepts in the early phases of drug discovery to enhance the translational perspective, and thus decrease clinical attrition rates. In **Chapter 3**, the drug-target binding kinetics of CB_2R agonists were investigated and related to their signaling profiles. However, allosteric modulation (**Chapter 5**) and the impact of single point mutations (**Chapter 6**) were approached as individual concepts. Recent findings on other GPCRs suggests that these concepts may be intertwined in diverse manners and offer new therapeutic possibilities, which will be expanded upon in the following paragraphs.

7.2.3.1 Biased allosteric modulation

Combining allosteric modulation and biased signaling is a newly emerging approach in drug discovery that provides spatial, temporal and signal pathway specificity[64]. Biased allosteric modulators (BAMs) exert their effect by selectively modulating one pathway activated by an orthosteric ligand over another pathway while binding to the allosteric binding site[65–69]. The feasibility of designing and employing BAMs has recently been demonstrated for several GPCRs in *in vitro* and *in vivo* studies, of which two are further presented below.

For example, a selective ß-arrestin-biased NAM was identified for the $ß_2$-adrenoceptor ($ß_2AR$) which in the presence of endogenous agonist antagonized the interaction with ß-arrestin-2 without affecting cAMP production via $G\alpha_s$ signaling[65]. Current clinical treatments for asthma or chronic obstructive pulmonary disease (COPD) rely on balanced clinical $ß_2AR$ agonists[70]. However, it has been described that the therapeutic effects are mediated via activation of the $G\alpha_s$ pathway, whereas ß-arrestins may contribute to the pro-inflammatory and pathogenic effects in asthma mouse models[65]. To this end, ß-arrestin-biased NAMs may provide a novel class of drugs that modify endogenous $ß_2AR$ activation with improved selectivity on receptor binding and signaling effects.

In the case of the neurotensin receptor 1 (NTSR1), a ß-arrestin biased PAM has shown promise for the treatment of drug addiction in *in vivo* studies[68]. Activation of this receptor offers therapeutic possibilities by restoring homeostatic dopamine signaling, but clinical

applications have been precluded by the occurrence of severe side effects due to NTSR1's involvement in regulation of fundamental physiological processes, such as regulation of body temperature, blood pressure and motor control[68]. Nevertheless, preclinical data showed that the regulation of addiction-associated behavior in rodents was primarily mediated via ß-arrestin-2. A screening effort led to the discovery of a ß-arrestin-2 biased NTSR1 activator, SBI-553. This compound selectively antagonized $G\alpha_q$ signaling in the presence of endogenous neurotensin (NTS), while ß-arrestin-2-mediated pERK generation was stimulated. These promising effects of SBI-553 were further exhibited by the attenuation of psychostimulant-associated behavior in mouse models of drug abuse, without introducing side effects seen with balanced agonists[68].

Altogether, the development of BAMs presents a promising strategy for the design of more selective drugs for GPCRs that target therapeutic relevant pathways while minimizing side effects via other pathways[64]. To date, the mechanism for the desired therapeutic effects at CB_2R and the potential importance of biased signaling is largely unknown. Here, BAMs could serve as tool compounds to provide more insight into the mechanism of receptor modulation.

7.2.3.2 Mutations introducing biased signaling

Biased signaling not only refers to the possibility of ligands inducing differential signaling, as studied in **Chapter 3**, but it also extends to biased receptors. Single point mutations, either natural variants in the population or associated with disease, can modify a receptor to adopt a specific conformation, thereby favoring stimulation of one signaling pathway over another[71]. Such mutations may play an important role in the disease progression by stimulation or inhibition of certain pathways. Consequently, genetic variation, and as a result variation in signaling, could contribute to variations in drug efficacy and toxicity[71]. To this end, it is imperative to investigate the impact of mutations on signaling.

Several natural variants in CB_2R have been described, of which a glutamine to arginine point mutation on position 63 (Q63R) is widely reported and has been suggested to affect several psychiatric disorders[21]. Additionally, a substitution of tyrosine for histidine was found in the C-terminal at position 316 (H316Y) and a high mutant allele frequency of leucine to isoleucine mutation (L133I) was found in bipolar disorder patients[21,72]. *In vitro* studies showed that the CB_2R variants Q63R and L133I had similar $G\alpha_i$ activation and consequently cAMP production as WT but showed distinct GRK and ß-arrestin-2 binding. Specifically, the Q63R mutant showed increased GRK2 and GRK3 binding compared to WT and consequently increased ß-arrestin-2 binding, whereas GRK2, GRK3 and ß-arrestin-2 binding was decreased for CB_2R-L133I[21]. Another study found compromised agonist-mediated inhibition of cAMP production on Q63R and H316Y receptors and the constitutive activity of H316Y, but not Q63R was increased compared to WT[72]. Of note, all experiments in this thesis were carried out on CB_2R with Q63, L133 and H316.

In the case of the cysteinyl leukotriene receptor 2 (CysLTR2), it was found that a leucine to glutamine mutation on position 129 ($L129^{3.43}Q$) was a recurrent hotspot in uveal melanoma

(UVM) patients[73]. Furthermore, the mutated receptor served as a driver oncogene in UVM and other melanocytic tumors[73]. Closer examination revealed that mutant receptor CysLTR2-L129$^{3.43}$Q was constitutively active with stronger $G\alpha_q$ coupling, while recruitment of ß-arrestins was attenuated compared to the WT receptor, and thus the receptor escaped down-regulation mechanisms associated with this pathway[73].

Studies on disease-associated mutations in extracellular loop 3 (ECL3) of the adhesion G protein-coupled receptor G1 (ADGRG1) revealed that mutated receptors ablated the serum response factor (SRF) response, while the signaling to nuclear factor of activated T cells (NFAT) pathways was unaffected[74]. Further elucidation of these signaling events uncovered mechanistic differences in these two pathways, which were initially brought to light by studying the disease-associated mutations.

While the precise implications of disease-related mutations in disease progression may not be fully understood, studying them offers an opportunity for obtaining a fundamentally better understanding of receptor signaling and their role in pathophysiology. Furthermore, this may lead to a potentially improved pharmacological strategy for conditions influenced by these mutations.

7.2.3.3 Mutations altering target-binding kinetics

While natural variants or disease-associated mutations in GPCRs can drastically influence downstream signaling, ligand binding may also be impacted which was described in **Chapter 6**. The impact of disease-associated mutations on receptor targeting by agonists and antagonists is generally investigated on the level of equilibrium binding affinity[75–80], while the effect on kinetic parameters association and dissociation rate constants (k_{on} and k_{off}) is less understood. Nevertheless, various studies have reported that single point mutations in GPCRs, introduced to better understand binding mechanisms, may affect one or both of these rate constants, and consequently the binding affinity.

A study with mutations introduced into the adenosine A_{2A} receptor ($A_{2A}R$) demonstrated the differential impact of single point mutations on antagonist dissociation, which was either decreased, increased or not affected[81]. Specifically, mutations in the binding pocket on amino acids typically involved in hydrogen bonding with the ligand prevented the formation of the hydrogen bonds and as such opened up the pocket and decreased the RT[81]. On the other hand, mutations on residues that are involved in the formation of a salt bridge with the ligands increased the dissociation rate constant of long RT ligands, while the effect on short RT ligands was less pronounced[82]. Similarly, in the muscarinic M_3 receptor, mutations on residues that were involved in locking the ligand into the receptor drastically decreased the RT[83].

While these studies only focused on the effect of mutations on ligand RT, a study by Swinney *et al.* also explored the effect of mutations in the human CC chemokine receptor 5 on the association rate constant[84]. They identified a kinetic fingerprint of residues that differentially affected k_{on} and/or k_{off} values of the ligand. Similarly, a study on mutations in $A_{2A}R$ demonstrated that changes in k_{on} values were observed, but that differences in binding

affinity were often derived from altered k_{off} values. Interestingly, while both k_{on} and k_{off} values of ligands for some mutated receptors were affected, the overall binding affinity of the ligands remained unchanged[85].

Altogether, these studies emphasized the influence single point mutations may have on kinetic binding parameters, which are overlooked when only reporting binding affinity. Accordingly, investigating target binding kinetics on mutated receptors, natural variants or disease-associated mutations, contributes to the overall understanding of receptor targeting and downstream signaling. Ultimately, this could contribute to more accurate selection of drugs in the application of precision medicine.

7.3 Final notes

In essence, this thesis explored the molecular pharmacological mechanisms of targeting CB_2R via investigation of novel drug discovery concepts such as target binding kinetics, allosteric modulation and biased signaling. Central to the investigation of CB_2R pharmacology was developing new assays and providing an overall kinetic view, aimed at bringing fresh insights that could be further integrated into the field of GPCR research. To this end, the development and application of state-of-the-art and novel cellular and biochemical assays contributed to a better understanding of agonist-mediated CB_2R activation and signaling, which can advance drug discovery efforts for treatments of diseases that involve CB_2R. Finally, *it's about time* that novel concepts for GPCRs are incorporated into early drug discovery programs, where a kinetic view is applied to provide a better translational perspective.

References

1. Hauser, A. S., Attwood, M. M., Rask-Andersen, M., Schiöth, H. B. & Gloriam, D. E. Trends in GPCR drug discovery: New agents, targets and indications. *Nat Rev Drug Discov* **16**, 829–842 (2017).
2. Chan, H. C. S., Li, Y., Dahoun, T., Vogel, H. & Yuan, S. New Binding Sites, New Opportunities for GPCR Drug Discovery. *Trends Biochem Sci* **44**, 312–330 (2019).
3. Waring, M. J. *et al.* An analysis of the attrition of drug candidates from four major pharmaceutical companies. *Nat Rev Drug Discov* **14**, 475–486 (2015).
4. Sun, D., Gao, W., Hu, H. & Zhou, S. Why 90% of clinical drug development fails and how to improve it? *Acta Pharm Sin B* **12**, 3049–3062 (2022).
5. Janero, D. R. Current strategic trends in drug discovery: the present as prologue. *Expert Opin Drug Discov* **19**, 147–159 (2023).
6. Coussens, N. P. *et al.* Assay Guidance Manual: Quantitative Biology and Pharmacology in Preclinical Drug Discovery. *Clin Transl Sci* **11**, 461–470 (2018).
7. Wang, F. I., Ding, G., Ng, G. S., Dixon, S. J. & Chidiac, P. Luciferase-based GloSensor™ cAMP assay: Temperature optimization and application to cell-based kinetic studies. *Methods* **203**, 249–258 (2022).
8. Copeland, R. A., Pompliano, D. L. & Meek, T. D. Drug–target residence time and its implications for lead optimization. *Nat Rev Drug Discov* **5**, 730–739 (2006).
9. Copeland, R. A. The drug–target residence time model: a 10-year retrospective. *Nat Rev Drug Discov* **15**, 87–95 (2016).
10. IJzerman, A. P. & Guo, D. Drug–Target Association Kinetics in Drug Discovery. *Trends Biochem Sci* **44**, 861–871 (2019).
11. O'Hayre, M. *et al.* The Emerging Mutational Landscape of G-proteins and G-protein Coupled Receptors in Cancer. *Nat Rev Cancer* **13**, 424 (2013).
12. Bongers, B. J. *et al.* Pan-cancer functional analysis of somatic mutations in G protein-coupled receptors. *Sci Rep* **12**, 1–15 (2022).
13. Huh, E. *et al.* Recurrent high-impact mutations at cognate structural positions in class A G protein-coupled receptors expressed in tumors. *Proc Natl Acad Sci U S A* **118**, (2021).
14. Chaudhary, P. K. & Kim, S. An Insight into GPCR and G-Proteins as Cancer Drivers. *Cells* **10**, 3288 (2021).
15. Hoare, S. R. J., Tewson, P. H., Quinn, A. M., Hughes, T. E. & Bridge, L. J. Analyzing kinetic signaling data for G-protein-coupled receptors. *Sci Rep* **10**, 12263 (2020).
16. Zaccolo, M., Zerio, A. & Lobo, M. J. Subcellular Organization of the cAMP Signaling Pathway. *Pharmacol Rev* **73**, 278–309 (2021).
17. Guo, D., Mulder-Krieger, T., IJzerman, A. P. & Heitman, L. H. Functional efficacy of adenosine A_{2A} receptor agonists is positively correlated to their receptor residence time. *Br J Pharmacol* **166**, 1846–1859 (2012).
18. Petrucci, V. *et al.* Pepcan-12 (RVD-hemopressin) is a CB2 receptor positive allosteric modulator constitutively secreted by adrenals and in liver upon tissue damage. *Sci Rep* **7**, 1–14 (2017).
19. Cullum, S. A., Veprintsev, D. B. & Hill, S. J. Kinetic analysis of endogenous β_2-adrenoceptor-mediated cAMP GloSensor™ responses in HEK293 cells. *Br J Pharmacol* **180**, 1304–1315 (2022).
20. de Vries, L., Finana, F., Cathala, C., Ronsin, B. & Cussac, D. Innovative Bioluminescence Resonance Energy Transfer Assay Reveals Differential Agonist-Induced D2 Receptor Intracellular Trafficking and Arrestin-3 Recruitment. *Mol Pharmacol* **96**, 308–319 (2019).
21. Turu, G. *et al.* Biased Coupling to β-Arrestin of Two Common Variants of the CB_2 Cannabinoid Receptor. *Front Endocrinol (Lausanne)* **12**, 903 (2021).
22. Møller, T. C., Moo, E. Von, Inoue, A., Pedersen, M. F. & Bräuner-Osborne, H. Characterization of the real-time internalization of nine GPCRs reveals distinct dependence on arrestins and G proteins. *Biochim Biophys Acta Mol Cell Res* **1871**, 119584 (2024).
23. DeWire, S. M., Ahn, S., Lefkowitz, R. J. & Shenoy, S. K. β-Arrestins and Cell Signaling. *Annu Rev Physiol* **69**, 483–510 (2007).
24. Crépieux, P. *et al.* A comprehensive view of the ß-arrestinome. *Front Endocrinol (Lausanne)* **8**, (2017).
25. Grundmann, M. *et al.* Lack of beta-arrestin signaling in the absence of active G proteins. *Nat Commun* **9**, (2018).
26. Soethoudt, M. *et al.* Cannabinoid CB_2 receptor ligand profiling reveals biased signalling and off-target activity. *Nat Commun* **8**, 1–14 (2017).

27. Xu, C. *et al.* REV, a BRET-based sensor of ERK activity. *Front Endocrinol (Lausanne)* **4**, 95 (2013).
28. Thorne, N., Inglese, J. & Auld, D. S. Illuminating Insights into Firefly Luciferase and Other Bioluminescent Reporters Used in Chemical Biology. *Chem Biol* **17**, 646–657 (2010).
29. Moroz, M. A. *et al.* Introducing a new reporter gene, membrane-anchored Cypridina luciferase, for multiplex bioluminescence imaging. *Mol Ther Oncolytics* **21**, 15–22 (2021).
30. Pandey, S. *et al.* Intrinsic bias at non-canonical, β-arrestin-coupled seven transmembrane receptors. *Mol Cell* **81**, 4605-4621.e11 (2021).
31. Kawakami, K. *et al.* Heterotrimeric Gq proteins act as a switch for GRK5/6 selectivity underlying β-arrestin transducer bias. *Nat Commun* **13**, (2022).
32. Boursier, M. E. *et al.* The luminescent HiBiT peptide enables selective quantitation of G protein-coupled receptor ligand engagement and internalization in living cells. *Journal of Biological Chemistry* **295**, 5124–5135 (2020).
33. Soave, M., Kellam, B., Woolard, J., Briddon, S. J. & Hill, S. J. NanoBiT Complementation to Monitor Agonist-Induced Adenosine A1 Receptor Internalization. *SLAS Discovery* **25**, 186–194 (2020).
34. Villalobos, V. *et al.* Dual-color click beetle luciferase heteroprotein fragment complementation assays. *Chem Biol* **17**, 1018–1029 (2010).
35. French, A. R., Meqbil, Y. J. & van Rijn, R. M. ClickArr: a novel, high-throughput assay for evaluating β-arrestin isoform recruitment. *Front Pharmacol* **14**, (2023).
36. Kumar, B. A., Kumari, P., Sona, C. & Yadav, P. N. GloSensor assay for discovery of GPCR-selective ligands. in *Methods in Cell Biology* vol. 142 27–50 (Academic Press Inc., 2017).
37. Remy, I. & Michnick, S. W. A highly sensitive protein-protein interaction assay based on Gaussia luciferase. *Nat Methods* **3**, 977–979 (2006).
38. England, C. G., Ehlerding, E. B. & Cai, W. NanoLuc: A Small Luciferase Is Brightening Up the Field of Bioluminescence. *Bioconjug Chem* **27**, 1175–1187 (2016).
39. Keegan, B. M. & Blagg, B. S. J. A Split Renilla Luciferase Complementation Assay for the Evaluation of Hsp90/Aha1 Complex Disruptors and Their Activity at the Aha1 C-Terminal Domain. *ACS Chem Biol* **18**, 184–192 (2023).
40. Liang, Y. & Li, Z. Split-Luciferase Complementation for Analysis of Virus–Host Protein Interactions. in *Plant Virology. Methods in Molecular Biology* (eds. Wang, A. & Li, Y.) vol. 2400 55–62 (Humana, New York, NY, 2022).
41. Kuchimaru, T. *et al.* A luciferin analogue generating near-infrared bioluminescence achieves highly sensitive deep-tissue imaging. *Nat Commun* **7**, (2016).
42. Gaitonde, S. A. & Bouvier, M. Enhanced Bystander BRET (ebBRET) Biosensors as Biophysical Tools to Map the Signaling Profile of Neuropsychiatric Drugs Targeting GPCRs. in *Schizophrenia. Methods in Molecular Biology* (eds. Urigüen, L. & Díez-Alacia, R.) vol. 2687 15–30 (Humana, New York, NY, 2023).
43. Wright, S. C. & Bouvier, M. Illuminating the complexity of GPCR pathway selectivity – advances in biosensor development. *Curr Opin Struct Biol* **69**, 142–149 (2021).
44. Wright, S. C. *et al.* BRET-based effector membrane translocation assay monitors GPCR-promoted and endocytosis-mediated G_q activation at early endosomes. *Proc Natl Acad Sci U S A* **118**, e2025846118 (2021).
45. Namkung, Y. *et al.* Monitoring G protein-coupled receptor and β-arrestin trafficking in live cells using enhanced bystander BRET. *Nat Commun* **7**, (2016).
46. Olsen, R. H. J. *et al.* TRUPATH, an open-source biosensor platform for interrogating the GPCR transducerome. *Nat Chem Biol* **16**, 841–849 (2020).
47. De, A., Ray, P., Loening, A. M. & Gambhir, S. S. BRET3: a red-shifted bioluminescence resonance energy transfer (BRET)-based integrated platform for imaging protein-protein interactions from single live cells and living animals. *The FASEB Journal* **23**, 2702–2709 (2009).
48. Dragulescu-Andrasi, A., Chan, C. T., De, A., Massoud, T. F. & Gambhir, S. S. Bioluminescence resonance energy transfer (BRET) imaging of protein-protein interactions within deep tissues of living subjects. *Proc Natl Acad Sci U S A* **108**, 12060–12065 (2011).
49. Boon, K., Vanalken, N., Meyen, E., Schols, D. & Van Loy, T. REGA-SIGN: Development of a Novel Set of NanoBRET-Based G Protein Biosensors. *Biosensors (Basel)* **13**, (2023).
50. Scott-Dennis, M. *et al.* Development of a membrane-based Gi-CASE biosensor assay for profiling compounds at cannabinoid receptors. *Front Pharmacol* **14**, (2023).

51. Ma, X., Leurs, R. & Vischer, H. F. NanoLuc-Based Methods to Measure β-Arrestin2 Recruitment to G Protein-Coupled Receptors. in *G Protein-Coupled Receptor Screening Assays. Methods in Molecular Biology.* (eds. Martins, S. A. M. & Prazeres, D. M. F.) vol. 2268 233–248 (Humana, New York, NY, 2021).
52. Janicot, R. *et al.* Direct interrogation of context-dependent GPCR activity with a universal biosensor platform. *Cell* **187**, 1–20 (2024).
53. Kayser, C., Melkes, B., Derieux, C. & Bock, A. Spatiotemporal GPCR signaling illuminated by genetically encoded fluorescent biosensors. *Curr Opin Pharmacol* **71**, 102384 (2023).
54. Yeh, H.-W. & Ai, H.-W. Development and Applications of Bioluminescent and Chemiluminescent Reporters and Biosensors. *Annual Rev. Anal. Chem. 2019* **12**, 129–150 (2019).
55. Demby, A. & Zaccolo, M. Investigating G-protein coupled receptor signalling with light-emitting biosensors. *Front Physiol* **14**, 1310197 (2024).
56. Radoux-Mergault, A., Oberhauser, L., Aureli, S., Luigi Gervasio, F. & Stoeber, M. Subcellular location defines GPCR signal transduction. *Sci Adv* **9**, (2023).
57. Eiger, D. S., Hicks, C., Gardner, J., Pham, U. & Rajagopal, S. Location bias: A "Hidden Variable" in GPCR pharmacology. *BioEssays* **45**, (2023).
58. Inoue, A. *et al.* Illuminating G-Protein-Coupling Selectivity of GPCRs. *Cell* **177**, 1933–1947 (2019).
59. Li, A., Liu, S., Huang, R., Ahn, S. & Lefkowitz, R. J. Loss of biased signaling at a G protein-coupled receptor in overexpressed systems. *PLoS One* **18**, e0283477 (2023).
60. Chen, G. & Obal, D. Detecting and measuring of GPCR signaling – comparison of human induced pluripotent stem cells and immortal cell lines. *Front Endocrinol (Lausanne)* **14**, (2023).
61. White, C. W., Vanyai, H. K., See, H. B., Johnstone, E. K. M. & Pfleger, K. D. G. Using nanoBRET and CRISPR/Cas9 to monitor proximity to a genome-edited protein in real-time. *Sci Rep* **7**, 3187 (2017).
62. White, C. W., Caspar, B., Vanyai, H. K., Pfleger, K. D. G. & Hill, S. J. CRISPR-Mediated Protein Tagging with Nanoluciferase to Investigate Native Chemokine Receptor Function and Conformational Changes. *Cell Chem Biol* **27**, 499–510 (2020).
63. Avet, C. *et al.* Effector membrane translocation biosensors reveal G protein and Parrestin coupling profiles of 100 therapeutically relevant GPCRs. *Elife* **11**, e74101 (2022).
64. Slosky, L. M., Caron, M. G. & Barak, L. S. Biased Allosteric Modulators: New Frontiers in GPCR Drug Discovery. *Trends Pharmacol Sci* **42**, 283–299 (2021).
65. Ippolito, M. *et al.* Identification of a β-arrestin-biased negative allosteric modulator for the β_2-adrenergic receptor. *Proc Natl Acad Sci U S A* **120**, (2023).
66. Cook, A. E. *et al.* Biased allosteric modulation at the CaS receptor engendered by structurally diverse calcimimetics. *Br J Pharmacol* **172**, 185–200 (2015).
67. Rook, J. M. *et al.* Biased $mGlu_5$-Positive Allosteric Modulators Provide In Vivo Efficacy without Potentiating $mGlu_5$ Modulation of NMDAR Currents. *Neuron* **86**, 1029–1040 (2015).
68. Slosky, L. M. *et al.* ß-Arrestin-Biased Allosteric Modulator of NTSR1 Selectively Attenuates Addictive Behaviors. *Cell* **181**, 1364–1379 (2020).
69. Wang, J. *et al.* β-arrestin–biased allosteric modulator potentiates carvedilol-stimulated β adrenergic receptor cardioprotection. *Mol Pharmacol* **100**, 568–579 (2021).
70. De Pascali, F. *et al.* β_2-Adrenoceptor agonist profiling reveals biased signalling phenotypes for the β_2-adrenoceptor with possible implications for the treatment of asthma. *Br J Pharmacol* **179**, 4692–4708 (2022).
71. Yang, L. K., Hou, Z. S. & Tao, Y. X. Biased signaling in naturally occurring mutations of G protein-coupled receptors associated with diverse human diseases. *Biochim Biophys Acta Mol Basis Dis* **1867**, (2021).
72. Carrasquer, A., Nebane, N. M., Williams, W. M. & Song, Z. H. Functional consequences of nonsynonymous single nucleotide polymorphisms in the CB2 cannabinoid receptor. *Pharmacogenet Genomics* **20**, 157–166 (2010).
73. Ceraudo, E. *et al.* Direct evidence that the GPCR CysLTR2 mutant causative of uveal melanoma is constitutively active with highly biased signaling. *Journal of Biological Chemistry* **13**, (2020).
74. Kishore, A. & Hall, X. R. A. Disease-associated extracellular loop mutations in the adhesion G protein-coupled receptor G1 (ADGRG1; GPR56) differentially regulate downstream signaling. *Journal of Biological Chemistry* **292**, 9711–9720 (2017).
75. Wang, X. *et al.* Cancer-Related Somatic Mutations in Transmembrane Helices Alter Adenosine A1 Receptor Pharmacology. *Molecules* **27**, 3742 (2022).

76. Wang, X. *et al.* Cancer-related somatic mutations alter adenosine A_1 receptor pharmacology - A focus on mutations in the loops and C-terminus. *The FASEB Journal* **36**, e22358 (2022).

77. Feng, C. *et al.* Cancer-Associated Mutations of the Adenosine A_{2A} Receptor Have Diverse Influences on Ligand Binding and Receptor Functions. *Molecules* **27**, 4676 (2022).

78. Wang, X. *et al.* Characterization of cancer-related somatic mutations in the adenosine A_{2B} receptor. *Eur J Pharmacol* **880**, 173126 (2020).

79. den Hollander, L. S. *et al.* Impact of cancer-associated mutations in CC chemokine receptor 2 on receptor function and antagonism. *Biochem Pharmacol* **208**, 115399 (2023).

80. van der Velden, W. J. C., Heitman, L. H. & Rosenkilde, M. M. Perspective: Implications of Ligand−Receptor Binding Kinetics for Therapeutic Targeting of G Protein-Coupled Receptors. *ACS Pharmacol. Transl. Sci* **2020**, 179–189 (2020).

81. Guo, D. *et al.* Molecular basis of ligand dissociation from the adenosine A_{2A} receptor. *Mol Pharmacol* **89**, 485–491 (2016).

82. Segala, E. *et al.* Controlling the Dissociation of Ligands from the Adenosine A_{2A} Receptor through Modulation of Salt Bridge Strength. *J Med Chem* **59**, 6470–6479 (2016).

83. Tautermann, C. S. *et al.* Molecular Basis for the Long Duration of Action and Kinetic Selectivity of Tiotropium for the Muscarinic M3 Receptor. *J Med Chem* **56**, 8746–8756 (2013).

84. Swinney, D. C. *et al.* A study of the molecular mechanism of binding kinetics and long residence times of human CCR5 receptor small molecule allosteric ligands. *Br J Pharmacol* **171**, 3364–3375 (2014).

85. Zhukov, A. *et al.* Biophysical mapping of the adenosine A_{2A} receptor. *J Med Chem* **54**, 4312–4323 (2011).

List of abbreviations

2-AG	2-arachidonoylglycerol
$A_{2A}R$	Adenosine A_{2A} receptor
AC	Adenylate cyclase
AD	Alzheimer's disease
ADGRG1	Adhesion G protein-coupled receptor G1
ADME	Absorption, distribution, metabolism and excretion
AEA	*N*-arachidonoylethanolamide, anandamide
Aha1	ATPase homologue 1
ALS	Amyotrophic lateral sclerosis
ANOVA	Analysis of variance
ATP	Adenosine triphosphate
AUC	Area under the curve
BAM	Biased allosteric modulator
BCA	Bicinchoninic acid
$ß_2AR$	$ß_2$-adrenoceptor
B_{max}	Receptor expression level
BRET	Bioluminescence resonance energy transfer
BUN	Blood urea nitrogen
cAMP	Cyclic adenosine monophosphate
CaR	Calcium-sensing receptor
CB_1R	Cannabinoid CB_1 receptor
CB_2R	Cannabinoid CB_2 receptor
CBD	Cannabidiol
CBD-DMH	Cannabidiol-dimethylheptyl
CBGluc	Click beetle green luciferase
CBluc	Click beetle luciferase
CBN	Cannabinol
CBR	Cannabinoid receptor
CBRluc	Click beetle red luciferase
CCR2	CC chemokine receptor 2
CHO	Chinese hamster ovary
CINV	Chemotherapy-induced nausea and vomiting
cLogP	Octanol-water partition coefficient
Cluc	Cypridina luciferase
CNS	Central nervous system
COPD	Chronic obstructive pulmonary disease
CREA	Creatinine
cryo-EM	Cryo-electron microscopy
C-term	C-terminus
CysLTR2	Cysteinyl leukotriene receptor 2
DAGL	Diacylglycerol lipase
Δ^9-THC	Delta-9-tetrahydrocannabinol
dpm	Disintegrations per minute
DTT	DL-dithiothreitol
EA	Enzyme acceptor
ebBRET	Enhanced bystander BRET
EC_{50}	Functional potency
eCBs	Endocannabinoids
ECL	Extracellular loops
ECS	Endocannabinoid system
ELISA	Enzyme-linked immunosorbent assay
E_{max}	Efficacy
ERK1/2	Extracellular signal-related kinase 1 and 2
ET	Engagement time
EYFP	Enhanced yellow fluorescent protein
f.c.	Final concentration
FAAH	Fatty-acid amide hydrolases
FCS	Fetal calf serum
FDA	Food and Drug Administration
Fluc	Firefly luciferase

FSK	Forskolin
GDC	Genomic Data Commons
GDP	Guanosine diphosphate
GFP	Green fluorescent protein
GIRK	G protein-coupled Inward Rectifying K+-channel
Gluc	Gaussia luciferase
GPCR	G protein-coupled receptor
GRK	G protein-coupled receptor kinase
GTP	Guanosine triphosphate.
HBSS	Hank's Balanced Salt Solution
HEK293T	Human embryonic kidney 293 T
HER2	Human epidermal growth factor 2
hiPSC	Human induced pluripotent stem cells
Hsp90	Heat shock protein 90
IBMX	3-isobutyl-1-methylxanthine
IBS	Inflammatory bowel disease
IC_{50}	Half-maximal inhibitory concentration
ICL	Intracellular loops
IR_{50}	Kinetic potency
IR_{max}	Kinetic efficacy
K_D	Kinetic affinity
K_i	Inhibition constant
KO	Knockout
k_{obs}	Observed association rate constant
k_{off}	Dissociation rate constant
k_{on}	Association rate constant
LgBiT	Large BiT
LIMBA	Lipid Membrane Binding Assay
LogD	Octanol/water distribution coefficient
MAGL	Monoacylglycerol lipase
MAPK	Mitogen-activated protein kinase
MS	Multiple sclerosis
NAL	Neutral allosteric ligands
NAM	Negative allosteric modulator
NanoBiT	NanoLuc Binary Technology
NAPE-PLD	*N*-acylphosphatidylethanolamine-specific phospholipase D
NFAT	Nuclear factor of activated T cells
NLuc	NanoLuc luciferase
NSB	Non-specific binding
N-term	N-terminus
NTS	Neurotensin
NTSR1	Neurotensin receptor 1
PAM	Positive allosteric modulator
PAMPA	Passive membrane permeability assay
PAS	Periodic Acid-Schiff
PBS	Phosphate buffered saline
PD	Parkinsons's disease
PDB	Protein Data Bank
PDE	Phosphodiesterase
PK	Prolink
PMSF	Phenylmethylsulfonyl fluoride
PTM	Post-translational modification
PTX	Pertussis Toxin
Rab	Rab-GTPase
Rluc	Renilla luciferase
RMSD	Root mean square deviation
RT	Residence time
rt	Room temperature
$S1P_1$	Sphingosine-1-phosphate receptor 1
SD	Standard deviation
SEM	Standard error of the mean
SmBiT	Small BiT
SRF	Serum response factor
TB	Total binding
TBS	Tris-buffered saline
TBST	Tris-buffered saline TWEEN 20

TM	Transmembrane
TMB	3,3',5,5'-Tetramethylbenzidine
UVM	Uveal melanoma
WT	Wild type
YFP	Yellow fluorescent protein

Nederlandse samenvatting

Minstens een derde van alle op de markt gebrachte geneesmiddelen grijpen aan op G eiwit-gekoppelde receptoren (GPCRs). Echter zijn er veel kandidaat-geneesmiddelen die in de klinische fasen afvallen door een gebrek aan effectiviteit in de mens. Zodoende is er een betere vertaalslag tussen *in vitro* preklinische resultaten en *in vivo* effecten nodig voor een succesvoller translationeel perspectief. Om deze reden zijn nieuwe concepten ontwikkeld en toegepast die steeds meer erkenning krijgen binnen de vroege stadia van geneesmiddelonderzoek. Dit proefschrift richt zich specifiek op de concepten van receptorbindingskinetiek, allostere modulatie en voorkeurssignaaltransductie voor de cannabinoïde CB_2 receptor (CB_2R), een veelbelovende GPCR voor de behandeling van ontstekingsaandoeningen.

Hoofdstuk 1 bespreekt de hoofdthema's die centraal staan in dit proefschrift. Na een introductie over de structuur, functie en signaaltransductie van G eiwit-gekoppelde receptoren worden de nieuwe concepten receptorbindingskinetiek, allostere modulatie en voorkeurssignaaltransductie toegelicht. Hierna wordt het endocannabinoïde systeem, waar CB_2R deel van uitmaakt, geïntroduceerd en de therapeutische mogelijkheden voor CB_2R activatie besproken.

In **Hoofdstuk 2** wordt een uitgebreid protocol beschreven voor het rekruteren van ß-arrestine-2 na activatie van cannabinoïde receptoren door agonisten. Het protocol kan ook gebruikt worden voor binding van antagonisten en inverse agonisten door respectievelijk co-incubatie met een agonist of verlenging van de incubatietijd. Het hoofdstuk toont aan dat de PathHunter ß-arrestine-2 technologie eenvoudig te gebruiken is voor een snel onderzoek naar ligand-gemedieerde activatie van cannabinoïde receptoren. Deze technologie is verder toegepast in **Hoofdstuk 5** voor het onderzoeken van orthostere en allostere activatie van CB_2R.

Hoofdstuk 3 beschrijft de ontwikkeling van een nieuwe methode om twee verschillende signaaltransducties na activatie van CB_2R te meten. Het combineren van twee luminescente technologieën presenteert voor het eerst de mogelijkheid om gelijktijdig en kinetisch cAMP productie en de rekrutering van ß-arrestine-2 te detecteren na CB_2R activatie. De toepasbaarheid van deze gecombineerde methode is bewezen door het screenen van veelgebruikte preklinische en klinisch geteste agonisten voor CB_2R. De functionele resultaten zijn geïnterpreteerd via het gebruik van een eindpunt, een semi-kinetische en een kinetische analyse om de tijdsafhankelijkheid van de agonist-gemedieerde CB_2R activatie te bepalen. De bindingskinetiek van de agonisten is bepaald in radioligand bindingsstudies voor een uitgebreide profilering van alle stoffen. Agonist-gemedieerde activatie en signaaltransductie van CB_2R was tijdsgevoelig voor verschillende synthetische agonisten, terwijl dit niet van toepassing was op de endogene agonisten. Vergelijkbare activatie parameters werden verkregen uit semi-kinetische en kinetische analysemethoden, terwijl de laatste aanvullende snelheidsconstanten opleverde voor het beginnen en afnemen van het signaal. Snelle associatie (k_{on}) van agonisten met CB_2R resulteerde in verhoogde affiniteit en activatie, terwijl langzaam dissocierende (k_{off}) agonisten de interactie tussen CB_2R en ß-arrestine-2

verlengden. Er werd geen significante voorkeurssignaaltransductie waargenomen in ons systeem. Alles bij elkaar toont dit hoofdstuk de mogelijkheid voor het combineren van functionele responsen en het uitvoeren van kinetische analyses om GPCR activatie door agonisten uitgebreid te profileren. Deze profilering creëert de mogelijkheid om de *in vivo* farmacologische effecten van GPCR activatie beter te voorspellen.

Hoofdstuk 4 toont een andere toepassing van de associatiesnelheidsconstante om een nieuw toegangsmechanisme te voorspellen voor lipofiele agonisten. In dit hoofdstuk zijn *in silico*, *in vitro* en *in vivo* methodes gecombineerd om een nieuwe selectieve CB_2R agonist LEI-102 te karakteriseren. Vier cryo-elektronenmicroscopie (cryo-EM) structuren zijn opgehelderd met selectieve CB_2R agonisten LEI-102, APD-371 en HU308, en niet-selectieve agonist CP55,940. Op basis van deze structuren is de invloed van verschillende aminozuren op agonist-gemedieerde receptoractivatie onderzocht door middel van functionele mutagenese experimenten. Alhoewel de algehele receptor structuren vergelijkbaar waren, hadden de agonisten verschillende interacties met aminozuren rond de bindingsplaats. Verder werden twee potentiële toegangsmechanismes voor de agonisten naar de bindingsplaats onderzocht, enerzijds via de extracellulaire lus 2 of anderzijds via een membraankanaal tussen de transmembraandomeinen 1 en 7. Het combineren van de mutagenese data en de associatiesnelheidsconstanten van de agonisten leidde tot de constatering dat lipofiele agonisten, zoals HU308 en de endogene agonisten, gebruik lijken te maken van een membraankanaal om de bindingsplaats te bereiken, terwijl de meer polaire agonisten een andere route gebruiken. Als laatste werd de veelbelovende *in vivo* werkzaamheid van orale toediening van LEI-102 aangetoond in een chemotherapie-geïnduceerd nefropathiemodel zonder het veroorzaken van bijwerkingen via het centraal zenuwstelsel.

In **Hoofdstuk 5** is een alternatieve toepassing van de dissociatiesnelheidsconstante beschreven om allostere interacties met CB_2R aan het licht te brengen. Positief allostere interacties met CB_2R werden gesuggereerd voor cannabidiol-dimethylheptyl (CBD-DMH), maar niet structurele analoog cannabidiol (CBD), door het concentratie-afhankelijk beïnvloeden van de dissociatiesnelheidsconstante van een radioactieve inverse agonist. In functionele experimenten gedroeg CBD-DMH zich als negatieve allostere modulator van verschillende synthetische en endogene agonisten op de activatie van het G eiwit, maar niet voor het rekruteren van ß-arrestine-2. Daarnaast gedroeg CBD-DMH zich ook als partiële orthostere agonist voor G eiwit activatie en ß-arrestine-2 rekrutering. Samen suggereert dit een dubbele allosteer en orthosteer werkingsmechanisme voor CBD-DMH op CB_2R, wat een nieuwe klasse moleculen zou kunnen opleveren voor CB_2R activatie.

In **Hoofdstuk 6** wordt de overstap gemaakt naar gemuteerde CB_2Rs door het focussen op mutaties in CB_2R die in tumorweefsel van patiënten zijn gevonden. De implicaties op de functionaliteit van de muteerde receptoren en de doelgerichtheid van geneesmiddelen wordt onderzocht. Mutaties rond de bindingsplaats of in de buurt van geconserveerde motieven beïnvloedden de receptoractivatie aanzienlijk. De mate van binding en activatie van de gemuteerde CB_2R wisselde afhankelijk van de mutatie-agonist combinatie onderzocht. De effecten op binding en activatie waren minder uitgesproken voor mutaties in de N- en C-uiteinden. Dit hoofdstuk benadrukt het belang van het onderzoeken van het CB_2R genotype van patiënten alvorens toediening van geneesmiddelen gebaseerd op CB_2R

agonisten.

Tot slot vat **Hoofdstuk 7** het hele proefschrift samen aan de hand van belangrijke aspecten binnen de vroege fasen van geneesmiddelonderzoek. Daarnaast wordt er uitgeweid over mogelijkheden om het onderzoek beschreven in dit proefschrift te vervolgen met het oog op nieuwe analyses, verdere ontwikkeling van experimentele methodes en het combineren van de verschillende concepten die centraal stonden in dit proefschrift.

Alles bij elkaar benadrukt het werk in dit proefschrift het belang van het bestuderen van kinetische bindings- en activatieparameters voor het ophelderen van orthostere en allostere activatie van CB_2R. Door het combineren en ontwikkelen van verschillende biochemische en cellulaire methodes samen met de implementatie van nieuwe analysemethodes brengt dit proefschrift nieuwe mogelijkheden om de profilering van orthostere en allostere liganden te verbeteren tijdens de vroege fasen van geneesmiddelonderzoek. Daarnaast wordt de toegevoegde waarde van het bestuderen van verschillende CB_2R varianten beschreven voor enerzijds een beter fundamenteel begrip van ligand-receptor interacties, maar ook de implicaties voor geneesmiddeltoediening aan patiënten met gemuteerde CB_2Rs. Deze waardevolle bevindingen kunnen bijdragen aan de verbetering van toekomstig onderzoek en ontwikkeling van geneesmiddelen voor CB_2R en andere GPCRs.

List of publications

Part of this thesis

Bouma, J., Kumar, S.S., van den Berg, B.J.W., van der Horst, C., Hoare, S.R.J., Guba, W., Wittwer, M., Grether, U., van der Stelt, M., Heitman, L.H. (2024). Kinetic multiplex assay to assess biased signaling of clinical agonists at the cannabinoid CB_2 receptor. *Manuscript in preparation*.

Bouma, J., Broekhuis, J.D., van der Horst, C., Kumar, P., Ligresti, A., van der Stelt, M., & Heitman, L.H. (2023). Dual allosteric and orthosteric pharmacology of synthetic analog cannabidiol-dimethylheptyl, but not cannabidiol, on the cannabinoid CB_2 receptor. *Biochemical Pharmacology*, **218**, 115924.

Li, X.*, Chang, H.*, **Bouma, J.***, de Paus, L. V., Mukhopadhyay, P., Paloczi, J., Mustafa, M., van der Horst, C., Kumar, S.S., Wu, L., Yu, Y., van den Berg, R.J.B.H.N., Janssen, A.P.A., Lichtman, A., Liu, Z.-J., Pacher, P., van der Stelt, M., Heitman, L.H., Hua, T. (2023). Structural basis of selective cannabinoid CB_2 receptor activation. *Nature Communications*, **14**(1), 1447.

Bouma, J., Soethoudt, M., van Gils, N., Xia, L., van der Stelt, M., & Heitman, L.H. (2022). Cellular assay to study β-arrestin recruitment by the cannabinoid receptors 1 and 2. In *Endocannabinoid Signaling: Methods in Molecular Biology* (pp. 189-199). New York, NY: Springer US.

** These authors contributed equally*

Other publications

Mach, L., Omran, A., **Bouma, J.**, Radetzki, S., Sykes, D. A., Guba, W., Li, X., Höffelmeyer, C., Hentsch, A., Gazzi, T., Mostinski, Y., Wasinska-Kalwa, M., de Molnier, F., van der Horst, C., von Kries, J.P., Vendrell, M., Hua, T., Veprintsev, D.B., Heitman, L.H., Nazare, M. (2024). Highly Selective Drug-Derived Fluorescent Probes for the Cannabinoid Receptor Type 1 (CB1R). *Manuscript accepted; Journal of Medicinal Chemistry.*

Wasinka-Kalwa, M., Omran, A., Mach, L., **Bouma, J.**, Scipioni, L., Li, X., Radetzki, S., Mostinski. Y., Schippers, M., Gazzi, T., van der Horst, C., Brennecke, B., Hanske, A., Kolomeets, Y., Guba, W., Sykes, D., von Kries, J.P., Broichhagen, J., Hua, T., Veprintsev, D., Heitman, L.H., Oddi, S., Maccarrone, M., Grether, U., Nazare, M. (2024). Visualization of membrane localization and functional state of CB2R pools by matched agonist and inverse agonist probe pairs. *Manuscript submitted.*

Vlachodimou, A., **Bouma, J.**, De Cleyn, M., Berthelot, D., Pype, S., Bosmans, J.P., van Vlijmen. H., Wroblowski, B., Heitman, L.H., IJzerman, A.P. (2023). Kinetic profiling of novel spirobenzo-oxazinepiperidinone derivatives as equilibrative nucleoside transporter 1 inhibitors. *Purinergic Signalling*, 1-13.

Nakladal, D., Buikema, H., Romero, A.R., Lambooy, S.P.H., **Bouma, J.**, Krenning, G., Vogelaar, P., van der Graaf, A.C., Groves, M.R., Kyselovic, J., Henning, R.H., Deelman, L.E. (2019). The (*R*)-enantiomer of the 6-chromanol derivate SUL-121 improves renal graft perfusion via antagonism of the α_1-adrenoceptor. *Scientific Reports*, **9**(1), 13.

Oral and poster communications

Biased signaling of clinical CB_2R agonists

2023 **Oncornet2.0 Final symposium** (*poster*)
Amsterdam, the Netherlands

2023 **ACS Fall 2023** (*oral*)
Hybrid, online presentation

2023 **Gordon Research Conference "Cannabinoid Function in the CNS"** (*poster*)
Barcelona, Spain

2023 **Gordon Research Seminar "Cannabinoid Function in the CNS"** (*poster*)
Barcelona, Spain

Structural basis of CB_2R activation

2023 **LACDR Spring symposium** (*poster*)
Leiden, the Netherlands

2023 **Oncode TU/e meeting** (*oral*)
Leiden, the Netherlands

2023 **Guest lecture at F. Hoffmann-La Roche Ltd.** (*oral*)
Basel, Switzerland

2022 **ULLA Summer school** (*poster*)
Uppsala, Sweden

2022 **International Cannabinoid Research Society Meeting** (*oral*)
Galway, Ireland
Awarded predoctoral presentation award

2022 **FIGON Dutch Medicines Day & EUFEPS Annual meeting** (*oral*)
Leiden, the Netherlands
Awarded EUFEPS WIPS Women in Pharmaceutical Sciences Award 2022

Allosteric modulation of CB_2R

2022 **LACDR Spring symposium** (*poster*)
Leiden, the Netherlands

2021 **FIGON Dutch Medicines Day** (*poster*)
Leiden, the Netherlands

2021 **LACDR Spring symposium** (*poster*)
Online

2020 **LACDR Spring symposium** (*poster*)
Online

Curriculum vitae

Jara Bouma was born in Woerden, the Netherlands, on April 4th 1996. She graduated from pre-university education at Stellingwerf College, Oosterwolde (Friesland, the Netherlands) in 2014, after which she continued with the Bachelor's program Life Science & Technology at the University of Groningen (Groningen, the Netherlands) with a major in Medical Pharmaceutical Sciences. Her Bachelor internship into the molecular mechanisms of a novel α_1-adrenoceptor antagonist under supervision of dr. Dalibor Nakladal, dr. Leo Deelman and dr. Hendrik Buikema at the Department of Clinical Pharmacy and Pharmacology, University Medical Center Groningen (Groningen, the Netherlands), resulted in a co-authorship on a publication. During these three years, she also took the opportunity to attend a semester at Umeå University (Umeå, Sweden).

After graduating in 2017, she started the Master's program Bio-Pharmaceutical Sciences at Leiden University (Leiden, the Netherlands). As part of her Master's, she performed a nine-month internship at the division of Medicinal Chemistry (formerly known as Drug Discovery and Safety) under supervision of dr. Anna Vlachodimou and prof.dr. Laura H. Heitman. This project focused on the characterization of structure-affinity and structure-kinetic relationships of inhibitors for the equilibrative nucleoside transporter 1 (ENT1), which resulted in co-authorship on a publication. A second internship was performed at the Central Laboratory Animal Facility/Department of Anatomy and Embryology at Leiden University Medical Center (Leiden, the Netherlands) under the supervision of prof. dr. Daniela Salvatori where she performed a comparative analysis of stem-cell derived xenografts and human germ cell tumors. During the second year of her Master's Jara also joined the Leiden Leadership Program, an extracurricular honours program at Leiden University, for which she performed a consultancy project at insurance company Zorg en Zekerheid (Leiden, the Netherlands).

In 2019 she started as a PhD candidate at the division of Medicinal Chemistry of the LACDR under supervision of prof. dr. Laura H. Heitman and prof. dr. Mario van der Stelt. Her project focused on the molecular pharmacological characterization of the cannabinoid CB_2 receptor by applying novel drug discovery concepts. This project was funded by the Dutch Research Council (NWO Vidi #16573) and as such she frequently shared her research findings with experts in the field as part of the User Committee. Her PhD project was highly collaborative in nature, while she also took part in multiple external collaborations, reflected by the publications listed in this thesis. Moreover, she presented her work at national and international conferences. In 2022 she was awarded the EUFEPS Women in Pharmaceutical Sciences Award at the FIGON Dutch Medicines Days, as well as the predoctoral presentation award at the International Cannabinoid Research Society Meeting for her presentation 'Molecular basis for selective activation and target engagement of cannabinoid CB_2 receptor agonists'. In 2023 she visited the Pharma Research and Early Development site of F. Hoffmann-La Roche (Basel, Switzerland) as guest scientist for two weeks to get acquainted with preclinical drug research in the pharmaceutical industry.

Jara is currently working as program manager at ZonMw in Den Haag.

Acknowledgements

I am grateful to have been surrounded by inspiring scientists and wonderful people these past years without whom my PhD and the work presented in this thesis would not have been realized. Hence, *it's about time* to thank all the remarkable people that have helped me through this journey.

First of all, I would like to express my gratitude to my promotors Laura and Mario for their trust, guidance and support during every stage of my PhD. Laura, your extensive pharmacological knowledge, dedication and constructive criticism have helped me become a better scientist. Mario, your knowledge of the cannabinoid field has challenged me to put results into perspective and focus on the bigger picture.

My PhD projects relied greatly on collaborations with various academic and industrial partners. I would like to convey my thanks to Xiaoting Li, Tian Hua (iHuman Institute, ShanghaiTech University), Pal Pacher (NIH), Anthe Janssen (Leiden Institute of Chemistry), Alessia Ligresti (National Research Council of Italy), Wolfgang Guba, Matthias Wittwer (Roche), Isabelle Geron (Revvity) and Sam Hoare (Pharmechanics) for their significant theoretical, practical and analytical input. Your contributions have been key for the successful completion of my PhD. I wish to extend my appreciation to Ad IJzerman (LACDR), Herman van Vlijmen (Johnson & Johnson), Arne Rufer, Uwe Grether (Roche) and Rob Hermans (NWO), for their endless advice and support during all our Vidi meetings. I would like to give special credit to Uwe for initiating and inviting me to join many collaborations and welcoming me into his home whilst visiting Roche.

I am grateful to all my students, Jeremy, Sanjay, Silke, Ikram, Barry, Mea, Lynn, Jenny and Yasmine, for their enthusiasm and contributions to various projects in this thesis. Their help was invaluable to complete the projects and they have taught me to become a better supervisor.

Special thanks to all my colleagues from the division with whom I shared many scientific discussions, coffee breaks, lab outings, parties and more fun times. It was great being part of this group. In particular I want to thank Cas, Rongfang and Jaco for their excellent support in the lab. Lisa and Xuesong, thank you for your great scientific insights, but more importantly being there to just talk and vent about failed experiments and so much more. Inge, thank you for joining me to all the classes at the USC to clear our minds and just let go of the stress (for a bit). I have been lucky to have started this PhD journey alongside two more amazing female scientists. Majlen and Marina, thank you for the support that I received during the ups and downs of this PhD by means of dinner evenings, many glasses of wine or cocktails and relaxing spa trips.

Thank you to all my friends for their fun distractions, support and down-to-earth perspective that have kept me going these years. Ilse, I am very grateful to have you by my side during my defense. Also lots of thanks to my family for their unconditional love and continuous support.

Lastly and most importantly, Sebas (or dr. Dekkers), you have been my favorite discovery during my PhD. You celebrated my achievements, supported me through the low points, and helped me put things into perspective. Thank you!